Laser powder bed fusion fabrication of Alloy 718: an insight from printing to post-machining processes

Thesis submitted to the University of Nottingham for the degree of
Doctor of Philosophy (PhD)

Lingshan Li

Supervised by:
Dr. Hao Chen
Dr. Zhirong Liao
Prof. Dragos Axinte

Department of Mechanical, Materials and Manufacturing Engineering
Faculty of Science and Engineering

August 2024

PREFACE

This thesis is submitted for the degree of Doctor of Philosophy at the University of Nottingham. The research was carried out under the supervision of Dr Hao Chen, Dr Zhirong Liao and Professor Dragos Axinte in the Faculty of Science and Engineering.

It is certified that the work presented in this thesis is original, and suitable references are made to any work cited from the literature.

The list of publications from the work presented in this thesis is presented here:

[1] Lingshan Li, Hao Chen, Zhirong Liao, Yue Yang, Dragos Axinte, "**Investigation of the grain deformation to orthogonal cutting process of the textured Alloy 718 fabricated by laser powder bed fusion**". Int. J. Mach. Tools Manuf. 190 (2023), 104050. https://doi.org/10.1016/j.ijmachtools.2023.

[2] Lingshan Li, Hao Chen, Zhirong Liao, "**Effects of vector length on the melt pool morphology and grain structure characteristics of Alloy 718 in laser powder bed fusion**". J. Mater. Process. Technol. 326 (2024), 118317. https://doi.org/10.1016/j.jmatprotec.2024.118317.

[3] Lingshan Li, Shusong Zan, Zhirong Liao, Hao Chen, Dragos Axinte, "**Influence of Grain Morphology and Orientation on the Chip Formation Mechanisms of Wrought and Laser Powder Bed Fusion (LPBF) Fabricated Alloy 718**". J. Mater. Process. Technol. (Under review)

Lingshan Li

August 2024

ABSTRACT

Laser powder bed fusion (LPBF), an additive manufacturing (AM) technology, shows its potential in the fabrication of low-volume and high-geometrical complexity productions, owing to the unique vector-layer-part manufacturing manner. The process involves intense energy inputs that create melt pools characterised by steep thermal gradients and high cooling rates ranging from 10^4 to 10^6 K/s. This rapid solidification triggers the development of epitaxial grain growth patterns aligned with the build direction (BD), leading to unique microstructures when compared to conventional cast and wrought alloys.

Generally, the microstructure of LPBF-fabricated components mainly depends on scanning strategies and laser parameters, which control the preferential grain growth directions and form specific crystallographic textures. To evaluate the microstructure evolutions of different rotational angles, Alloy 718 samples with different crystallographic textures were fabricated by LPBF via three laser rotation angles, namely 0°, 67° and 90°. Moreover, different vector lengths are also widely used in the LPBF process to fill in the corners near the fabricated geometry borders. However, the effect of vector lengths on the microstructure is not well understood. Therefore, various vector lengths with unidirectional scanning direction were used to further investigate the effect of vector lengths on the microstructure. For the first time, multi-vector-length scanning strategies, namely Long-vector (4000 μm), Short-vector (80 μm), Long-Short vectors (4000 μm and 80 μm), and Incremental

vectors (ranging from 80 µm to 400 µm), are employed in this work for controlling the microstructure of as-built samples.

It was shown that the melt pool depth for Short-vector printing (about 138 µm) exceeded that of Long-vector printing (about 85 µm). This was due to that the energy densities were not the same at different vector lengths when considering the actual laser motion. The slow scanning speed caused excessive energy input in short vectors, resulting in narrow and deep melt pools. In addition, with the increase in vector length, grain size correspondingly increased from less than 20 µm in Short-vector printing to over 50 µm in Long-vector printing. However, this increase in grain size was accompanied by a reduction in microhardness, declining from approximately 347.6±7.5 to 298.2±4.4 HV(0.2). This is the first time in the literature to report the vector length effect on the grain structure characteristics in LPBF.

Since high dimensional accuracy and surface finish are required for the end-use of LPBF-fabricated parts, post-machining is employed to improve the surface quality of the as-built components. To further understand the machining-induced deformation and chip formation of components fabricated by LPBF, the Alloy 718 samples with typical textures (fabricated by 0°, 67° and 90° rotational scanning strategies) are employed for the post-machining tests. A “quasi-in-situ” grain deformation investigation method and a quick-stop cutting method are used with the pendulum-based orthogonal cutting machine to investigate the machined surface deformation and chip formation mechanisms, respectively.

The crystallographic level deformation history for hundreds of microns during a high strain rate shear removal deformation was illustrated. Due to the carefully retained deformation history (i.e., typical bulges and slip bands) on the surface, a repeated deformation pattern was observed, attributing to the non-homogeneous deformation of typical build-directional blocks. The most active slip trace of deformed grain was calculated and verified based on the dominated slip bands within individual grains. The slip trace direction and intensity were quantified for different textured Alloy 718. Since the slipping-based deformation for an orientated grain was represented by its most active slip trace, a deformation tendency map was obtained by combining the shear direction, slip system and grain morphology. It was revealed that grains in high texture intensity workpieces generally followed the macro shear-based deformation, while with the decrease in texture intensity, the plastic anisotropy was significant at the grain scale.

By retaining chips on the workpieces in the quick-stop cutting test, it was found that the elongated grains in LPBF-fabricated Alloy 718 significantly influenced the material pile-up behaviour along the shear direction. This leads to an increase in shear angle and a decrease in chip ratio when compared with the machining of equiaxed grains in the wrought sample. This is because the transition of shear deformation from the cutting edge to the free surface is hindered by long grain boundaries that are perpendicular to the cutting direction. Since the shear bands are hard to cross long grain boundaries, the deformation of LPBF-fabricated Alloy 718 is governed by grain boundary bending in the primary shear zone.

ACKNOWLEDGEMENTS

I would like to express my sincere gratitude to my supervisors, Dr Hao Chen, Dr Zhirong Liao and Professor Dragos Axinte, for their support and guidance throughout my project and thesis writing. I am especially grateful to Hao for his invaluable assistance with my PhD project and thesis writing. His meticulous attention to detail and comprehensive guidance have been instrumental to the success of this project. My thanks go to Zhirong for his crucial support with my experiments and exchange experience. His encouragement has been instrumental in finishing our project successfully. I also extend my deepest appreciation to Dragos for supporting my exchange at UNUK, fostering my critical thinking skills and expanding my academic horizons. His assistance has greatly contributed to my academic and personal growth during this period.

I appreciate all the help received from the technicians, John Zhu and Helen Xu from UNNC, as well as Stephen Hall and Daniel Forman from the University Technology Centre (UTC) UNUK. I would like to thank Dr Nigel Neate from the Nanoscale and Microscale Research Centre, University of Nottingham, for their support for EBSD training. I also thank Dr Rui Yang and Mr Zhe Guo from Ningbo Institute of Materials Technology and Engineering, Chinese Academy of Sciences, for their support for the micro-hardness test.

I thank my friends and fellow PhD students, Yue Yang, Shusong Zan, Yifei Zeng, Fengrui Zhang, Kege Xie, Jinyi Li, Xiao Han, Huimin Wangzi, Lei Qiu, Erik Abba,

Kieran Winter, Artem Bogatyrev, Dr Jose Robles, Dr Omkar Mypati, for their support and friendship throughout all my unique PhD experiences.

I would like to express my gratitude to my parents, Jiaji Yang and Xuemei Li, and my grandmother for unwavering support throughout my student life. Their encouragement and belief in me have been the cornerstone of my achievements. I would also thank my girlfriend, Jing Zheng, for her support, understanding and love during my PhD period. Her presence has brought balance to my life and provided me with the strength to persevere.

Abbreviations

AFM	Abrasive flow machining
AM	Additive manufacturing
ASTM	American Society for Testing and Materials
BD	Build direction
BUE	Build-up edge
CA	Curving angle
CAD	Computer-aided design
CD	Cutting direction
CET	Columnar-to-equiaxed transition
CNC	Computer numerical control
CRSS	Critical resolved shear stress
DC	Direct current
DED	Directed energy deposition
DIC	Digital image correlation
DSP	Digital signal processor
EPBF	Electron powder bed fusion
EB-DED	Electron beam-directed energy deposition
EBSD	Electron backscatter diffraction
ECCI	Electron channelling contrast imaging
ED	Energy density
EDM	Electrical discharge machining
EDS	Energy dispersive spectroscopy
FCC	Face-centred cubic
FSD	Forescatter diodes
GB	Grain boundary
GND	Geometrically necessary dislocation

HCP	Hexagonal close-packed
HSSZ	High Shear Strain Zone
HV	Vickers hardness
IA	Incline angle
IPF	Inverse pole figure
ISO	International Organization of Standardization
KAM	Kernel average misorientation
LDED	Laser-directed energy deposition
LPBF	Laser Powder Bed Fusion
LSSZ	Low Shear Strain Zone
MA	Misorientation angle
MC	Metal carbide
MPB	Melt pool boundary
OM	Optical microscopy
PAS	Primary arm spacing
PBF	Powder bed fusion
PF	Pole figures
PIV	Particle image velocimetry
QS	Quick stop
RTC	Real-time controller
SD	Shear direction
SE/ SE2	Secondary electron
SEM	Scanning electron microscopy
SLM	Selective laser melting
SP	Shear plane
SPN	Shear plane normal
STL	Stands for stereolithography
TEM	Transmission electron microscopy
TKD	Transmission Kikuchi diffraction
UI	User interface

VED	volumetric energy density

Nomenclatures

D	Laser beam diameter
$\boldsymbol{F}$	Deformation gradient
$\boldsymbol{F}^{*}$	Deformation caused by lattice rotation
$\boldsymbol{F}^{\boldsymbol{p}}$	Deformation caused by plastic shearing
H	Hatch spacing
P	Laser power
T	Layer thickness
V	Scanning speed
$\overline{VED}$	Average volumetric energy density
$\mathrm{a}^{\alpha\beta}$	Dimensionless coefficient
b	Burger vector
b^{α}	Slip direction for slip system α
d_{g}	Distance to the closest GB
$g_{ik}^{she \to sample}$	Transformation matrix
h_o	Hardening parameter for slip system β
$h^{\alpha\beta}$	Hardening moduli
K_{S}	Dimensionless constant that controls the storage of dislocations
l^{s}	Dislocation mean along the system s
m	Sensitivity of the hardening moduli
n^{α}	Slip plane normal for slip system α
$q^{\alpha\beta}$	Latent hardening ratio
s_s	Saturation stress
s^{β}	Slip resistance at hardening saturation
t_a	Acceleration time
t_m	The most active slip trace

t_s	Tracking error time
v_t	Target speed
x_s	Distance delay
$\mathrm{y_c}$	Effective annihilation distance between dislocations
α	Slip system α
β	Slip system β
ε	Shear strain
$\dot{s}^{\alpha}$	Slip resistance
$\dot{\rho}^{s}$	Dislocation density
$\in_{ij}^{crystal}$	Shear strain loaded in the crystal frame
$\in_{ij}^{sample}$	Shear strain loaded in the sample frame
$\in_{shear}$	Shear deformation gradient
$\mathrm{\rho}^{\mathrm{\beta}}$	Dislocation density in β slip system
$\mathrm{\tau_c^a}$	Critical resolved shear stress
γ_n	Rake angle
$\delta\gamma^{\alpha}$	Shear increment at slip system
ϕ_n	Shear angle
$\mathrm{\delta w}$	Work increment
$\mathrm{\mu}$	Shear modulus

Contents

List of Figures

List of Tables

Chapter 1 Introduction

1.1 Background

After over 30 years of development, metal additive manufacturing (AM) has demonstrated its capability in designing and manufacturing structural-functional components for end-use in industries [1–3], especially for the fabrication of small-batch components with great geometrical complexity [4] that are used in aviation and aerospace fields. Laser powder bed fusion (LPBF) is a category of AM that utilises the laser as the heat source to melt metal powders to form 3D components [5]. In the LPBF process, the extremely thin metal powder layer (about 20 to 200 μm [6,7]) is spread on the substrate. Then the powder bed is selectively melted by a laser beam under the control of the galvanometer. The substrate is then lowered with the thickness of the powder layer for the next powder spreading and laser scanning. By repeating this process, melted laser tracks are bonded to each other on a layer and layers are stacked to form the component. Many alloys (e.g., AlSi10Mg, Ti6Al4V, Alloy 718, etc.) have been successfully manufactured by LPBF with high density and good mechanical properties compared with traditional cast products.

For the component fabricated by LPBF, its quality and microstructure are dependent on laser parameters such as laser power, scanning speed and scanning strategies [8]. Laser power controls the amount of energy delivered to the metal powder bed, influencing the melting of the powder and temperature distribution of the melt pool. The energy deposition rate is decided by the scanning speed, further affecting the thermal conduction and solidification rate of the melt pool. An appropriate combination of laser power and scanning speed is crucial for the stability of the powder melting and solidification. This can further affect the porosity, grain morphology and crystallographic texture of fabricated components. Moreover, since the combination of laser power and scanning speed provides different energy densities to melt the metal powder, the grain growth pattern during melt pool solidification can be controlled by the provided thermal condition. This finally leads to unique grain morphologies that are different from those formed via conventional methods (e.g., casting and forging). The LPBF-fabricated microstructure can be further developed via scanning strategies, which control the grain growth pattern among layers. This usually can be achieved by the rotational scanning directions or customised laser scanning paths on each layer [9]. Therefore, LPBF technology appears to have great potential in controlling the microstructure of metallic components [10,11] due to the flexible utilisation of laser parameters and scanning strategies.

LPBF is widely recognised as a technique to fabricate components from multiple vectors in a single layer, then to multiple layers, and finally to finished components. However, the common design of printing parameters usually starts from an individual layer that is composed by many individual vectors. This cannot fulfil the potential of LPBF technology in the localised microstructure control down to the vector scale. The main challenge is that the scanning strategy is not designed for an individual vector but for a large area consisting of multiple vectors. Few works tried to manipulate each vector to control the microstructure of LPBF-fabricated components. It has been reported that the melt pool morphology and fabrication quality might be influenced by vector lengths [12–14]. However, few works tried to systematically investigate the melt pool morphology evolution of different vector lengths.

Moreover, the formation of unique grain morphology and crystallographic texture during the LPBF process is mainly attributed to the epitaxial grain growth in the rapid melt pool solidification. The cooling rate of a melt pool usually reaches 10^4 ~10^6 K/s [15], leading to cellular structures within the LPBF-fabricated grains. Since these grains are preferred to grow along the build direction (BD), the high aspect ratio of LPBF-fabricated grains usually leads to anisotropic mechanical properties. Therefore, the typical grain morphology and orientation, as well as the substructure within the grains, lead to different mechanical properties when compared to cast and wrought components.

One of the nickel-based superalloys, Alloy 718, has been widely recognised for its excellent mechanical properties and corrosion resistance in aerospace industry and LPBF technology has been successfully used to build Alloy 718 components with different crystallographic textures. It is also recognised that the additively manufactured Alloy 718 components are often subjected to post-mechanical machining operations to achieve the required dimensional accuracy and functional surface performances [16]. Understanding the response of the textured structure and grain morphology to mechanical machining is, therefore, critical to evaluating the machinability of LPBF-fabricated alloy. Moreover, chip formation is also significantly important to the machining quality and surface accuracy [17]. Hence, it is also necessary to understand the underpinning effects of the crystallographic textures on the chip formation. However, it is quite challenging to characterise the deformation behaviour of textured grains near the primary shear zone due to the separation of the chip and workpiece after cutting.

1.2 Aims and objectives

This thesis aims to investigate the role of scanning strategies in additively manufactured microstructure and then to analyse the effect of microstructure on machining-induced deformation and chip formation. In particular, LPBF technology is employed to fabricate crystallographic textured Alloy 718 with different rotational angles and vector lengths. A pendulum-based orthogonal cutting machine with a customised quick-stop module is used for the machining tests.

Accordingly, the specific objectives of this project are:

1) To investigate the grain morphology and texture influenced by rotational scanning strategies.
2) To analyse the role of the laser control system in the LPBF-fabricated process.
3) To control the printing parameters for each vector and characterise the microstructure evolution in LPBF-fabricated Alloy 718 with different vector lengths.
4) To analyse the influence of unique grain structure and texture formed by

LPBF on the machining-induced deformation.

5) To design a quick-stop module for the pendulum-based cutting machine.
6) To investigate chip formation mechanisms influenced by the grain structure and texture formed by LPBF.

1.3 Structure of the thesis

This PhD thesis mainly includes the following contents: **Chapter 1** provides the research background and motivation and objectives of the study. In **Chapter 2**, a comprehensive literature review introduces the principle of additive manufacturing, the microstructure of Alloy 718 influenced by printing parameters, the principle of the laser control system, as well as microstructural impacts on post-machining and chip formation mechanisms. **Chapter 3** details the experiment methods in this thesis, including Alloy 718 fabrication via laser powder bed fusion, pendulum-based cutting test with/without quick-stop module and microstructure characterisation, as well as the crystal plasticity simulation. **Chapter 4** presents the effect of vector lengths on the melt pool and microstructure of LPBF-fabricated Alloy 718. **Chapter 5** studies the microstructure evolution during pendulum-based cutting for three representative textured Alloy 718 formed by LPBF technology via a “quasi-in-situ” investigation method. **Chapter 6** investigates the chip formation mechanisms of these three typical textured Alloy 718 by the pendulum-based cutting machine with a quick-stop module. Finally, the main conclusions for this thesis are summarised in **Chapter 7** and suggestions for future work are given in **Chapter 8**.

Chapter 2 Literature Review

2.1 Additive manufacturing (AM)

2.1.1 Metal additive manufacturing

Additive manufacturing (AM), also known as 3D printing, enables the fabrication of components from a digital 3D model layer by layer. It has a unique advantage for low-volume production fabrication, especially for those with high geometry complexity or for design validation of prototype parts [4,18]. Owing to its revolutionary manufacturing process that builds an object layer by layer via transferring a 3D model (generally designed by CAD software with stereolithography (STL) format [19]) into multiple individual 2D layers. This allows many structures with high cost and difficulty in traditional manufacturing (e.g. lattice and topological structures) to be fabricated directly. It exhibits great potential in different industries, such as aerospace, medical, nuclear and automotive [20].

According to the International Organization of Standardization (ISO)/ American Society for Testing and Materials (ASTM) [21], there are five categories of AM process: (i) powder bed fusion (PBF) [22–24], (ii) directed energy deposition (DED) [25,26], (iii) material jetting [27,28], (iv) binder jetting [29], and (v) sheet lamination [30]. PBF and DED are well developed and widely used technologies, being classified into laser-based and electron-based processes according to differences in the heat source. The laser-based process includes laser powder bed fusion (LPBF) and laser directed energy deposition (LDED), while electron beam powder bed fusion (EBM or E-PBF) and electron beam directed energy deposition (EB-DED) belong to the electron-based process.

2.1.2 Laser powder bed fusion (LPBF)

Laser powder bed fusion (LPBF) is a category of AM that utilises the laser as the heat source to melt metal powders to form 3D components [31–33]. Many alloys (e.g., AlSi10Mg [34], Ti6Al4V [35], Alloy 718 [36], etc.) have been successfully manufactured by LPBF with high density and good mechanical properties compared with traditional cast products. The digital model of a 3D part is generated using computer-aided design (CAD) software and is sliced into multiple layers along the build direction (BD), with each layer having a thickness of approximately tens of microns. After reading the slicing data, the machine controls the laser and scanner to work with the platform and recoater co-ordinately, and then the laser can melt the powder with the designated path and laser parameters. Both LPBF and EBM are melting powder layer by layer to build the object. However, the former melts the powder in a gas-protected chamber (argon or nitrogen) rather than a near-vacuum chamber. Compared to a hundred microns of powder thickness in EBM [37], the powder layer thickness of LPBF is usually not more than a hundred microns (20 μm to 60 μm in general [38,39]). The thinner powder thickness in LPBF allows higher precision but lower manufacturing efficiency than EBM.

A schematic of LPBF process is shown in Figure 2.1. The optical system mainly consists of fibre laser, scanner mirrors and f-θ lens. The final laser scanning path is controlled by two scanner mirrors (galvanometer scanners). One mirror governs the laser beam path along the x-axis, whilst the other mirror controls laser placement along the y-axis. The laser is then focused by f-θ lens and positioned at the selected point. The building system consists of a build platform, substrate, powder storage (residual powder collection), powder collector and recoater. After one layer is printed, the build platform will drop one layer thickness and the powder storage platform will rise one layer thickness. Then the recoater moves from right to left along its track, pushing the powder to spread on the building platform. Since the powder storage platform area is larger than its building area, the rest of the powder will be collected by the powder collector. Finally, after the powder is spread on the previous layer/substrate, the laser will melt the selected area on the powder bed. During this printing cycle, the continuous gas flow (N_2 or Ar) is provided to remove the black smoke from the laser-powder reaction zone.

The unique layer-by-layer fabrication process of LPBF technology has been developing rapidly since this concept was proposed in the 1990s. It has the potential to enhance the material properties, both in performance and function, by printing the right materials in the right positions [1]. Multi-material manufacturing is investigated to combine the advantages of different metals, aiming to obtain comprehensive mechanical properties [40,41]. Moreover, the application in aerospace and automotive industries usually requires high printing efficiency and large building areas. The multi-laser powder bed fusion was developed to employ two or more lasers scanning the selected area simultaneously [42]. This allows larger building area and speed during the printing process. Laser beam shape also exhibits an important role in process stability, surface quality and mechanical properties. Although the Gaussian beam is still the commonly used laser beam in LPBF technology, other beam shapes, such as donut, variable ring, top-hat, and elliptical, are also showing the potential to further improve productivity, melt pool morphology and microstructure [43].

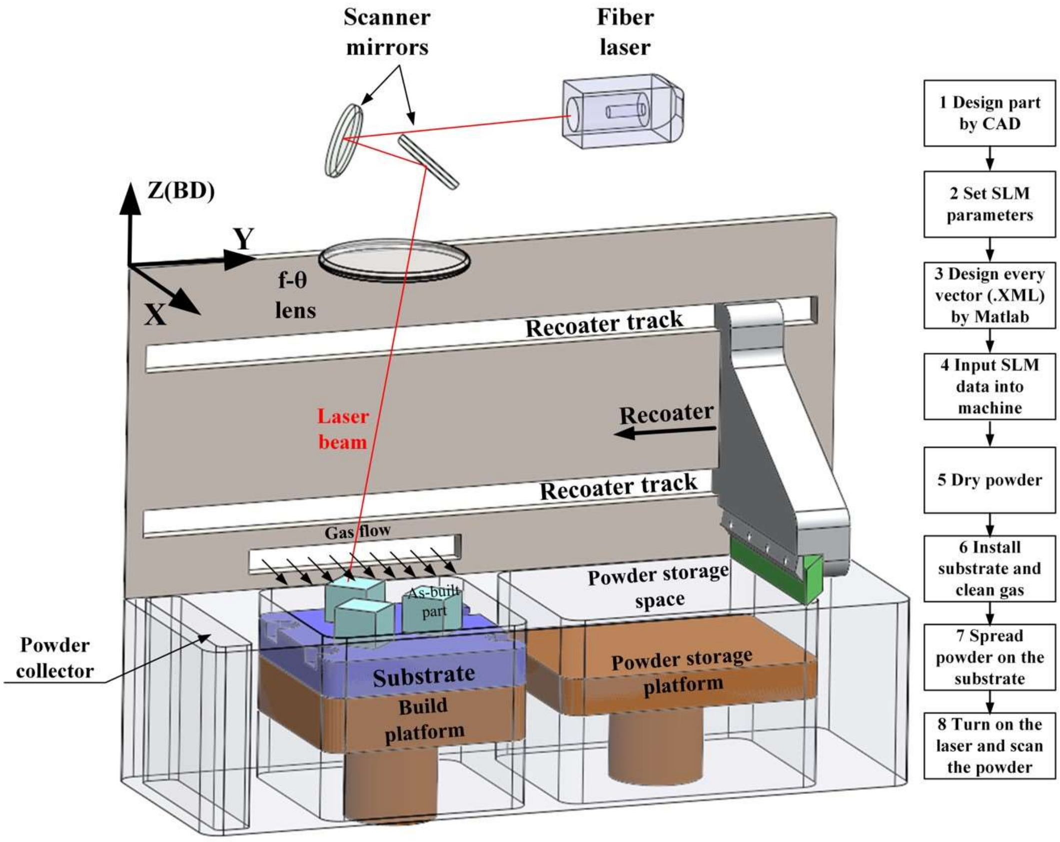

Figure 2.1: A schematic diagram of the laser powder bed fusion (LPBF) process.

2.1.3 Laser scanning control system

Laser scanning systems play a crucial role in precisely controlling the movement and positioning of the laser beam during the LPBF process. The laser motion is controlled by the real-time controller (RTC), a software driver for real-time control of scan heads and lasers based on a fast digital signal processor (DSP) system. The

RTC consists of two kinds of commands: control commands and list commands. The former is used for setting some general parameters and controlling execution of the codes whilst the latter is opened by a control command and is processed by RTC in real time, including jump commands, mark commands as well as commands for laser parameters (e.g., jump speed, mark speed and laser power). The jump and mark commands are referred to as vectors as they are depicted by multiple segment lines with specific directions and lengths.

Figure 2.2 shows the schematics of jump and mark vectors. A mark vector is a line with a specific direction, while a polyline consists of serval mark vectors [44]. The jump vector connects two non-contiguous mark vectors. These vectors require the X and Y coordinates of the endpoint as parameters. When the jump command is executed, the laser is switched off, and the scanner mirrors move fast. In contrast, the controller automatically turns on the laser at the beginning of a mark command and the laser moves along the vector with a defined scanning speed and laser power to melt the powder during LPBF.

In order to control the galvanometer scanners to scan a vector, each vector (including both jump and mark vectors) is divided into small steps as shown in Figure 2.2(b). The scan head is, therefore, able to implement these micro steps with a constant time rate Δt. It is noted that the period Δt is in the order of 10 μs and the length of each micro-step is dependent on the scanning speed.

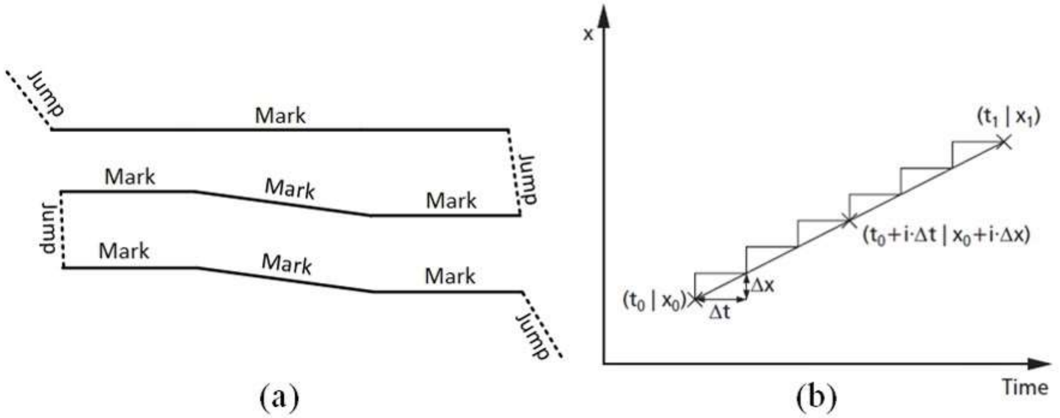

Figure 2.2: (a) Schematic of mark and jump commands (or vectors) and (b) Micro-steps of a vector [44].

In the actual laser scanning process, due to the moment of inertia of the limited rotation direct current (DC) galvo motor and its rotary coil carrying the mirror for the laser, it requires time and distance to decelerate to zero velocity, turn, and then accelerate to achieve constant velocity [45]. For example, when the laser moves through the intersections of jump-mark vector and mark-mark vector in Figure 2.2(a). This implies that at the beginning/end of a vector, the scanning speed may fail to reach the target speed, resulting in excessive energy input. Moreover, the real scanning distance is shorter than the vector length due to the acceleration/deceleration phase. To compensate for the length error, a commonly used method is to introduce a series of delays that extend the actual scanning time. This allows the laser to scan for a longer time with the target speed, reducing the error caused by the inertia of the mirrors (or mirror acceleration).

Figure 2.3 [44] shows three kinds of delays in the laser scanning process. A vector scanning process is implemented by many microvectors (or micro steps) as shown in Figure 2.3 (a), but the scan mirror needs to accelerate to the target speed in the actual scanning process. As a result, there is a lag occurring between the set and actual position. To reduce the error caused by this lag, a jump delay is set at the end of the jump vector. This jump delay provides extra time to ensure that the laser reaches the end position. Similarly, the delay is also employed in the mark vector for the same reason. However, since the laser turns on in the mark vector, the mirror acceleration leads to the excessive energy input (or burn-in effect) at the beginning and end of a vector. To mitigate the burn-in effect (overheating induced by high energy input [46]), laser on/off delays are used in this command (Figure 2.3(b)). The laser is switched on after the completion of the initial micro steps, allowing the mirrors to reach a certain scanning speed. Furthermore, the laser should not switch off immediately due to the lag between the set and the real position. Therefore, the laser off delay is used to offset the lag by extending the scanning time as shown in Figure 2.3(b). It should be noted that the laser on/off period can be treated as instantaneous (less than 10^{-6} s), leading to limited impact on energy input. Therefore, the energy input deviation is mainly caused by the speed change during laser-on/off delay.

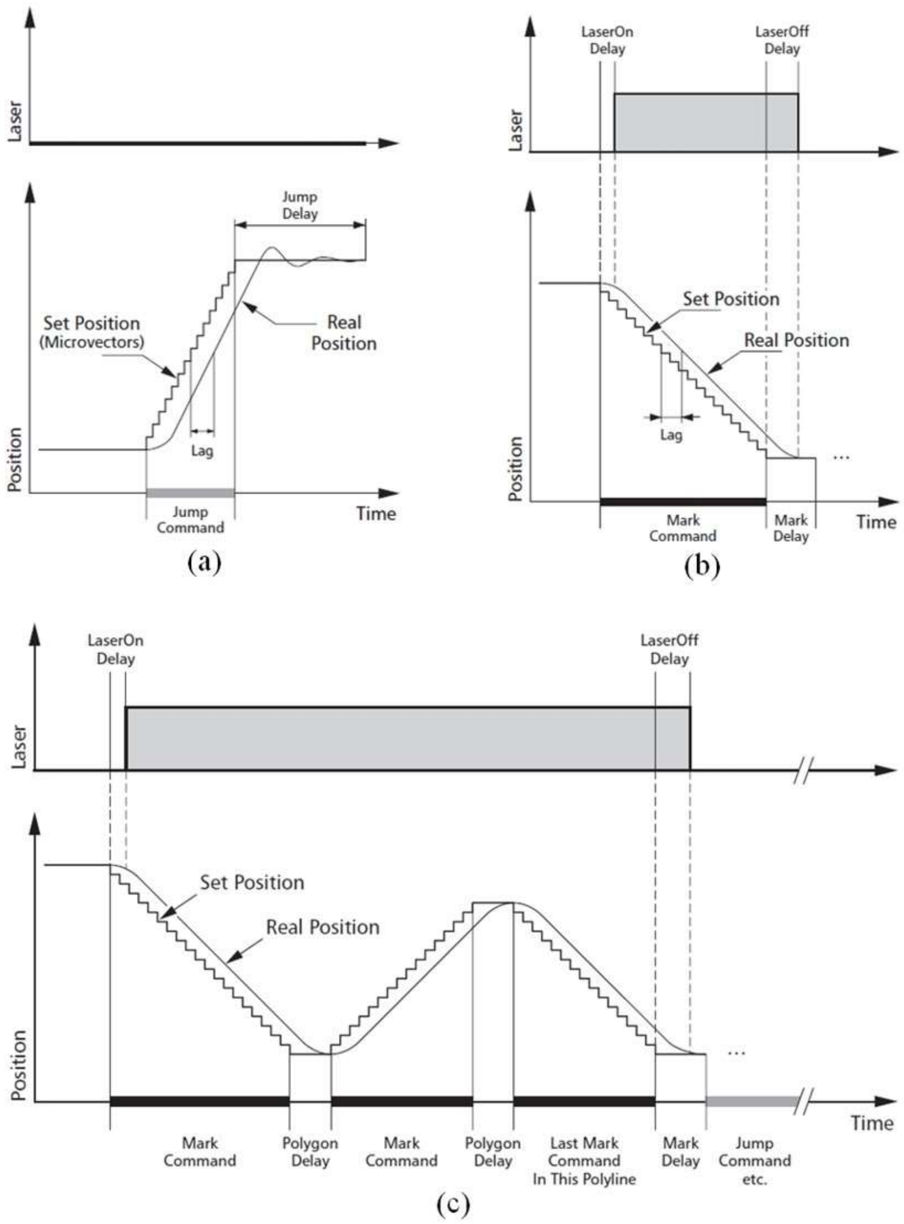

Figure 2.3: Laser and scan head control timing during different commands [44]. (a) Jump vector, (b) Mark vector and (c) Polyline.

Polygon delay is employed for two successive mark vectors as depicted in Figure 2.3(c), because there is no need to stop the scanners as mark delay in Figure 2.3(b). Generally, the laser is not switched off when scanning two successive mark vectors unless the adjacent vectors are defined in two individual execution sequences, respectively. However, if the angle between two marks is too large (e.g., 180°), the laser will be switched off and turned to the next vector. The laser on/off delay is a result of the balance between melt pool quality and productivity based on the thermal properties of the material.

2.1.4 Process parameters

For LPBF, fabrication quality is strongly dependent on process parameters that generally include laser power, scanning speed, layer thickness, hatch spacing, as well as variable scanning strategies [47]. The first four parameters mainly contribute to the energy input, which is key to fully melting powder, bonding adjacent layers/tracks and controlling defects such as porosity and crack.

To estimate the energy input, laser power is not sufficient to show the actual energy input because (i) scanning speeds vary laser reaction time at a unit distance of a laser track, producing differences in energy input; (ii) layer thicknesses influence the laser absorption, affecting the actual energy input; (iii) different widths of the hatch spacing affect the proportion of solidified alloy and powder (i.e. wider hatching spacing means that laser reacts with more powder compared with narrow hatching spacing). In order to quantify energy input during laser reaction with powder, energy density (ED) is defined. As mentioned above, it consists of laser power, scanning speed, layer thickness and hatch spacing. It should be noticed that ED shows pronounced differences even when the laser beam diameter (or focal offset) is slightly changed [48,49]. This may partly explain why an optimal laser parameter is unreliable when used in another machine of different companies [50–53].

ED is a function with laser power P, scanning speed V, layer thickness t, hatch spacing H and beam diameter D. The function is initially defined as linear energy density in which P is divided by V, describing the energy input condition directly. Further, areal energy density and volumetric energy density (VED) are used to reveal energy input more specifically. Although VED has its limitation [54] in linking the laser parameters with component characteristics [55,56] such as melt pool morphology, defects and surface roughness, it is a widely used function to represent the relationship among laser parameters. Details of commonly used energy density functions are shown in Table 2.1.

Table 2.1: Different energy density function

Equation	**Energy density**	**References**
$\boldsymbol{ED_L = \frac{P}{V}}$	Linear energy density	[57–59]
$\boldsymbol{ED_a = \frac{P}{VH}}$	Areal energy density	[60]
$\boldsymbol{ED_a = \frac{P}{VD}}$		[61]
$\boldsymbol{VED = \frac{P}{VDH}}$	Volumetric energy density	[62]
$\boldsymbol{VED = \frac{P}{VDt}}$		

Scanning strategies only change the way of energy input via either different laser moving directions or a certain rotation degree among layers, revealing potentials to change grain texture [63] and balance residual stress accumulation [47]. Commonly used scanning strategies in LPBF process are summarised in Figure 2.4 [47], including chessboard/island (Figure 2.4(a)) [64–67], ZigZag/bi-directional (Figure

2.4(b)) [63,68], ZigZig/unidirectional [69,70], degree-rotation between adjacent layers (Figure 2.4 (c-f)) and in/out scanning (Figure 2.4(g) and (h)) [71–73]. Some self-defined scanning strategies were reviewed by Jia et al. [9], including point melting scan, helix scan and Hilbert scan. By rotating the laser scanning directions (usually 67° [47], 90° [35] or 0° [74]) layer by layer, it is efficient to relieve the inhomogeneous thermal circle induced by laser scanning.

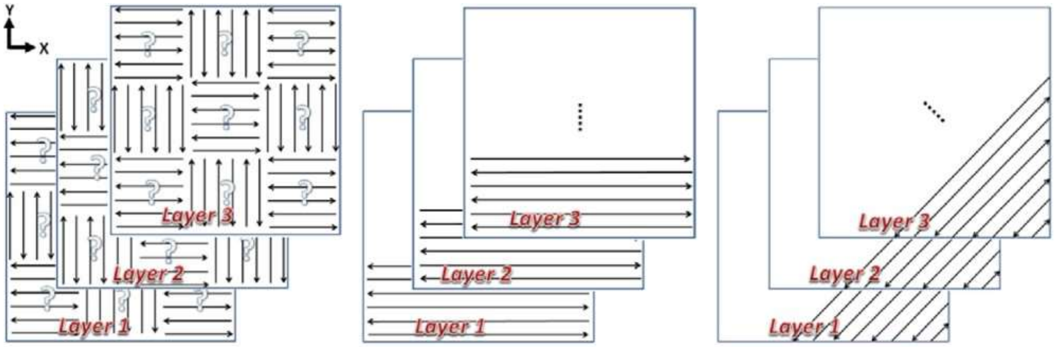

(a) Island scanning (b) Line scanning (c) 45° line scanning

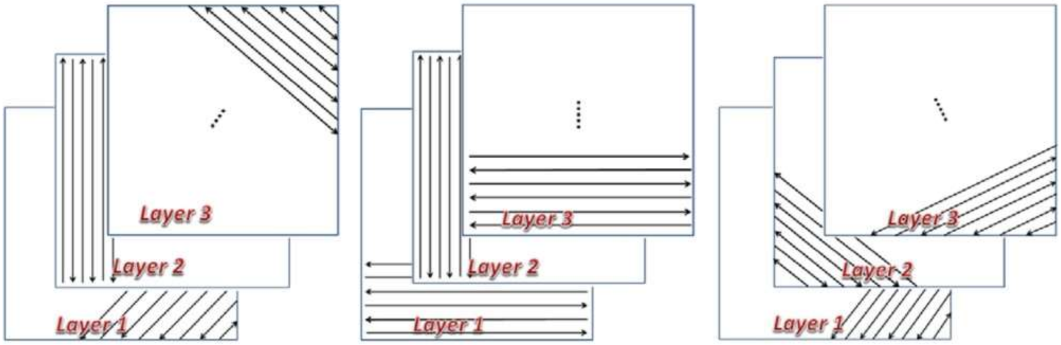

(d) 45° rotate scanning (e) 90° rotate scanning (f) 67° rotate scanning

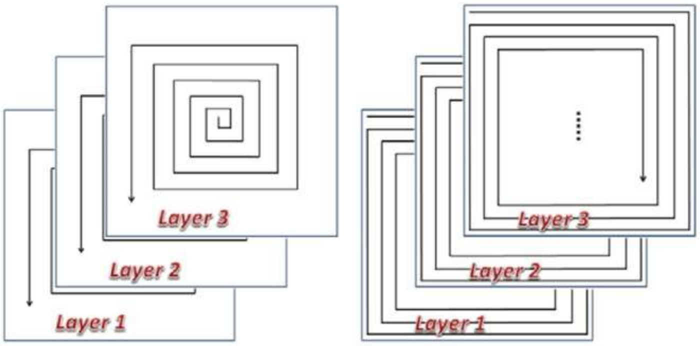

(g) In-out scanning (h) Out-in scanning

Figure 2.4: Different scanning strategies [47]. (a) Island scanning; (b) Line scanning; (c)

45° line scanning; (d) 45° rotate scanning; (e) 90° rotate scanning; (f) 67° rotate scanning; (g) In-out scanning; (h) Out-in scanning.

2.2 LPBF-fabricated Alloy 718

2.2.1 Alloy 718

As the laser scanning strategy exhibits the potential to determine the quality and mechanical properties of as-built components, it is also essential to understand the mechanisms of scanning strategy that influence a specific material. Alloy 718, one of the most commonly used nickel-based superalloys, is widely used in aviation, aerospace and energy industries due to its stable thermomechanical properties over 650 °C [75]. Owing to its excellent resistance to hot corrosion and oxidation, as well as high-temperature strength, it is usually exposed to extremely high-temperature environments, such as turbine blades and compressors [76]. Alloy 718 is mainly composed of elements of nickel, iron and chromium, as well as small amounts of niobium, molybdenum, titanium, aluminium, cobalt, carbon and manganese [77]. γ is the matrix phase in Alloy 718, primarily consisting of a face-centred cubic (FCC) structure of nickel and iron, providing good mechanical properties. There are two major strengthening mechanisms in Alloy 718: (1) solid solution strengthening (elements such as molybdenum, chromium, and iron dissolved in the nickel matrix, creating a solid solution that distorts the lattice and impedes dislocation motion); (2) precipitation strengthening (the γ' and γ'' phases precipitate within the γ matrix, impeding dislocation movement and thus increasing strength) [78].

The continuous γ matrix in Alloy 718 is shown in Figure 2.5 [79,80], a face-centred cubic (FCC, A1) (lattice constant: 0.3553 nm) with a high fraction of solid solution elements (Fe, Cr and Mo). Other strengthening carbide and inter-metallic phases consist of metal carbide (MC), metal nitride, fcc $\gamma' Ni_3$(Al, Ti, Nb) (L12) and ordered Body-centred tetragonal (BCT, $D0_{22}$) structure $\gamma'' Ni_3Nb$ ($D0_{22}$) [80] as well as phases, such as Hexagonal close-packed (HCP) Laves (Ni, Fe, Cr)$_2$(Nb, Mo, Ti) (C14) and orthorhombic δ(Ni_3(Nb, Ti), D0a). It is noted that L12 and $D0_{22}$ are named according to the lattice structures composed of different elements.

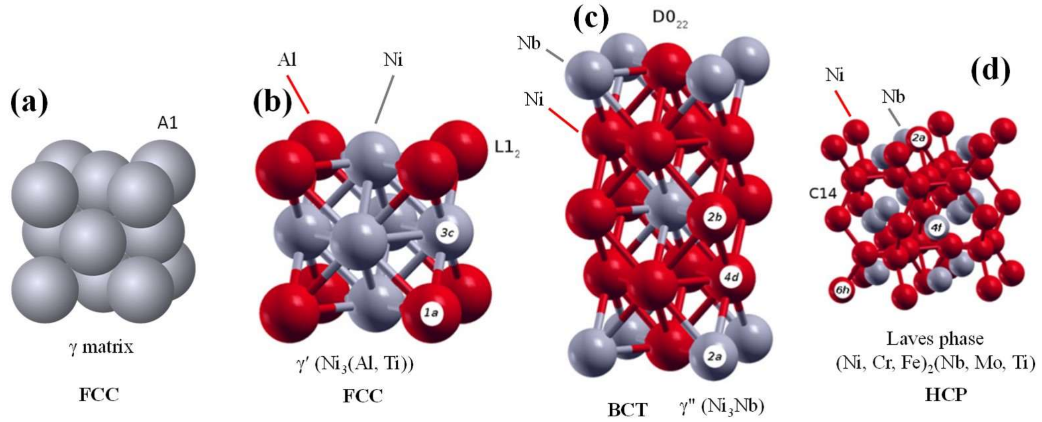

Figure 2.5: Four phases in Alloy 718. (a) Face-centred cubic (FCC, A1); (b) Face-centred cubic (FCC, $L1_2$); (c) Body-centred tetragonal (BCT, $D0_{22}$); (d) Hexagonal close-packed (HCP) [79,80].

Figure 2.6 [81–84] shows the different phases in the cast and LPBF-fabricated Alloy 718. Laves phase is recognised as a detrimental phase as it consumes elements for precipitation strengthening and causes hot cracking (Figure 2.6(a), (b) [81] and (e) [82]). For element consumption, Laves phase depletes the amount of Nb to reduce the principal element for $\gamma'' Ni_3Nb$. Its brittle nature typically result in poor ductility, toughness, and creep properties. It is formed when microsegregation of Nb occurs in the inter-dendrite region during solidification, appearing as irregular globules or platelets due to long-time high temperature exposure. However, it partly dissolves into γ matrix when the temperature is lower than its melting point of Laves phases (about 1165 °C) [85].

MC-type (Figure 2.6(c) [83]) in Alloy 718 provides secondary phase strengthening by preventing grain boundary sliding and stress relaxation. It improves the creep and rupture strength as it is stable up to 1200 °C [86]. γ'' is principal strengthening phase in Inconel 718 (Figure 2.6(d) [84] and (f) [87]), in which nickel and niobium combine to form BCT Ni_3Nb, precipitating disk-shaped particles with lattice parameters of $a_{\gamma''} = b_{\gamma''} \sim a_{\gamma} = 0.5093$ nm and $c_{\gamma''} = 2a_{\gamma} = 0.7406$ nm. It has an average diameter of approximately 600 Å and a thickness range of 50 – 90 Å, formed on the $\{100\}$ matrix planes with the c-axis perpendicular to the disks [88]. This phase is coherent with the γ matrix with large mismatch strains (of the order of 2.9%) due to the tetragonal lattice distortion (c/a = 2.04) [89].

γ' is the main strengthening phase (Figure 2.6(f) [87]) in current Ni-based superalloys for turbines, while it is not the predominant hardening phase for Nb-rich Alloy 718. It contains the amount of γ' phase with a ratio of 2.5% - 4% between γ' and γ'' while aged between 700 °C and 750°C [90]. This phase forms from aluminium and titanium that react with nickel and are coherent with the austenitic γ matrix. Its crystal lattice has a similar lattice constant (0.3572 nm) compared with γ matrix and the lattice varies slightly in size (0 to 0.5%). Other elements, such as niobium, tantalum and chromium, are also observed in γ', whose shapes vary from spheres to cuboids based on temperature [88].

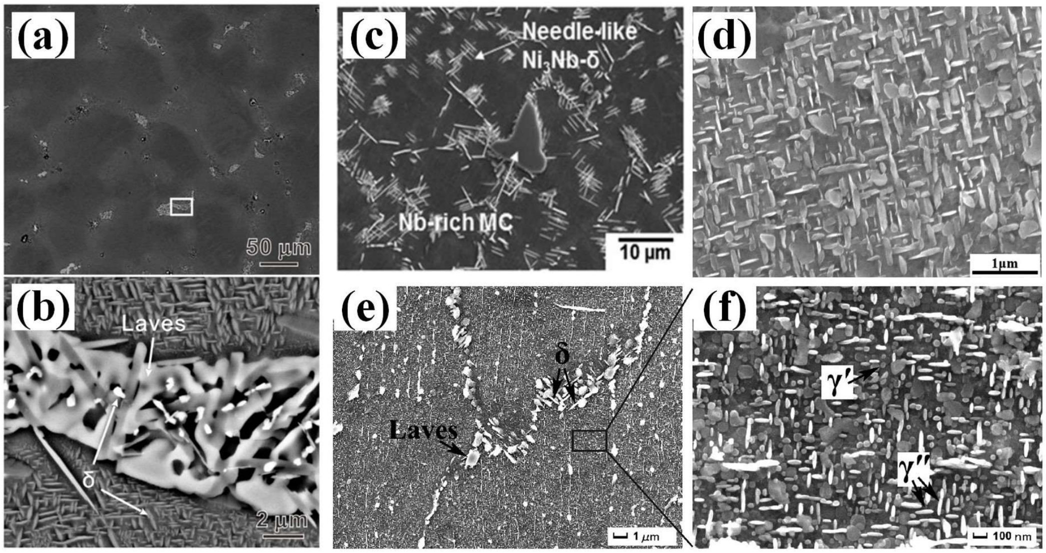

Figure 2.6: Phases in cast and LPBF-fabricated Alloy 718. (a) and (b) Laves in As-cast Alloy 718 [81]; (c) Metal carbide in AM-ed Alloy 718 [83]; (d) γ'' in heat-treated cast Alloy 718 [84]; (e) Laves phase in heat treated LPBF-fabricated Alloy 718 [82]; (f) γ' and γ'' in heat treated LPBF-fabricated Alloy 718 [87].

2.2.2 Melt pool morphology

Since the principle and process of laser reacting with powder has been introduced in Section 2.1.4, this section specifically summarises the effect of laser parameters on Alloy 718. Similar to laser welding, physical phenomena such as melting and solidification, spattering and keyhole effects also occur in LPBF-fabricated Alloy 718 [91]. However, some significant differences are attributed to the characteristics of phase and element segregation during solidification. One of the most significant features in LPBF is rapid solidification with a cooling rate of 5×10^4 K/s to 5×10^7 K/s [92], resulting in cellular grain growth and inter-cellular Laves phase emerging induced by Nb and Mo micro-segregation. However, another work reported that only Nb was rich in inter-dendritic but Mo was almost uniformly distributed [93]. In the rapid solidification process, solute trapping, where solute partitioning decreases across the solid-liquid interfaces [94], differs the element distribution compared with equilibrium solidification. γ-Laves eutectic structure, emerging when Nb content is more than 10% during the casting or welding process, can be obtained in the rapid solidification process where Nb content is only about 5% [95].

In LPBF, the thermal gradient is almost antiparallel to the build direction (BD) (it may be along the laser moving direction near the upper melt pool) during solidification, inducing epitaxial growth of cellular dendrite along BD. It is shown as anisotropic properties which has been widely reported [52,96–98], for example, different tensile test results are observed from samples printed vertically, diagonally (45°) and horizontally [77]. This observation mainly indicated that higher ductility, lower yield/ultimate strength and elastic modulus were obtained in the direction parallel to BD [96,97]. Such anisotropy in strength is attributed to the typical <001> texture and the columnar grain morphology [99].

LPBF-fabricated Alloy 718 shows different microstructure characteristics under macro (mm), meso (10-100 μm) and micro (≤ 10 μm) scales. To describe 3D laser paths clearly, “laser track” is defined as the cross-section of the laser path on the top surfaces (XY plane in Figure 2.7(a)) because the laser scanning direction is on this surface [100–103]. “Melt pool” is the section of the laser path on the side surface (XZ and YZ planes in Figure 2.7(b)) as its boundary is arcuate and its depth shows the feature like the “pool” [104,105].

Typical morphologies of melt pool under optical microscopy (OM) in the XY, XZ and YZ planes are shown in Figure 2.7 [82,106,107]. On the top surface (XY plane), the laser track reveals the scanning direction and rotation of subsequent layer clearly (Figure 2.7(a) and (b)). On the side surface (XZ and YZ plane), semi-circle or arc-shaped melt pools are partly overlapped and "depth" can only be observed from this direction. Compared with Figure 2.7(c), AlSi10Mg has similar melt pool morphology as Alloy 718, suggesting that this unique feature is induced by LPBF processing rather than the material itself.

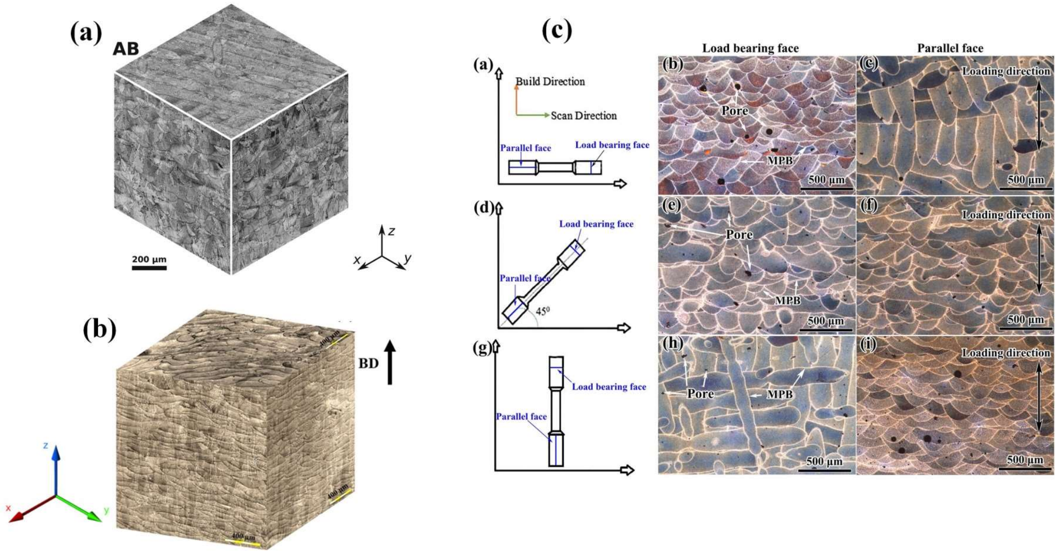

Figure 2.7: Typical melt pools under OM. (a) and (b) As-built Alloy 718 [106,107]; (c) AlSi10Mg [82].

Although laser track and melt pool arrangements can be obtained by OM, more detailed features have to be identified by scanning electron microscopy (SEM). Melt pool boundary, sub-structure and grain boundary can be seen in Figure 2.8 [52,108–110]. Since elements have different etching resistance, significant contrast can be observed under SEM. According to the chemical composition of Alloy 718, Ni-Fe-Cr has a different etching resistance compared with Nb-Mo, leading to dark and bright zones (Figure 2.8 (a)-(e)), respectively.

Fine equiaxed cells and columnar dendrites with different sizes were mainly distributed in the XY-plane, while columnar grains were mainly in the XZ-plane according to Zhao et al. [108] (Figure 2.8(a)-(d)). This is mainly attributed to its unique temperature gradient mentioned before. Many fine cellular sub-structures are presented in individual grains with nearly the same crystallographic orientation due to rapid solidification [109] (Figure 2.8(e)). Moreover, melt pool boundaries do not show significant relevance with the generation of the grain boundary. According to Lee et al.'s research [110], no apparent differences in size, shape, and distribution were found under different printing heights (Figure 2.8(h) [110]).

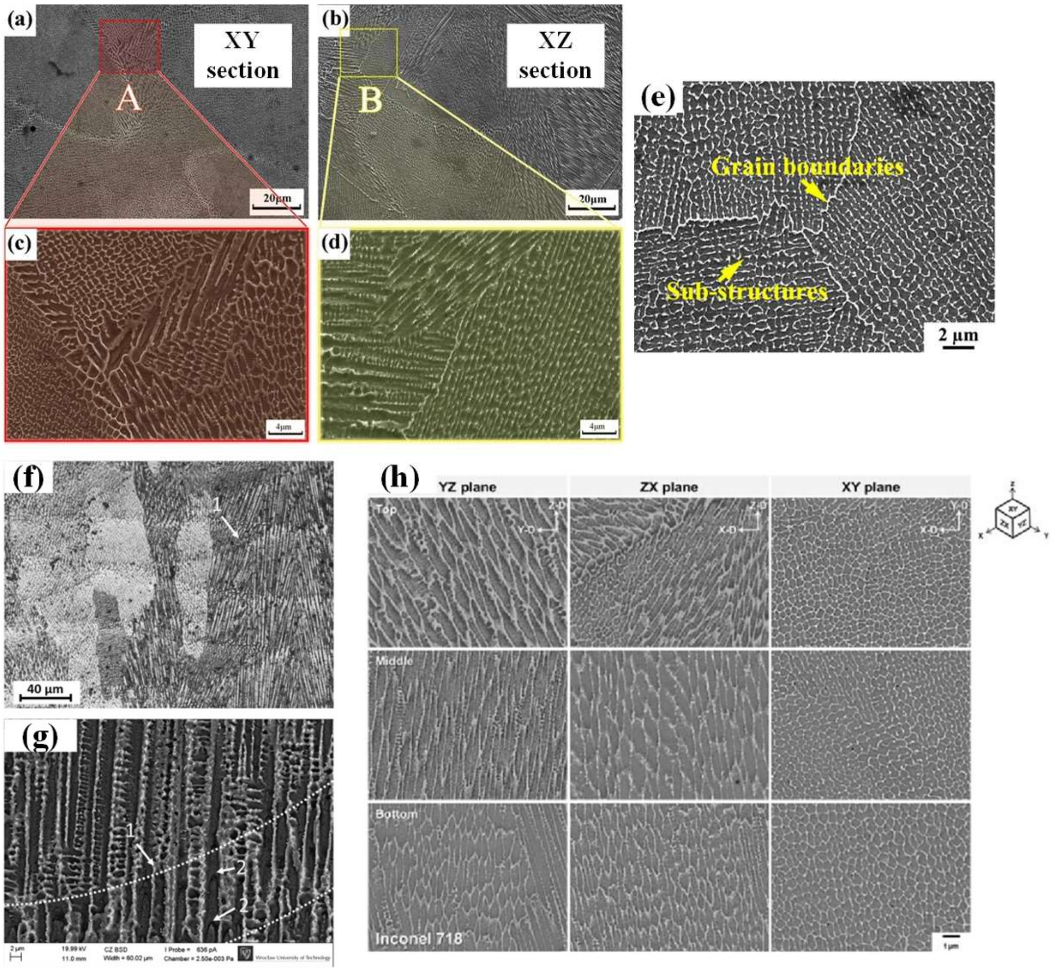

Figure 2.8: Microstructure of Alloy 718 under SEM. (a) and (b) As-built Alloy 718; (c) and (d) zoomed in figures of (a) and (b) [108]; (e) grain boundaries and sub-structures in Inconel 718 [109]; (f) and (g) melt pool boundaries and cellular-dendrite of Alloy 718 [52]; (h) different sub-structures from bottom to the top [110].

Melt pool size and primary arm spacing (PAS) from some published works are summarized in Table 2.2. The PAS is the width of individual cellular structures (or substructures as shown in Figure 2.8(e)). Various laser parameters and scanning strategies were used to fabricate Inconel 718 samples, in which the layer thickness ranges from 20 μm to 40 μm. Input energy density is affected by laser beam diameter as the energy presents Gaussian distribution. Therefore, if the laser power is the same, the energy density of the larger laser beam is not as intensive as the smaller one. A larger laser beam diameter (100 μm or larger), compared with a smaller beam diameter (50 μm), needs higher laser power to fully melt powder at the same scanning speed. The PAS is not significantly changed when the parameters are varied (parameters here mean those acceptable for component fabrication). It keeps in a range from 0.5 μm to 1.5 μm, suggesting a similar cooling rate during the LPBF process.

For melt width and depth, data of depth shows more dramatic fluctuation than width [92,111], indicating that melt pool depth is more sensitive to energy input instability, which may be induced by spattering [112,113] or denudation [114,115] that affects subsequent layer thickness. Scanning strategies do not play a key role in the width and depth of the melt pool, while laser power and scanning speed decide the size of the melt pool [71,87,111], because they significantly affect the actual energy input during scanning when compared to the scanning strategy.

Table 2.2: Summary of different laser parameters and their melt pool characteristics.

Laser power (W)	**Laser beam diameter (µm)**	**Scanning speed (mm/s)**	**Hatch spacing (µm)**	**Layer thickness (µm)**	**Scanning strategies**	**Rotation degree (°)**	**Melt pool width (µm)**	**Melt pool depth (µm)**	**PAS (µm)**	**Ref.**
200	80	900	70	20	Island zigzag	67	70	50	-	[39]
200	-	500-1900	100	20	-	-	100-120	20-40	0.5-1.0	[196]
195	100	1200	90	20	Zigzag	67	50-60	40	0.5-1.0	[71]
170	80	500-1000	56	30	Zigzag	0	62-86	32-90	0.5-1.0	[111]
200	80	900	120	30	Stripe	16	90-100	100	0.5-1.5	[69]
180	80	600	90	30	Zigzag	67	50-70	-	0.5-1.0	[264]
285	100	960	110	40	Zigzag	67	141	75	0.26-1.4	[92]
285	-	960	100	40	Zigzag	67	110	-	0.7-1.4	[87]

2.2.3 Grain structure and texture

Grain morphology (shape and size) of LPBF-fabricated is different from the counterparts formed by traditional ways (e.g., wrought) as shown in Figure 2.9 [116,117]. Grains in wrought 718 are equiaxed and the average grain size is about 14.8 µm (Figure 2.9(a)). The grain size becomes larger (73.6 µm) after heat treatment, as shown in Figure 2.9(b). Moreover, many twin grains are observed in wrought 718 with the misorientation angle of 60° between grains [118], but few twin grains are observed in AM-ed grains [119]. The grain size of the LPBF-printed component is larger than wrought 718, as shown in Figure 2.9(a) and (c). Due to the layer-by-layer manufacturing process, the grains printed by LPBF have a tendency to grow across several layers along the BD, forming the elongated grains along the build direction (Figure 2.9(c)). However, the grains oriented perpendicular to the BD exhibit a more homogeneous morphology, with a smaller grain size compared to those aligned parallel to the BD (Figure 2.9(d)). The variation in grain morphology also contributes to anisotropies in mechanical properties when subjected to different loading directions [120,121]. This highlights the significance of considering the build direction when studying the final mechanical properties of a printed component, as it differs from the properties of those formed by wrought processes.

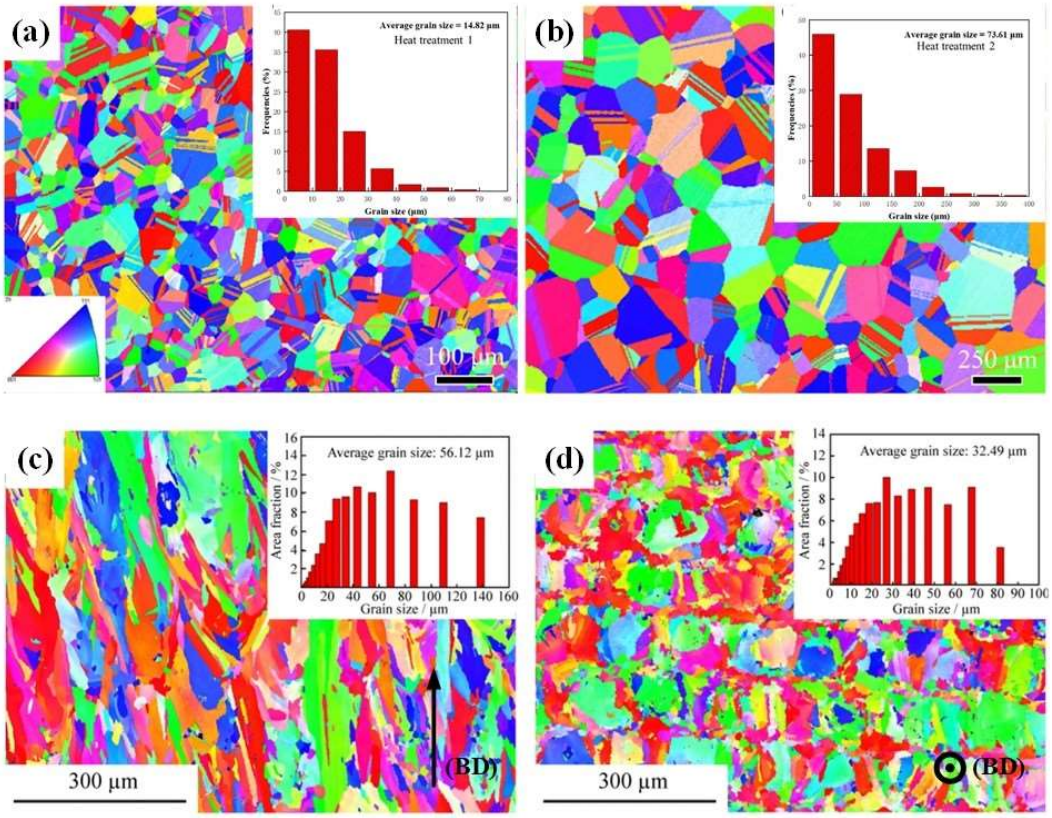

Figure 2.9: Grain morphology (shape and size) comparison. (a) and (b) wrought Alloy 718 after two heat treatments [116]; (c) and (d) as-printed Alloy 718 without heat treatment [117]. (Grain size distributions are depicted in the insets)

Laser power and scanning speed are two critical parameters that determine the quality of as-printed components [122–124]. It has been reported that laser power and scanning speed can significantly change grain shape and orientations during the LPBF process [125,126]. Figure 2.10 reveals the grain structure and orientation affected by laser power and scanning speed [127,128]. Highly oriented coarse grains are formed by high laser power while fine grains are yielded by low laser power as shown in Figure 2.10(a). The coarse columnar grain has a strong <001> texture with respect to the build direction, but the fine grained zone exhibits no preferred orientation [127]. This also reveals the potential of additive manufacturing to produce the graded material that faces functional performance requirements.

Figure 2.10(b) shows the manipulated microstructure and orientation fabricated by variable laser power and scanning speed. The combination of these two parameters affects the thermal gradient and solidification rate, resulting in crystallographic lamellar microstructure, single-crystal-like microstructure and polycrystalline-like microstructure respectively [128].

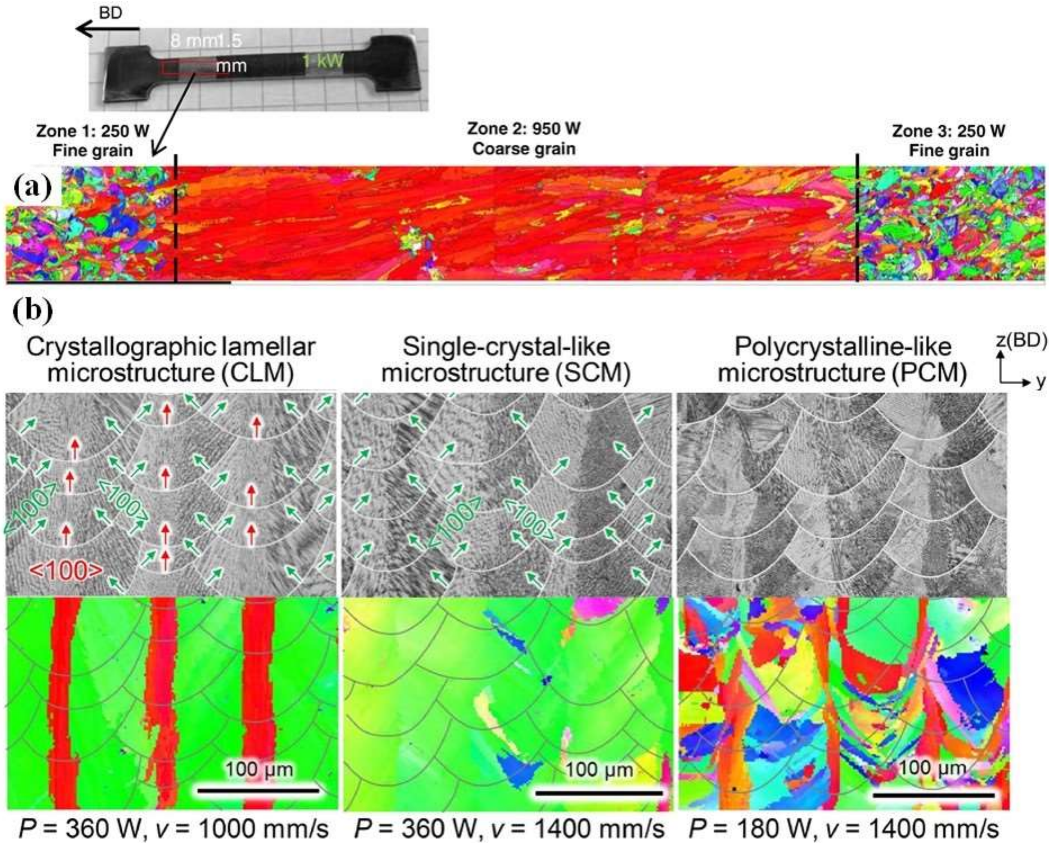

Figure 2.10: Grain structure and orientation affected by laser power and scanning speed. (a) Fine and coarse grains fabricated by different laser power [127]; (b) Microstructure evolution caused by the combination of laser power and scanning speed [128].

In general, laser power and scanning speed control the energy input [127,129] while rotational scanning directions between adjacent layers dominate the build directional thermal history [3]. By rotating the laser scanning directions layer by layer, it is efficient to relieve the inhomogeneous thermal circle induced by laser scanning. The microstructure is consequently changed in different scanning strategies, as illustrated by four examples in Figure 2.11 [130]. The laser scanning direction is not changed layer-by-layer, leading to a <001> texture (Figure 2.11(a) to (a2)) aligned with the BD [130]. The similar microstructure was also reported in another work [131]. The rotated scanning strategy disrupts the thermal profile along the build direction, promoting the formation of non-preferred crystal orientation (Figure 2.11(b) to (b2)). The laser direction changes 90° in neighbouring layers and forms epitaxial growth crossing several layers Figure 2.11(c1). The strong <001>//BD texture is consequently observed in Figure 2.11(c2). The cheeseboard (island) scanning strategy divided the scanning region into several parts and the grain grows helically, shown as the elongated grain in the 2D EBSD mapping Figure 2.11(c) and (c1). Moreover, the texture is weak because the individual islands and rotated scanning direction randomise the grain growth directions. It exhibits ring-like texture as shown in Figure 2.11(c2).

Since the grain growth direction tends to follow the previous grain orientation in previous layer, scanning strategy is able to tailor grain morphology and orientation by creating different types of thermal profiles among layers. Moreover, since grains of FCC alloys (Alloy 718 as an example) have three preferred growth directions belonging to <001> family (i.e., [100], [010] and [001]), the grain growth direction with a change of 90° belongs to the same grain due to the epitaxial grain growth pattern [132]. As a result, the grain printed by LPBF usually has large aspect ratio (i.e., more likely to be elongated along the BD) and strong texture is more likely to be observed when a stable thermal profile is provided. This will finally lead to anisotropy mechanical properties in different directions.

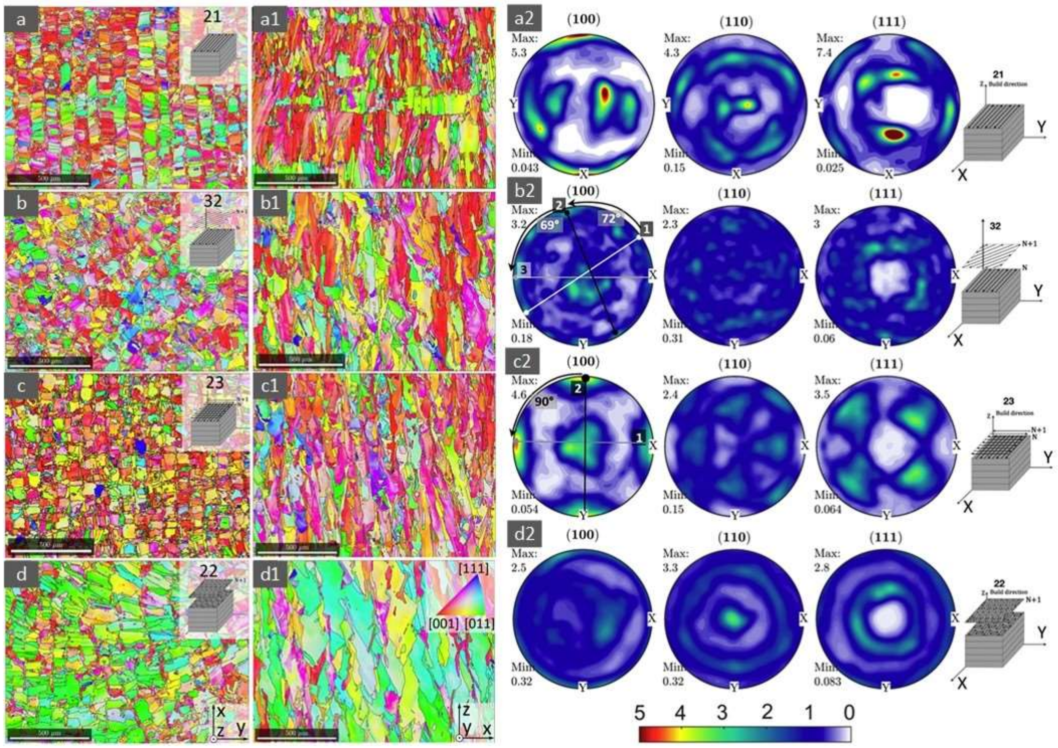

Figure 2.11: Grain structure and orientation controlled by scanning strategies [130]. Inverse pole figure (IPF) maps and pole figure for (a), (a1) and (a2) X direction; (b), (b1) and (b2) 67° rotation; (c), (c1) and (c2) 90° rotation; (d), (d1) and (d2) chessboard 67° rotation.

2.3 Post-machining of LPBF-fabricated Alloy 718

2.3.1 Machining of LPBF-fabricated 718

The LPBF-fabricated parts typically exhibit a relatively rough surface [133,134] due to the sintering of alloy powder near the part surface, whilst dimensional accuracy is also required for their applications [135]. Hence, the LPBF-fabricated components are often subjected to post-mechanical machining operations to achieve the required dimensional accuracy and functional performance [136,137]. Moreover, the improved surface integrity after machining is important in applications with constraints on fatigue performance, wear resistance and corrosion properties [138]. These are able to expand the potential applications of LPBF-fabricated alloys.

LPBF technology has been successfully used to build Alloy 718 structures with different crystallographic textures as introduced in Section 2.2. The unique microstructure formed via a layer-by-layer fabrication manner can have a strong influence on structure-property relationships, such as tensile [139], creep and compression [140]. Understanding the influence of microstructure on mechanical properties is critical to estimate the machinability of LPBF-fabricated alloy. Figure 2.12 illustrates the microstructural characteristics that can potentially influence the mechanical properties and machinability [138]. The variations in microstructural characteristics (e.g., crystallographic texture, grain size, dislocation density and oxide inclusions), along with the density of defects, influence the tensile properties like yield and tensile strength, ductility (elongation at fracture) and strain hardening [141]. It is noted that the influence of microstructure on thermal conductivity (Figure 2.12) is mainly attributed to the two-phase materials (e.g., Ti6Al4V). Because the thermal conductivity might change between these phases during the fabrication process. For Alloy 718, limited segregation of elements would not significantly affect thermal conductivity during machining.

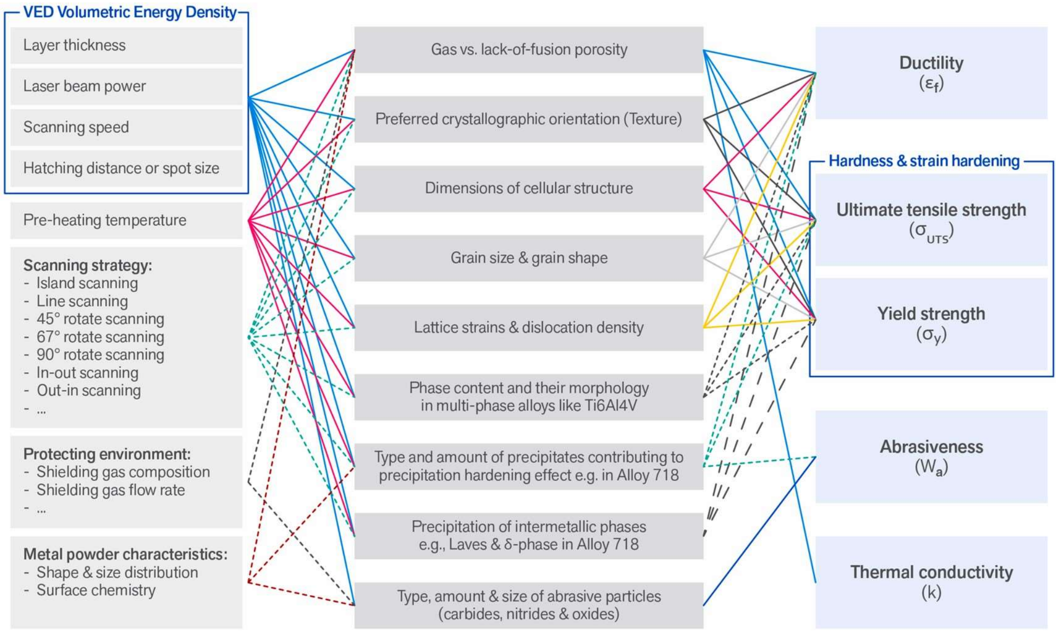

Figure 2.12: Relation between some of the key parameters of PBF-LB and DED-LB technologies, the microstructural characteristics of AM materials and their potential influence on properties with large impacts on machinability [138].

In numerous studies it is reported that the machining process is sensitive to the microstructures of conventionally manufactured Alloy 718 [142–144]. Different cutting forces were obtained when machining the nickel-based alloy with different grain sizes of about 16 µm and 127 µm respectively [145]. Moreover, the size and volume fraction of MC carbides and Ti-rich nitrides in wrought and cast materials exhibit significant impacts on the tool wear rate [146].

Similarly, the machining of LPBF-fabricated Alloy 718 would be largely dependent on the microstructure of the as-built condition. To summarise the microstructural impacts on the machining, Figure 2.13 shows the relationship between microstructure and machinability [147,148]. The combination of these aspects (Figure 2.13(a)), such as grain size distribution, grain shape, Kernel Average Misorientation (KAM), preferred crystallographic texture and amounts of precipitates, leads to a large difference in cutting force, tool wearing and heat generation in machining [147]. Importantly, the preferred crystallographic texture and the unique grain shape formed by LPBF would lead to different machining responses. When the cutting tool motion direction was parallel to the build direction (Case 3 in Figure 2.13(b)), the cutting force was lower than the forces in Cases 1 and 2. This is because the grain boundary density is lower along the build direction, resulting in relatively low cutting resistance (Figure 2.13(b)). Such unique microstructure finally leads to the directional dependency of machinability when compared with conventionally manufactured Alloy 718 [148].

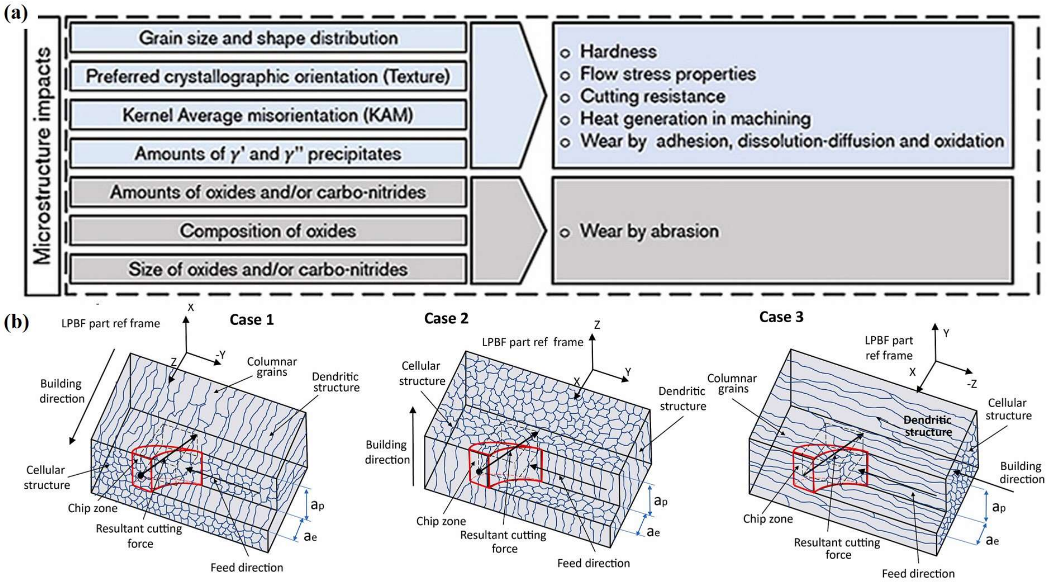

Figure 2.13: Microstructure impacts on the machinability. (a) microstructural characteristics (grain size distribution, grain shape, preferred crystallographic texture, Kernel Average misorientation (KAM) and amount of precipitates) that influences the machinability [147]; (b) three different directional machining cases for LPBF-fabricated columnar grains [148].

Figure 2.14 compared the hardness and cutting force of the Alloy 718 fabricated by wrought, laser powder bed fusion (LPBF) and electron powder bed fusion (EPBF) [147]. The hardness of as-built/received conditions (Figure 2.14(a)) is lower than those after heat treatment (Figure 2.14(b)). The hardness measurements on the LPBF samples in the as-built condition showed a higher average hardness than the wrought material in the as-received condition. The average hardness of 274±6.9 is within the range for solution-treated materials with comparable grain size due to limited γ' and γ'' precipitation in the as-received condition. The average hardness of the LPBF samples after solution and double aging treatment surpassed the wrought and EPBF materials. No difference in the measured hardness on the bottom and top samples was noticed. For EPBF, the average hardness measured on the bottom and top samples showed a slight difference: 370±7.7 and 402±6.1, respectively. This is because γ' and γ'' and precipitate during EPBF since the material is kept at a high temperature (975 ± 25°C) during the entire manufacturing process and experiences slow cooling rates to room temperature. The partial precipitation of γ' and γ'' resulted in higher hardness than the wrought and LPBF samples in their as-received and as-built state, respectively.

The cutting force for wrought, LPBF and EPBF material in as-received or as-built condition and after the heat treatment were compared in Figure 2.14(c) and (d). The cutting forces were approximately the same during the machining of the LPBF and wrought Alloy 718, whilst the highest cutting force was observed in the machining of EPBF Alloy 718. This is partly attributed to the hardening effect from the precipitation of γ' and γ'' in the EPBF 718. But two additional factors should be considered according to the work from Amir et. al [147]: texture and the extent of material work-hardening prior to the onset of crack formation during material removal.

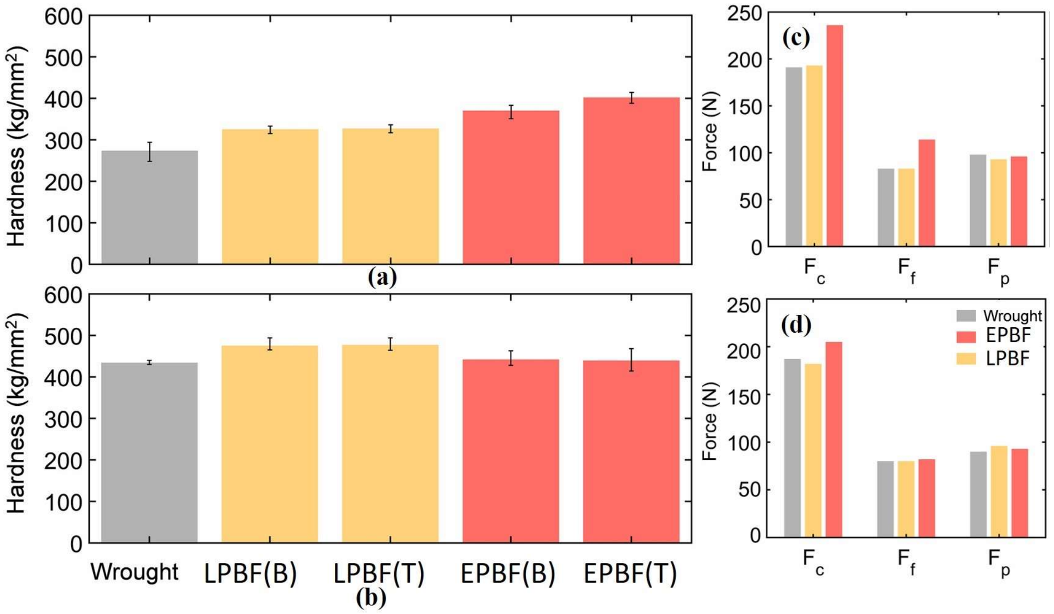

Figure 2.14: Hardness of the wrought, LPBF and EPBF samples in as-built/as-received conditions (a), and after heat treatment (b). B and T refer to the bottom and top samples. The error bars include the maximum and minimum recorded hardness values. A cutting (Fc), feed (Ff) and passive (Fp) forces were measured when machining wrought, EPBF and LPBF materials in as-received and as-built conditions (a) and after solutionising and ageing treatment (b). The results represent the measurements at the beginning of the tests (10 s) using a fresh tool [147].

The cutting forces for wrought and LPBF 718 are measured under different cutting speeds ranging from 20 to 100 m/min (Figure 2.15) [149]. It is noted that, in Figure 2.15, W 718 refers to wrought 718 and PBF 718 represents LPBF 718 in our work. The larger specific cutting force was observed in wrought 718 when compared to LPBF 718 under the different cutting speeds. This was attributed to the higher density of grain boundaries, and the presence of twin boundaries leads to higher strain-hardening behaviour in the deformation area and increases the specific cutting force. The specific cutting force and passive force are larger under the XZ-Z (cutting in BD) condition than those under the XY-Y (cutting in the direction perpendicular to BD) condition. It is suggested that more cutting energy is consumed when machining wrought 718, followed by XZ-Z, and XY-Y represents the lowest cutting energy. Moreover, the specific cutting force decreased with increasing of cutting speed for both wrought and LPBF 718. This is because of the thermal softening effect and the reduction of flow stress with increasing strain rate.

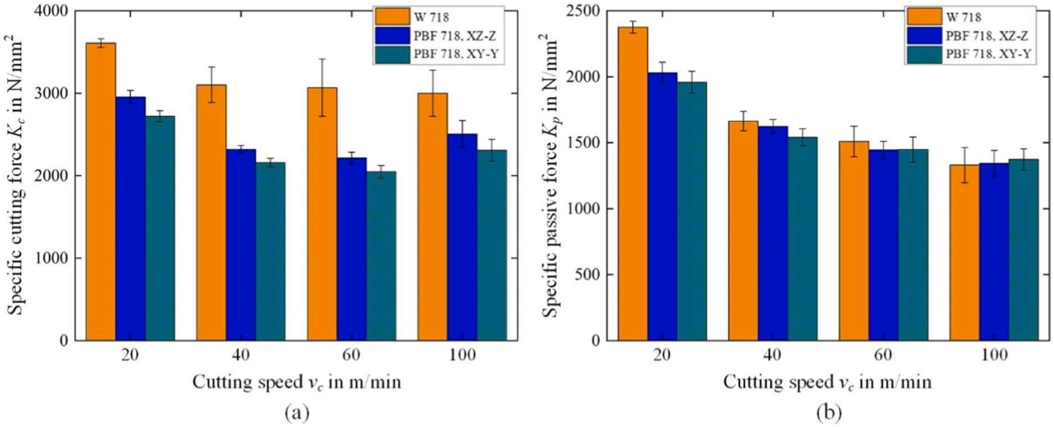

Figure 2.15: Comparison of specific forces when cutting Inconel 718 in different versions. (a) Specific cutting force and (b) specific passive force. (Error bars represent standard deviations of the recorded dynamic force signals). XY-Y and XZ-Z refer to the cutting directions that are perpendicular to the build direction (BD) and in the build direction (BD), respectively [149]. (W 718 refers to wrought 718 and PBF 718 refers to LPBF-fabricated 718)

It is noted that the cutting force results for wrought and LPBF 718 in Figure 2.15(a) are in contradiction with that measured in Figure 2.14(c). It was observed that the cutting force of PBF 718 was slightly larger than the wrought case in Figure 2.14(c), but the cutting force of wrought 718 (Figure 2.15(a)) was larger than PBF 718. In these two studies, wrought alloy 718 workpieces underwent similar heat treatment and exhibited approximately the same average grain size (about 12 μm). However, the rotation angle for PBF 718 in Figure 2.14(b) and Figure 2.15(a) are 67° and 90°, respectively, leading to different textures and grain morphologies. Moreover, the cutting test for the results in Figure 2.14(c) was carried out on an EMCO TURN 365 CNC lathe whilst the results in Figure 2.15(a) were based on a machine tool (Berger Gruppe, Germany) that is specially designed for fundamental chip formation analysis. The same cutting speed of 40 m/min was employed in both cutting tests but under different cutting depths (0.4 mm and 0.1 mm, respectively). The detailed cutting parameters comparison is listed in Table 2.3.

Table 2.3 Cutting parameters comparison for the cutting test in Figure 2.14 [147] and Figure 2.15 [149]

Cutting parameters	**Cutting test in Figure 2.14**	**Cutting test in Figure 2.15**
Test machine	EMCO TURN 365 CNC lathe	Special machine for chip analysis
Cutting tool	CNMG 120404-MF1 uncoated with WC-Co inserts	Cemented carbide tool (TPGN 160308) without coating
Uncut chip thickness	0.4 mm	0.1 mm
Cutting speed	40 m/min	20, 40, 60 100 m/min
Rake angle	6°	-6°
Dynamometer	Kistler 9257A	Kistler 9263

The previously reported results suggest that it is challenging to draw a conclusion about whether the LPBF 718 is easier or more difficult for machining when compared to the wrought one. This is because the microstructure of LPBF-fabricated Alloy 718 is sensitive to the laser parameters and scanning strategies. Subsequently, the material properties (e.g., strength, hardness and ductility) will vary with the use of different fabrication parameters. It is hard to evaluate the basic material properties of LPBF fabricated components unless laser parameters and scanning strategies are detailed.

To understand the role of microstructure in the machining process, microstructural features are characterised to reveal the mechanisms behind the mechanical behaviour during machining. The severe plastically deformed grain near the machined surface can be observed via SEM (Figure 2.16(a)) after polishing and etching the sample surface [150]. The curved grain boundaries can be used to evaluate the grain elongation near the machined surface whilst slip bands are helpful to understand the plastic deformation induced by machining. Moreover, for the nickel-based Alloy 718, dynamic recrystallization and white layer formation can also be observed under SEM [151]. For the specific crystallographic texture and grain orientation near the machined surface, the grain orientation change and local strain caused by machining are quantified via EBSD, as shown in Figure 2.16 (b). The strain gradient from the near machined surface to the subsurface can be evaluated via the misorientation information within grains and the role of grain boundaries in machining could be investigated [152]. For the detailed deformation quantification near the machined surface, transmission electron microscopy (TEM) and transmission Kikuchi diffraction (TKD) techniques are used to obtain the grain orientation, lattice distortion and dislocation densities of the nano-crystalline structures (Figure 2.16 (c)), especially for the highly-deformed layers that are hard to be captured via SEM [153].

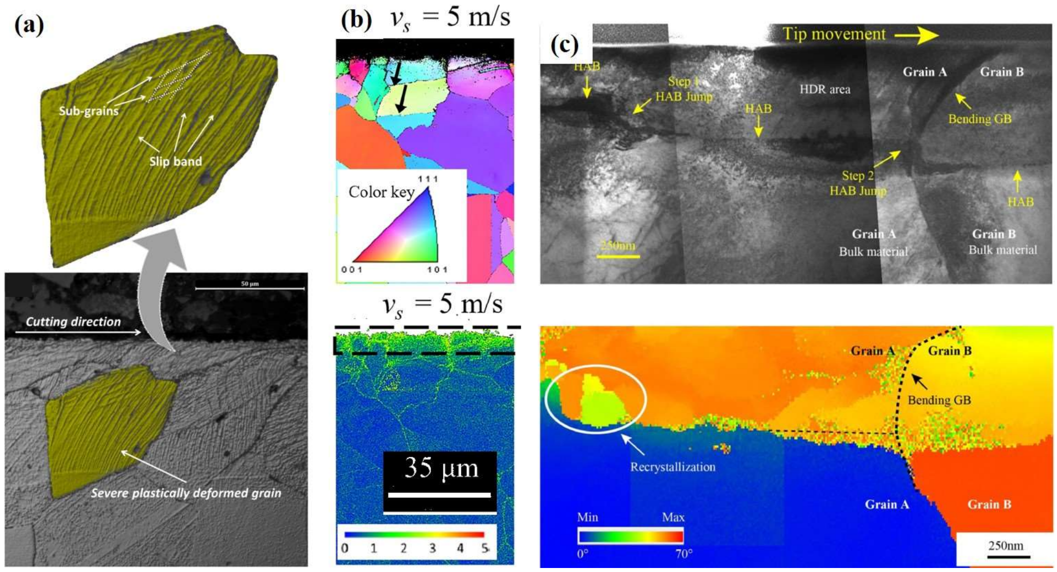

Figure 2.16: Microstructure characterisation of machined surface. (a) Machining-induced deformation obtained by SEM [150]; (b) IPF and KAM mappings obtained by EBSD [152]; (c) dislocation and grain orientation obtained by TEM and TKD (transmission Kikuchi diffraction) [153].

Although the deformed details after machining, like orientation change, slip bands and recrystallization, can be captured via advanced characterisation techniques, it is still not easy to fully understand such a shear-based deformation. This is because machining involves a complex loading condition and is accompanied by a relatively high strain rate. The dramatic plastic deformation leads to significant changes in the microstructural features (e.g., grain size, orientation and dislocation density) near the machined surface when compared with the original microstructure before machining. Moreover, such microstructural changes are hard to trace at the grain scale since the severe deformation occurs in a very short period (e.g., about 10^{-5}s). Therefore, numerous studies can only conclude that microstructural characteristics influence machinability by comparing general differences in microstructural features (Figure 2.13(a)), but few works can provide evidence to identify how such original microstructure actually evolves during the machining-induced deformation.

2.3.2 Machining-induced plastic deformation

To understand the mechanisms of machining-induced plastic deformation caused by orthogonal cutting, it is crucial to identify the active slip systems within the deformed grains [154]. Since Alloy 718 has the FCC crystal structure, the slip can occur on 12 slip systems [155]. Figure 2.17 shows the slip system number, slip plane normal and slip directions for the FCC structure [156]. The primary slip planes in Alloy 718 (FCC structure) are the {111} planes with the highest atomic density. The slip direction is along the <110> direction, which has the shortest lattice vector, exhibiting the easiest direction for dislocation moving. The 12 slip systems can be derived from the combination of 4 different {111} slip planes and 3 unique <110> slip directions within each plane.

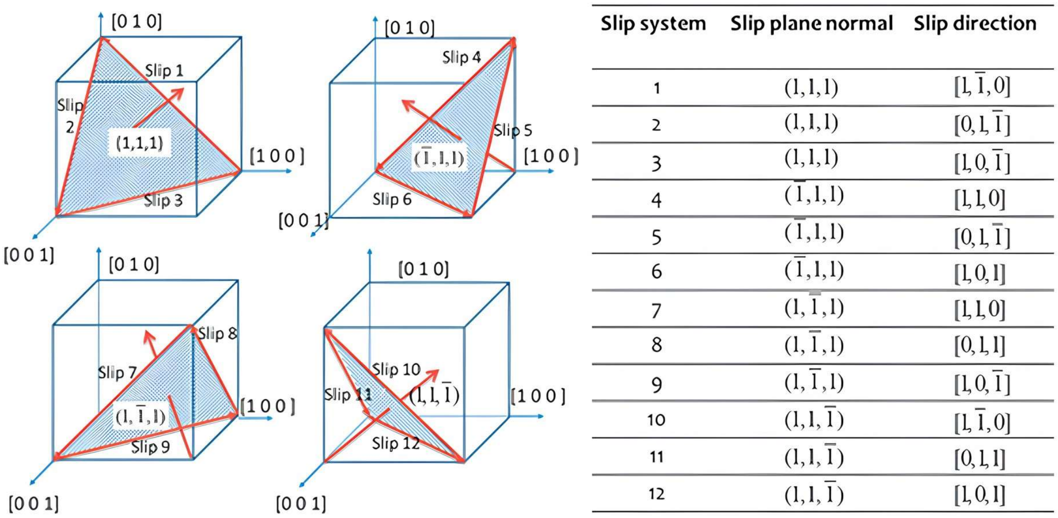

Slip system	Slip plane normal	Slip direction
1	$(1,1,1)$	$[1,\bar{1},0]$
2	$(1,1,1)$	$[0,1,\bar{1}]$
3	$(1,1,1)$	$[1,0,\bar{1}]$
4	$(\bar{1},1,1)$	$[1,1,0]$
5	$(\bar{1},1,1)$	$[0,1,\bar{1}]$
6	$(\bar{1},1,1)$	$[1,0,1]$
7	$(1,\bar{1},1)$	$[1,1,0]$
8	$(1,\bar{1},1)$	$[0,1,1]$
9	$(1,\bar{1},1)$	$[1,0,\bar{1}]$
10	$(1,1,\bar{1})$	$[1,\bar{1},0]$
11	$(1,1,\bar{1})$	$[0,1,1]$
12	$(1,1,\bar{1})$	$[1,0,1]$

Figure 2.17: Identification of slip systems, slip plane normal and slip directions for FCC crystal structure [156].

The most common approach to identifying active slip systems is to combine slip trace analysis with EBSD data [157], as shown in Figure 2.18. The slip trace of FCC structure (aluminium sample) was observed under the SEM (Figure 2.18(a)) during the tensile test. It was observed that the slip trace directions changed when grain orientations were different, such as g8 and g10 (Grains 8 and 10 in Figure 2.18(b)). Moreover, according to the grain orientation data obtained by EBSD, the slip traces for all four slip planes (Figure 2.17) were calculated and coloured by red, blue, yellow and green lines, respectively (Figure 2.18(c)). Thus, the deformation-induced slip plane can be identified by comparing the observed and calculated slip traces. For example, it was observed that the slip traces within g1 (Grain 1) were closely aligned with blue and yellow plane traces when it was close to the boundary (marked as 2 in Figure 2.20(c)). This indicated a slip direction transfer near the grain boundary when the orientation changed between the adjacent grains. It was also observed that the lack of slip transfer between grains near the grain boundary 9. The possible reason is that grain boundaries may consist of various dislocations that act as barriers, preventing other dislocations from passing through [158].

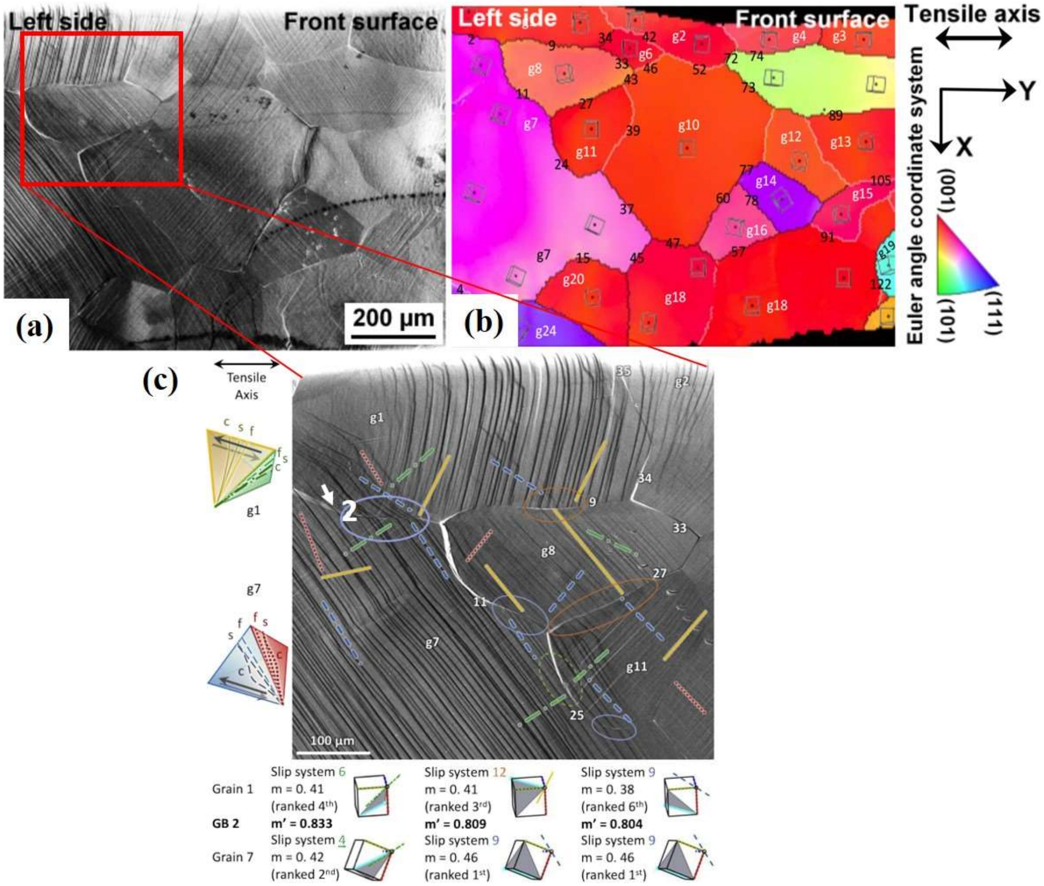

Figure 2.18: In-situ identification of slip traces and corresponding EBSD data. (a) Slip traces in different grains for the deformed polycrystalline FCC structure (Al sample); (b) corresponding IPF mapping for the deformed grains; (c) Slip systems within oriented grains. Four slip traces are highlighted by coloured lines and corresponding grain are numbered. [157].

For the machining-induced plastic deformation, it is still challenge to use the in-situ observation method to investigate the deformation on the subsurface during a macro orthogonal cutting process. The grain morphology and slip bands as well as the corresponding IPF mapping can be identified [159], as shown in Figure 2.19. It can be observed that the slip bands and multiple slip (Figure 2.19(a)) near the machined subsurface. This is similar to the phenomena that are observed in the in-situ tensile test (Figure 2.18(a)). But it is difficult to identify the specific slip systems based on the corresponding IPF mappings. This is because the recrystallization (ultrafine grain in Figure 2.19(b)) and lattice rotation near the machined surface change the original grain orientation. The slip planes within the grains are hard to calculate precisely based on the obtained EBSD data. Therefore, it is still a challenge to understand the machining-induced slip transfer during orthogonal cutting. In addition, the LPBF-fabricated grains are usually elongated along the build direction and exhibit the preferred orientations. Precisely identifying the slip transfer within such unique grains will be helpful in understanding the machining-induced deformation during orthogonal cutting of LPBF-fabricated Alloy 718.

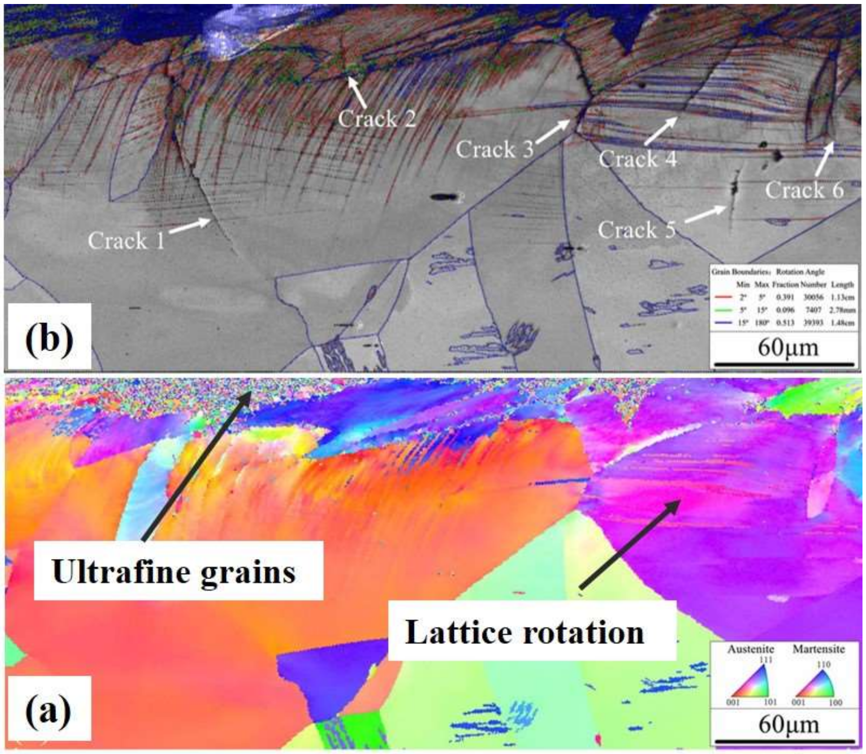

Figure 2.19: Machining-induced microstructural changes. (a) Distribution of grain boundary, crack and slip bands; (b) Orientation changes and recrystallization in IPF mapping [159].

2.3.3 Orthogonal cutting

To investigate the microstructure evolution during machining, it is better to employ the orthogonal cutting method for the machining test, as it provides a clear shear-based deformation condition that commonly occurs in more complex machining processes. This makes it relatively representative of the machining process and easier to study the relationship between microstructure and plastic deformation.

In metal cutting theory, all operations performed with the wedge-shaped tool when a layer of metal is removed as a continuous or discontinuous chip can be divided into two general cases, termed orthogonal and oblique cutting [160]. Orthogonal cutting represents a 2D mechanical problem because the edge of the tool is perpendicular to the cutting speed.

A schematic diagram of orthogonal cutting is shown in Figure 2.20. The 3D cutting model is simplified as a 2D model as there is no relative motion between the workpiece and the cutting tool along the Y direction. The workpiece consists of two main areas: the workpiece itself and the chip, which is a part of the workpiece removed by the cutting tool. For the cutting tool, the face contacting with a chip is called the rake face, while the face contacting with the machined face is defined as the flank face. The angle α is the rake angle (the normal line is a boundary, negative left and positive right) and γ is the clearance angle. ϕ is the shear angle between the shear plane and the workpiece. There are three areas (highlighted by dashed lines) where the cutting tool contacts with the workpiece, classifying into three zones: primary deformation zone, secondary deformation zone and tertiary deformation, which are also known as primary zone, secondary zone and tertiary zone, respectively. Vc is the velocity of workpiece motion, and Fc is the cutting force. w and h are geometrical parameters of cutting width and cutting depth.

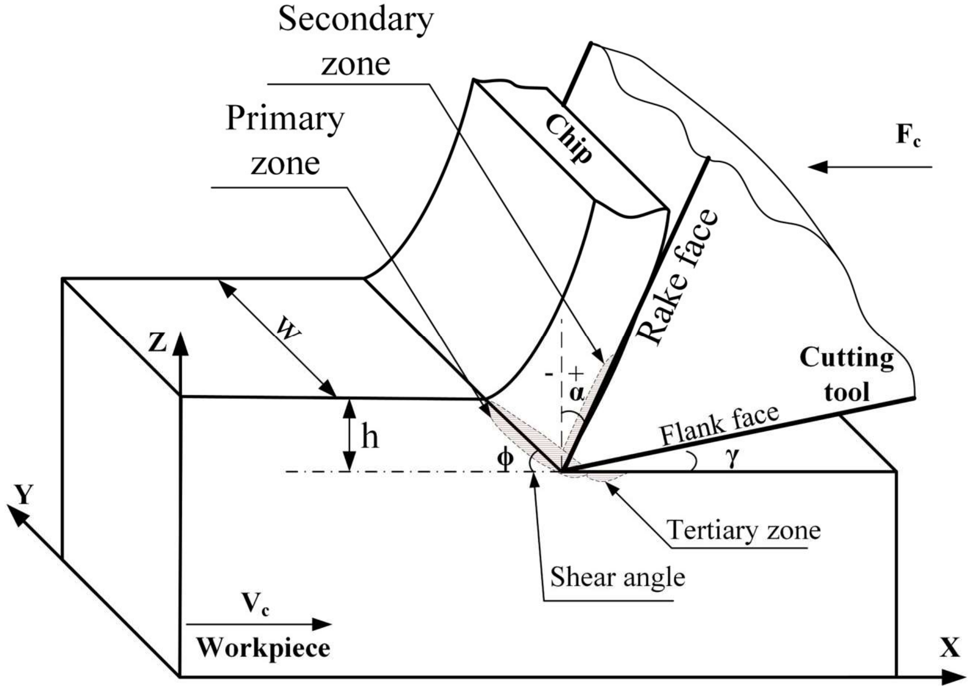

Figure 2.20: Schematics of orthogonal cutting.

Orthogonal cutting test has been a widely used method to investigate the machinability of difficult-to-cut materials [161,162]. Figure 2.21 shows some machining devices designed for the investigation of orthogonal cutting [163–165]. For the cutting test on the computer numerical control (CNC) lathe, the cylindrical workpiece is clamped into the chuck of the CNC lathe and the cutting tool is usually clamped to a special tool holder at the orthogonal cutting condition with zero cutting edge inclination angle (Figure 2.21(a)). Then, the workpiece begins to rotate at a predetermined speed (RPM) and the cutting edge moves along the length of the workpiece with a target feed rate for the orthogonal cutting test Figure 2.21(b). The orthogonal cutting test can also be conducted by a pendulum-based cutting machine (Figure 2.21(c)). The workpiece is attached to the sample holder on the pendulum and the cutting tool is fixed into the tool holder below the pendulum (Figure 2.21(d)), with the cutting edge perpendicular to the cutting direction. Various cutting speeds are provided by the different release angles of the pendulum (Figure 2.13(c)), and the cutting force is measured by the dynamometer (Kistler 9257B). Moreover, the uncut chip thickness can be set by changing the height of the wedge lever under the tool holder Figure 2.21(d).

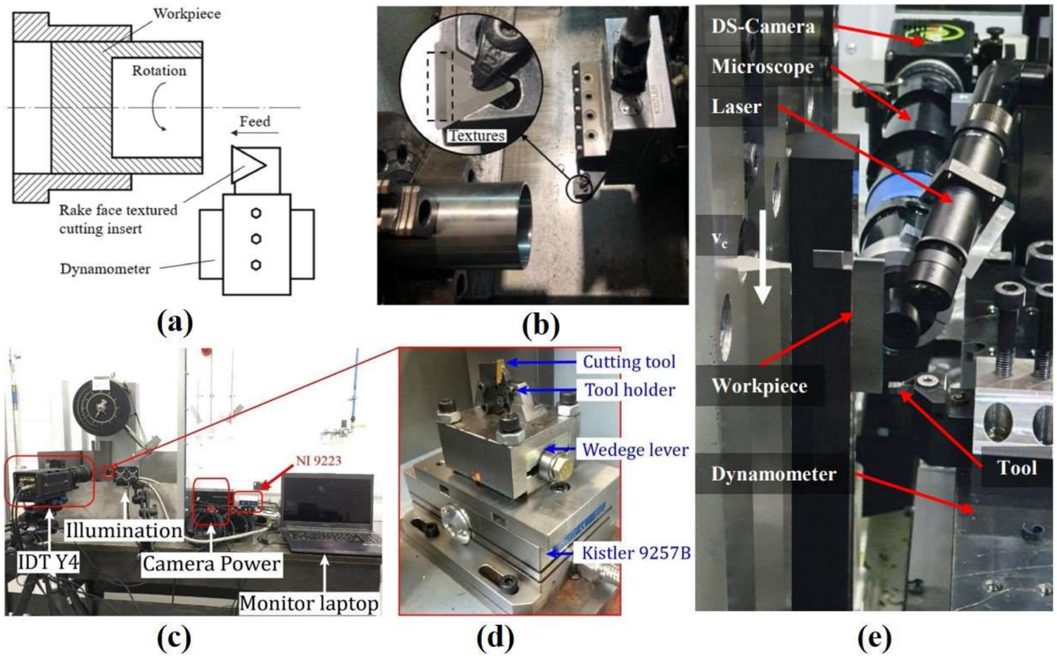

Figure 2.21: Machining devices for orthogonal cutting tests. (a) and (b) are the experimental setup for orthogonal cutting on a computer numerical control (CNC) lathe [163]; (c) and (d) show the pendulum-based orthogonal cutting machine [164]; (e) vertical external broaching machine tool for the orthogonal cutting [165].

Figure 2.21(e) shows a vertical external broaching machine tool for the orthogonal cutting tests. The cutting tool is fixed on a platform that can measure the cutting force via the dynamometer, and the workpiece is clamped into the broaching tool holder for the main cutting movement during orthogonal cutting (Figure 2.21(e)).

2.3.4 Chip formation

When a workpiece comes into contact with a flat-faced tool at a specific cutting speed, chips are formed and leave the chip formation zone. Chip is formed with dissimilar morphologies due to workpiece properties and cutting conditions [166]. The chip classification is based on the mechanism of material deformation and fracture, involving discontinuous and shear types of chips [167].

Chips are usually classified into four categories as shown in Figure 2.22, including continuous chip, lamellar chip, segmented chip and discontinuous chip. Continuous chip (Figure 2.22(a)) is observed when most ductile materials, such as copper and aluminium [168,169], because they do not fracture on the shear plane. Continuous chip with build-up edge (BUE) occurs when the friction between the workpiece and tool is so great that a part of the chip is welded to the tool face. BUE changes real cutting depth and condition of chip formation due to the irregular shape of materials that adhere to either rake face or flank face, deteriorating final surface roughness and dimension accuracy.

A discontinuous chip (Figure 2.22(d)) is generally formed when machining brittle materials [170] or difficult-to-cut materials with high cutting speed [171,172]. It may also be produced when machining ductile materials at very low speeds and high feeds [160]. In this case, shear bands between adjacent segments increase dramatically or there may be no plastic deformation in brittle materials. A crack is generated from the cutting edge and then propagates to the free surface, dividing a chip into separated segments.

Continuous and discontinuous chips are not two sharply defined categories. For example, the same materials can exhibit different chip formation behaviours such as lamellar chip (Figure 2.22(b)) and segment chip (Figure 2.22(c)), depending on its microstructure, cutting speeds and uncut chip thickness [17]. These chips are observed in materials with low thermal conductivity and low thermal capacity such as titanium alloy [173,174], nickel-based superalloy [175] and hardened steel [176]. For these materials, the plastic deformation of a chip is unstable and the shear zone is localized in a narrow area. With the increasing in cutting speed or localised deformation, the chip is finally separated into segments.

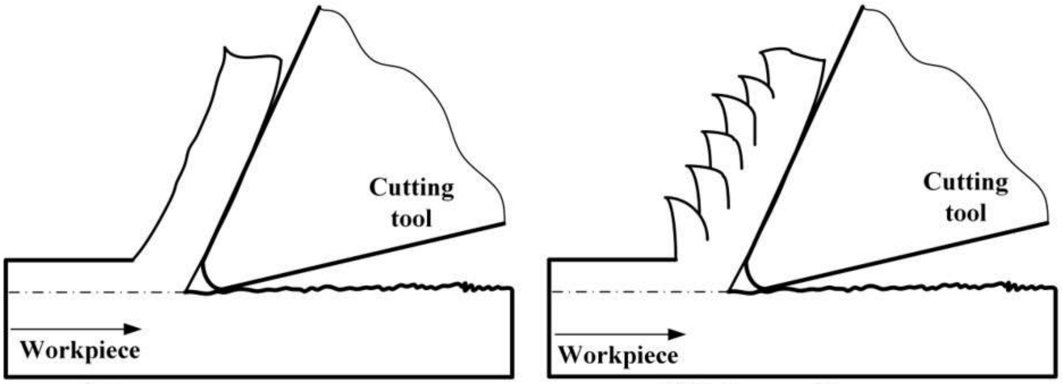

(a) continuous (b) lamellar

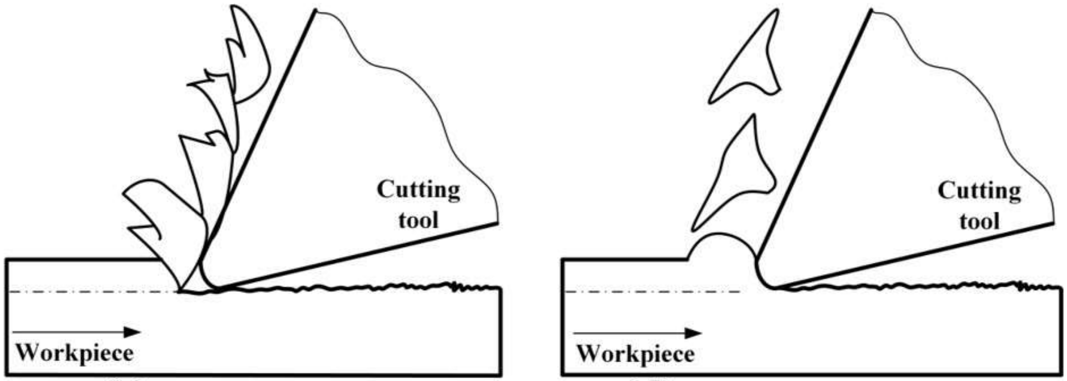

(c) segmented (d) discontinuous

Figure 2.22: Four types of chips. (a) Continuous chip; (b) lamellar chip; (c) segmented chip; (d) discontinuous chip.

Chip formation during the machining process affects the surface integrity of the workpiece and can provide insights into the subsequent surface finish and corresponding microstructure evolution [177]. The morphologies of the chips are strongly dependent on the ductility and strength of the workpiece, which are further influenced by its microstructure. During the machining process, part of the workpiece in front of the cutting tool is transformed into chips due to the severe plastic deformation. The chip morphologies tend to transfer from continuous to serrated when the cutting speed increases [149] (Figure 2.23(a)). Moreover, for the LPBF-fabricated Alloy 718, it is observed that the serrated chip is easier to form when the cutting direction is perpendicular to the BD (Figure 2.23(b)) compared to when the cutting direction is parallel to the BD (Figure 2.23(c)). In order to understand the microstructural impacts on chip formation, the grain structure evolution and local grain misorientation in the chip are identified, as shown in Figure 2.23(d) and (f). Ultra-fine grains are observed in the shear band regions between two chip segments whilst distorted grains are retained in the chip segments [178] (Figure 2.23(e)). In addition, high dislocation densities (high value of KAM) degenerate into crystallisation when it is close to the shear band regions. Such microstructural features are helpful in understanding the grain refinement (or recrystallization) mechanism in such a high-strain condition.

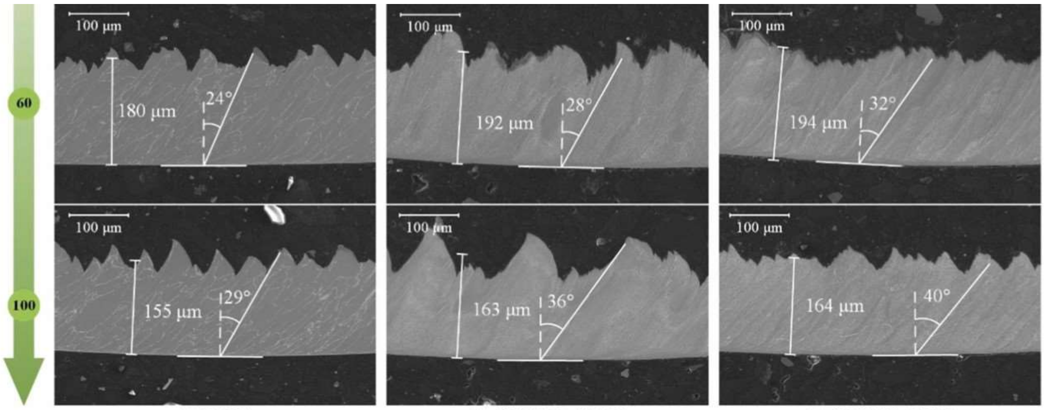

(a) W 718 (b) PBF 718, XY-Y (c) PBF 718, XZ-Z

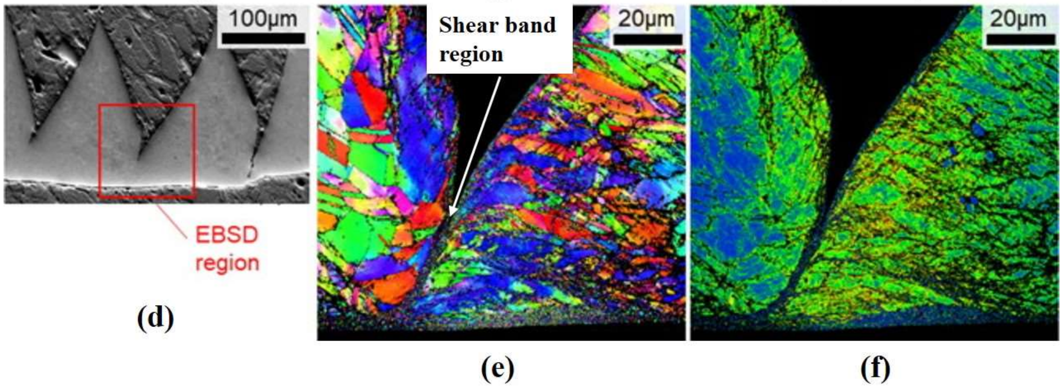

Figure 2.23: Microstructure of chips. (a) to (c) are different chip morphologies for wrought and PBF 718 with cutting speeds of 60 m/min and 100 m/min, respectively [149]; (e) and (f) are IPF and KAM mappings of the serrated chip from the region of (d) [178].

As previously introduced, chip formation is caused by the severe plastic deformation of the workpiece in front of the cutting tool. The chip and the machined workpiece will be separated into two parts after cutting. Therefore, the characterisation of the microstructure of the machined surface and chip individually may not fully demonstrate the chip formation process. This is because the microstructure near the primary shear zone (Figure 2.20) cannot be totally retained. This impedes the understanding of material pile-up behaviour in front of the cutting tool, which is crucial for studying the mechanism of chip formation.

2.3.5 Quick-stop cutting test

To study the chip formation during machining, one way is to trace the dynamic chip formation via image correlation techniques, such as particle image velocimetry (PIV) [179,180] and digital image correlation (DIC) [181,182]. Another way is to interrupt the machining process, namely quick-stop so that the chip can be attached to the workpiece [183,184]. Since this work mainly focuses on the microstructural impacts on the machining process, the quick-stop method is selected in this project to obtain the workpiece with the retained chip for microstructure characterisation.

To “freeze” the chip on the workpiece, the “quick-stop” of the cutting process can be achieved by interrupting the movement of the cutting tool or workpiece when the cutting tool is at the target position (Figure 2.24 [185,186]). In order to achieve a quick-stop function on the specific cutting platform, the quick-stop module is typically a custom-designed component for the cutting machine. Quick-stop device in Figure 2.24 (a) is designed to stop the motion of the cutting tool, including a bolt gun, shear pin pivoting rod and tool holder. When the shear pin is broken and moves the tool from the workpiece in a very short time, it abruptly stops the cutting process [185]. To stop the motion of the workpiece, the customised pendulum-based cutting machine in Figure 2.24(b) mainly includes a pendulum, sample holder, tool holder and a workpiece with a weak point. During the pendulum moves along its trajectory (Figure 2.24(c)), the weak point of the workpiece is broken due to the impact between the pin and tool holder, hence, retaining the chip on the workpiece [186].

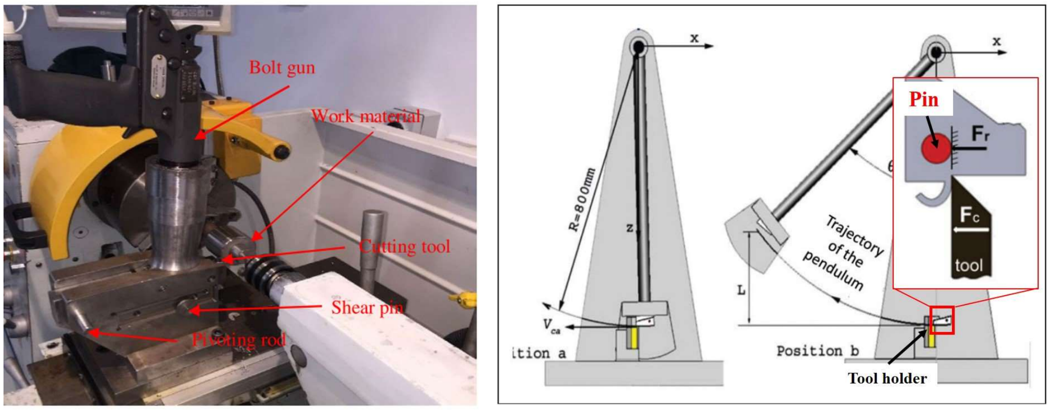

(a) (b) (c)

Figure 2.24: Examples of two quick-stop devices for attaching the chip on the workpiece. (a) Stop the movement of the cutting tool by shear pin [185]; (b) Stop the workpiece by breaking the weak point of the sample [186].

Since the quick-stop cutting test retains the chip on the workpiece, the microstructure of the primary shear zone can also be characterised. This allows to analyse different deformation mechanisms and quantify the strain gradient during chip formation (Figure 2.25 [150,187]). Imbrogno et al. [150] identified two different deformation zones in the serrated chip, namely Low Shear Strain Zone (LSSZ) and High Shear Strain Zone (HSSZ) (Figure 2.25(a) and (b)). In LSSZ, the microstructure is less deformed and the grains have almost the same size as the as-received microstructure whilst the grains in HSSZ are elongated and refined due to the extremely large deformation. Moreover, the deformation fades away from the machined surface to the deeper area (Figure 2.25(c) to (f)). By marking the workpiece surface with a micro-grid spacing of 3.5 μm, the strain gradient of the chip and the machined surface can be quantified via these distorted grids [187]. It reveals that the deformation in the chip formation zone is highly localised and likely to result in plastic instability. In addition, the deformation map indicates that the local strain value is up to 2.2 near the machined surface and then decreases from the machined surface to the subsurface. Compared with the separated microstructure of the chip and workpiece individually, the sample obtained by the quick-stop cutting method provides more details for the understanding of the chip formation mechanism. This is mainly attributed to the characterisation of microstructure evolution from the primary shear zone to the chip segments.

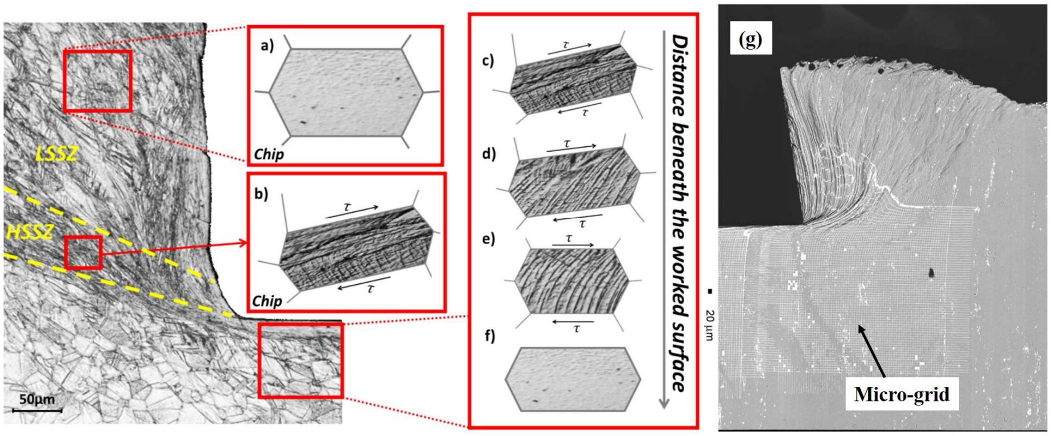

Figure 2.25: Typical microstructure characterisation of chip and workpiece after quick-stop cutting test. (a) to (f) is the different deformation mechanisms of the chip and workpiece [150]; (g) is the strain field during chip formation [187].

In Section 2.3.1, it is discussed the complexity of machining of LPBF-fabricated Alloy 718 due to the unique crystallographic texture and grain morphology. It is still challenging to analyse the relationship between microstructural features and machinability. As the quick-stop cutting test shows the potential to identify the grain deformation in the primary shear zone and chip, it is worth to use method to reveal the machining-induced deformation and chip formation mechanisms of LPBF-fabricated Alloy 718.

2.4 Summary

Overall, a comprehensive literature review on laser powder bed fusion (LPBF), including the relationship between printing parameters and microstructures, the principle of the laser control system, and the machinability of LPBF-fabricated Alloy 718, is provided in this chapter.

It is widely acknowledged that the part quality and microstructure generated by LPBF are highly dependent on the stability of melt pool evolution [188]. This is mainly controlled by laser parameters such as laser power, scanning speed and scanning strategies [8] as discussed in Section 2.1.4. Many studies [189–191] have reported the effects of laser parameters on the melt pool evolution. Meanwhile, novel scanning strategies are also being explored to optimise the performance of LPBF-fabricated alloys [128].

The intense energy inputs in LPBF generate melt pools with sharp thermal gradients (**G**) and high cooling rates (10^4 ~10^6 K/s), causing rapid solidification [92]. This leads to quite different microstructures when compared with the conventional cast and wrought alloys [192,193]. The microstructure could be controlled by scanning strategies [138], such as the degree-rotation between layers (e.g., 0°, 67° or 90° rotations) [9,194]. These scanning paths have a dominant effect on the grain growth pattern, resulting in different crystallographic textures and characteristic grain morphologies in as-built alloys.

As one of the target materials for additive manufacturing, nickel-based superalloys (e.g., Alloy 718), have been widely used in aerospace and nuclear industries due to their high-temperature stability [77]. In particular, the additively manufactured Alloy 718 exhibits anisotropic properties with unique crystallographic textures [91] as described in Section 2.2.3. Since scanning strategies change grain growth patterns by providing different thermal conditions, various grain morphologies (size and shape) are formed in as-printed Alloy 718. Elongated grains with high aspect ratios are commonly observed in <001>//BD texture [68,195], where grains usually grow along the BD. In addition, the columnar grains are much easier to grow in the <011> direction in the 0° rotation scanning strategy. In the 67°-rotation scanning strategy, the grain growth pattern is more randomised by alternating the scanning direction in each layer, suppressing elongated growth and varying grain orientations [196]. It was found that 90° and 67° specimens exhibited higher yield strength than that of 0°-built specimens [197]. Moreover, samples with stronger retained texture exhibited higher yield strength and lower elongation when compared with weaker-textured samples under the build-directional loading direction [198].

Meanwhile, different vector lengths were also reported for parts fabrication [199], and it was shown that the melt pool morphologies were also influenced by the vector length, especially when the vectors were short [13]. It was further found that short vectors led to poor geometry tolerance with more defects [200], whilst dense structures were obtained using long vectors [201]. It is thus believed that the vector length has a significant impact on the microstructure in LPBF. It may be a potential method to control the local microstructure and fabricate the component with heterogeneous microstructure for the application.

The effects of vector length on the melt pool morphology and grain structure evolution have not been widely studied. Although the dynamic melt pool evolution of different vector lengths has been investigated by numerical simulation [202], constant laser parameters (e.g., scanning speed and power) are usually assumed as initial conditions in these studies [203]. However, the actual laser motion, which is driven by the galvo motors, has limits on acceleration and deceleration, as explained in Section 2.1.3, especially when the vector length is short [204]. The nominal laser scanning speed may not be achieved in short vectors due to the short travel distance. As a result, the melt pool morphology and microstructure can be significantly different at various vector lengths. However, the melt pool morphology and grain structure characteristics formed at different vector lengths in LPBF have not yet been reported.

The unique microstructure formed via a layer-by-layer fabrication manner can have a strong influence on structure-property relationships, such as tensile [139], creep and compression [140], for AM-ed alloys. Nevertheless, different from the tension or compression, in which the uniaxial loading is applied for the whole sample, the machining-induced deformation only occurs in a roughly 100 µm region close to the free surface. Therefore, plastic deformation is confined to a narrow region, where dramatic deformation often leads to grain refinement and orientation change [147].

Due to the difficulty of tracing grain evolution in such a narrow region [205] as discussed in Section 2.3.1, the deformation mechanism of the resultant crystallographic textures caused by the cutting process is still not well understood. Indeed SEM-based in-situ machining deformation has been investigated within several grains [153,206]. However, few attempts were reported to precisely trace the machining-induced deformation grain by grain in a high-strain-rate machining process. Since the shear process is conducted at the macro level, the deformation mechanism within several grains [153,207] has a limit on explaining the texture-based deformation. This is attributed to the complexity of slip transfer across the grain boundaries and the uncertainty of stress loading at the grain level [140]. It indicates that the texture-based deformation should be investigated based on statistical analysis at the grain scale. The counted grains should be representative of the deformation caused by macro-cutting.

On the other hand, chip formation is crucial to achieve reliable surface integrity and the variations in grain morphology and texture also significantly influence the chip formation during machining [147]. To investigate the chip formation mechanism, quick-stop testing was proposed to study the chip formation as it could maintain the crystallographic characteristics of the chip on the workpiece after cutting [186]. This method allows to characterise the grain deformation near the primary shear zone (PSZ) and to understand the material pile-up behaviour that may be influenced by the unique grain morphologies formed by LPBF.

Chapter 3 Methodology

This chapter includes the materials and experimental procedures used in this research. As this work focuses on the microstructure affected by scanning strategies (e.g., rotational scanning and vector lengths) and the deformation of such unique microstructures during machining, a customised scanning strategy method is employed to design multi-vector scanning strategies. Among such scanning strategies, three commonly used in the commercial printing process are selected to investigate their influence on machining-based deformation and chip formation mechanisms. In order to understand the plastic deformation pattern caused by machining, a novel method is implemented to enable a "quasi-in-situ" investigation of grain morphology and orientation change before and after cutting. The quick-stop cutting test is also conducted to investigate the influence of microstructure on chip formation. Taylor model and a crystal plasticity model are employed to study the mechanism of plastic deformation in orthogonal cutting.

3.1 Laser power bed fusion

3.1.1 Materials

In this work, spherical gas atomised Alloy 718 powder (obtained from BLT, China) was used for the sample fabrication. The majority of powder particles are spherical particles with a few solidified materials, satellites and protrusions as shown in Figure 3.1(a). The average powder diameter is about 38 μm and the specific powder particle distribution is shown in Figure 3.1(b). D_{10}, D_{50} and D_{90} for Alloy 718 powder are 19.01 μm, 37.30 μm and 61.76 μm, respectively. The element composition of Alloy 718 is shown in Table 3.1.

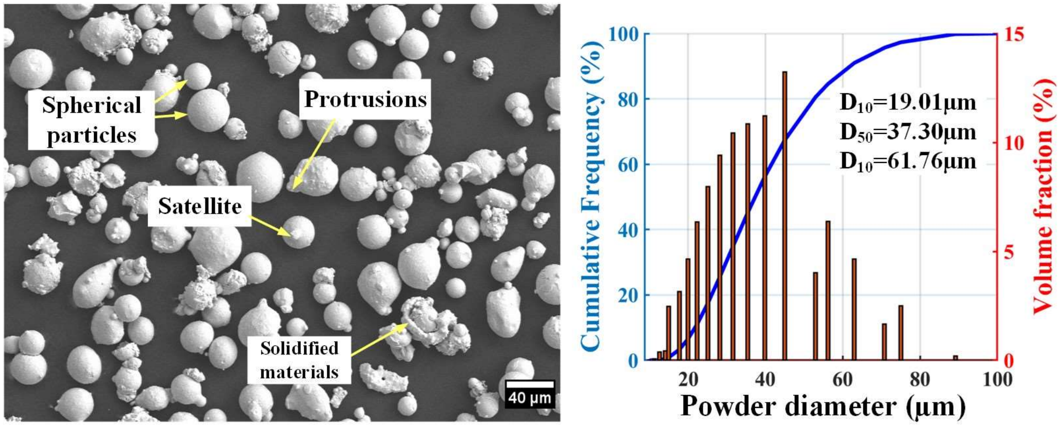

(a) (b)

Figure 3.1: Alloy 718 powder used in this work: (a) morphology of powder; (b) particle size distribution of the powder (average powder diameter: 38 μm, D_{10}=19.01 μm, D_{50} =37.30 μm and D_{90}=61.76 μm).

Table 3.1 Element composition of Alloy 718 in this work.

Element	**Ni**	**Fe**	**Cr**	**Nb**	**Mo**	**Al**	**Ti**	**Mn**	**Co**
Wt%	Bal	28.3.	18.1	5.04	2.8	0.7	1.1	0.3	0.2

3.1.2 LPBF machine

Alloy 718 samples were fabricated by BLT S200 with 500 W Yb fibre laser (wavelength: 1060 - 1080 nm, beam quality: $M^2 < 1.1$). The real building volume is 105 mm × 105 mm × 200 mm. The machine is shown in Figure 3.2(a). The substrate, powder and blower speed are controlled via the manual user interface (UI) (Figure 3.2(b)). The printing process was monitored by indicators that measured chamber pressure, O_2 concentration, status of all motors and remaining powder.

Their conditions are shown in UI (Figure 3.2(c)). Once any value is abnormal, the machine will stop working and the indicator lamp (upper right, Figure 3.2(a)) will turn red from green.

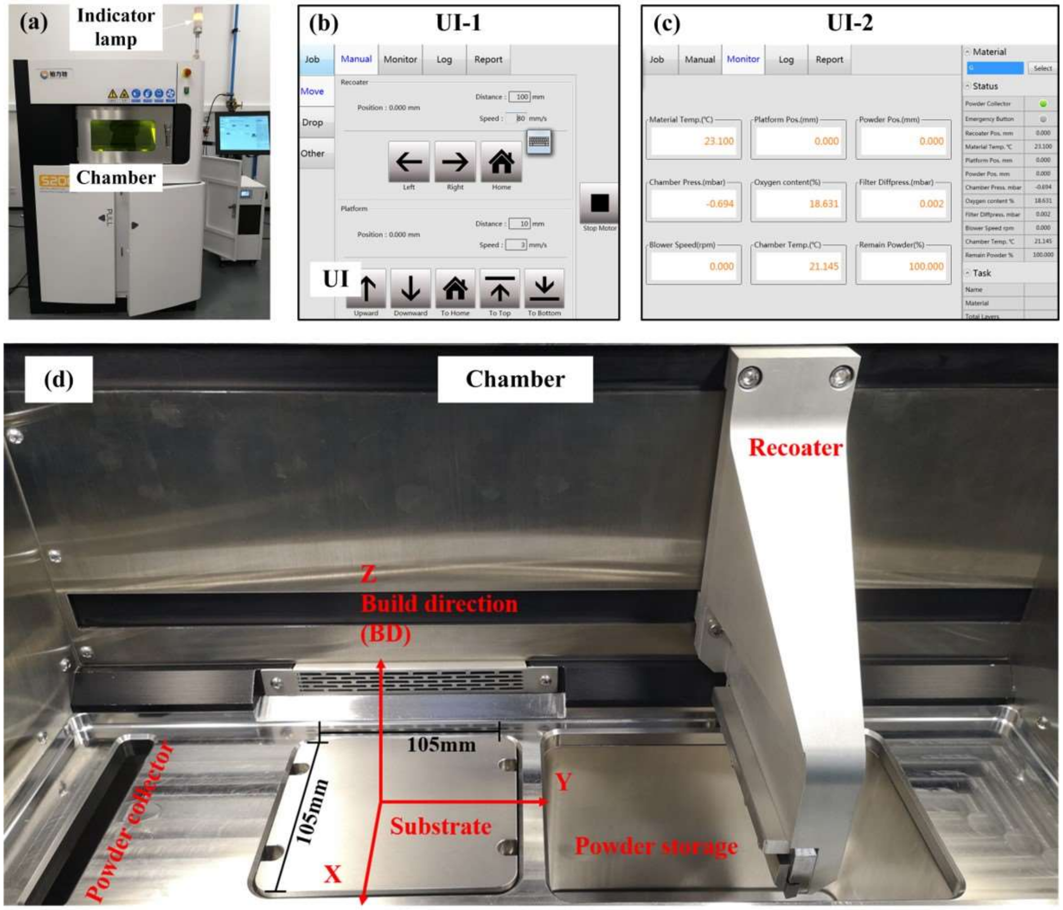

Recoater
Position : 0.000 mm
Distance : 100 mm
Speed : 80 mm/s

Platform
Position : 0.000 mm
Distance : 10 mm
Speed : 3 mm/s

Material Temp.(℃): 23.100
Platform Pos.(mm): 0.000
Powder Pos.(mm): 0.000
Chamber Press.(mbar): -0.694
Oxygen content(%): 18.631
Filter Diffpress.(mbar): 0.002
Blower Speed(rpm): 0.000
Chamber Temp.(℃): 21.145
Remain Powder(%): 100.000

Powder Collector	●
Emergency Button	●
Recoater Pos. mm	0.000
Material Temp. ℃	23.100
Platform Pos. mm	0.000
Powder Pos. mm	0.000
Chamber Press. mbar	-0.694
Oxygen content %	18.631
Filter Diffpress. mbar	0.002
Blower Speed rpm	0.000
Chamber Temp. ℃	21.145
Remain Powder %	100.000

Name	
Material	
Total Layers	

Figure 3.2: Chamber and user interface (UI) of LPBF machine. (a) BLT S200; (b) UI-1 motors motion manual; (c) UI-2 machine condition monitor; (d) chamber for printing.

Key components in the building chamber include a powder collector, a substrate, a powder storage and a recoater (Figure 3.2(d)). The whole printing process is under the protection of N_2, which keeps the O_2 concentration less than 200 ppm. The metal powder is stored in the powder storage and the powder is positioned slightly higher than the layer thickness to ensure sufficient powder supply for each layer. After a layer is scanned, the substrate is lowered by one layer thickness to provide the space for the spreading of the next layer's powder. Then the recoater moves from right to left above the substrate, spreading the powder and ensuring an even distribution of powder on the substrate (or the previously scanned layer). Since the volume of supplied powder should be more than what is actually needed on each layer, the excess powder is collected by the powder collector for recycling. Finally, the laser scans the selected region on the powder layer for manufacturing. By repeating the previous steps, samples could be printed on the substrate (Figure 3.2(d)).

3.1.3 Multi-scale vector scanning strategies

To understand the effects of vector lengths on melt pool morphology and microstructure, four multi-scale vector scanning strategies were employed in this study, as shown in Figure 3.3, and the detailed fabrication parameters are tabulated in Table 3.2. In all scanning strategies, the scanning speed, hatch spacing and layer thickness are kept constant. A zig-zag scanning pattern is used between adjacent laser tracks. Figure 3.3(a) presents the Long-vector strategy (reference strategy) with a vector length of 4 mm. The length of each vector in the Short-vector strategy is 80 μm for a total travel distance of 4 mm, consisting of 50 short vectors, as shown in Figure 3.3(b). The Long-Short vector strategy (Figure 3.3(c)) alternates long vectors and short vectors along the zig and zag directions, respectively. The increment vectors strategy (Figure 3.3(d)) consists of vectors from 80 μm to 400 μm with an increment of 20 μm (i.e., 80 μm, 100 μm, 120 μm, …, 400 μm) along zig direction, followed by vectors decreasing from 400 μm to 80 μm along zag direction. The code in .XML format that controls the vector is detailed in Appendix

B.

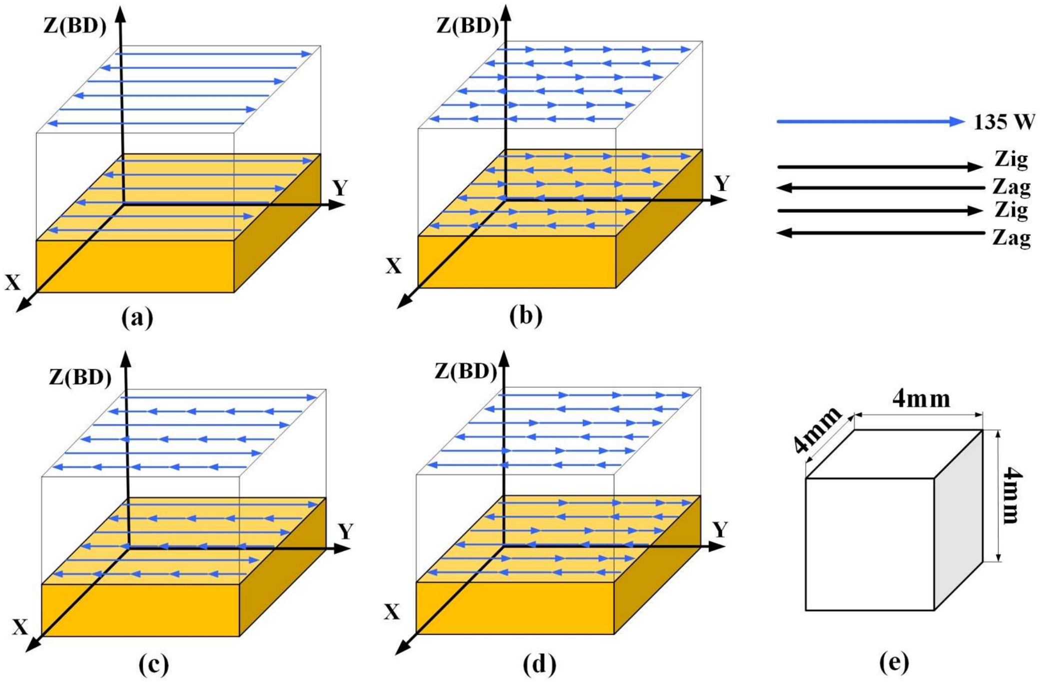

Figure 3.3: Multi-scale vector scanning strategies. (a) Long-vector strategy (vector length: 4 mm); (b) Short-vector strategy (vector length: 80 μm); (c) Long-Short vector strategy; (d) Increment vector strategy (length increases from 80 μm to 400 μm), (e) Size of printed cubes. Z axis represents the build direction (BD). Laser scanning is along the Y-axis.

The key parameters of the laser control system are given in Table 3.3. Laser on/off delays are 50 μs and 90 μs respectively, which are employed to offset the scanning distance error caused by the laser acceleration/deceleration phase. Since there is no spacing between adjacent short vectors, the gap time between them is approximately 50 μs, matching the laser-on delay. The tracking error is the time that the scanner reaches the target speed. Skywriting is set to enable the laser transfer to another track with initial speed. The polygon and vector delays are set in this work but not activated since short vectors are arranged in a straight line instead of polylines. It is noted that all these laser control parameters in this work are commonly used in commercial LPBF machines that are equipped with the

SCANLAB laser control system, but the values may vary due to different requirements.

Table 3.2 Fabrication parameters of multi-scale vectors corresponding to scanning strategies in Figure 3.3.

Scanning strategies	**Laser power (W)**	**Scanning speed (mm/s)**	**Hatch spacing (μm)**	**Layer thickness (μm)**	**Vector length (μm)**	**Refer to**
Long-vector	135	800	80	40	4000	Figure 3.3a
Short-vector					80	Figure 3.3b
Long-Short vector					80 and 4000	Figure 3.3c
Increment vector					80 to 400	Figure 3.3d

Table 3.3 Laser control parameters.

Laser control system	**Value**
Laser On Delay	50 μs
Laser Off Delay	90 μs
Tracking error	150 μs
Skywriting	On
Polygon Delay	On (not activated)
Vector Delay	On (not activated)

3.1.4 Rotational scanning strategies (0°, 67° and 90°)

To investigate the microstructure characteristics affected by rotational scanning strategy, three kinds of different scanning strategies are shown in Figure 3.4. Laser scanning directions of three scanning strategies on Layer N and subsequent Layer

N+1 are 0°, 67° and 90° degrees, respectively. The sample size is designed as 24 mm × 24 mm × 32 mm (L × W × H) to reserve enough machining allowance for subsequent machining. These three scanning strategies can fabricate typical microstructures that have been widely recognised in LPBF 718, making them suitable for investigating subsequent deformation responses.

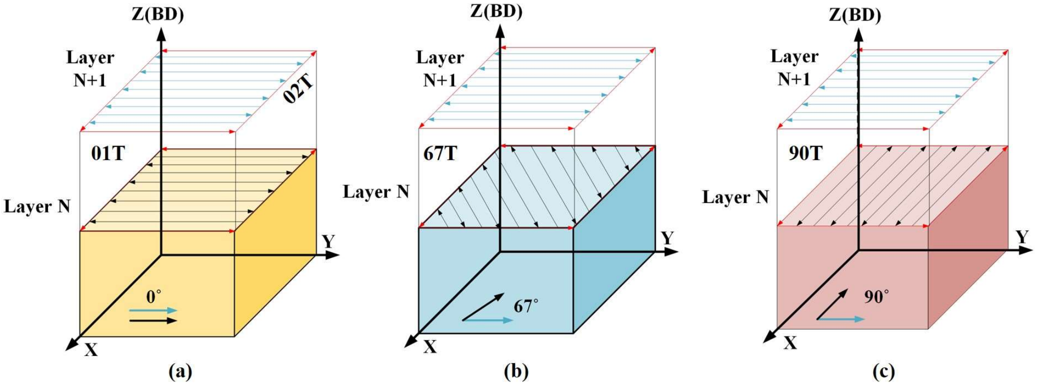

Figure 3.4: Three kinds of scanning strategies. (a) 0° rotation; (b) 67° rotation; (c) 90° rotation. (Laser power: 135 W, scanning speed: 800 mm/s)

To ensure the quality of the as-built sample, 135 W laser power with a scanning speed of 800 mm/s and 20 μm layer thickness were chosen as constant parameters for sample fabrication but with the rotational degrees of 0°, 67° and 90°, respectively. More detailed parameters are shown in Table 3.4. In the three scanning strategies (Figure 3.4), XZ and YZ planes of 90° and 67° rotation strategies are equivalent due to the repeatedly rotated angles layer by layer, while XZ and YZ planes in the 0°-rotation strategy are dissimilar for their unidirectional scanning pattern. Therefore, two workpieces were obtained from the XZ and YZ planes from Figure 3.4(a), named 01T and 02T (Table 3.4), respectively. Workpieces of 90T and 67T (Table 3.4) were obtained from the XZ plane of specimens printed by 90° and 67°-rotation strategies, respectively, as shown in

Figure 3.4(b) and (c).

Table 3.4 Processing parameters for Alloy 718 fabrication with three scanning strategies to enable the generation of different crystallographic textures.

Specimen	**Scanning strategies**	**Laser power (W)**	**Scanning speed (mm/s)**	**Hatch spacing (µm)**	**Layer thickness (µm)**	**Section**
01T	0°-rotation	135	800	80	20	YZ
02T						XZ
90T	90°-rotation					XZ
67T	67°-rotation					XZ

3.2 Microstructure characterisation

Scanning electron microscopy (SEM) (ZEISS Gemini SEM 300) was used to observe microstructure of Alloy 718 with voltage of 15.0 kV. After polishing by silicon carbide abrasive paper of different meshes (from 400 to 2400 mesh) with water lubrication, the samples were then polished on the polishing pad with the diamond polishing spray of 5 µm, 2.5 µm, 1 µm and 0.5 µm successively. Final polishing was finished by 0.04 µm silica suspension. Etchant-acetic glyceregia (15 ml HCl, 5 ml HNO3, 10 ml acetic acid and 2 drops glycerol)-was prepared to etch every sample in a fume cupboard for about 15 s.

Microscopic characteristics such as melt pool size and melt pool arrangement were studied by optical microscope while the microstructure characteristics such as phases, grain morphology and orientation were investigated by SEM with electron backscatter diffraction (EBSD) (magnification from 400X to 8000X). EBSD (from

Bruker company) is used to investigate grain orientation, grain size and misorientation. The step size is set as 0.5 μm and 1.0 μm (beam current: 120 μA) for high and low magnification, respectively. The scanning area is about 1 mm × 1 mm. Electron channelling contrast imaging (ECCI), an imaging technique in SEM based on electron channelling applying a back-scatter electron detector, was used to study lattice defects such as dislocations and stacking faults (i.e. identify grain boundary fast without specific grain orientations).

3.3 Pendulum-based orthogonal cutting test

3.3.1 Pendulum-based cutting machine

The pendulum-based cutting machine is mainly composed of a cutting system and a monitor system (Figure 3.5(a) and (b)). The cutting system consists of a variable-mass pendulum and a height-adjusted base, on which the workpiece is clamped and the cutting tool is mounted, respectively (Figure 3.5(c)). The monitor system includes a high-speed camera (IDT Y4) for cutting process recording and a Kistler 9257A dynamometer for cutting force measurement. An uncut thickness was measured via a compact scissor lift (THORLABS LJ750M) under the tool holder with an accuracy of 0.01 mm. A laptop is used to monitor cutting signals from the high-speed camera and dynamometer (Figure 3.5(b)).

Various cutting speeds are obtained by releasing the pendulum of different counterweights and swinging angles, as shown in Figure 3.5(a). As the cutting tool is installed at a fixed position, the initial cutting speed keeps constant once the releasing angle is set. A high-speed camera records the whole cutting process and the changing of cutting speed is calculated by the displacement of the workpiece and exposure frequency of the camera. At the same time, the raw electrical signal of the dynamometer is transformed into a force signal and collected automatically.

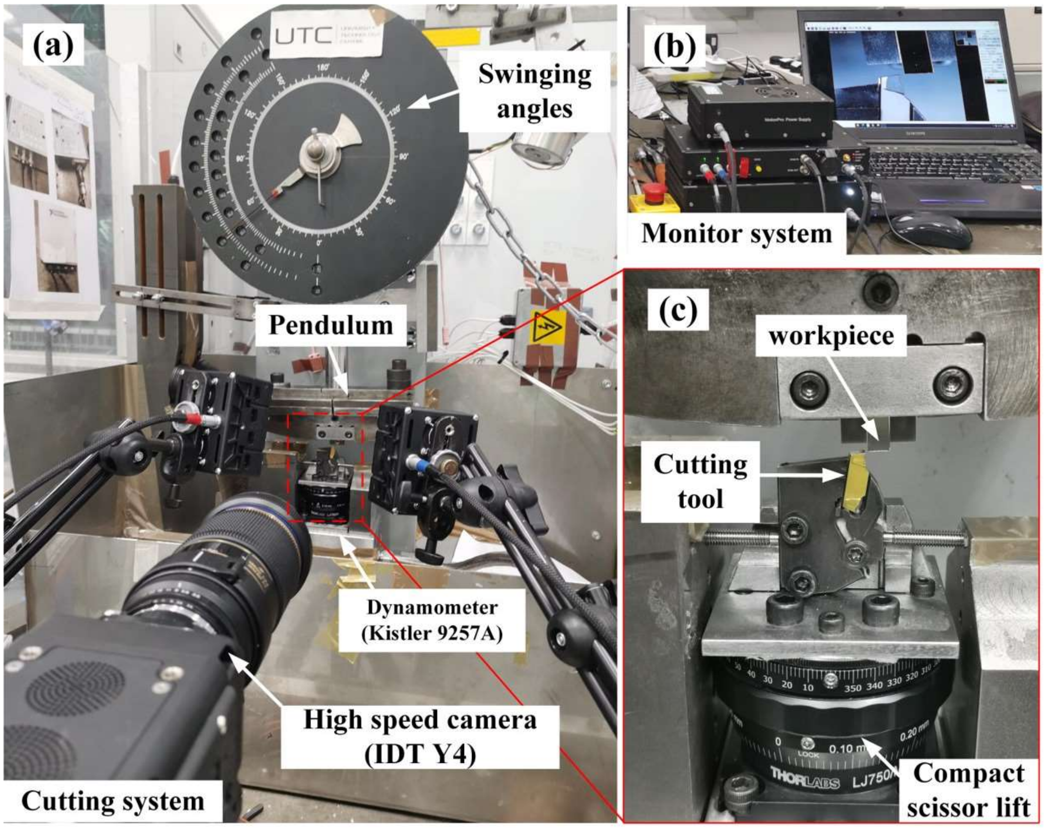

Figure 3.5: Setup of the pendulum-based cutting test. (a) Pendulum-based cutting machine; (b) Laptop monitor; (c) Positions of cutting tool and workpiece (The cutting thickness is controlled by a compact scissor lift).

3.3.2 Sample for orthogonal cutting

The sample size design (25 mm × 6 mm × 1mm) is the balance of cutting stability and convenience of EBSD observation. Since such a sample size is not suitable for fixing, an adapter is used for holding the sample, as shown in Figure 3.6(b). The dimensions of the U-shape adapter are 27.5 mm × 20 mm, ensuring to fill the entire sample slot highlighted in Figure 3.6(a).

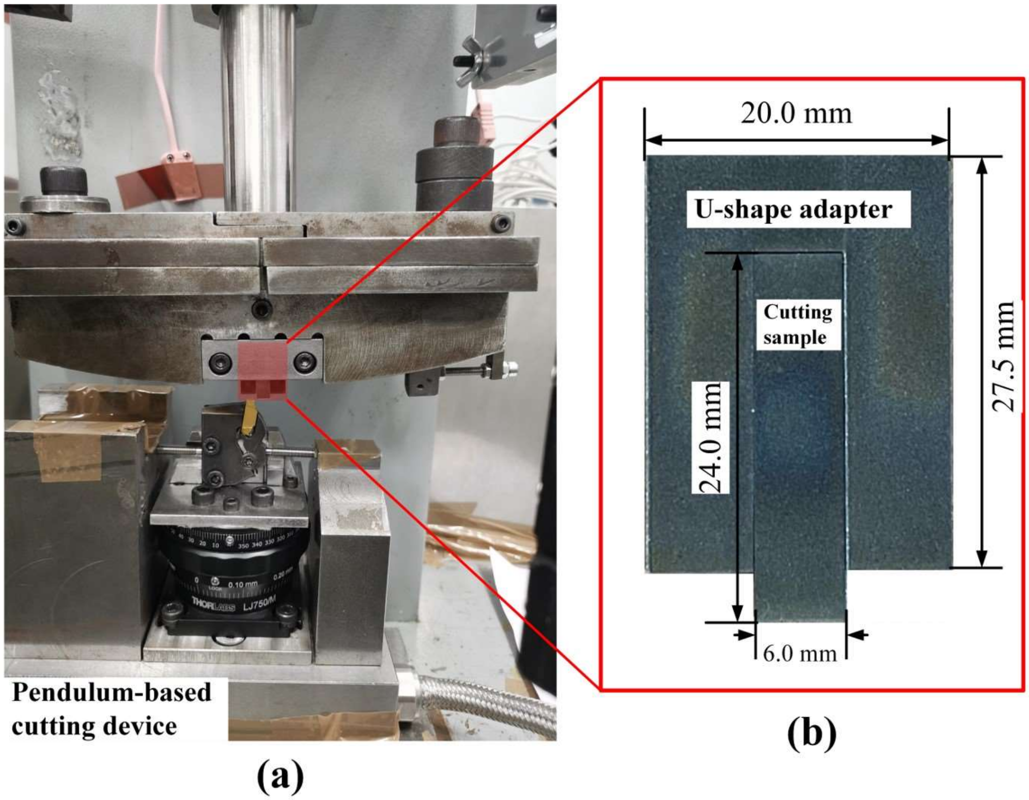

Figure 3.6: Orthogonal cutting machine and adapter for sample fixing. (a) Pendulum-based orthogonal cutting machine; (b) Dimensions of U-shape adapter and sample.

3.3.3 Quasi-in-situ machining investigation

A diagram of samples prepared for quasi-in-situ machining investigation by SEM&EBSD is shown in Figure 3.7(a). To compare the deformation of typical grains in the textured Alloy 718 before and after cutting, EBSD&SEM characterisation at the same zone near the machined surface was performed. A "T-shape" label was marked on the carefully polished samples as a reference, allowing the same area to be detected under EBSD&SEM before and after cutting as shown in Figure 3.7(a). It should be noted that the "quasi-in-situ" investigation was only conducted for the machining process instead of the LPBF process. The workpieces obtained from as-built cubes, namely 01T, 02T, 67T and 90T according to Table

3.4, were shown in Figure 3.7(b). All cutting directions in this work are perpendicular to the build direction. Four test workpieces with dimensions of 24 mm × 6 mm × 1 mm were obtained from as-built specimens by electrical discharge machining (EDM) as shown in Figure 3.7(c).

To observe the grain responses before and after machining, the experimental process is shown in Figure 3.7(c), (d), (e). Each test piece was polished and then scratched with a T-shape mark at the centreline of the workpiece and 2.5 mm from the top free surface before cutting (Figure 3.7(e)). The centreline mark on the polished sample was scratched by the scriber of the height gauge and used as the reference to locate the EBSD mapping area before and after cutting.

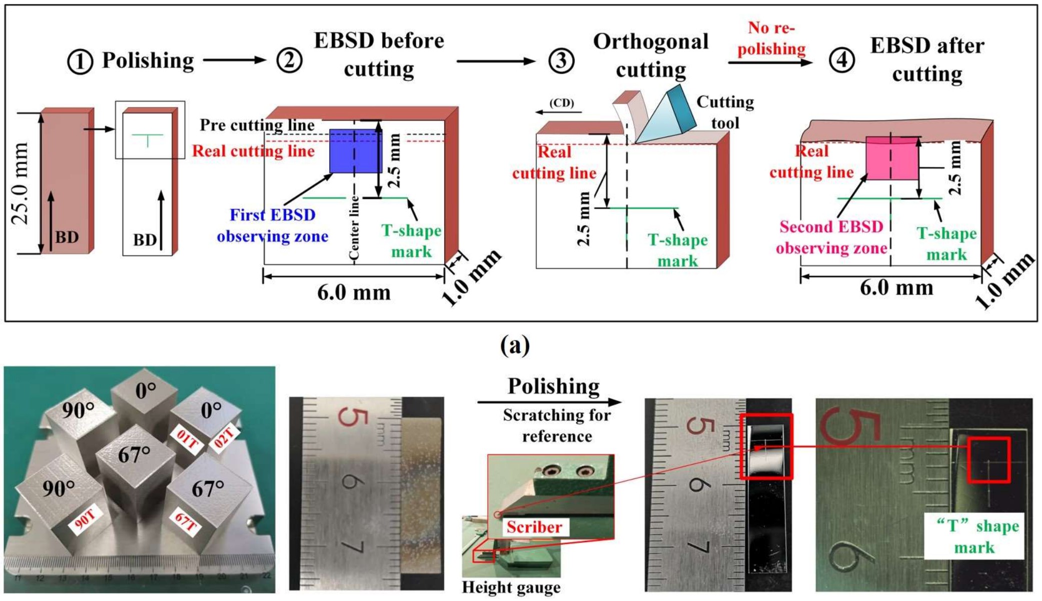

(a)

(b) (c) (d) (e)

Figure 3.7: Sample preparation schematics and reference mark scratching. (a) Schematics of quasi-in-situ investigation processing, including polishing, first EBSD&SEM observation, orthogonal cutting and second observation; (b) As-built cubes of 0°-rotation, 90°-rotation and 67° rotation scanning strategies; (c) Unpolished samples; (d) Polished samples; (e) “T” shape mark (scratched by scriber of height gauge) as the reference for observing the same zone before and after cutting.

3.4 Pendulum-based quick-stop cutting test

3.4.1 Quick-stop module

To achieve “quick-stop” and retain the chip on the workpiece during orthogonal cutting, it requires the cutting process to be interrupted in a controlled manner. In this work, the pendulum-based cutting device with a self-designed quick-stop module was illustrated in Figure 3.8(a) and (b), where the key components are numbered. The sample fixture (1) was assembled on the pendulum (2) (Figure 3.8(a)) and a stopper (3) was designed to interrupt the cutting process (Figure 3.8(a)) by blocking the workpiece moving forward. The cutting tool (5) was fixed in the tool holder (4) and placed below the pendulum (2) as illustrated in Figure 3.8(b). A specific sample design, including the workpiece (6), an H-shape spacer (7), a stop pin (8), and a U-shape adapter (9) (Figure 3.8(c)), was adopted to achieve the “quick-stop” function and maintain a stable cutting process. The stop pin (8) was fitted into the slot (10) machined on the workpiece (Figure 3.8(d)), which allows the movement of the workpiece (6) to be interrupted. To retain the chip on the workpiece at the target cutting speed, a weak joint (11) (Figure 3.8(d)) was designed by machining a groove (12) on the workpiece and the H-shape spacer (7) was inserted into the groove to minimise the cutting instability. The above four components (6-9) were assembled as shown in Figure 3.8(e) and mounted in the sample fixture (1) on the pendulum (2) for the cutting test.

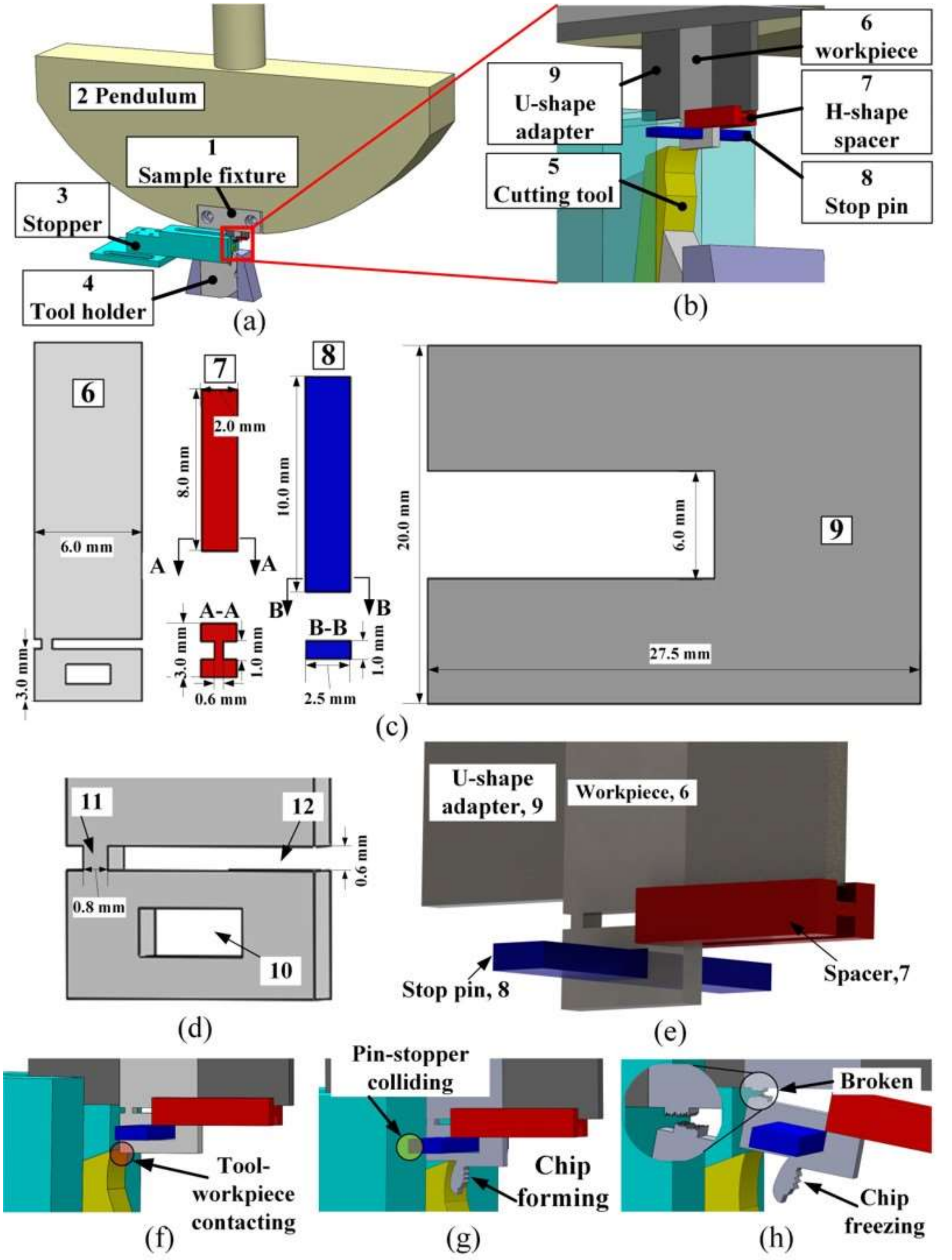

Figure 3.8: Quick-stop module and cutting process schematics. (a) and (b) are schematics of pendulum-based cutting machine, quick-stop module and the cutting tool; (c) and (d) are components for quick-stop cutting test, including spacer, stop pin, sample and U-shape adapter; (e) schematic of assembled components; (f), (g) and (h) schematics of the quick-stop cutting test. (1. Sample fixture, 2. Pendulum, 3. Stopper, 4. Tool holder, 5. Cutting tool, 6. Workpiece, 7. H-shape spacer, 8. Stop pin, 9. U-shape adapter, 10. Slot, 11. Weak joint, 12. Groove)

The cutting procedure was demonstrated in Figure 3.8(f)-(h) from workpiece-tool contacting, chip forming to weak joint breaking. The pendulum was released at an angle of 60° and the cutting started when the workpiece was in contact with the cutting tool at a given cutting depth (0.2 mm) (Figure 3.8(f)). Subsequently, the chip was formed as the pendulum moved progressively until the pin (8) collided with the stopper (3) (Figure 3.8(g)). The collision led to a significant impact on the stop pin and produced a high stress concentration at the weak joint which was then broken down rapidly (Figure 3.8(h)). A cutting speed of approximately 112 m/min at the quick-stop moment was calculated from the frames captured by a high-speed camera (IDT Y4 (Figure 3.5(a))). Finally, after removing the stop pin (8) and H-shape spacer (7), the chip was collected for further analysis.

It was measured that the cutting speeds usually decreased from 112±3 m/min to 105±4 m/min before the fracture. The chip formation process is not significantly changed by such a cutting speed fluctuation. It was observed that the fracture of the weak joint consists of three sequential steps: ideal plastic deformation, work hardening and fracture. To reduce the influence of fracture of the weak joint, the H-shape spacer (7) provided a constraint condition to allow the shear deformation of the weak joint almost parallel to the cutting direction at the beginning of cutting. Hence, a relatively stable chip formation process can be obtained during work hardening of the weak joint due to less deformation at this stage. Finally, the constraint from the H-shape spacer (7) restricted the fracture at the weak joint only along the cutting direction, achieving a stable cutting process. The cutting tool information and parameters are listed in Table 3.5. Since the uncut chip thickness

(0.2 mm) and the cutting edge radius (0.02 mm) are not in the same order, the cutting edge radius has limited influence on the cutting test. The cutting parameters are also the same in all four cutting tests to ensure that the chip formation processes of wrought and LPBF-fabricated Alloy 718 are comparable. Moreover, a steady-state orthogonal cutting test was performed under the same cutting parameters without the quick-stop module. Cutting forces were measured using a dynamometer (Kistler 9257A) for each case. A micro-hardness was performed via a Buehler Wilson VH3300 hardness tester from the workpiece to the chip with 0.2 kgf loads at a dwell time of 15 s.

Table 3.5 Cutting tool information and cutting parameters.

Cutting tool	**Material**	**Coolant**
LCGE160402-4-0400-GS, SECO	Carbide uncoated	Dry cutting
Cutting parameters	Rake angle, γ (˚)	18.0
	Cutting speed at quick-stop moment (m/min)	112.0
	Uncut chip thickness (mm)	0.2
	Cutting length at quick-stop moment (mm)	3.0
	Cutting width (mm)	1.0
	Edge radius (mm)	0.02

3.4.2 Sample for quick-stop cutting test

To retain the chip on the workpiece via the quick-stop module and ensure the stability during the cutting test, the sample (Figure 3.6(b)) is optimised as shown in

Figure 3.9(a). Since the fracture of the weak joint consists of three sequential steps: ideal plastic deformation, work hardening and fracture. To reduce the influence of fracture of the weak joint, the spacer (Figure 3.9(a)) was designed to provide a constraint condition to allow the shear deformation of the weak joint almost parallel to the cutting direction at the beginning of cutting. Hence, a relatively stable chip formation process can be obtained during work hardening of the weak joint due to less deformation at this stage. During the cutting process (Figure 3.9(b)), the constraint from the H-shape spacer (7) restricted the fracture at the weak joint only along the cutting direction, achieving a stable cutting process. The stop pin was designed to abruptly stop the cutting process when the pin collided with the stopper and the weak joint was broken. It should be noted that the sample was polished before cutting to minimise the effect of EDM machined surface on the cutting test [208]. No heat treatment was conducted for the as-built Alloy 718 to retain the unique grain structure.

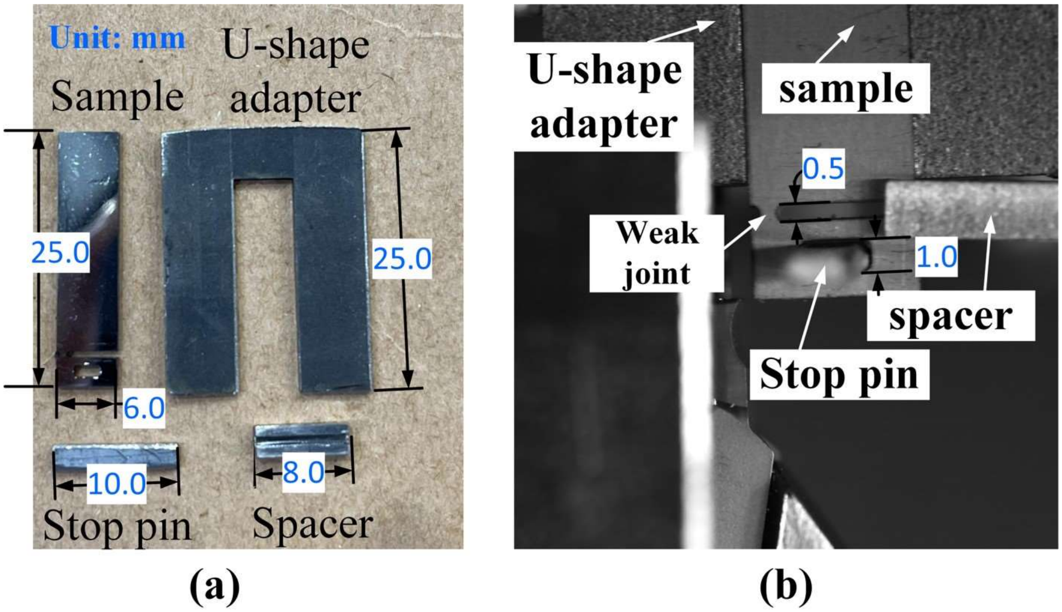

Figure 3.9: Customised sample for quick-stop cutting test. (a) Test sample composed of four parts: sample, U-shape adapter, stop pin and spacer (Unit: mm); (b) corresponding parts in (a) are assembled for quick-stop cutting test.

3.5 Mathematic models

3.5.1 Taylor-based model

To investigate the crystallographic texture-based deformation, a Taylor-based plastic model was used to evaluate the relationship between the shearing of the Alloy 718 workpiece and crystal orientation [209]. According to the minimum energy theory proposed by Taylor, accomplishing a general deformation needs five independent slip systems and the one with a minimum sum of internal work in a crystal will be active. In an FCC metal, there are four slip planes, and each plane has three slip directions as shown in Table 3.6.

Table 3.6 Slip planes and corresponding slip directions for FCC metals.

Slip plane, n		(111)			$(\bar{1}\bar{1}1)$	
Slip direction, b	$[01\bar{1}]$	$[\bar{1}01]$	$[1\bar{1}0]$	$[0\bar{1}\bar{1}]$	$[101]$	$[\bar{1}10]$
Slip plane, n		$(\bar{1}11)$			$(1\bar{1}1)$	
Slip direction, b	$[01\bar{1}]$	$[101]$	$[\bar{1}\bar{1}0]$	$[0\bar{1}\bar{1}]$	$[\bar{1}01]$	$[110]$

The schematic of orthogonal cutting is shown in Figure 3.10, in which the cutting tool is perpendicular to the cutting direction (CD), and the chip is removed from the workpiece under the shear stress in the shear plane (SP), as shown in reference [210]. The shear plane (SP) is parallel to the shear direction and recognised as a 2D plane (the normal of shear plane is perpendicular to the shear direction).

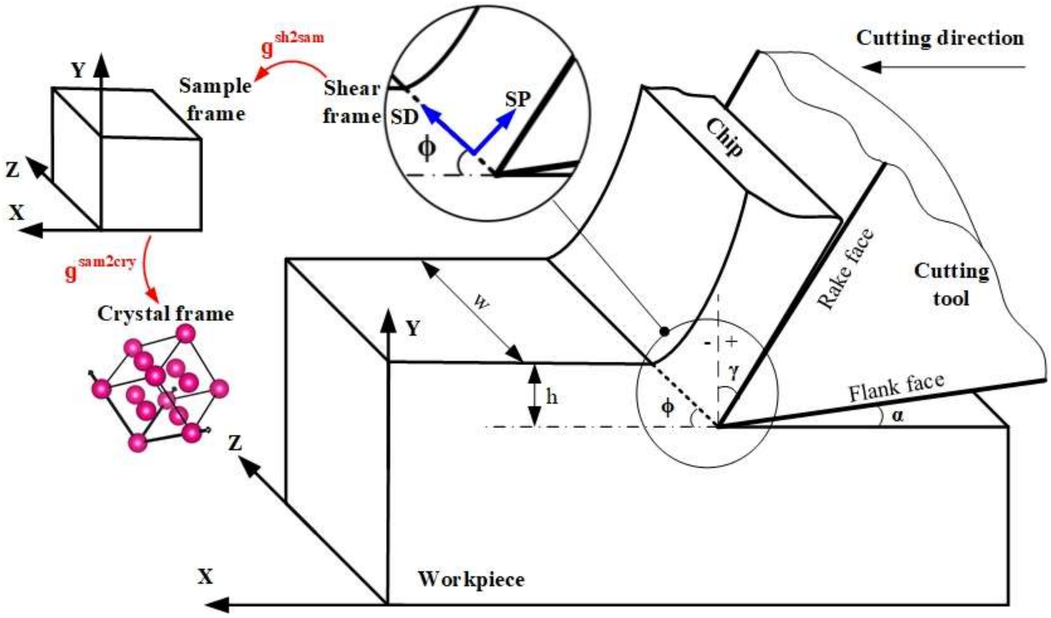

Figure 3.10: Orthogonal cutting model and the frame relationship among shear plane, sample and crystal. Shear direction (SD) and shear plane (SP) are shown as blue arrows.

The Taylor-based model can calculate the shear deformation gradient ($\in_{she}$) in the SP with the plane-strain condition [209]:

$$\in_{shear}= \frac{d\varepsilon}{2}\begin{pmatrix}0 & 1 & 0\\ 1 & 0 & 0\\ 0 & 0 & 0\end{pmatrix} \tag{3-1}$$

The shear strain ε in the shear plane is estimated based on [211]:

$$\varepsilon = \frac{\cos\gamma_n}{2\sqrt{3}sin\phi_n\cos(\phi_n-\gamma_n)} \tag{3-2}$$

where γ_n is the rake angle and ϕ_n is the shear angle, which was estimated by the Merchant theory [210]. The angle calculated by analytical method is decided by the cutting tool geometry and cutting direction by Equation 3-2. The plane-strain transformed from the shear plane (SP) into the sample frame (Figure 3.10) via transformation matrixes in Equation 3-2:

$$g^{\text{shear}\rightarrow\text{sample}} = \begin{pmatrix}\cos\phi & -\sin\phi & 0\\ \sin\phi & \cos\phi & 0\\ 0 & 0 & 1\end{pmatrix} \tag{3-3}$$

The shear strain loaded in the sample frame is calculated by Equation 3-4:

$$\in_{ij}^{sample}= g_{ik}^{shear\rightarrow sample} g_{jl}^{shear\rightarrow sample} g_{kl}^{shear} = \frac{d\varepsilon}{2}\begin{pmatrix}-\sin2\phi & \cos 2\phi & 0\\ \cos2\phi & \sin 2\phi & 0\\ 0 & 0 & 0\end{pmatrix} \tag{3-4}$$

where $g_{ik}^{shear\rightarrow sample}$ is the transformation matrix used to rotate the deformation gradient of Equation 3-1 to the sample frame. The transformation from the sample frame to the crystal frame is via Equations 3-5 and 3-6:

$$g^{\text{sample}\rightarrow\text{crystal}} = \begin{pmatrix} \mathrm{u} & \mathrm{o} & \mathrm{h} \\ \mathrm{v} & \mathrm{p} & \mathrm{k} \\ \mathrm{w} & \mathrm{q} & \mathrm{l} \end{pmatrix} \qquad 3\text{-}5$$

$$\in_{ij}^{crystal} = g_{ik}^{sample\rightarrow crystal} g_{jl}^{sample\rightarrow crystal} g_{kl}^{sample} \qquad 3\text{-}6$$

where [uvw] and (hkl) represent the cutting direction and the cutting plane, respectively. The coordinate transformation matrix $\mathrm{g}^{\text{sample}\rightarrow\text{crystal}}$ is dependent on both the current sample frame and orientated crystal coordinates [212]. The shear strain then can be applied to each grain to calculate the most active slip direction. It should be noted that the final shear strain in each crystal frame is different for the different oriented crystal frames.

To calculate the most active slip trace for each grain in the FCC structure, the deformation gradient $\in^{crystal}$ is based on five independent slip systems and can be written as:

$$\in^{crystal} = \sum_{i=1}^{5} m^{\alpha} \delta\, \gamma^{\alpha} \qquad 3\text{-}7$$

where $m^{\alpha} = b^{\alpha} \otimes n^{\alpha}$, b^{α} is slip direction for slip system α, n^{α} is the slip plane normal for slip system α, $\delta\gamma^{\alpha}$ denotes shear increment at slip system. It should be noted that the five independent slip systems here are employed to calculate the minimum work in slip system. This not means that five slip system will be observed in real plastic deformation. The deformation occurs with minimum energy and the work increment, δw can be written as:

$$\delta \mathrm{w} = \tau_c \sum_{i=1}^{5} \delta\gamma \tag{3-8}$$

All slip system:

$$\begin{array}{cccccc}
u & v & w & h & k & l \\
0 & -1 & -1 & -1 & 1 & -1 \\
-1 & -1 & 0 & -1 & 1 & -1 \\
1 & 0 & -1 & -1 & 1 & -1 \\
0 & -1 & 1 & -1 & -1 & -1 \\
1 & -1 & 0 & -1 & -1 & -1 \\
1 & 0 & -1 & -1 & -1 & -1 \\
0 & -1 & 1 & 1 & -1 & -1 \\
-1 & 0 & -1 & 1 & -1 & -1 \\
-1 & -1 & 0 & 1 & -1 & -1 \\
0 & -1 & -1 & 1 & 1 & -1 \\
1 & -1 & 0 & 1 & 1 & -1 \\
-1 & 0 & -1 & 1 & 1 & -1
\end{array} \tag{3-9}$$

In this minimum energy deformation system [213], we assume the shear deformation is based on the minimum energy theory. For a grain with an orientation, there is an angle (θ) between the shear direction (s) and slip system (Equation 3-9), slip plane normal, **n** (h, k, l), and slip direction, **d** (u, v, w)). Since the burgers vector (b) is parallel to the slip direction (in general) and this model assumes that all slip directions have the same critical resolved shear stress, the strain in the crystal frame can be normalized and calculated along each slip direction. The mean value of activated slip in the slip system is b^{α}.

Since the strain is symmetric and only 5 slip systems need to be calculated by Equation 3-7, the minimum W was obtained by the sum of critical resolved shear stress. The most active slip direction has the maximum displacement component along the slip direction and the corresponding slip plane is the most active. The most active slip system is given by:

$$b^{\alpha} = Max\left|b^{i}(\delta \mathrm{w})\right| \tag{3-10}$$

The relevant slip plane (most active slip plane) is:

$$n^{\alpha} = |(b^{\alpha}_{Max})| \tag{3-11}$$

Since the most active slip planes of oriented grains are calculated in individual crystal frames, they should be transformed from the crystal frame to the sample frame based on Equations 3-5 and 3-6. After the frame transformation, the most active slip trace t_m is defined as the intersecting line of the most active slip plane and the sample plane, XY plane (Plane_{xy}) in:

$$t_m = n^{\alpha} \cap \mathrm{Plane}_{xy} \tag{3-12}$$

Considering the Euler angle of each pixel in the EBSD, the most active slip direction from 12 slip systems (24 slip directions if consider opposite direction) was calcuated. Since the Euler angle within a grain may be similar, the calculation step can be set as 5 μm to save computing time. The intensity is the weight of a slip trace in all slip trace. The grain size is considered because the large grain (more pixels) have high weight than small grain.

3.5.2 Crystal plasticity model

The simulation of the crystal response to the orthogonal cutting process is carried out using a well-established framework based on resolved shear stress and hypoelasticity, which was originally proposed by Hill, Rice, and many others [214]. The deformation gradient, $\boldsymbol{F}$, can be written as:

$$\boldsymbol{F} = \boldsymbol{F}^{*} \cdot \boldsymbol{F}^{\boldsymbol{p}} \qquad \text{3-13}$$

where $\boldsymbol{F}^{*}$ is caused by stretching and rotation of crystal lattice with reference to the intermediate configuration and $\boldsymbol{F}^{\boldsymbol{p}}$ is the deformation due to plastic shearing on crystallographic slip systems.

The PRISMS-Plasticity, an open-source software was employed here to simulate full-field crystal plasticity [214]. The evolution of slip resistance for slip system α can be calculated by:

$$\dot{s}^{\alpha} = \sum_{\beta} h^{\alpha\beta} \dot{\gamma}^{\beta} \qquad \text{3-14}$$

where $h^{\alpha\beta}$is hardening moduli, which defines the variation of slip resistance for slip system α due to the slip rate on slip system β. The hardening moduli $h^{\alpha\beta}$is considering the combined effect of work hardening and recovery as follows:

$$h^{\alpha\beta} = q^{\alpha\beta} h_o (1 - \frac{s^{\beta}}{s_s})^m \qquad \text{3-15}$$

where $q^{\alpha\beta}$is the latent hardening ratio, h_o denotes the hardening parameter for slip system β, $s^{\beta}$is the slip resistance at hardening saturation, s_s is the saturation stress where large plastic flow initiates and m is a material constant that governs the sensitivity of the hardening moduli to the slip resistance. The crystal plasticity model is detailed in [215] and the material constants for the simulation are obtained from [216]. The material constants used in the four cases are identical because the fabrication parameters are also the same. Therefore, the simulation only varies in terms of grain morphology and orientation.

To mesh the EBSD data for plasticity simulation, a 400 × 90 μm region was directly processed using Gmsh [217] as illustrated in Figure 3.11. As the EBSD results were obtained prior to the cutting process, the preserved grain morphologies were carefully retained to prevent errors arising from distortions near the machined surface. This approach could enhance the simulation accuracy since the loading is applied to the original grains. To fix the bulk material, a nodal boundary condition was employed, while a loading condition (obtained from the analytical model of Eq. 3-2) was applied to the region near the machined surface. The total simulation time was set as 1×10^{5} s to reach a high strain rate whilst the time increment was $\times10^{9}$ s for simulation convergence. The post-processing was finished by ParaView, an open-source software for visualization.

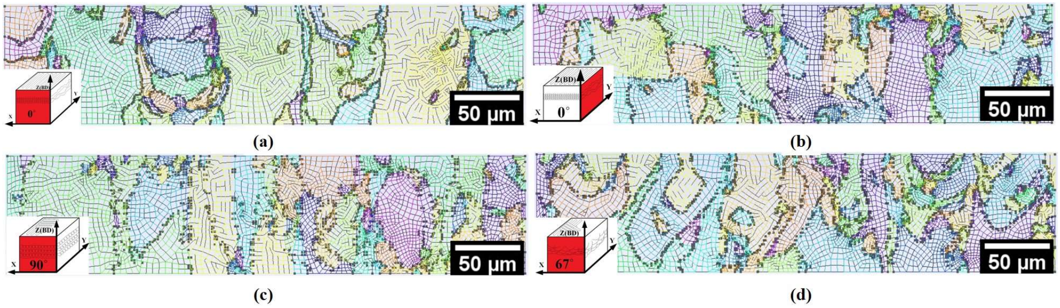

(a) (b) (c) (d)

Figure 3.11: EBSD data meshed by Gmsh with element type of Hex. The grain boundaries are depicted by dark dashed lines. The grain orientation information is extracted from EBSD data and applied to each grain during simulation. (a) 01T, (b) 02T, (c) 90T and (d) 67T.

Chapter 4 Microstructure of Alloy 718 fabricated by multi-scale vectors

To investigate the effect of vector length on melt pool morphology, microstructure and printing quality, this chapter includes the detailed microstructure characterisations for multi-vector scanning strategies introduced in Sections 3.1.3, respectively. The microstructure is mainly identified via OM, SEM and EBSD and the effect of scanning strategies on grain growth patterns is discussed.

4.1 Effect of vector length

4.1.1 Microstructure evolution in XY-plane

4.1.1.1 Melt pool and grain morphologies of long and short vectors (XY-plane)

The melt pool morphologies perpendicular to the build direction (refer to XY plane in Figure 3.3) are shown in Figure 4.1. Vectors with different lengths and directions are highlighted by the blue arrows. The reference sample printed by the Long-vector strategy is shown in Figure 4.1(a). This strategy has been proven to build nearly defect-free components [218]. Continuous melt pools can be seen in Figure 4.1(a) and some necking and breaking (Figure 4.1(a) black rectangles) occur due to the melt pool instability caused by thermal perturbation [219].

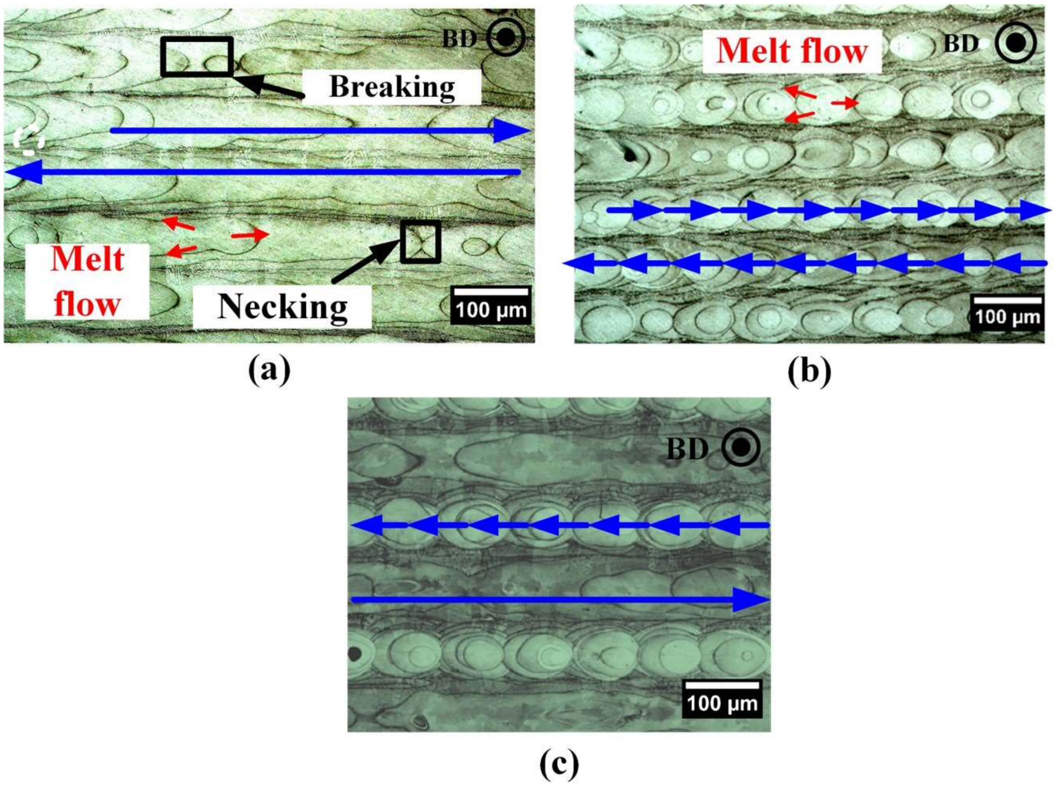

Figure 4.1: Comparison of microstructures that are perpendicular to the build direction (XY plane): (a) Long vectors; (b) Short vectors; (c) Long-Short vectors.

Figure 4.1(b) depicts the melt pool morphology of the Short-vector strategy. Unlike the reference sample in which a single vector length is equivalent to the part size (4 mm in length), this sample in Figure 4.1(b) consists of 50 short vectors and the length of each vector is 80 µm. Many spot-like melt pools along the laser tracks can be seen in Figure 4.1(b) in this Short-vector scanning strategy. Since the laser turns on at the beginning of a vector and then turns off at the end of the vector in the LPBF process, the spot-like melt pools are mainly attributed to the laser on/off switching at the vector ends. Since the melt pool flow direction is mainly from laser centre to the head/end of the melt pool during the laser scanning, the laser scanning direction is able to be identified by the melt pool morphologies in Figure 4.1. The scanning direction is highlighted by blue arrows, which are decided by the melt flow near the laser beam centre (red arrows). The spot-like characteristics are unique in Short-vector printing due to the large number of short vectors in Figure 4.1(b). Some voids are found at the boundaries of neighbouring vectors, which is likely due to the lack of fusion at the vector ends.

Figure 4.1(c) presents alternating long and short vectors in the sample, corresponding to the Long-Short vector scanning strategy in Figure 3.3(c). The long vectors of 4 mm and short vectors of 80 μm are aligned in antiparallel directions (i.e., long vector scans from the left to the right and short vector scans in the opposite direction). The characteristics of long and short vectors in Figure 4.1(c) are in good agreement with features in Figure 4.1(a) and (b) respectively. It shows continuous melt pools of long vectors and spot-like melt pools of short vectors. This demonstrates that both melt pools are not significantly affected by the alternating scanning strategies. The small spherical pores in Figure 4.1(c) likely resulted from a lack of fusion. Due to the unstable bonding between long and short vectors, they are mostly distributed near the boundaries of neighbouring laser tracks. Similar defects are also seen in Figure 4.1(b), suggesting that the defects in this Long-Short scanning strategy are mainly caused by the short vectors.

The corresponding inverse pole figures (IPF) and pole figures (PF) are shown in Figure 4.2. The numbers of grains for PF in three cases are 1156, 1432 and 1289 respectively. The coordinate frame for the PF is consistent with the sample frame in Figure 3.3 in this work. Figure 4.2(a)-(c) compares the grain structures formed by three scanning strategies, and the laser path is also highlighted by blue arrows. During the laser scanning process, the highest temperature is near the laser centre, leading to a perpendicular thermal gradient to the laser path. Subsequently, grain grows along the direction of the thermal gradient, and the grain boundary is likely to be perpendicular to the laser path, as shown in Figure 4.2(a) and (c). Moreover, some large grains are observed in Figure 4.2(a) and the preferred orientation (011)⊥BD is depicted in Figure 4.2(b), indicating that a long vector provides a stable thermal field for grain growth. For the Long-vector, fine grains are primarily concentrated along the centre of the melt pool (blue arrows in Figure 4.2(a)). This phenomenon can be attributed to the fact that the highest cooling rate (about $10^{5\text{-}7}$ K/s as reported by Liang et al. [220]) during laser scanning. Since grain grows from the melt pool boundary to the melt pool centre, there is limited space along the path of the laser centre for grain growth, leading to fine grains along the melt pool centre (Figure 4.2(a)).

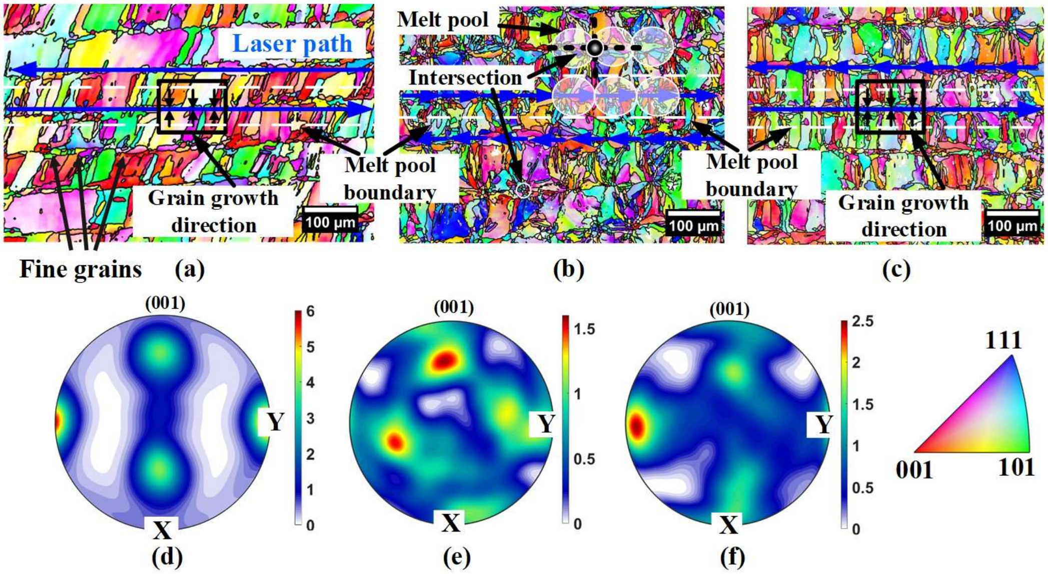

Figure 4.2: Inverse pole figure (IPF) mappings and pole figure (PF) for Long vectors (a) and (d), Short vectors (b) and (e), Long-Short vectors (c) and (f). (Lack of fusion is labelled by yellow dashed circles and gas entrapped pore is labelled by white dashed circles. The numbers of grains for PF in (g), (h) and (i) are 1156, 1432 and 1289 respectively.

In the Short-vector, some fine grains are distributed along the melt pool centre, similar to the Long-vector. However, fine grains are also observed between two neighbouring short vectors. This indicates that laser on/off leads to a high cooling rate between adjacent short vectors. Therefore, in the XY plane, there are two dominant ways for the fine grains to form in the Short-vector scanning strategy: (1) thermal gradient direction is along the laser path within a short vector; (2) thermal gradient direction is perpendicular to the laser path near the intersection of two adjacent melt pools, as shown by black dashed lines between two melt pools (white circles) in Figure 4.2(b). Considering the boundary shape of the melt pool is curved, the fine grain distribution in the Short-vector therefore resembles a “radiant” pattern, originating from the intersection of short melt pools. This phenomenon can be observed at each intersection between neighbouring short vectors in Figure 4.2(b). It is noted that the actual thermal gradient undergoes perturbations, which can explain why the distribution of fine grains is sometimes more randomised. It can be speculated that the number of fine grains in the Long-Short vector should be less than that in Short-vector. Because the melt pool formed by a long vector is wider than that formed by short vectors. A long vector is able to partially inhibit fine grains to grow from neighboured short-vector melt pools. The grain growth direction is dominated by the long vector in the Long-Short vector printing case. Therefore, fine grains are mainly distributed along the laser path and a few fine grains are distributed perpendicular to the laser path, which is indeed seen in Figure 4.2(c).

The distribution of fine grains suggest that the short vectors may lead to steep thermal gradients near the intersection, making it easier for fine grains to form than in a long vector. The grain orientation in the Long-Short vector (Figure 4.2(f)) is comparable to the Long-vector, but the texture intensity is lower. This also suggests that the grain growth direction is mainly affected by long vector, matching well with the grain structure in Figure 4.2(c). Moreover, short vectors may lead to unstable thermal gradients due to that the laser on/off occurs quite rapidly. Such a complex thermal gradient consequently interrupts the formation of preferred grain growth direction (Figure 4.2(e)) and limits the formation of large grains.

4.1.1.2 Melt pool and grain morphologies of incremental vectors (XY-plane)

Figure 4.3(a) shows melt pool morphologies of incremental vectors from 80 μm to 400 μm with 20 μm increments between each consecutive vector. Pores are randomly embedded across the sample but the lack of fusion mainly occurs in the short vector zone (e.g., 80 – 180 μm). The narrow melt pool formed by the short vector results in relatively weak bonding when compared with the long vector. The lack of fusion is more likely observed in the short vector zone. Due to the laser on/off transition, the steep thermal gradient in a short vector is not only perpendicular to the laser scanning path but also perpendicular to the melt pool boundary at the head/end. Since the high cooling rate may lead to multi-directional thermal gradients, the grain growth directions are randomised in the short vector region (80 – 180 μm in Figure 4.3(b)). The grain structure is, therefore, irregular when compared with the long vector region (380 – 4000 μm). This phenomenon is similar to the grain structure in the long and short vectors in Figure 4.2(a) and (b). Figure 4.3(c) illustrates the evolution of textures with the increment vectors, in which each pole figure (PF) is derived from a region of 700 μm × 400 μm with about 1000 grains. In the short vector region, the texture is very weak. But the texture intensity is gradually enhanced with the vector length and the preferred orientation is <011>⊥BD, which is the same as the Long-vector in Figure 4.2(d).

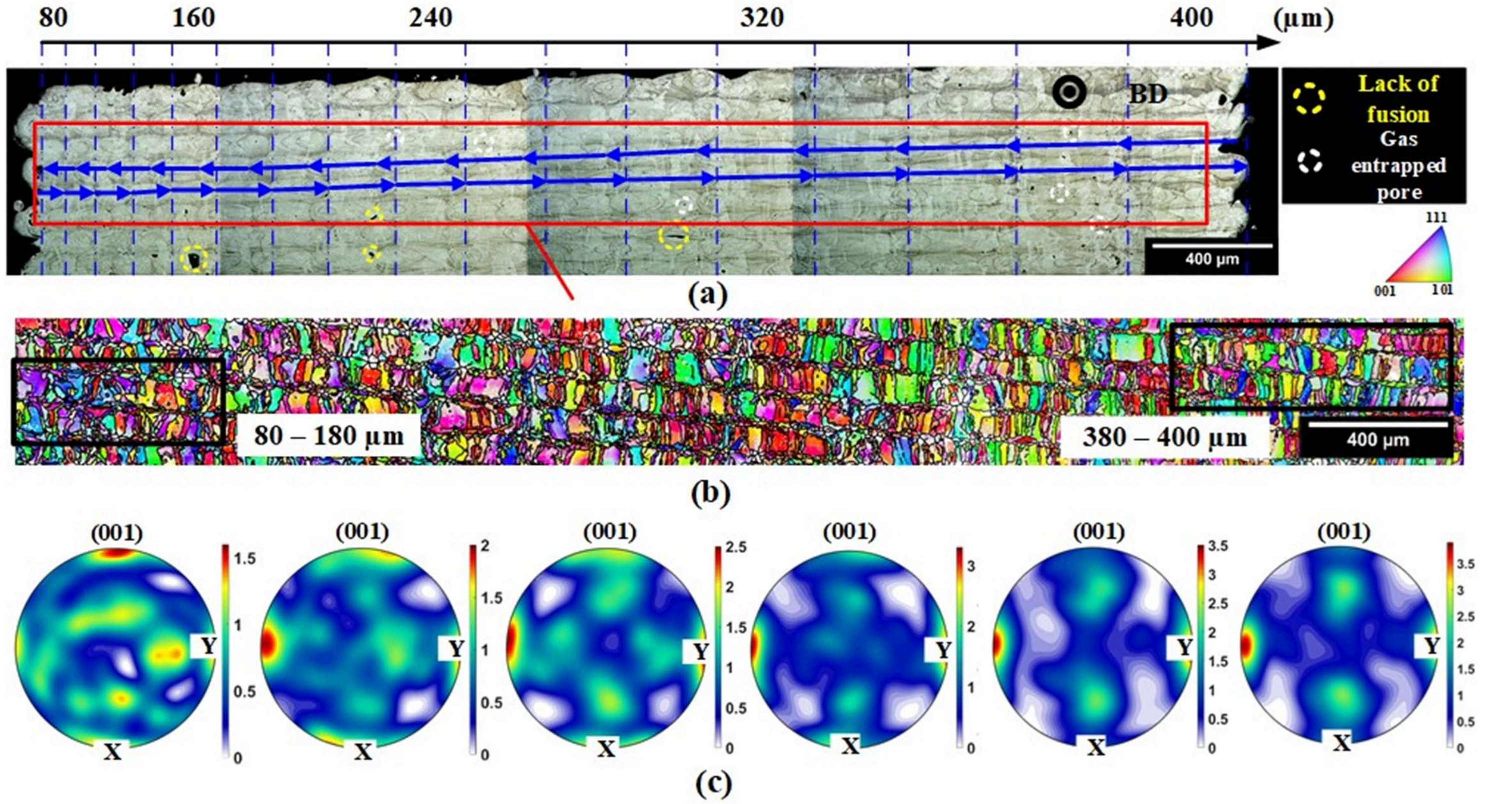

Figure 4.3: Microstructure evolution of increment vectors in the XY plane. (a) Melt pool morphologies; (b) grain structures and (c) Pole figures (PF) evolution with the increment of vectors. (Lack of fusion is labelled by yellow dashed circle and gas entrapped pore is labelled by white dashed circles, the numbers of grains for 6 PFs in (c) are 1072, 1055, 961, 937, 911 and 915 respectively.

4.1.2 Microstructure evolution in XZ/YZ plane

4.1.2.1 Melt pool and grain morphologies of long and short vectors (XZ-plane)

Figure 4.4 presents the melt pool morphologies and grain structures that are perpendicular to the laser scanning direction (refer to XZ plane in Figure 3.3) using Long-vector, Short-vector and Long-Short vector strategies. The laser scanning direction is either into the plane or out of the plane in each laser track (Zig-Zag), as marked in the figure. The Long-vector printed sample (Figure 4.4(a)) shows semi-circle melt pool boundaries with a defect-free structure. The Short-vector printed sample (Figure 4.4(b)) exhibits a narrower melt pool width than the long-vector while more defects are found near the boundaries. Figure 4.4(c) shows the printed structure with the alternating long and short vectors in adjacent laser tracks. It can be seen that the melt pool width of long vectors is larger than that of short vectors. Some voids due to lack of fusion can be found in the laser track at short vectors in Figure 4.4(c).

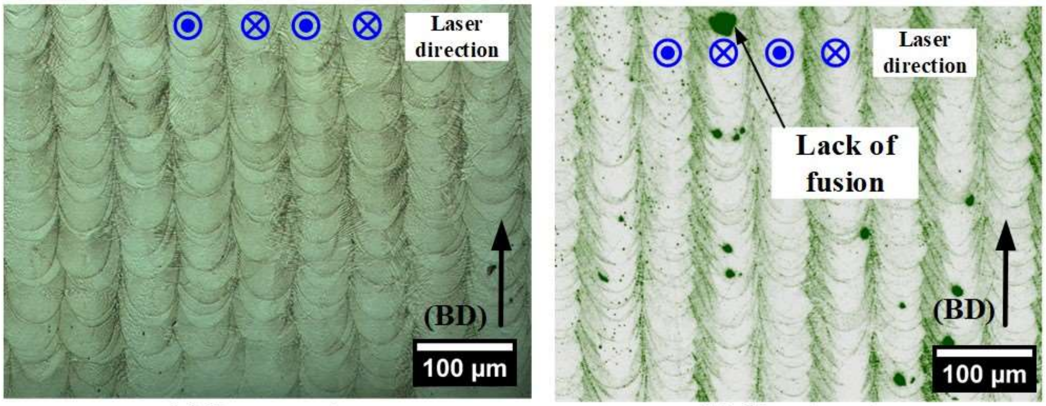

(a) Long vector **(b) Short vector**

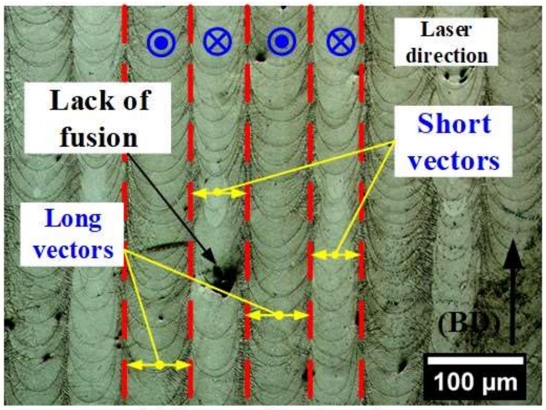

(c) Long-short vector

Figure 4.4: Melt pool morphologies in the XZ plane defined in Figure 3.3: (a) Long vector; (b) Short vector; (c) Long-Short vector (the overlapping zones are marked by red dashed lines).

The corresponding inversed pole figures (IPFs) are presented in Figure 4.5(a-c) respectively. The PFs shown in Figure 4.5(d-f) are calculated from 586, 762 and 801 grains respectively. Since the laser scanning direction is unchanged between adjacent layers, the build-directional columnar grains are seen in all three samples. This characteristic is consistent with the work reported in the literature when the as-built components are fabricated by the 0° rotation scanning strategy [68,132,221]. However, the grain morphology and texture variation are significant when the vector length changes. Strong <011>//BD texture (maximum intensity: 7.0) and largest columnar grains are observed in the Long-vector sample (Figure

4.5(a) and (d)). However, <001> direction along the scanning direction is slightly inclined to build direction (Z-axis). This indicates that the preferred grain growth direction <001> may be affected by thermal gradient along the laser scanning direction and build direction in the Long-vector. In the Short-vector sample (Figure 4.5(b)), the columnar grain is smaller than that in the Long-vector and the same texture (<011>//BD) with a maximum intensity of 3.6 is observed in Figure 4.5(e). The weakest texture is seen in the Long-Short vector case (Figure 4.5(c)) when the part is fabricated by alternating long and short vectors. This is because the melt pools of short vectors are narrower than long vectors and overlap with the neighbouring long-vector melt pool, as depicted by the red dashed lines in Figure 4.4(c).

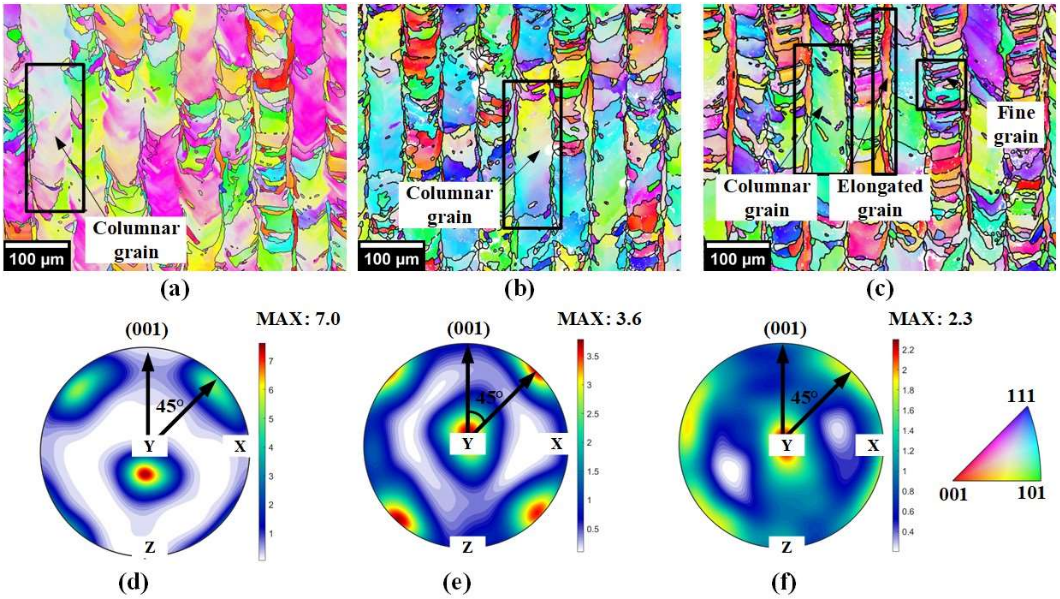

Figure 4.5: Inverse pole figure (IPF) maps and pole figure (PF) of three strategies. (a) and (d) Long vector; (b) and (e) Short vector; (c) and (f) Long-Short vector (typical grains are highlighted by black rectangles); the numbers of grains for PF in (d), (e) and (f) are 586, 762 and 801 respectively.

The thermal gradient direction near the overlapping zone (area near the dashed lines in Figure 4.4(c) may change and impede the side branching growth. This leads to three dominated grain growth patterns (narrow elongated grain, columnar grain and fine grain) in Figure 4.5(c). For the melt pool printed by long vectors, slender elongated grains grow along the BD at the centre of melt pool whilst small grains grow perpendicular to the melt pool boundary at the side of melt pool, as illustrated in Figure 4.5(c).

In all three scanning strategies, <001> parallel to the scanning direction (Y-axis) is observed in PFs (Figure 4.5(d-f)). This indicates that vector length may not disturb the grain growth along the laser scanning direction. However, since the two kinds of melt pool morphologies formed in long and short vectors (the reason will be discussed in Section 4.2.1) provide two thermal-gradient patterns, grain orientation is probably changed around the Y-axis. Therefore, the grain orientation distribution is more discrete near the 45° to the build direction in the (001) plane (Figure 4.5(f)).

Due to the narrow overlapping area between the short and long vector tracks, the subsequent short vectors failed to remelt the previous fine grains in the melt pool printed by long vectors in Figure 4.5(c). As a result, the growth of side-branching grains is hard to continue, forming the fine grains at the side of the melt pool in Figure 4.5(c). This phenomenon is similar to the polycrystalline-like microstructure formed with large hatch spacing [222]. Meanwhile, the columnar grains exhibit similar grain morphology and orientation as compared to those from the Short-vector printing in Figure 4.5(b). This suggests that Long-vector melt pools are likely to sustain the grain growth pattern generated in the adjacent short-vector melt pool in the sample printed by Long-Short vector strategy in Figure 4.5(c).

4.1.2.2 Melt pool and grain morphologies of incremental vectors (YZ-plane)

The overview on the microstructure evolution of the increment vector printing on the YZ plane from 80 μm to 400 μm with an increment of 20 μm is presented in Figure 4.6(a). The laser scanning direction is along the y-axis according to Figure 3.3(d). Incremental vectors are divided by blue dashed lines as shown in Figure 4.6(a). It is shown that the morphology of melt pool gradually changes with the vector length, from narrow melt pools at short vectors to long melt pools at long vectors. Defects such as lack of fusion and pores are more likely to be observed in regions where short vectors are used (e.g., vector length < 180 μm). The corresponding inverse pole figure (IPF) maps are shown in Figure 4.6(b). It can be seen that grain morphology changes from small, irregular grains at short vectors to elongated grains at long vectors. The corresponding grain size and micro-hardness for each vector are presented in Figure 4.6(c). The values of the reference sample printed by Long-vector strategy with 4 mm vector length is also included for comparison in Figure 4.6(c). With the increment of vector length, the grain size increases from 19.5±6.4 μm to 53.3±13.8 μm (black line), suggesting that grain size is affected by the vector length when the laser parameters are the same. This will be discussed further in the subsequent section on the energy inputs of different vector lengths.

The microhardness within the melt pool and at the overlapping zone is depicted by orange and green lines respectively in Figure 4.6(c). The hardness is estimated by the average value of three measurements at both inside and intersection of melt pool as shown in the inset of Figure 4.6(c). Two test points are selected for the 380 μm and 400 μm vectors to evaluate the hardness fluctuation along the laser scanning direction. With the increment of vectors, the hardness decreases from 350 HV to 300 HV or even less. The hardness of the reference sample is about 325 HV (red square), which is similar to the reported results of the as-built Alloy 718 [223,224]. It can be seen from Figure 4.6(c) that the hardness at the intersection zone is generally higher than the melt pool inside.

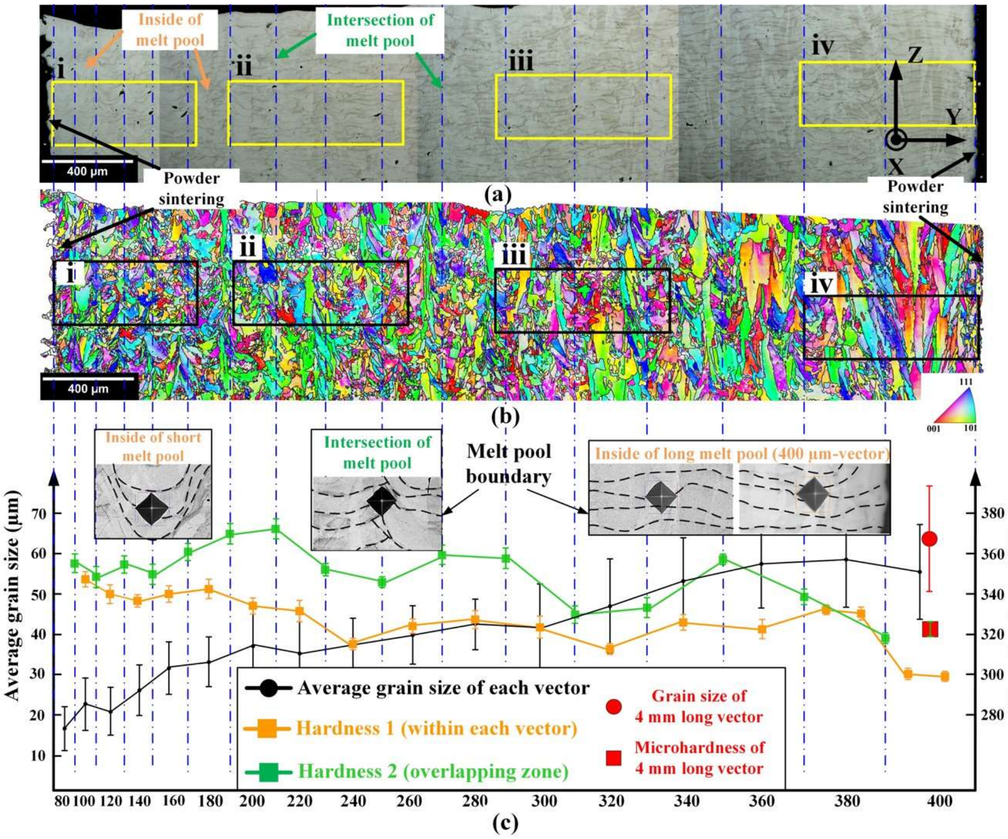

Figure 4.6: Multi-scale vector evolution in the increment vector strategy observed via OM and EBSD (YZ plane). Increment vectors are divided by blue dashed lines. (a) Outline of increment vectors from 80 μm to 400 μm; (b) Corresponding IPF maps of increment vectors (c) Grain size and hardness evolutions in the increment vectors, the values are compared with the reference sample of 4 mm-long vectors (reference grain size and hardness are highlighted by red circle and rectangle respectively). Each hardness value was obtained by taking the average of three measurements at both the inside and intersection of the melt pool, the error bar represents standard deviations.

Four areas are selected (yellow rectangles) in Figure 4.6(a) and (b) to show melt pool morphologies and grain structure in detail. The four selected areas are shown in Figure 4.7 to compare with the reference structure (Figure 4.7(i) and (j)) by the Long-vector printing. The numbers of grains for 5 PFs are 1121, 1058, 964, 897 and 708 respectively. The melt pools fabricated by short vectors (Zone i, Figure 4.7(a)) are irregular and melt pool boundaries are not as smooth as shown in Figure 4.7(i), indicating the dramatic melt pool dynamics occurred at the Short-vector printing. It is mainly caused by the momentum of upward liquid along the rear depression wall, where the Marangoni convection/recoil pressure is strong [225]. Since the Marangoni effect is decided by surface tension ($\sigma(T) = \sigma_0 - \sigma_s^T(T - T_l)$) [226], the metal liquid flows from the bottom to the surface of the melt pool. The metal liquid is unstable under recoil pressure in the narrow melt pool [112], likely leading to a significant lack of fusion in Figure 4.6(a). Such unstable melt pools (shown as uneven melt pool boundary) are more likely to break consecutive grain growth along the BD, resulting in small grains in the short-vector zone as seen in Figure 4.7(c). With the increment of vector length, a longer melt pool forms and provides a larger space for the flow of molten metal, which solidifies slower than that in the Short-vector printing and has sufficient time to wet the neighbouring region [227] due to heat accumulation. The molten metal thus can flow more stably and fill more gaps than in the short vectors. This allows columnar grains to grow across several layers along the BD, forming large grains in Figure 4.7(h) at 400 μm vector length. The grain size is also similar to the reference sample of 4 mm long vectors in Figure 4.7(j).

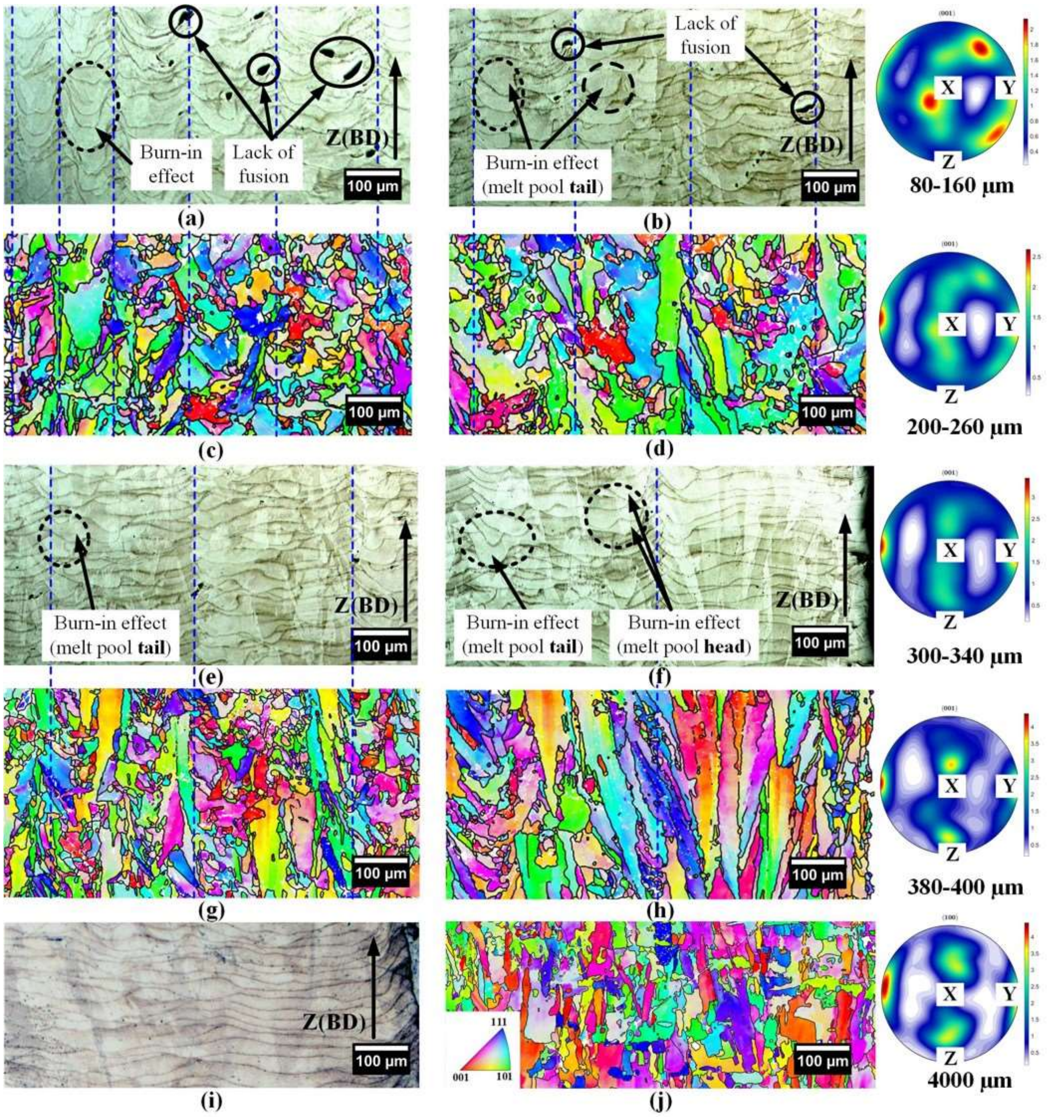

Figure 4.7: The four selected areas from the increment vector (Scanning direction (Y): east to west). (a), (b), (e) and (f) are the OM images of increment vector, the deeper melt pools caused by burn-in effect are marked by black dashed circles and the defects are also highlighted; (c), (d), (g) and (h) are the IPFs of selected areas (Corresponding PFs of <001> for four selected areas are listed on the right side, (a) and (c): 80-160 μm, (b) and (d): 200-260 μm; (e) and (g): 300-340 μm, (f) and (h): 380-400 μm); (i) and (j): 4000 μm.

It was expected that the beginning of a melt pool should be shallower than its middle part due to less heat accumulation. However, the deepest regions are observed at the head and tail of vectors as highlighted by the dashed circles in Figure 4.7(a), (b), (e) and (f), suggesting the higher energy density inputs in both regions (known as the burn-in effect in laser welding [46]). Similar melt pool morphologies were also reported in as-built components fabricated by different metal 3D printers [12,14], whilst this phenomenon was usually ignored due to its limited effects in long vectors and the capability of short vector printing in some laser control systems. Small grains are mainly near the overlapping area of adjacent vectors (blue dashed lines). This may be because of the unstable melt pool condition at the head/tail of a melt pool. The steep thermal gradient between two vectors leads to such small grains. The small grains result in higher strength, which is in good agreement with the high hardness at the overlapping zone shown in Figure 4.6(c).

In contrast, the burn-in effect is caused by excessive energy input near the head/tail of a melt pool, making it easier for large grain growth. Since it can be recognised as a localised excessive energy input at hundreds of microns, the large grain growth matches well with the as-built components formed by constant high energy input [127]. The texture intensity increases with the increment of vector length and the orientation rotated about 45° to <011>⊥BD. The orientation and intensity at the vector length of 400 μm in Figure 4.7(h) are close to the Long-vector printed reference sample in Figure 4.7(j).

The distribution of pore shape and size are presented in Figure 4.8, as measured by ImageJ. The aspect ratios are used to indicate the pore shape and most of them are close to 1 in Figure 4.8. This means that the majority of pores from are in circular shapes. The circular diameter is thus quoted as the pore size in Figure 4.8. More than 80% of pore sizes are smaller than 15 μm and pore sizes tend to be less than 10 μm when the vector length becomes longer (e.g., long vectors at 380-400 μm).

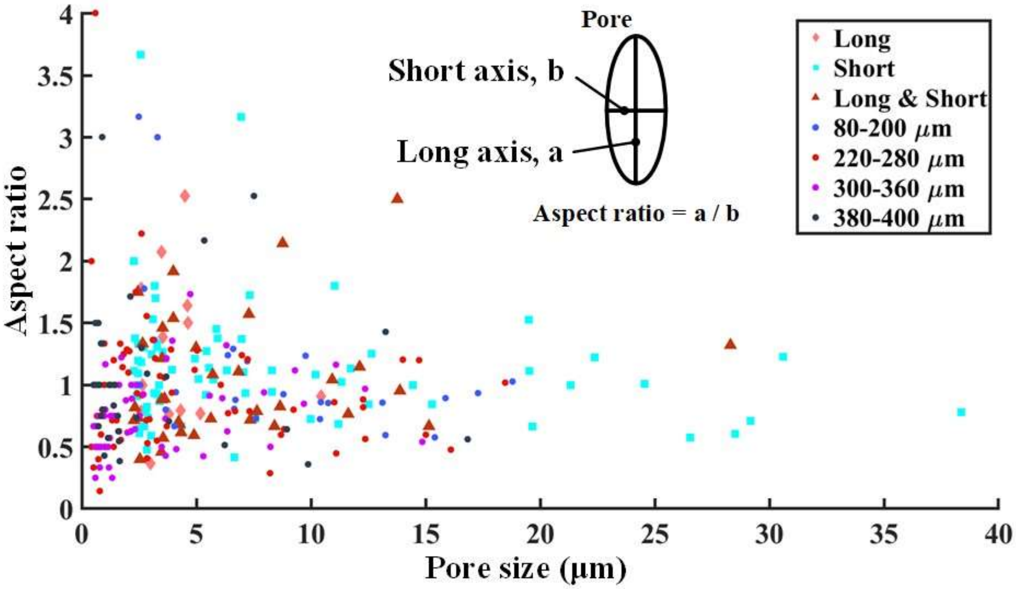

Figure 4.8: Pore shape and size distribution in all scanning strategies (the sample printed by increment vector scanning strategy is divided into four parts, 80-200 µm, 220-280 µm, 300-360 µm and 380-400 µm, for similar statistical areas).

The largest porosity is found in the Short-vector printing strategy (Figure 4.9), and the porosity decreases with the increment of the vector length. Since the same laser power and scanning speed are used among the four scanning strategies, the only variable here is the vector length. The actual laser motion and heat input dynamics need to be further considered to elucidate the microstructural difference between short vectors and long vectors. Large standard deviation in short vector indicates that the bonding between short vectors may be weaker than long vectors. This suggests that the short vector is likely to introduce the defects during printing process.

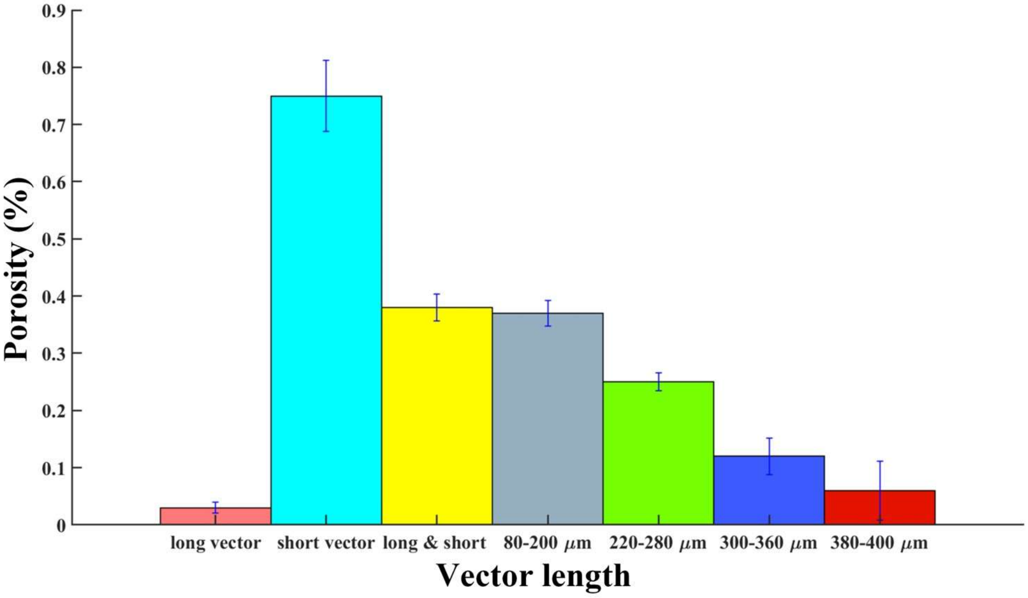

Figure 4.9: Porosity of different vector length in all scanning strategies(the sample printed by increment vector scanning strategy is divided into four parts, 80-200 μm, 220-280 μm, 300-360 μm and 380-400 μm, for similar statistical areas). The error bar refers to the standard deviation.

4.2 Discussion

4.2.1 Role of the actual scanning mirror motion in the microstructure

In the LPBF fabrication process, the high-precision laser beam movement is controlled by a Real-Time Controller (RTC) that synchronizes laser control with scanning mirror movement and image field correction, which then melts the defined laser path with set parameters [44]. The laser control and mirror motion algorithm are shown in Figure 4.10, where a short vector (80 μm) and a long vector (400 μm) are used as examples to represent two different scanning speed conditions. When printing a vector in LPBF, the scanning mirror needs an acceleration phase to reach the target scanning speed, which means the head of a vector will be exposed to a small scanning speed initially. If the laser switches on at the very beginning of the mirror movement, it will cause a very high energy input at the head of the vector when the scanning speed is small. Due to this, the burn-in effect can occur at the head of the vector. It should be noted that retaining the burn-in effect (high energy input due to small scanning speed) at the head of a vector is necessary. Because materials with high melting point need to be pre-heated at the head of a vector, the burn-in effect thus can ensure the full melting at the initial position. But to avoid too high energy input at the head of the vector, a laser-on delay of 50 μs is defined as shown in Figure 4.10(a). This value is empirically decided and restricted by the machine for different materials to balance productivity and stability during the printing process. It is strongly dependent on the laser and material thermal parameters, but there is still a lack of theoretical model for calculation. This delays the laser input for 50 μs, allowing the scanning speed to accelerate for 50 μs to provide a reasonable scanning speed (Figure 4.10(b)), and then the laser will switch on. Similarly, a deceleration phase is set at the end of a vector to slow down the mirror for the next command. And a laser-off delay is compensated to reduce the displacement error between the set position and laser beam position. The delay time is defined according to the laser absorptivity of the material. The scanning speed at the end of a long vector (Figure 4.10(b)) is not decelerated to zero but the laser switches off to weaken the burn-in effect at the tail of the vector.

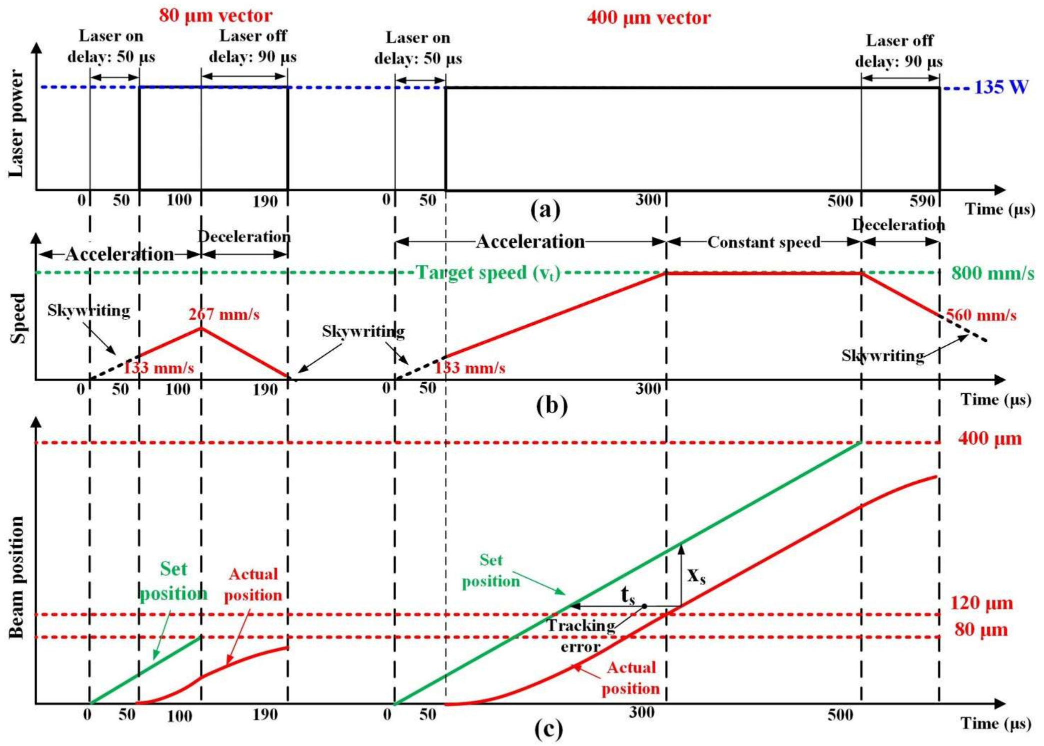

Figure 4.10: Scanning mirror control algorithm during LPBF processing: (a) and (b) are the laser on-off switch and mirror scanning speed in a vector; (c) Comparison of laser exposure position and set position.

To simplify the control of the scanning mirror in the LPBF system, the acceleration time (t_a) for the target speed is a constant in the laser control algorithm. For example, the scanning speeds accelerating from 0 to 400 mm/s or from 0 to 800 mm/s will use the same acceleration time, t_a. Therefore, a distance delay between the actual position and set position is defined as x_s (Figure 4.10(c)) according to a constant tracking error time t_s shown in Figure 4.10(c). The tracking error time t_s is given in Equation 4-1,

$$t_s = \frac{v_t t_a - \frac{1}{2}\left(a {t_a}^2\right)}{v_t} = \frac{1}{2} t_a \qquad \text{4-1}$$

where v_t is the target speed as seen in Figure 4.10(b). The actual speed v and distance delay (or lag error) x_s are then calculated by $v = at$ and $x_s = v_t t_s$ respectively.

In this case, the tracking error time t_s is defined as 150 µs by SCANLAB and the target scanning speed (v_t) is set as 800 mm/s. According to Eq. 4-1, it requires 300 µs (t_a) to achieve the target scanning speed. The acceleration distance is 120 µm (x_s) with an acceleration of 1/375 µm/µs^2 (calculated by v_t/t_a) in the linear acceleration condition. And then the laser speed reaches the target speed of 800 mm/s. The distance scanned by the target speed depends on the actual vector length. Finally, the scanning speed decelerates in 90 µs laser off delay, in order to offset the distance delay (x_s) as shown in Figure 4.10(c) at the tail of the vector. Thus, the vector lengths that are shorter than 120 µm are classified as short vectors. This means the 80 µm vector is too short to allow the scanning mirror to reach the target speed.

To quantify the energy input in short and long vectors, the energy density can be calculated according to the volumetric energy density (VED) [228] by considering the speeds at different positions in Equation 4-2, as a function with laser power P, scanning speed V, hatch spacing H and layer thickness T.

$$VED(x) = \frac{P}{V(x)HT} \qquad 4\text{-}2$$

Since the laser power, hatch spacing and beam diameter are kept constant, the actual scanning speed changes with the laser beam position (x), which depends on the vector length as shown in Figure 4.10(b). $V(x)$ can be expressed as below,

$$V(x) = \begin{cases} \sqrt{2ax}, & x < 120\ \mu m\ (acceleration) \\ 800, & x \geq 120\ \mu m\ (constant\ speed) \\ V(x) - at, & t\ is\ laser\ off\ delay\ (decelertion) \end{cases} \quad 4\text{-}3$$

Combining the actual vector length and corresponding speed calculated by Equation 4-3, the influence of scanning speeds on the VED for different vector lengths is obtained by integrating the VED with respect to the distance:

$$\overline{VED} = \frac{1}{l}\int_0^l VED(x)\,dx \quad 4\text{-}4$$

where l is the length of the vector and x is the laser beam position when the laser scans within the vector. The relation between average energy density and vector length is seen in Figure 4.11. When the vector length is shorter than 120 µm, the printing process is dominated by scanning mirror acceleration. Since the actual speed increases quickly but does not reach the target speed, the actual energy density is dropping rapidly but still larger than 200 J/mm^3. With the increment of vector length, the scanning process is gradually dominated by a constant-speed segment as seen in Figure 4.10(b). The energy density becomes more stable when the vector length increases to 400 µm in Figure 4.11.

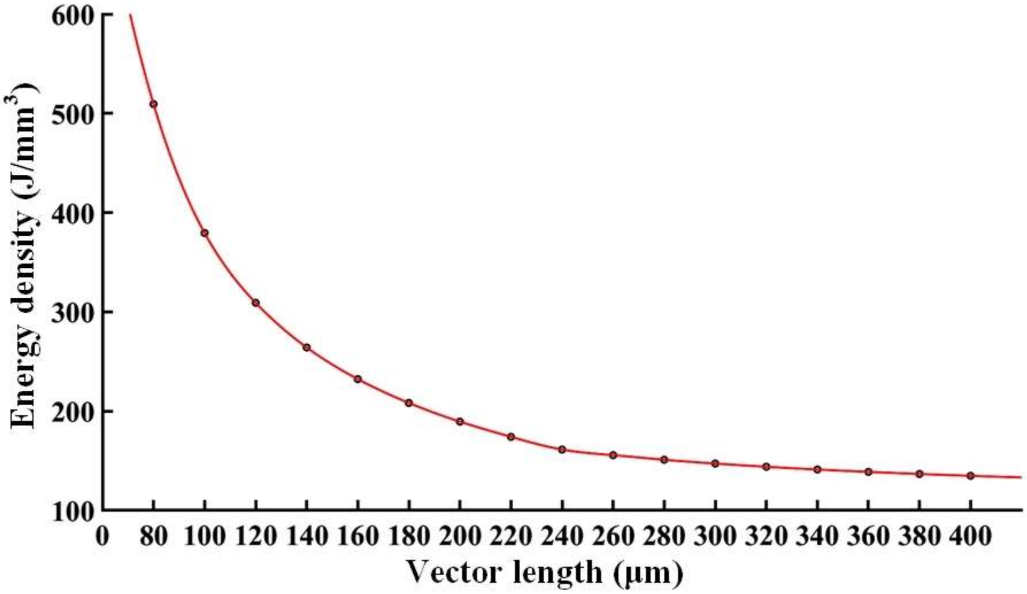

Figure 4.11: Actual energy input in different vectors by considering the real laser motion.

In the 80 μm short vector, the actual laser scanning process is completed within the acceleration and deceleration phases and the maximum scanning speed is lower than 800 mm/s (Figure 4.10(b)). Therefore, the higher input energy density combined with short metal flowing space leads to a significant burn-in effect in the Short-vector printed melt pool as shown in Figure 4.7(a) and (b). With the increment of vector length, the scanning mirror can reach the target scanning speed and keep the constant speed until the deceleration phase as shown in Figure 4.10(b). The longer melt pool provides more space for molten metal flow, releasing the burn-in effect at the head of a melt pool. However, the burn-in effect still exists at the tail of a melt pool due to that the deceleration phase results in higher heat accumulation and deeper melt pools when compared to the constant-speed segment in a melt pool. This phenomenon is seen at the tails of melt pools in Figure 4.7(e) and (f). The burn-in effect usually can be alleviated by extending the skywriting time, but the commercial fabrication process needs to balance quality and productivity. When the burn-in effect is not significant in the commonly used long vectors (e.g. Figure 4.7(i)), shortening skywriting time can increase efficiency since there are millions of skywriting (or laser on/off) being implemented [229] during a printing process. However, when the vector becomes short (less than 120 μm), the burn-in effect may be aggravated due to a narrow melt pool and high energy input. This indicates that the vector length should be considered for optimising the laser motion control parameters. Such length effect is often ignored because the most common calibration part is 1 mm cube. But it becomes more crucial, especially for thin-walled structures [230] or lattice structures [231], in which the short vector printing is crucial at corners or edges.

Figure 4.12 shows the melt pool morphology comparison at different vector lengths. As previously discussed, the short-vector melt pool is deeper than a long-vector as highlighted by the yellow dashed line in Figure 4.12(a). The depth of a short melt pool is 143 μm, deeper than a long melt pool of 124 μm, demonstrating that the mirror acceleration causes higher energy density in a short-vector melt pool. According to the melt pool depth-width ratio, the morphology of the long-vector melt pool matches well with the conduction mode [221,232], in which the melt pool shape is shallower but wider due to that heat conduction is dominating during melting (Figure 4.12(a)). It provides a stable melt pool and builds a good bonding with adjacent laser tracks. But a short-vector melt pool is close to the keyhole mode, in which the fluid and recoil pressure dominate, resulting in unstable melt pool dynamics with a higher possibility of defects [233,234]. Since the acceleration and deceleration distance are not changed, the constant speed segment in Figure 4.10(b) becomes more dominant in the Long-vector printing. The melt pool thus transits from keyhole mode to conduction mode when the vector length increases. Meanwhile, the melt pool depth decreases and then becomes stable with the increment of vector length.

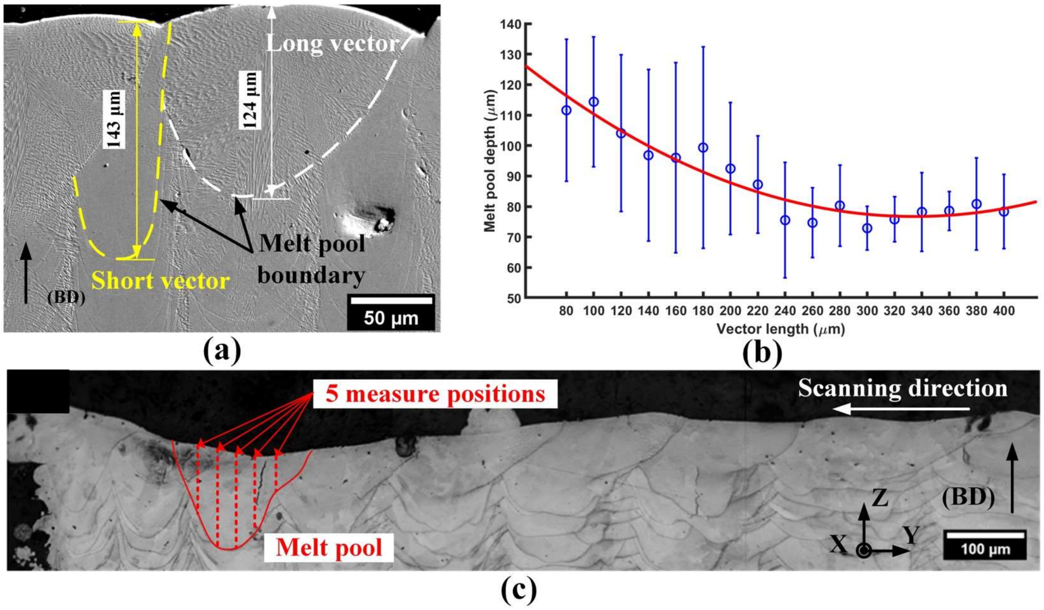

Figure 4.12: Melt pool depth comparison. (a) Melt pool depth difference in Long-Short vector printed sample (b) Melt pool depth evolution in the increment vectors; (c) Melt pool morphology comparison in increment vector scanning strategy (the melt pool was divided into six equal parts and five positions are measured to reflect the melt pool depth evolution, the error bar represents standard deviation).

In a short vector of 80 μm, the melt pool may be only scanned by the acceleration phase then directly by the deceleration in Figure 4.10(b). The scanning speed is not reaching the target speed during scanning. According to Eq. 4-4, the average energy density is higher than that in long vector. High energy density causes the burn-in effect at the head and the tail of the vector (i.e., dominated by keyhole mode), resulting in a deeper melt pool within a short melting period. According to the dynamic viscosity (μ) of the melt pool defined by equation [235]: $\mu = \frac{15}{16}(\sqrt{\frac{m}{kT}}\gamma)$, where m is atomic mass, k is Boltzmann constant, T is the absolute temperature and γ is the liquid surface tension. μ decreases at the high energy density, leading to lower viscosity. The significant thermal gradient results in surface tensions (or Marangoni flow). The combination of lower viscosity and Marangoni convection flow may lead to the unstable melt pool flow within the short vector. This is evidenced by the melt pool morphology in the short vector region Figure 4.12(c). In a long vector, the acceleration phase and deceleration phase are separated by a constant speed segment as 400 μm vector in Figure 4.10(b) (i.e., dominated by conduction mode), releasing the heat accumulation at the melt pool head and leading to a shallower melt pool. This trend can be seen in Figure 4.12(b) and (c) (The error bar is defined as standard deviation).

It should be noted that, due to the "U" shape melt pool formed in the printing process, the melt pool depth changes dramatically if the observation surface is not close to the melt pool centre. To reduce the observation error, the surface observed in Figure 4.12(c) was polished three times. It was observed that the individual melt pool depth was affected by the observation position (i.e., after polishing, all melt pools became deeper). However, the melt pool depth evolution with the increment of vector length may not be significantly affected by observation position. There is a tendency that the melt pools become shallower with the increase of vector length in all observation tests. To balance the observation accuracy and experiment cost, when the largest melt pool depth (139 μm) is close to the short vector melt pool depth (143 μm) in Figure 4.10(a), the melt pool section is treated as close to the melt pool centre. The melt pool depth becomes shallower from 100 μm to around

70 μm, suggesting the effect of acceleration and deceleration is gradually weakened when the vector length increases. The melt pool depth evolution from 80 μm-vector to 400 μm-vector is presented in Figure 4.12(b), in a good agreement with the relationship between vector length and the actual energy input shown in Figure 4.11. However, some fluctuations in the melt pool depth are noticed in Figure 4.12(c). This is likely caused by the tail burn-in effect, which is found even in some longer vectors as shown in Figure 4.7(e) and (f).

4.2.2 Melt pool morphology and grain structure evolution

Excessive energy input changes melt pool morphology of short vector and also leads to different grain growth patterns when compared with that of long vector. The schematic of length effect on the microstructure evolution is shown in Figure 4.13. In the transverse section of short vector, a narrow melt pool with steep melt pool boundary enables rapid grain growth from the side of melt pool to the centre. This restricts the elongated grain (<001>//BD) growth at the centre of melt pool. Therefore, few elongated grains can be found in Short-vector printing (Figure 4.4(e)) when compared with the Long-vector printing (Figure 4.4(d)). The grain orientation changes are depicted by IPFs heat maps, which are statistically mapped with a similar number of grains (about 620 grains). The preferred grain growth direction in the Short-vector printing is between <011> and <111> in the build direction (Z-axis). This differs from the Long-vector, where the grains are mainly oriented to <011> and inclined to <001>. This is attributed to the melt pool morphologies formed at different vector lengths. In the short vector, the laser underwent the acceleration phase as depicted by the red line in Figure 4.13. Significant burn-in effect deepens the melt pool and consequently rotates the grain growth direction about 45°. Few grains are able to grow across several melt pools to become a large grain. Therefore, fine grains are dominating in Short-vector strategy with a weak texture intensity.

With the increment of vector length, the scanning speed is able to reach the target speed and keep it for a long distance. The stable melt pool morphology makes a grain easier to grow across melt pools layer by layer and to become large grain with preferred <011>⊥BD orientation. The microstructure evolution indicates that if many short vectors are used in an as-printed part (i.e., thin wall and stick), they may lead to localised microstructure differences when compared with the part printed by long vector. These short-vector printed structures may exhibit different mechanical properties, which are proved by the hardness test in Figure 4.6(c). Moreover, the length effect can be further employed to control the microstructure at the micron scale since it can rotate grain growth direction by changing melt pool morphology.

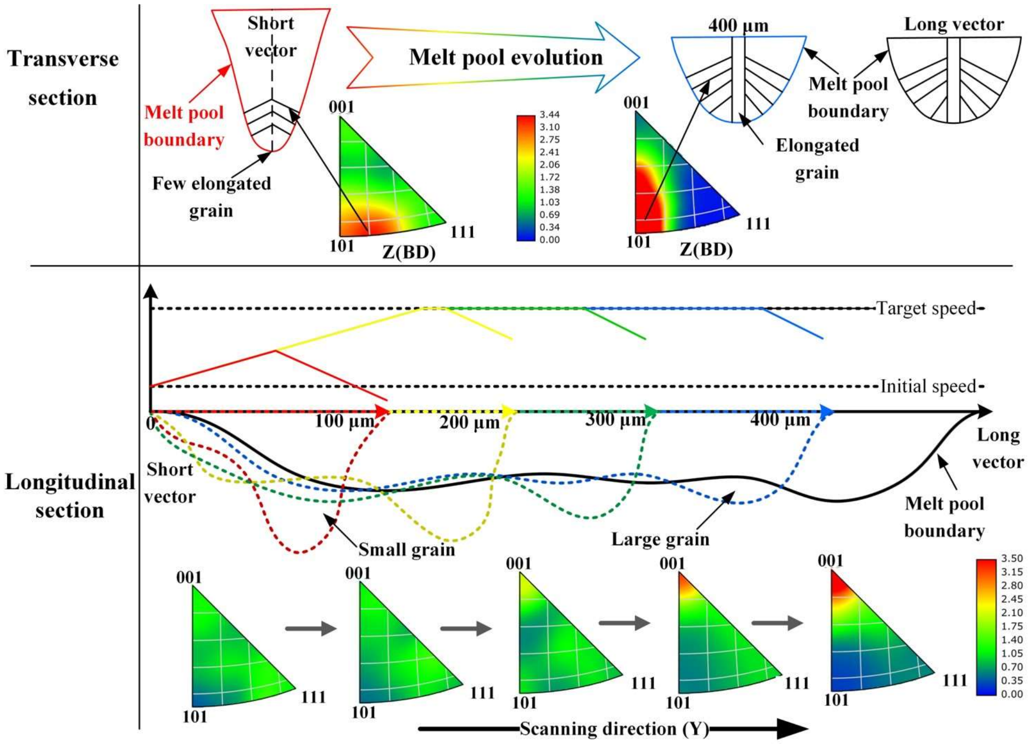

Figure 4.13: Schematic for the influence of vector length and real laser scanning speed on microstructure evolution. The IPF in transverse section is along to the Z (BD) and the IPF in longitudinal section is along the scanning direction (Y).

This work emphasised the importance of understanding the relationship between vector length and real laser motion (i.e., acceleration) in the LPBF process especially when the vector is shorter than about 200 μm. It indicates that laser scanning speed could not be treated as a constant when printing thin structures with short vectors. The process optimisation may not be limited to laser power and scanning speed whilst other process parameters, such as laser on/off time and skywriting time, should be considered as they can change the actual scanning speed in short vectors. In addition, short vectors also showed the potential to modify local microstructure and properties as depicted by the Long-Short vector and Increment vector. By evaluating the real energy input based on real laser scanning speed, one may be able to modify local microstructure (e.g., several layers or laser tracks) by selecting different vector lengths for the specific application scenario.

4.3 Summary

This work investigated the effect of vector lengths on the melt pool morphology and grain growth characteristics of LPBF-fabricated Alloy 718. It provided a novel approach to tailor the scanning strategy in the LPBF process, in which the length and position of each vector could be designed in the same layer. This allows for a direct comparison of melt pool morphology and grain structure within the same sample, which is impossible via the traditional method. Four fabrication strategies, namely Long-vector (4000 μm), Short-vector (80 μm), Long-Short vectors (4000 μm and 80 μm), and Incremental vectors (ranging from 80 μm to 400 μm), were employed and the microstructure evolution at different vector lengths was examined. This method exhibits the potential to enrich the scanning strategy design and control the local microstructure by manipulating the parameters of each vector.

The results showed that the melt pool depth (about 138 μm) in the short vector printing zone was greater than the depth in long vector printing zone (about 89 μm). This was because the actual scanning speed in short vector failed to reach target speed due to the acceleration at the beginning of the vector, leading to higher energy input in the short vector. Moreover, the deep and narrow melt pool formed by short vector constrained the grain growth across several layers along the build direction, resulting in finer grain size and higher micro hardness when compared to those in long vector. With the increment of vector length from 80 μm to 400 μm, the melt pool morphology transitioned from keyhole mode to conduction mode and the grain orientation transitioned from <111> to <001> in the scanning direction.

In addition, some limitations should be noted. The reduction of vector length has shown the potential to induce finer grains and enhance material hardness whilst it also leads to more defects. A balance between reducing defects while retaining fine grains needs further investigation. Since the laser parameters optimised for long vectors may not be suitable for short vectors, optimisation of the laser parameters based on vector length by considering the actual laser motion (or actual energy input) is necessary.

Chapter 5 Shear-based deformation mechanism of LPBF-fabricated Alloy 718 during the post-machining process

Chapter 5 has investigated the microstructure LPBF-fabricated 718 is strongly dependent on the scanning strategy. This may further affect the deformation during the post-machining process. This chapter selected three representative scanning strategies that are commonly used for LPBF technology to investigate the machining-induced deformation that is affected by scanning strategies and corresponding microstructures. The machining test was conducted by the pendulum-based cutting machine (Section 3.3.1) with the pre-polished sample (Section 3.3.2), aiming to trace the shear deformation via a "quasi-in-situ" investigation method. Moreover, a Taylor-based model (Section 3.5.1) and a crystal plasticity simulation (Section 3.5.2) were employed to investigate the deformation patterns formed by the unique microstructures.

5.1 Effect of rotational scanning strategy

5.1.1 Melt pool morphology under OM

Figure 5.1 shows three-dimensional optical metallography of samples with 0° rotational scanning strategy, illustrating melt pool arrangements on top (XY plane) and side (XZ and YZ plane) surfaces. Scanning strategies are identified according to the angle of laser tracks between the N layer and N+1 layer on the top surfaces (XY plane). In addition, some discontinuities in a laser track that looks like dotted line result from fluctuation of melt pool depth induced by energy input perturbation during laser scanning [202].

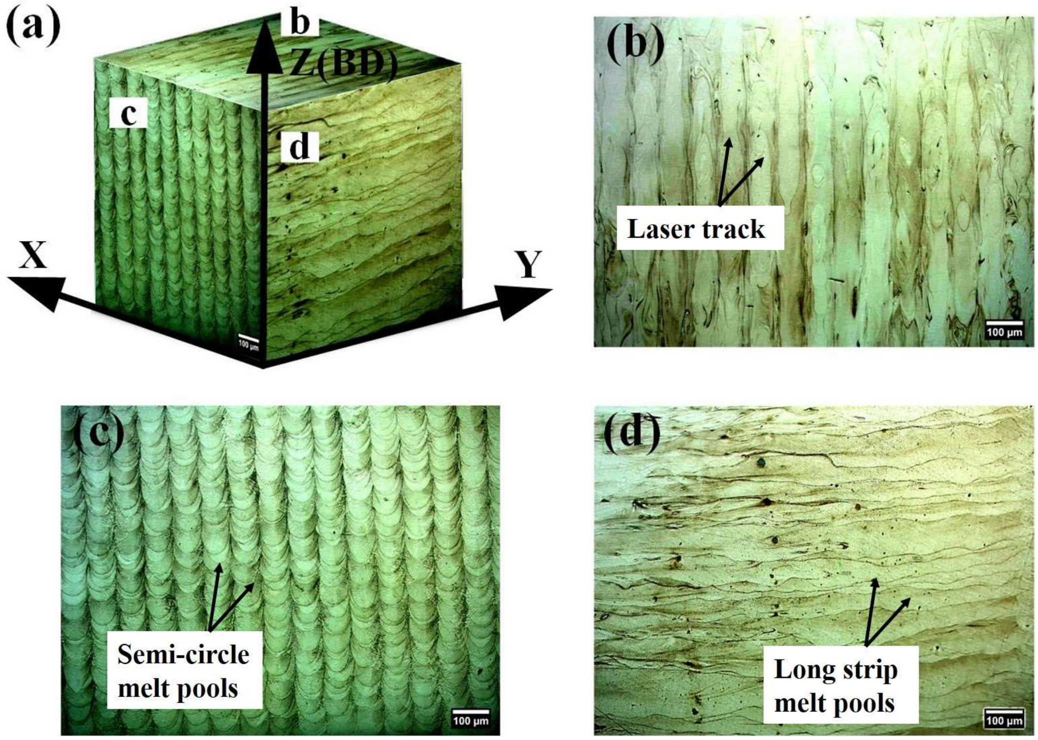

Figure 5.1: Microstructure of 0° rotation strategy under OM. (a) schematic of cube fabricated by 0° rotational scanning strategy; (b) XY plane; (c) XZ plane; (d) YZ plane. (Laser power: 135W, scanning speed: 800mm/s)

0° rotation strategy (Figure 5.1(a)) reveals a significant difference of melt pool in XZ and YZ planes because the laser scanning direction is always along the Y-axis in every laser track. The melt pools that are observed in the XY plane (Figure 5.1(b)) are attributed to the scanning strategy without rotation. This scanning strategy provides unchangeable laser track arrangements on every layer, decoupling the effect of laser scanning rotation in melt pool morphology observation. In the XZ plane (Figure 5.1(c)), semi-circle melt pools are regularly arranged along the X direction where a melt pool is partly overlapped by adjacent melt pools. However, pronounced fluctuation is shown in the Z (BD) direction. Some melt pools are almost entirely overlapped by melt pools of subsequent layers, while some are only overlapped in a small zone. The fluctuation of melt pool depth could also be verified by long-strip melt pools on the YZ plane (Figure 5.1(d)), where melt pool boundaries present an undulated profile rather than a straight line. These phenomena suggest that bonding between layers fluctuates due to laser-powder reactions.

Figure 5.2 shows the three-dimensional optical metallography of samples with 90° rotational scanning strategy. The laser track/melt pool morphologies formed by 90° rotation scanning strategy are shown in Figure 5.2(a). The laser track in the XY plane is perpendicular between adjacent layers (Figure 5.2(b)) due to the normal laser scanning direction between the neighbouring layers. Different from 0° rotation strategy where semi-circle melt pool and long-strip melt pool are on XZ plane and YZ plane, respectively, melt pools on both side surfaces (XZ plane, YZ plane) of 90° rotational scanning strategy are the same because directions of laser scanning rotated regularly during fabrication. It is shown as semi-circle and strip-like melt pools are interlaced in Figure 5.2(c) and (d), respectively.

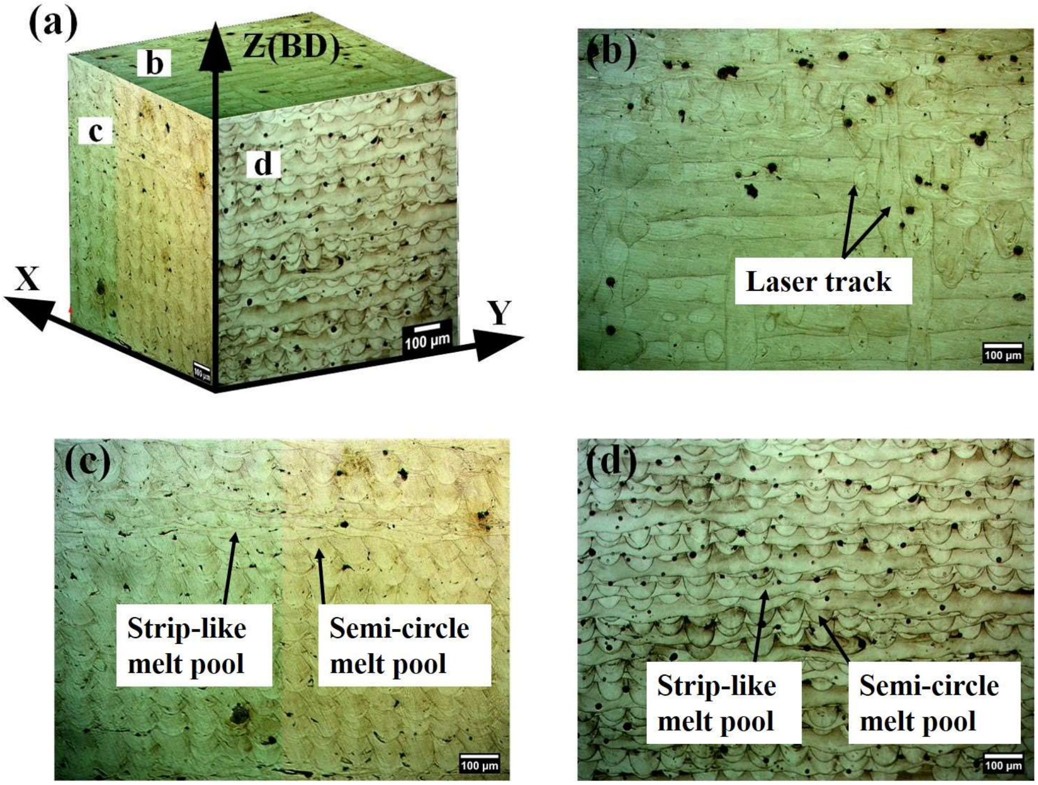

Figure 5.2: Microstructure of 90° rotation strategy under OM. (a) schematic of cube fabricated by 90° rotational scanning strategy; (b) XY plane; (c) XZ plane; (d) YZ plane. (Laser power: 135W, scanning speed: 800mm/s)

Figure 5.3 shows the three-dimensional optical metallography of samples with a 67° rotational scanning strategy. The melt pool shape of 67° rotation (Figure 5.3(a)) is not as semi-circled as the other two cases because the laser scanning direction is not perpendicular to the side surface (XZ or YZ plane) but with an intersection angle (67°). Therefore, the laser tracks in the XY plane exhibit a 67° angle between adjacent layers (Figure 5.3(b)). And melt pools in the XZ and YZ planes are arc-shape as shown in Figure 5.3(c) and (d).

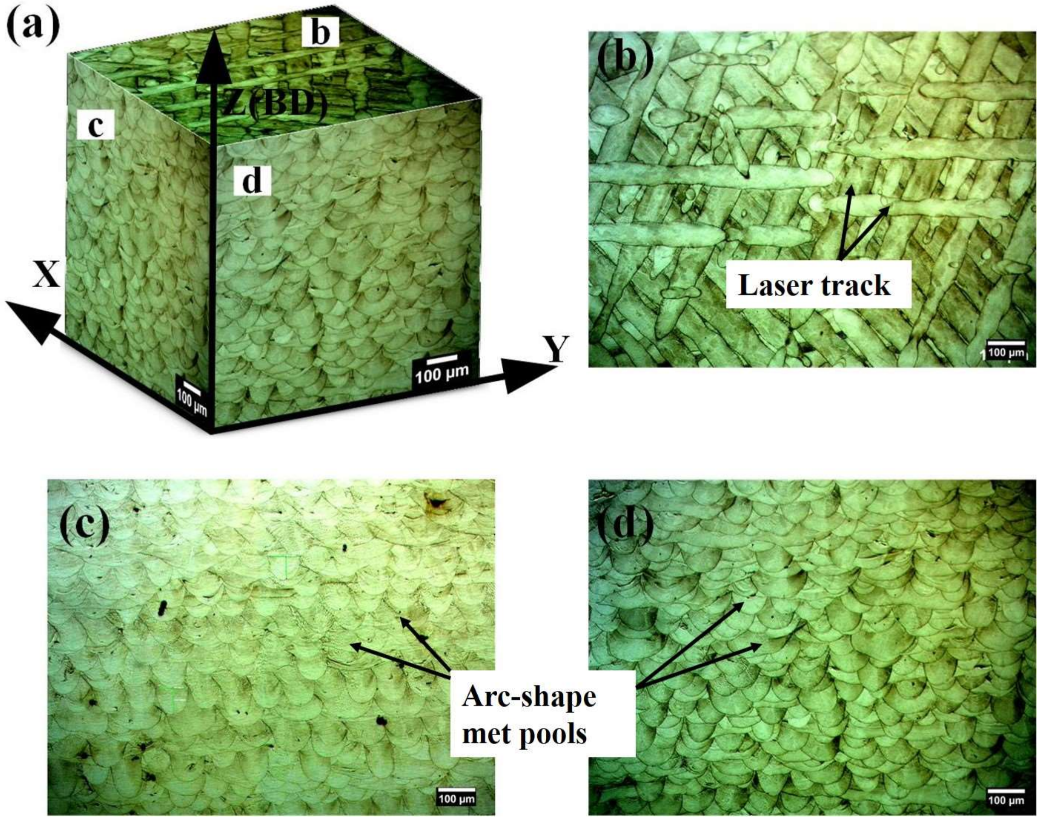

Figure 5.3: Microstructure of 67° rotation strategy under OM. (a) schematic of cube fabricated by 67° rotational scanning strategy; (b) XY plane; (c) XZ plane; (d) YZ plane. (Laser power: 135W, scanning speed: 800mm/s)

5.1.2 Microstructure under SEM

To investigate a laser track or melt pool, SEM images of three scanning strategies are shown in Figure 5.4. The observation plane is seen in the insets of every sub-figure. On the XY plane, the rotation degree is distinguished clearly by the intersection degree of the laser track in Figure 5.4(a), (b) and (c). Laser track boundaries and melt pool boundaries, as well as grain boundaries, are outlined in Figure 5.4(d), (e), and (f), respectively. As the grains grow epitaxially [236], the microstructure of three scanning strategies on the XY plane does not show various grain growth directions as on the XZ plane. According to the temperature gradient of the LPBF process (along with BD), most cellular dendrites grow parallel to BD, which matches well with Figure 5.4.

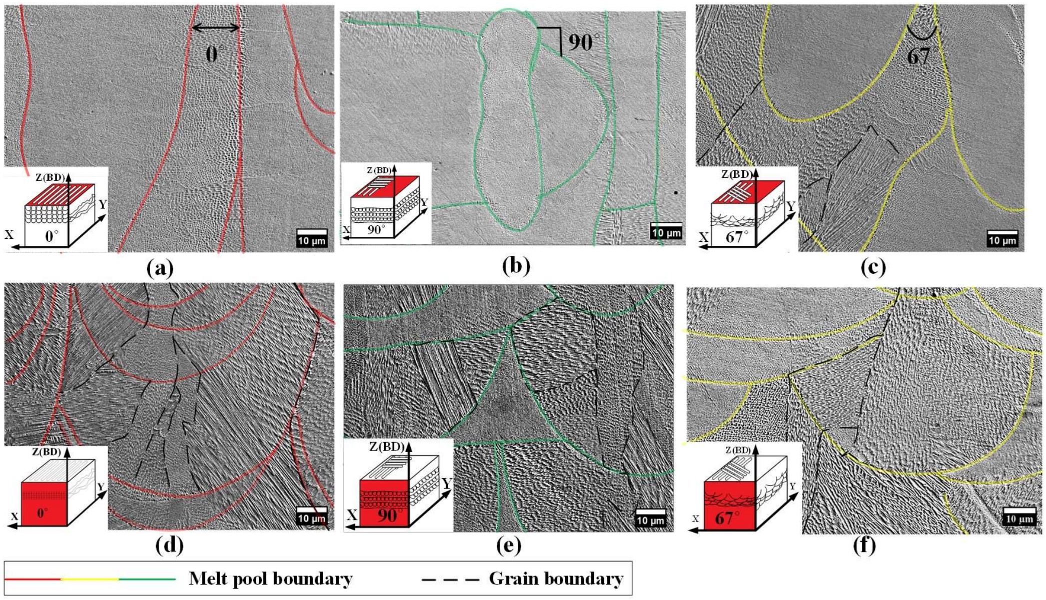

Figure 5.4: Microstructure of three kinds of rotation strategies under SEM. (a) and (d) XY and XZ section of 0° rotation; (b) and (e) XY and XZ section of 90° rotation; (c) and (f) XY and XZ section of 67° rotation. (Observation surface and build direction is seen in inset lower left; red, yellow and green line: laser track boundary and melt pool boundary; dashed line: grain boundary)

Microstructure on the side surface (YZ plane Figure 5.5 (a), (b), (c) and (d); XZ plane Figure 5.5(e), (f) and (g)) of sample fabricated by 0° rotation scanning strategy is shown in Figure 5.5. Number 1, 2, 3, and 4 are used to define different laser scanning directions of the adjacent melt pools. The red plane of insets in Figure 5.5(a) and (e) emphasize the observation plane on which melt pool features are outlined. It is noted that the same figure labels are used in Figure 5.6 and Figure 5.7 to mark the same characteristics of the melt pool.

The microstructure of the 0° rotation scanning strategy decouples the effect of rotation degree between layer N and layer N+1, indicating the microstructure under unidirectional and repetitive heat cycle history. The melt pool on the YZ plane is long-strip shape as shown in Figure 5.5(a), while the intersection points of melt pool boundaries (Figure 5.5(a), red rectangle nearby) suggest the part of one melt pool is remelted by the subsequent layer due to laser energy fluctuation. This phenomenon is dissimilar to ordinary overlapping shown as melts numbered by 3 and 4. Zoom-in microstructure near the melt pool boundary is depicted in Figure 5.5(c) and (d). The bright part (red arrow) in the inter-dendrite is Laves phase and the dark dots (blue arrow) are metal carbide [237]. The boundary here does not significantly transform cellular dendrite growth direction as Figure 5.5(b), where the dendrite growth direction is apparently changed on the upper and lower sides of the boundary.

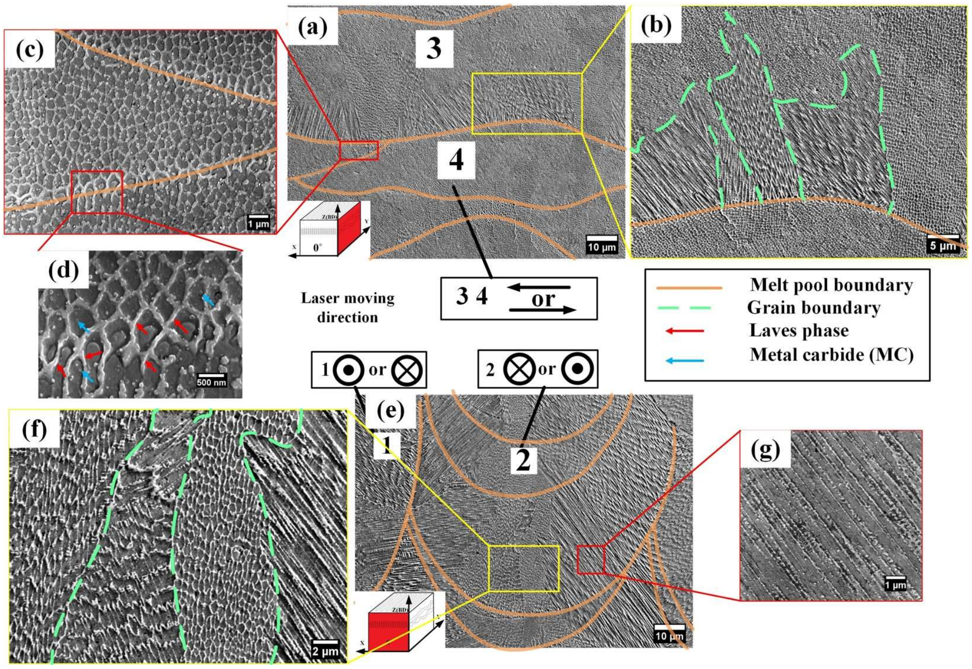

Figure 5.5: SEM microstructure of 0° rotation strategy. (a) YZ plane of 0° rotation (02T); (b) dissimilar cellular dendrite direction in long stripe melt pool; (c) and (d) Sub-structure and Laves phase and metal carbide; (e) Semi-circle melt pool (01T); (f) and (g) different growth direction in semi-circle melt pool. (Number 1, 2, 3 and 4 are different melt pools of different laser scanning directions. 1 and 2 are along to Y axis while 3 and 4 are along to X axis)

In Figure 5.5(f), the zone selected from the yellow rectangle, various growth orientations can be observed in a melt pool. And the growth direction in Figure 5.5(g) is succeeded from the previous melt pool. This is the reason why the melt pool boundary is not considered as a grain boundary. The curved-shaped melt pool is decided by a Gaussian-distributed laser beam, and the temperature gradient is vertical to the melt pool boundary. This melt pool-induced temperature gradient provides melt-pool-based growth direction while the grain has its preferred crystal orientation, such as (100) in FCC. Both two aspects finally decide the cellular dendrite growth direction.

For the 90° rotation strategy, two laser scanning directions are dominant on the XY plane and YZ plane (Figure 5.6(a)), and both two planes are also equivalent. Melt pools 1 and 3 are formed by the antiparallel laser scanning, which are perpendicular to melt pool 2 due to 90° rotated scanning direction between the neighbouring layers. Melt pools, therefore, are alternations of semi-circle-shaped and long-strip. The long-strip melt pool zone (melt pool 2) is composed of honeycomb-like structures that are equiaxed cells growing along to Y axis. The PAS (Figure 5.6(d)) is about 0.4 μm, finer than the spacing of melt pools 1 and 3. Figure 5.6(b) and (f) present that the sub-structure of the former dramatically transformed from equiaxed cell to cellular dendrite while the latter changes from elongated cellular to finer cell.

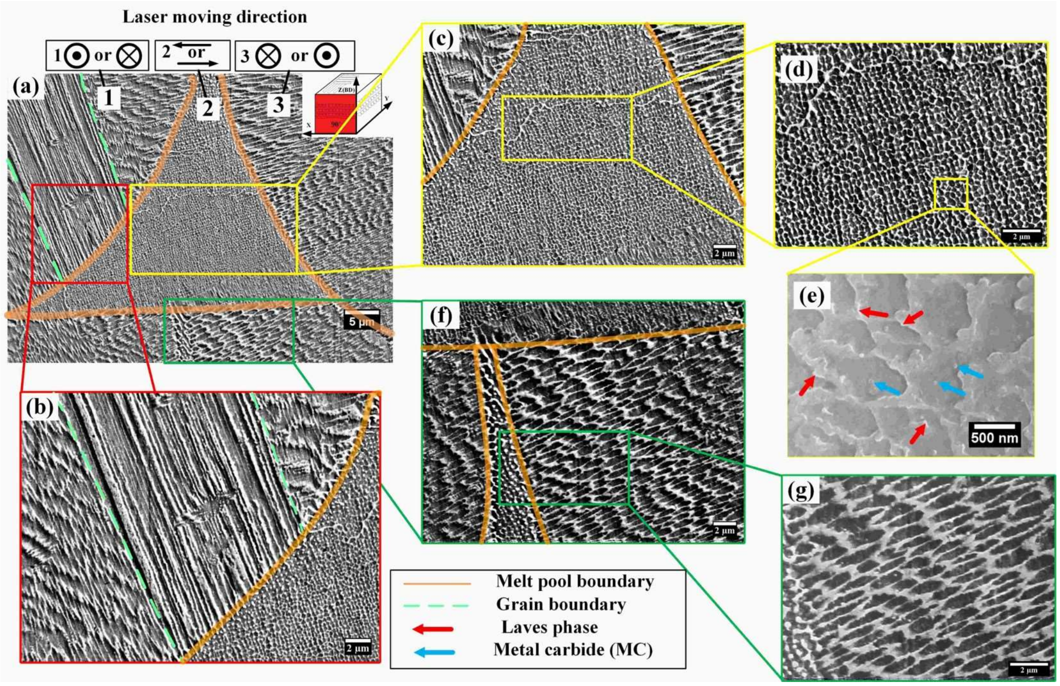

Figure 5.6: SEM microstructure of 90◦ rotation strategy (90T). (a) 90◦ rotation; (b) zoom-in semi-circle melt pool zone; (c) zoom-in long strip zone; (d) Sub-structure in long strip zone; (e) Laves phase and metal carbide; (f) and (g) different growth orientation compared with (b). (Laser power: 135W, scanning speed: 800mm/s)

For the 67° rotation strategy in Figure 5.7, the XZ plane and YZ plane are equivalent (i.e., there is no laser direction dominant on the XZ or YZ plane). Melt pools in Figure 5.7(a) are not regularly arranged as those shown in 0° rotation, where melt pools are ranged regularly on the XZ plane. The non-repeated laser scanning direction results in different thermal profile in each layer due to the 67° rotational scanning directions between layers, affecting the growth direction of the cellular dendrite across the layer. Comparing the microstructure of different zones near the melt pool boundary (Figure 5.7(b), (c) and (d)), few dendrites grow across the melt pool boundary, which differs from the phenomenon in Figure 5.5(g). Concerning the metallurgical state, only Laves phase and metal carbide are observed in Figure 5.7(e), which is similar to 0° rotation.

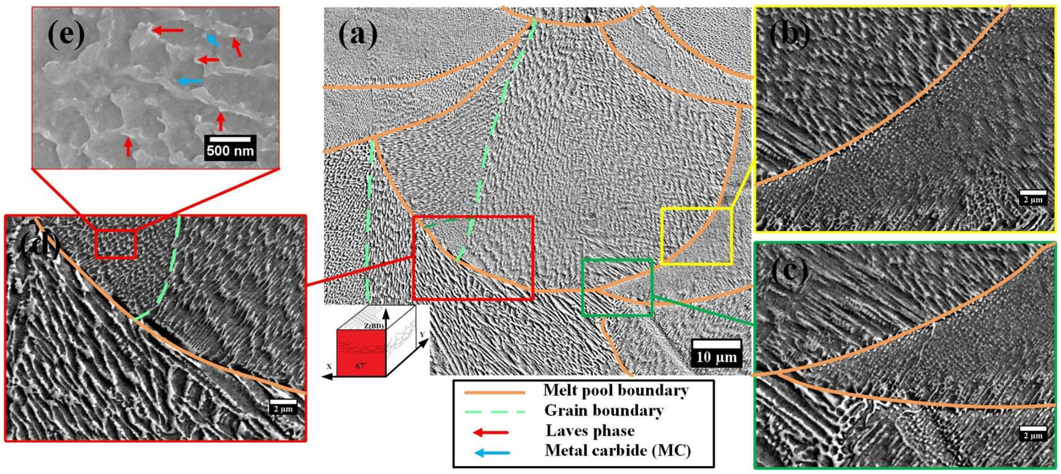

Figure 5.7: SEM microstructure of 67° rotation strategy (67T). (a) YZ plane of 67° rotation; (b), (c) and (d) Melt pool boundaries surrounded by different sub-structure; (e) Laves phase and metal carbide. (Laser power: 135 W, scanning speed: 800 mm/s)

The epitaxial growth microstructure of the Alloy 718 built by parameters in Table 3.4 is presented in Figure 5.8, whereby the coordinate system for the as-built sample is given in the inset and observing surfaces are marked in red. The scanning strategy changes laser path directions to provide a unique thermal pattern for grain growth.

In the micrographs, cells (the smallest unit in the melt pool with a size of 0.5 – 3 μm) are formed due to quick solidification. They are marked with dashed lines and arrows to indicate the growth direction, and the printed layers are numbered (layers 1-8) in Figure 5.8(a). The continuous growth of cells across several layers (Layers 1-8 in Figure 5.8(a)) along BD is only found in 01T and 90T. Their grain lengths (building axes) along the building direction reach 195.5 μm and 168.6 μm, as shown in Figure 5.8(a) and (b), respectively. Continuous epitaxial growths occur at the centre of melt pools and their growth directions are along BD, exhibiting a slender and elongated morphology.

However, the grain width in 01T and 90T are less than 20 μm, leading to a high aspect ratio (Z axis to X/Y axis). Side-branching frequently occurs at the side of a melt pool in 01T with an inclined angle of about 45° to BD, crossing four layers (layers 4-8), as shown by the green dash lines in Figure 5.8(a). The cell growth direction is nearly perpendicular to cells in neighbouring melt pools following the green arrows in Figure 5.8(a). However, the complex molten flow in the melt pool can also disturb the 45°-inclined growth pattern at the side of melt pools, resulting in various cell growth directions as shown in layers 1 to 4 (red arrows). In addition, the 45° inclined side-branching is likely to grow towards the centre of the melt pools, restricting the growth of the build-directional continuous cells. This is indeed seen in Figure 5.8(a) that the growth of continuous cells is limited in layers 5 to 8.

In Figure 5.8(b), laser scanning directions are perpendicular in adjacent layers, leading to 90°-rotational melt pools in neighbouring layers. For example, layer 3 is along the Y-axis and layer 4 is along the X-axis, according to the coordinate system in each inset. In the 90°-rotation strategy, the cells that grow at the side of a melt pool are disrupted by the subsequent layers as shown in layers 7 and 8, inhibiting the 45° inclined side-branching growth.

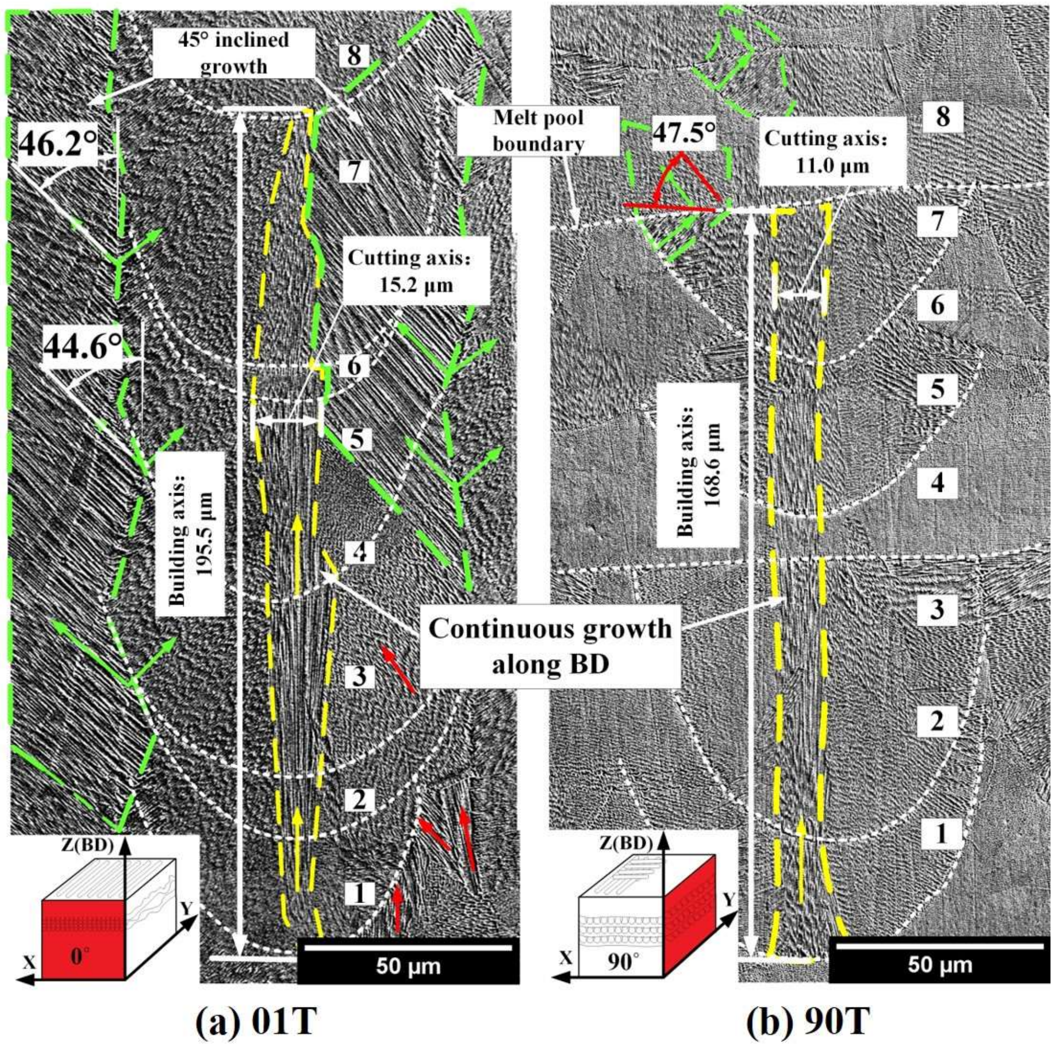

Figure 5.8: Representative microstructures for 01T and 90T. (a) The build direction (BD) is along the z-axis (see inset); the continuous growth of cells across several layers along the centre line of melt pools (highlighted by yellow dashed line) and the side-branching epitaxial growth with about 45° to BD (highlighted by green dashed line) in 01T; (b) Continuous growth along BD (see inset) in 90T and side-branching at the side of melt pools. The coordinate system and scanning strategies are in the inset, and observing surfaces are marked in red. Cell growth directions are marked with arrows.

Various cell growth directions can be found in a single melt pool of 02T (layer 3 in Figure 5.9(a)). Cell growth directions in 02T are nearly normal to the melt pool boundary (white dashed lines), but localised growth directions are different as shown in zone A, B and C (red arrows) in Figure 5.9(a). The growth direction of cells across different layers (layer 1-3) in zone D is in the same direction (out of the plane). It should be noticed that the side-branching growth (green arrows) was not found in 02T from Figure 5.9(a). This is because the out-of-plane directional growth is hard to track in a 2D figure. In the 67° (67T) built direction, as shown in Figure 5.9(b), the laser scanning direction rotated 67° in every subsequent layer, breaking the continuous growth of cells at the centre of the melt pool. The growth direction of the cell highlighted by a green dashed line is interrupted by the melt pool boundary (MPB) in layer 1, but the growth direction changed about 90° in layer 2 and another 90° in layer 3, resulting in the helical epitaxial growth pattern.

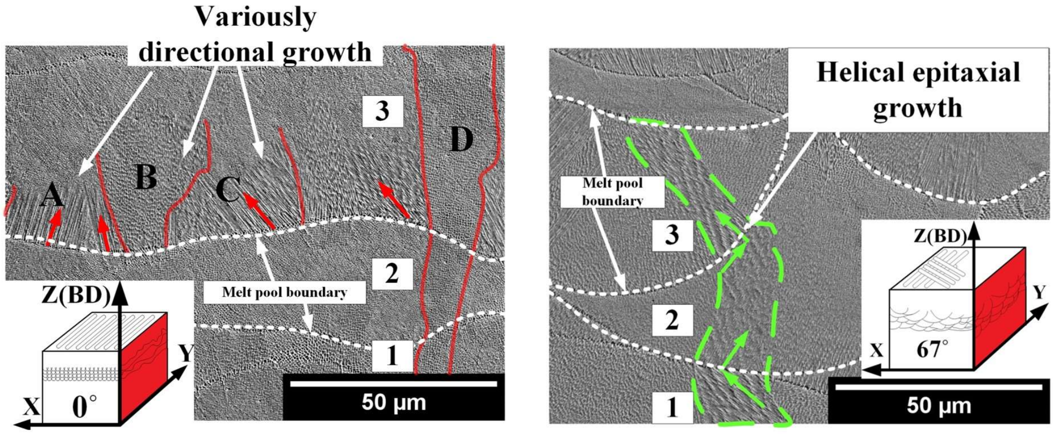

(a) 02T (b) 67T

Figure 5.9: Representative microstructures for 02T and 67T. (a) Various cell growth directions within a melt pool; (b) Side-branching growth at the side of the melt pool. The coordinate system and scanning strategies are in the inset, and observing surfaces are marked in red. Cell growth directions are marked with arrows.

5.1.3 Grain morphology and texture

Figure 5.10(a-c) presents the inverse pole figure (IPF) cubes of Alloy 718 printed by three scanning strategies. EBSD data was obtained from three orthogonal planes (XY, XZ, and YZ) and then merged to create 3D cubes for each of the three cases. However, it should be noted that the resulting cube represents a combination of three IPF maps rather than a true 3D grain structure. Due to the unchanged scanning direction in the 0° rotation strategy, the columnar grains are observed in the XZ plane, different from the grain morphology in YZ planes (Figure 5.10(a)). In contrast, since the scanning direction rotated 90° and 67° in each layer, the microstructures in XZ and YZ planes (Figure 5.10(b) and (c)) are equivalent in these two cases. The build direction is shown in the coordinate system and grain boundaries with a misorientation angle larger than 15° are identified as large-angle grain boundaries. It should be noted that grains in the selected regions have typical size, shape and orientation in each sample.

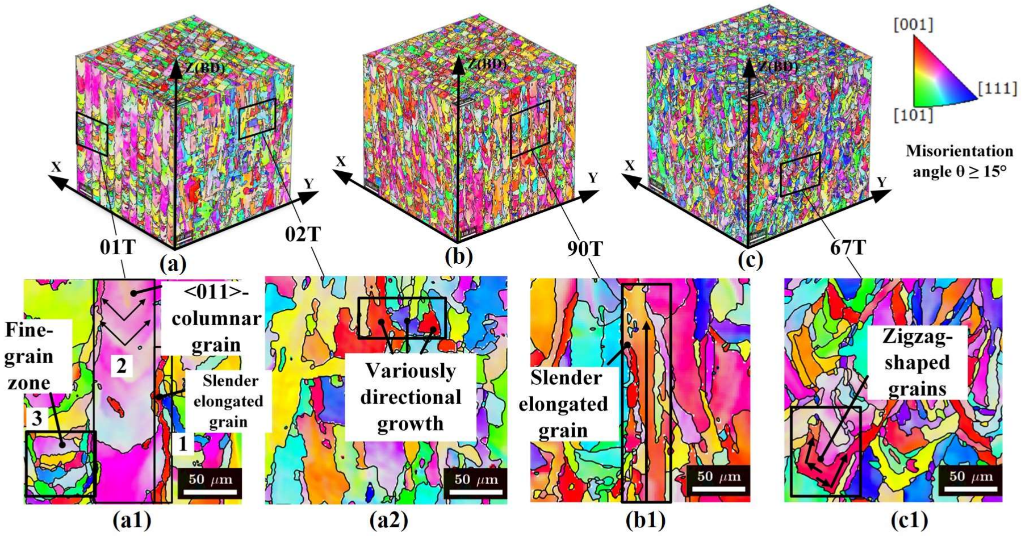

Figure 5.10: IPF cubes for three scanning strategies. (a) 0° rotation; (b) 90° rotation; (c) 67° rotation. IPF of machining areas were selected by black rectangles for (a1) 01T, (a2) 02T, (b1) 90T and (c1) 67T. (Grain growth patterns are marked with arrows)

The grain morphologies are highlighted in Figure 5.10(a1-c1). In Figure 5.10(a1), the slender elongated grains (zone 1) correspond to the previous build-directional continuous cells in Figure 5.8(a). Since the Alloy 718 exhibits an FCC structure, the grain orientation is not changed although the cell's growth direction changes to

90°. Therefore, the mentioned vertical growth cells in neighbouring melt pools in Figure 5.8(a) (green arrows) at the side of melt pools are from the same grain, forming the <011>-columnar grains (Zone 2) in Figure 5.10(a1). Various cell growth directions induced by perturbation in the melt pool result in the fine-grain zone as shown in Zone 3 from Figure 5.10(a1). Grains in 02T (Figure 5.10(a2)) are nearly along BD, which matches well with cells in Figure 5.9(c) that grow roughly normal to the melt pool boundary. The orientation varies in the highlighted area in Figure 5.10(a2) due to the inclined cell growth within a melt pool, while large grains are found because of the same growth direction in several layers. The slender and elongated grain formed by build-directional continuous cells is also observed as highlighted by the black rectangle in Figure 5.10(b1), which corresponds well to build-directional continuous cells in Figure 5.8(b). In Figure 5.10(c1) of 67T, the helical epitaxial growth cells result in zigzag-shaped grains in the 2D plane and the grain growth direction inclined angles against the BD. The non-repeatedly rotational scanning strategies randomise cell growth direction, resulting in various orientations and smaller grain sizes than the other three samples in Figure 5.10(c1).

The pole figures of <001>, <011> and <111> planes are shown in Figure 5.11, corresponding to the coordinate system in Figure 5.10. In the 0°-rotational scanning strategy, the 45° inclined grain growth direction shown in Figure 5.8(a) leads to a<011>//BD texture observed in the XZ plane and <011>⊥BD texture in the YZ plane (Figure 5.11(a)). In the 90°-rotational scanning strategy, since the laser scanning direction rotates 90° for each layer, the texture in the XZ and YZ planes is the same. The preferred grain growth is along the BD, resulting in the <001>//BD texture in the XZ and YZ planes (Figure 5.11(b)). In the 67°-rotational scanning strategy, the weak texture in three observation planes is attributed to the 67° rotational scanning strategy, which randomises the grain growth direction on each layer.

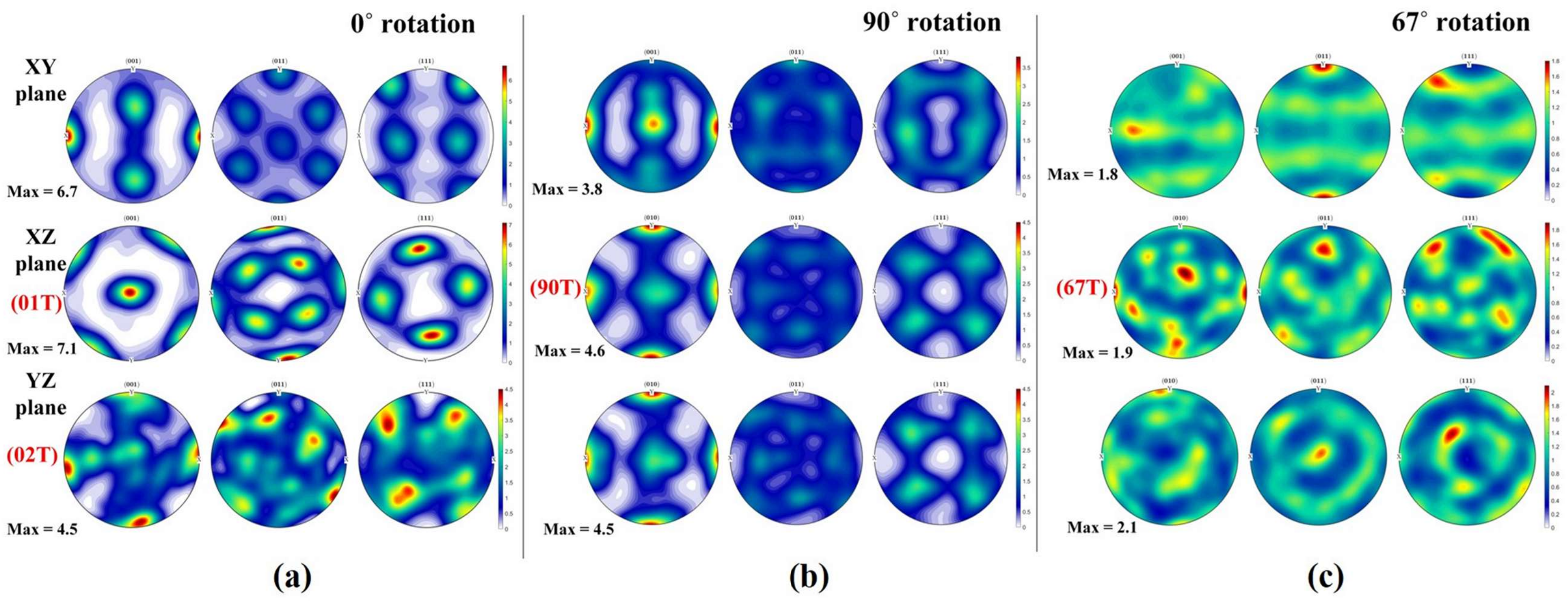

Figure 5.11: Crystallographic textures pole figures. (a) 0°-rotational scanning strategy, samples 01T and 02T are from XZ plane and YZ plane, respectively; (b) 90°-rotational scanning strategy, sample 90T is from XZ plane; (c) 67°-rotational scanning strategy, sample 67T is from XZ plane.

Figure 5.12 shows the corresponding crystallographic texture of the samples mentioned in Figure 5.10(a1-d1) and the lattice orientation as well as the possible slip systems. It should be noted that the intensities and orientations in these four selected regions (0.4 mm × 0.4 mm) are similar to those in the 1.2 mm × 1.2 mm regions, as shown in Figure 5.11. Since the differences in Euler angle data between the selected and original large regions are not significant, it indicates that these four selected regions can represent the four textured Alloy 718 samples.

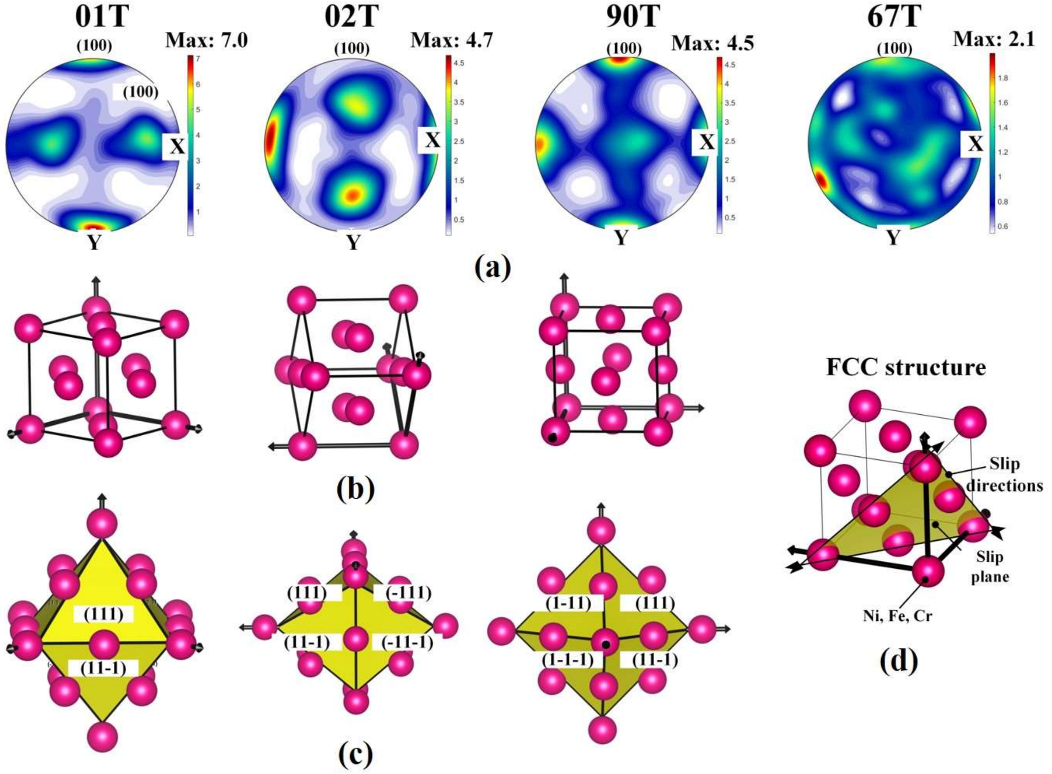

Figure 5.12: Pole figures (PF), corresponding lattice structures and slip systems for four samples. (a) Corresponding crystallographic textures in the XZ planes (YZ plane for 02T) (The {011} and {111} pole figures can refer to Figure 5.11.); (b) Different FCC lattice orientations for textured specimens; (c) Corresponding textured close-packed slip system in FCC (The texture of 67T was too weak to show distinctively textured lattice structure and slip system); (d) illustration of slip plane and slip directions in an FCC structure.

According to {100} pole figure in Figure 5.12(a), only 01T, 02T and 90T presented significant textures, but the texture of 67T was too weak to be identified due to the

67°-rotation scanning strategy. In 01T, <011>//BD and <001>//BD textures are observed, in which the <011> texture is caused by 45° inclined cells (as seen in Figure 5.8(a) (green arrows)) and the <001> texture is attributed to those continuous growth cells with <001> growth direction at the centre of a melt pool. This texture is consistent with previously reported studies [132,221]. A <011> texture along to Y-axis was obtained in 02T, of which the maximum intensity was 4.5, lower than 7 in 01T. A strong cube texture of three <001> aligned to X, Y and Z (BD) was obtained in 90T, which is in good agreement with previous studies for FCC metals with the same scanning strategies [238]. The maximum texture intensity of 67T was only 1.9 and no preferred grain orientations were found due to the non-repeated laser scanning rotation in every layer. The large area corresponding to {001} {011} and {111} pole figures can be referred to in Figure 5.11.

The lattice orientations of representative grains in the textured Alloy 718 are shown in Figure 5.12(b) to reflect the texture in Figure 5.12(a). And the illustration of the FCC lattice structure and slip system is shown in Figure 5.12(d). The red balls represent the metal atoms (Ni, Fe or Cr in this case) that form the FCC structure, and the yellow plane is the slip plane. Every slip plane has 6 slip directions marked with black arrows. Based on this illustration, Figure 5.12(c) presents corresponding slip planes and slip directions for 01T, 02T and 90T based on the crystallographic texture in Figure 5.12(a). It should be noted that the preferred lattice structure and slip system are not depicted in 67T due to its weak texture.

5.2 Deformation pattern of textured Alloy 718

5.2.1 Proposed concept

To study the effect of different textured Alloy 718 on shear-based deformation, three scanning strategies (0°, 67° and 90° rotation layer by layer) were used to fabricate crystallographic textured cubes as depicted in Figure 5.13 (a-c). The 0° rotation strategy repeats the same scanning path to provide a stable thermal gradient conducive to grain growth along the build direction. 90° rotation strategy repeats every two layers and forms strong cube textures while the 67° rotation strategy avoids repeating scanning directions, fabricating grains without preferred orientation. These three scanning strategies yield typical microstructures that are widely used in additive manufacturing field. Two samples (01T and 02T) were obtained from 0° rotation scanning strategy due to two different textures in the XZ and YZ planes. Only one sample was obtained from 90° (Figure 5.13 (b)) and 67° (Figure 5.13 (c)) rotation scanning strategies, respectively, since samples from XZ and YZ planes are equivalent in both scanning strategies. To compare the deformation of typical grains in the textured Alloy 718 before and after cutting, EBSD&SEM characterisation at the same zone near the machined surface was performed. It should be noted that the "quasi-in-situ" investigation was only conducted for the machining process instead of LPBF process. A "T-shape" label was marked on the carefully polished samples as a reference, allowing the same area to be detected under EBSD&SEM before and after cutting as shown in Figure 5.13 (d). It must be emphasised that no polishing was conducted after the cutting experiment to retain the history of cutting on the grains. As such, the original grains, including morphologies, orientations and slip traces, can be analysed before cutting, as in Figure 5.13 (e), and then be compared with grains after cutting as in Figure 5.13 (f). The dislocation density, grain boundary curving and orientation change were quantitatively investigated. Furthermore, the slip bands and grain bulging can be found after cutting by combining EBSD and SEM results (Figure 5.13 (g)).

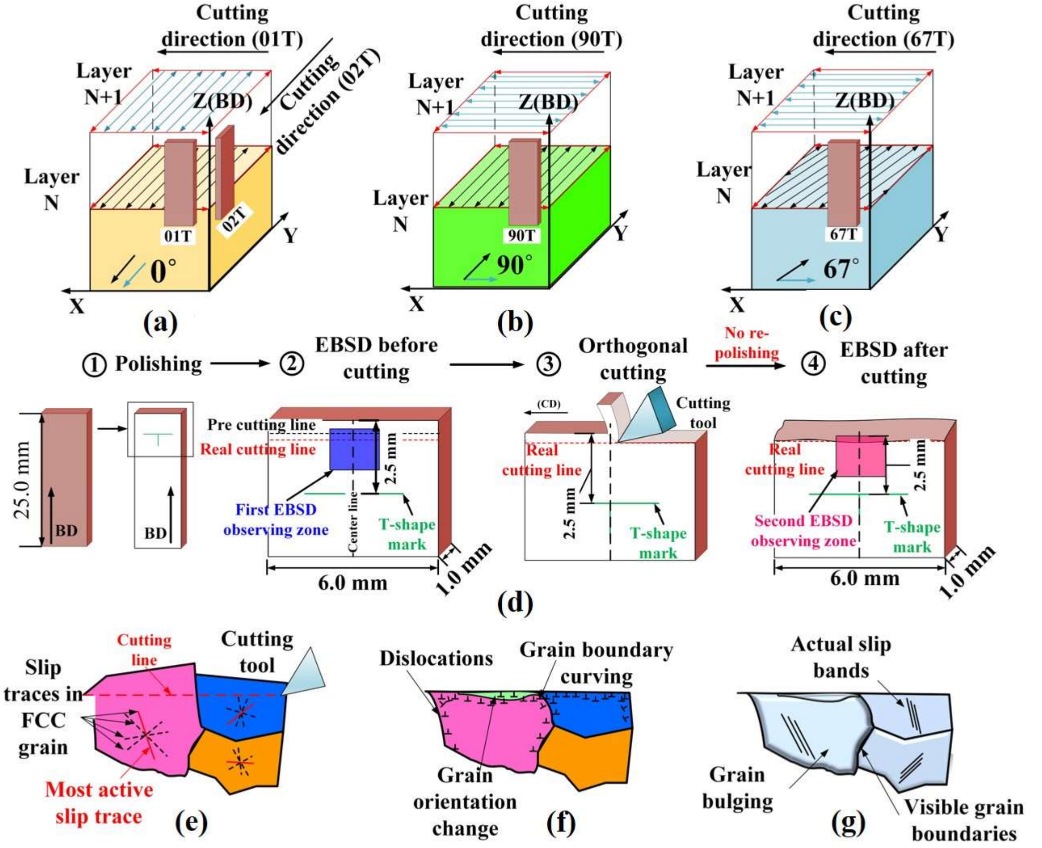

Figure 5.13: Illustration of quasi-in-situ investigation of grain deformation in crystallographic textured Alloy 718. (a-c) Schematics of scanning strategies and cutting directions for four samples - see brown parallelepipeds - (01T, 02T, 90T and 67T) obtained from different LPBF built cubes; (d) Schematics of quasi-in-situ investigation processing, including polishing, first EBSD&SEM observation, orthogonal cutting and second observation; (e) Schematics of grains observed under EBSD before cutting (slip traces in FCC can be calculated based on IPF); (f) Schematics of grains observed under EBSD after cutting; (g) Schematics of grains observed under SEM after cutting (the slip bands and part of grain boundaries are visible due to deformation).

The actual IPF mapping of the cutting zone from Figure 5.13(d) and corresponding ECCI results are shown in Figure 5.14, efficiently presenting grain mappings from the "T-shape" scratch mark zone to the sample edge. Every ECCI image is spliced by four images as the distance from the marked zone to the edge is about 2.5 mm, which is out of the range of electron scanning in a single image. In addition, the EBSD mappings can match well with the pattern of ECCI images at the same observing zone. For the cutting test, the cutting zone consists of two parts: a pre-cut zone (dark shadow area in red rectangle), a zone reserved for making a curve matched with the pendulum trajectory, and a real cut zone (red rectangle below the shadow area), a zone for the formal cutting test.

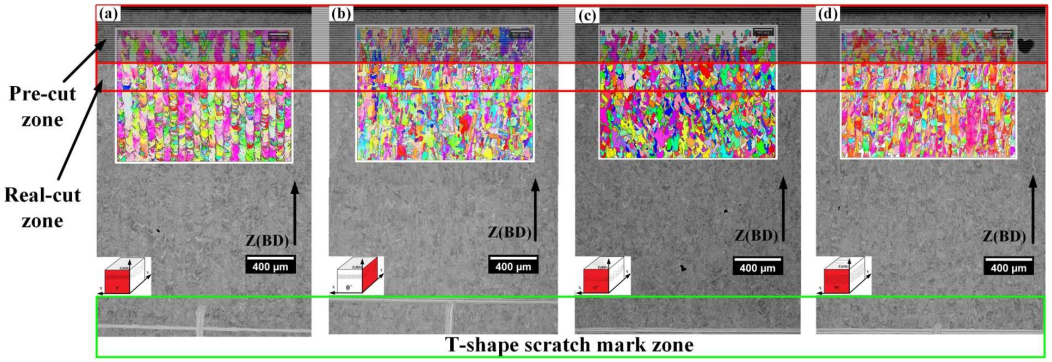

Figure 5.14: ECCI and EBSD results of three scanning strategies. (a) 0° rotation on the XZ plane; (b) 0° rotation on the YZ plane; (c) 67° rotation; (d) 90° rotation. (pre-cut zone and real-cut zone are labelled by the red rectangles. T-shape scratches are marked by a green rectangle. The plane information is shown in the inset)

5.2.2 Plastic deformation caused by orthogonal cutting

5.2.2.1 Grain deformation of 01T

Since the plastic deformation leads to poor Kikuchi pattern quality in chips, the chip deformation before and after cutting is not included in this work. It is noted that the EBSD data is fitted to reduce the noise of scratches. Since the de-noise step is small, the orientation and grain structure near the machined surface are not changed. The inversed pole figures (IPFs) of 01T before and after machining are presented in Figure 5.15 (a) and (b). Several build-directional blocks are observed as shown by the dashed lines and slender elongated grains are between the build-directional blocks. To trace the evolution of individual grains before and after cutting, deformed grain A′ and Grain B′ are compared with original Grain A and Grain B. It can be seen from Figure 5.15 (d) that Grain A and Grain B were slightly curved along the cutting direction. It should be noticed that the edge in Figure 5.15 (b) is not the machined surface but the EBSD detectable area beneath the machined surface as the Kikuchi pattern in the machined surface is difficult to index due to significant deformation. The deformation of Grains A′ and B′ still follows shear condition but the strain is not as large as the region near the machined surface [187]. The effect of temperature is disregarded in this study due to the relatively short total cutting time of approximately 220 μs. Additionally, the heat accumulation is expected to be minimal due to the small dimensions of the workpiece (cutting length: 6 mm, sample thickness: 1 mm) and the presence of adiabatic shear bands in the primary shear zone would not significantly impact the deformation of machined surface.

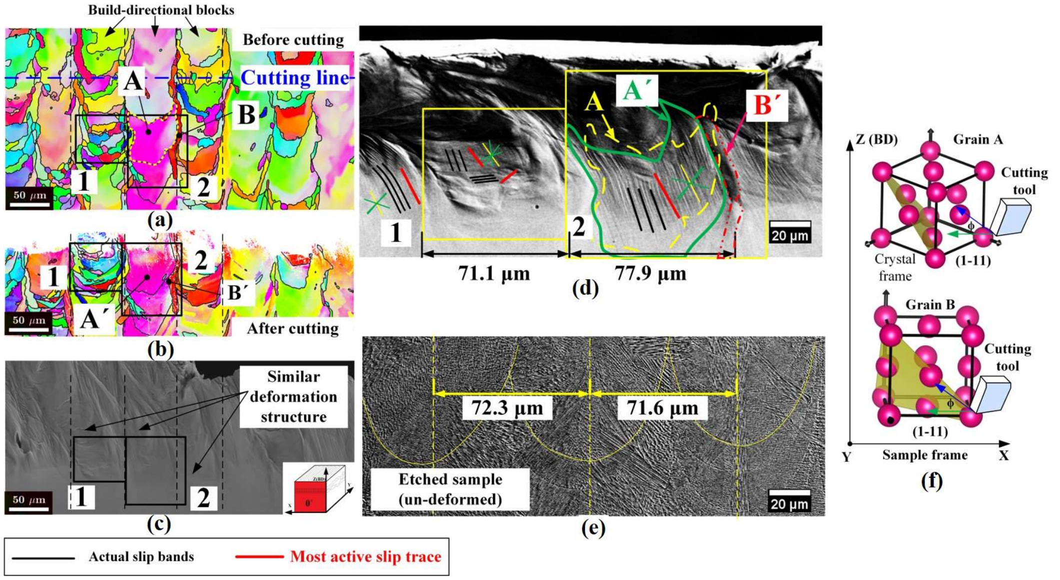

Figure 5.15: Quasi-in-situ observation of 01T. (a) Before orthogonal cutting; (b) after orthogonal cutting; build-directional blocks was divided by dashed lines; (c) SEM image on the EBSD stage (70° inclined) and similar deformation structure was marked with arrows; (d) SEM image of selected Zone 1 and Zone 2; outlines of original Grain A and deformed Grain A′ were highlighted by yellow lines and green lines (the most active slip trace and actual slip bands were marked by red line and black line respectively; the plane traces are highlighted by dark green lines and the activated slip trace is marked by yellow line); (e) The centre line spacing in an etched sample; (f) The slip plane and cutting direction is shown in the sample frame.

According to the characteristic bugling retained on the observation surface (Figure 5.15(d)), the deformed grains in the SEM image are linked with corresponding grains in the IPF as shown in Figure 5.15(b) and (d). In this way, the machining-induced deformation can be analysed based on grain morphologies and orientations. A similar deformation structure is observed (Figure 5.15(c), dashed lines) based on these typically repeated bulges, which matches well with the build-directional blocks in Figure 5.15(a) (black dashed lines). Due to the retained bulges on the surface, this is the first time that the similar deformed structure is reported in as-built LPBF structures (i.e. Alloy 718) during the shear-based deformation. The spacing of the similar structures (71.1 μm and 77.9 μm in Figure 5.15(d)) is close to the spacing of the melt pools (72.3 μm and 71.6 μm) in Figure 5.15(e), suggesting the similar structure is caused by slender <001>-elongated grains at the centre of melt pools and <011> columnar grains between the centre of each melt pool. The grain widths of columnar grains are approximately 50 μm, significantly wider than the slender elongated grains (about 10 μm). Since the cutting direction is parallel to the grain width direction, the deformation may be affected by such width difference.

Euler angles obtained from Figure 5.15(a) (before cutting) was used to compute the slip trace, this can decrease the error caused by distorted grain and lattice rotation near the machined surface as shown in Figure 5.15(b). It can only be implemented due to the carefully collected grain information before cutting. Grains in zone 1 and 2 from Figure 5.15(b) are tracked in an un-etched SEM image (Figure 5.15(d)) after cutting. The most active slip trace and actual slip bands were marked with red and black lines respectively. The relationship between representative FCC structures and machining direction is shown in the sample frame in Figure 5.15(f). The cutting direction is along the green arrow and the shear direction is along the blue arrow. The angle between the cutting and shear direction is the shear angle (ϕ). According to the diagram of the cutting tool and FCC structure of Grains A and B (Figure 5.15(f)), the most active slip trace in Grain A is nearly parallel to the shear direction whilst there is a spatial angle between the slip plane in Grain B and shear direction.

The traces of different slip planes are distinguished for the FCC structure with four slip planes. Four {111} plane traces are highlighted by green lines and the activated slip trace is marked by yellow lines (Figure 5.15(d)). The same mark is also used in the following three cases for slip trace analysis. Typical intensive slip bands are dominated in Grain A′, which is nearly parallel to the shear direction. A significant squeezing-out effect is likely found in Zone 1 (fine grain zone) and build-directional block boundary (e.g., Grain B), indicating that narrow grain width (cutting axis) along the cutting direction may lead to significant inhomogeneous deformation.

5.2.2.2 Grain deformation of 02T

Figure 5.16(a) and (b) show the IPFs before and after deformation for 02T. The relationship between representative FCC structures of grains and machining direction is shown in the sample frame. The dominated slip bands are marked with black lines. By comparing Grain A and A′, the lattice rotation is observed in Grain A′ (Figure 5.16(b)). It can be seen from Figure 5.16(e) that grain bulging occurs near the machining surface due to the low constraint in the free surface (YZ plane), causing the grain orientation change as highlighted by the red circle in Figure 5.16(d). The pink line across the grain is the scratch caused by sample fixation rather than twin or sub-grain boundary because the disorientation near this region is only about 1.4°. The grain boundary matches well with the corresponding counterpart retained in Figure 5.16(e). The lattice rotation is not limited in the observation (YZ) plane and the new grain boundary may be attributed to material pile-up. The high angle grain boundary may change the local stress status and impede slip transfer to the bulk. This is verified by different slip intensive in Grains n and A′. The local strain incompatibility near the grain boundary [239] causes slight lattice rotation in Grain A′, as shown in Figure 5.16(d). To the authors’ best knowledge, there is no research that reported this phenomenon in the orthogonal cutting process and this has been observed based on our quasi-in-situ grain evolution analysis method.

A large grain and several fine grains were deformed as shown in Zone 1, 2. Grain B′ is slightly deformed compared with original Grain B. In Figure 5.16(f), Grain B′ is highlighted by the yellow dashed line, which matches well Grain B′ in Figure 5.16(b). The original Grain B is also marked in Figure 5.16(f) according to Grain B in Figure 5.16(a). The roughly overlapped outlines of Grain B and B′ indicate that slight deformation occurred in Grain B. The slip bands are slightly inclined to the right (i), then gradually inclined to the left (ii and iii) and finally become curved (iv) in Figure 5.16(f). This slip bands evolution phenomenon indicates that the strain gradients near the grain boundaries is more significant than the centre of Grain B′. In Figure 5.16(g), there are no intensive slip bands in Grain C′ compared with original Grain C due to the small grain size. Comparing the outlines of Grain D and D′ in Figure 5.16(g), the grain causes a larger deformation depth than the small grain nearby. This indicates that the grain deformation is dependent on the grain morphologies (i.e., grain width) in the machining process.

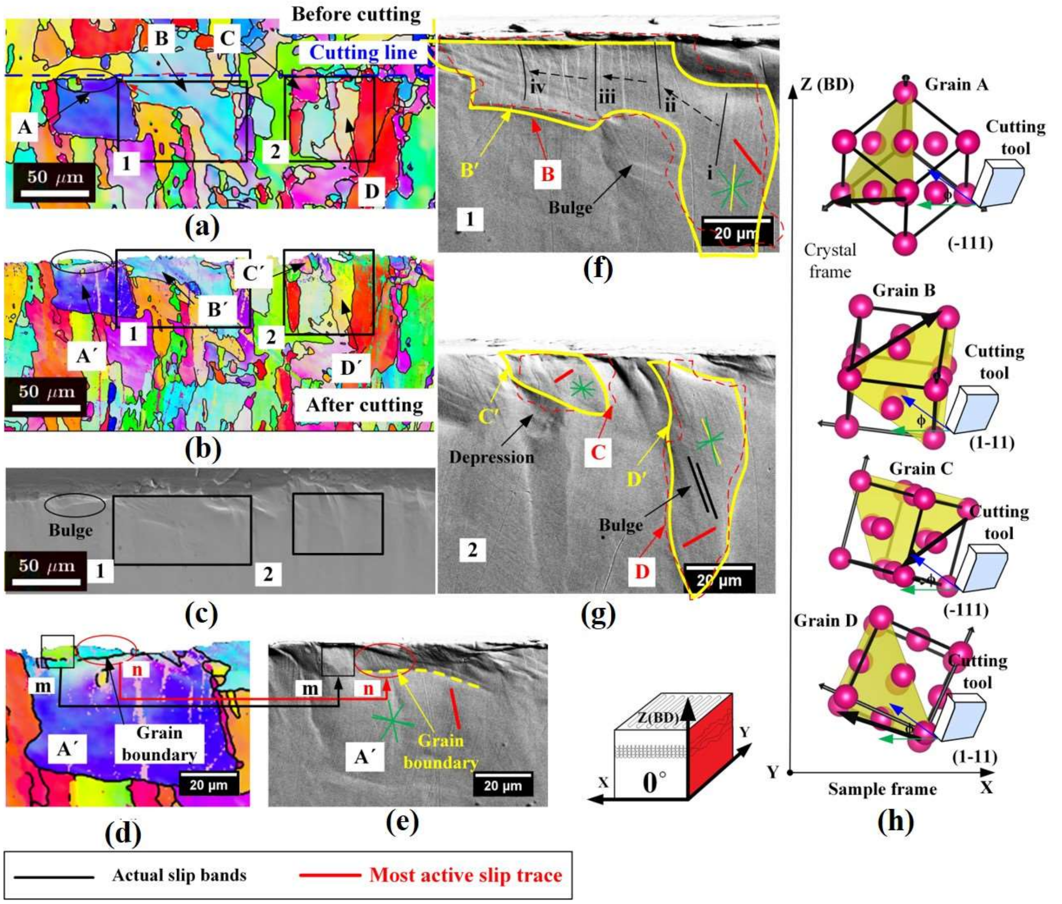

Figure 5.16: Quasi-in-situ observation of 02T. (a) Before orthogonal cutting; (b) After orthogonal cutting (c) SEM image on the EBSD stage (70° inclined) and a bulge causing orientation change was marked with circle; (d) The orientation change in Grain A′; (e) the corresponding Grain A′ in observed by SEM; (f) SEM image of selected zone 1; the outlines of the original Grain B and the deformed Grain B′ were highlighted by red dashed line and yellow line; and slip bands evolution were marked with i to iv; (g) SEM image of selected zone 2, grain deformation was highlighted by red and yellow line and a bulge and a depression were marked with arrows; (h) Corresponding slip system and shear direction are presented in the sample frame. (The most active slip trace and actual slip bands were marked with red line and black line respectively and the plane traces are highlighted by dark green lines and the activated slip trace is marked by yellow line).

5.2.2.3 Grain deformation of 90T

In Figure 5.17(a-c) of the 90T sample, Zone 1 is selected to analyse the deformation of elongated grains. The grain orientation of the upper region of Grain A and B is changed after deformation as compared to that of Grain A′ and B′ in Figure 5.17(b). In Figure 5.17(d), Grain A′ is inclined according to the outlines of Grains A and A′, and the wrinkling is found within the grain, corresponding to the orientation change in Figure 5.17(b). Similarly, the wrinkling also exists in Grain B′, leading to the local orientation change in Grain B′ (Figure 5.17(b)). In Figure 5.17(e), slip bands transmit from Grain D′ to Grain C′ with high compatibility between two grains (i.e., slip band direction is not changed). And the grain boundary between the two grains is not inclined or curved, suggesting less plastic strain accumulation at the grain boundary. Multi slips are activated in Grains C′ and D′ and the slip bands are then hindered by the grain boundaries below. In such orientations, it may be easier for more than one slip system to exceed the resolved shear stress during cutting, resulting in the formation of multi-slip bands. Additionally, since Grains C and D have similar orientations, neighbouring grains with high compatibility (or lower misorientation) allow slips to cross the grain boundary with original slip directions [157]. It should be noted that Grains A′ and D′ have similar grain areas (about 2000 μm^2) and orientations (<001>//BD). But due to the different grain morphologies, intensive slip bands were only observed in Grain D′, whilst significant wrinkling occurred in Grain A′. This indicates that the cutting axis (grain width along the cutting direction, Figure 5.17(d)) may be a better indicator for grain size estimation during the shear-based deformation, especially for the LPBF-fabricated grain with a high aspect ratio (building axis to cutting axis).

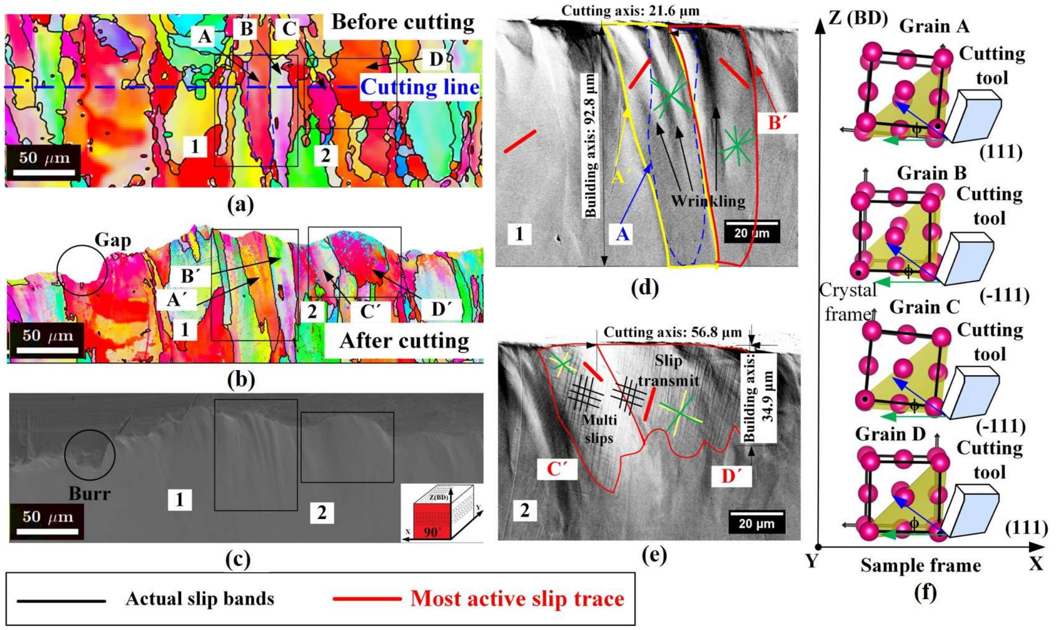

Figure 5.17: Quasi-in-situ observation of 90T. (a) Before orthogonal cutting; (b) After orthogonal cutting; (c) SEM image on the EBSD stage (70° inclined); (d) Grain inclining and wrinkling within Grain A′ and B′; (e) Slip transmitted across the grain boundary between Grain C′ and D′ as well as multi slips in Grain C′ (long and short axes were marked); (f) Corresponding slip system and shear direction are presented in the sample frame. (The most active slip trace and actual slip bands were marked with red and black lines respectively and the plane traces are highlighted by dark green lines and the activated slip trace is marked by yellow line).

5.2.2.4 Grain deformation of 67T

In Figure 5.18(a) and (b), the grain deformation of 67T is observed based on the typical shape of bulges, and grain features in Zone 1 and 2 matched well with Figure 5.18(c). The grain size of 67T is smaller than the previous three samples, resulting in more pronounced “wrinkling” near the machined surface as shown in Figure 5.18(c). In Figure 5.18(d), it is found that the boundary of Grain A′ is curved near the machined surface compared with its original outline, and slip bands only occur in Grain A′ as seen from Zone i and Zone ii in Figure 5.18(d) but are not found in Grain B′. According to the most active slip traces marked with red lines and FCC structure of Grains A and B in Figure 5.18(f), the activated slip trace in Grain A′ is parallel to the shear direction while the trace of Grain B′ is perpendicular to the shear direction. Thus, intensive slip bands are found in Grain A′ but the Grain B′ restricts the slip transmission and no slip bands are visible in Grain B.

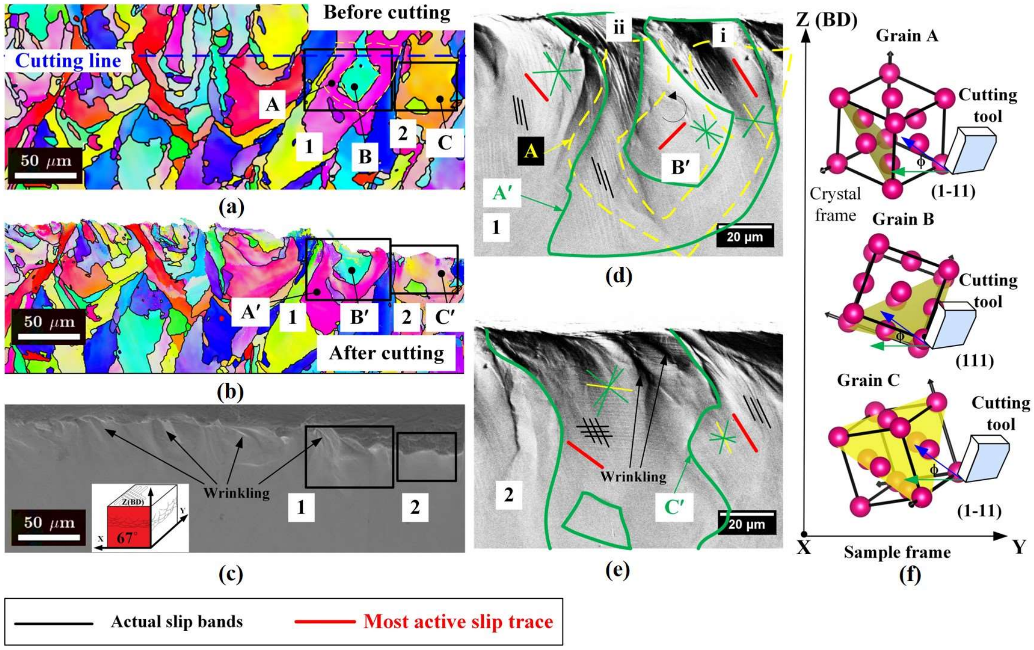

Figure 5.18: Quasi-in-situ observation of 67T. (a) Before orthogonal cutting; (b) After orthogonal cutting; (c) SEM image on the EBSD stage (70° inclined) and the wrinkling was marked with arrows; (d) SEM image of selected zone 1 and a grain rotation was observed in Grain B′; (e) SEM image of zone 2, the wrinkling occurred within Grain C′; (f) Corresponding slip system and shear direction are presented in the sample frame (the most active slip trace and actual slip bands were marked with red and black lines respectively and the plane traces are highlighted by dark green lines and the activated slip trace is marked by yellow line).

Moreover, the grain width near the machine surface is different in Grains A and B. In Figure 5.18(a), cutting line is through a very narrow part of Grain B but a relatively wide region of Grain A. Grain B may exhibit high deformation resistance due to the narrow grain boundary distance. Because such deformation is not only dependent on orientation but also grain morphology, the generally used indicator, for example Taylor factor or Schmid factor, may not be suitable to eliminate the grain formed by LPBF. It also indicates that the grain size in the cutting process may dependent on the grain width along the cutting direction. In Figure 5.18(e), non-homogenous deformation occurs within Grain C′, resulting in wrinkling and consequently orientation change near the machined surface.

5.3 Effect of texture on the deformation

Since the textured deformation were dependent on typically oriented grains in four textured samples, the most active slip trace of each grain in a large-scale region for textured Alloy 718 was quantified as shown in Figure 5.19(a-d). According to the retained deformation history observed on the free surface, it is found that most individual grains are dominated by single directional slip bands whilst multi-slip bands only occurred in a few grains. This experimentally observational phenomenon contributes to building a new relationship between orientated grains and shear-based process via the most active slip plane. The slip trace is calculated in a 3D coordinate system to identify the activated slip plane. In order to visualise the slip trace in 2D grain maps, the intersecting line of the most active slip plane and grain map plane is presented in Figure 5.19(a-d), namely the most active slip trace. It is observed that the activated slip planes in 01T Figure 5.19(a) are more likely parallel to the shear direction (F_s direction in Figure 5.20(b)) but the slip planes in 02T (Figure 5.19(b)) are roughly perpendicular to the shear direction. The activated slip planes in 90T (Figure 5.19(c)) exhibit either parallel or perpendicular to the shear direction, which is attributed to its high intensity of <001>//BD texture. However, the directions of the slip planes in 67T (Figure 5.19(d)) are relatively randomised distributed due to its weak texture.

According to the Taylor model, the most active slip trace can be calculated based on the shear strain imposed on each grain. It should be noted that the length of slip trace is normalised and multiplied by a grain size factor to match the actual grain size. Since the large grain generally caused a larger area with similar slip trace directions than the small grain, the grain area was considered to calculate the slip trace intensity for each grain.

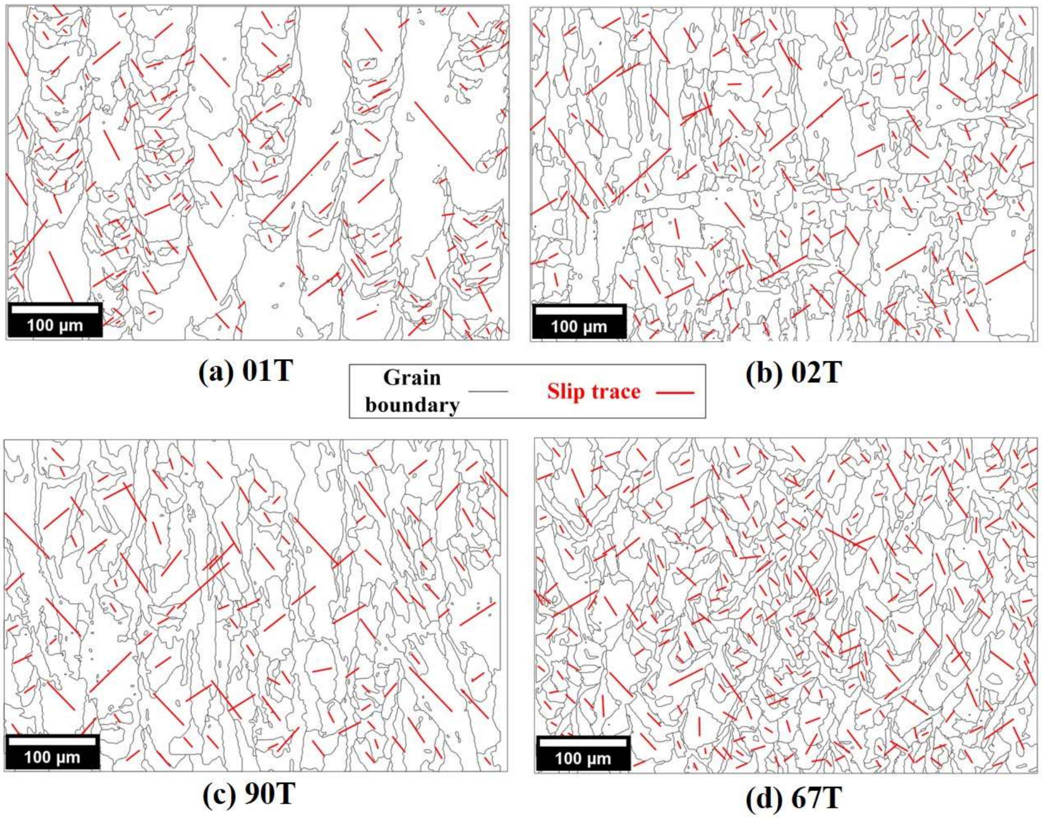

(a) 01T

(b) 02T

(c) 90T

(d) 67T

Figure 5.19: Most active trace of slip plane based on Taylor-model. (a) 01T; (b) 02T; (c) 90T, (d) 67T.

The intensity and direction of the most active slip trace for each textured sample are quantified in Figure 5.20(a), in which the activated slip trace for each grain was counted based on Figure 5.19(a-d). It statistically summarises the directions of activated slip planes for the oriented grains during the orthogonal cutting. The colour bar shows the density distribution of slip plane directions. Red colour represents that large number of slip planes orient in similar directions. The slip traces are mainly distributed in blue shaded areas and the most possible slip traces are marked with red arrows. In this way, the orientation of each grain is transformed to the corresponding most active slip trace in the shear condition. The force in an orthogonal cutting system is depicted in Merchant's circle (Figure 5.20(b)). The force R is the resultant of cutting force F_c and thrust force F_t. F_s is the shear force, α and ϕ are rake angle and shear angle, respectively.

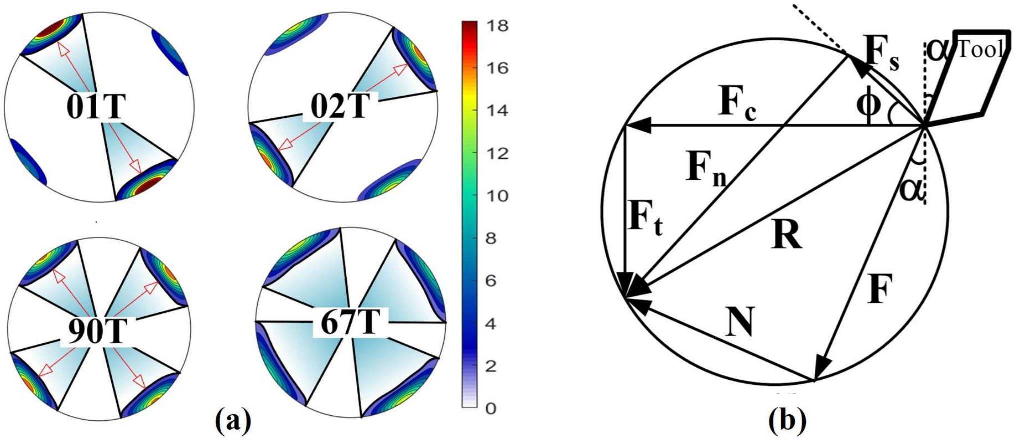

Figure 5.20: (a) The distribution of the most possible slip trace for each sample was calculated consider the grain size (the dominated slip trace was marked with red arrows); (b) The Merchant's Circle diagram.

Comparing the slip trace in Figure 5.20(a) with the texture in Figure 5.12(a), the high texture intensity (01T in Figure 5.12(a)) results in narrow distribution of slip traces. It is verified by the similar deformation structure as shown in 01T in Figure 5.19(a). And the weak texture intensity of 67T causes the wide distribution of slip traces as indeed seen in 67T of Figure 5.20(a). According to the slip trace distribution (shaded area and arrows) in Figure 5.20(a) and the shear force (F_s) direction in Figure 5.20(b), it can be observed that the major activated slip traces in 01T are almost parallel to the shear direction due to <011>//BD texture. Interestingly, different from 01T direction the majority of slip traces in the 02T sample are perpendicular to the shear direction. This is because the <011> texture in 02T is nearly perpendicular to the BD, as shown in Figure 5.12(a), indicating more activated slip planes perpendicular to the shear force direction. Different angles between the shear force direction and the most active slip trace may lead to texture-based bulk deformation. From Figure 5.20(a), it is also observed that there are two representative traces of slip planes in the 90T sample, exhibiting a mixed manner of 01T and 02T. However, the slip traces in 67T are varied due to the weak texture and it is hard to find a representative slip system that is parallel or perpendicular to the shear direction. This can be attributed to the randomised grain orientation caused by the 67°-rotation strategy.

5.4 Grain responses to machining-induced plastic deformation

5.4.1 Effect of misorientation angle and grain boundary

Although the most active slip trace reflects the texture-based deformation of Alloy 718, the individual grain deformation during cutting is further affected by grain misorientation, morphology and neighbouring grains. According to the plastic deformation of LPBF-fabricated Alloy 718 after cutting, the deformed grains can be divided into two categories as shown in Figure 5.21(a): (1) machined grain (yellow line) and (2) machine-affected grain (dashed line). The former is the grains damaged by the cutting tool contact (e.g. shear) and the latter is the grains indirectly affected during machining (i.e., grains that are not be cut through but deformed). The deformation of machined grain at the grain boundary can be presented by comparing incline angle (IA) and curving angle (CA) before and after cutting as shown in Figure 5.21(a). The incline angle (IA) is the angle between the initial grain boundary and the deformed grain boundary. The curving angle (CA) is the angle between the initial grain boundary and the tangential of the curved boundary, showing the deformation of grains near the machined surface for 02T, 90T and 67T in Figure 5.21(b)-(d) respectively. It should be noted that most grains in 01T shown in Figure 5.15(b) are machine-affected grains because the machined grains can hardly be EBSD indexed due to dramatic deformation (about 36 μm). The deformation of machined grains in 01T was not included in Figure 5.21.

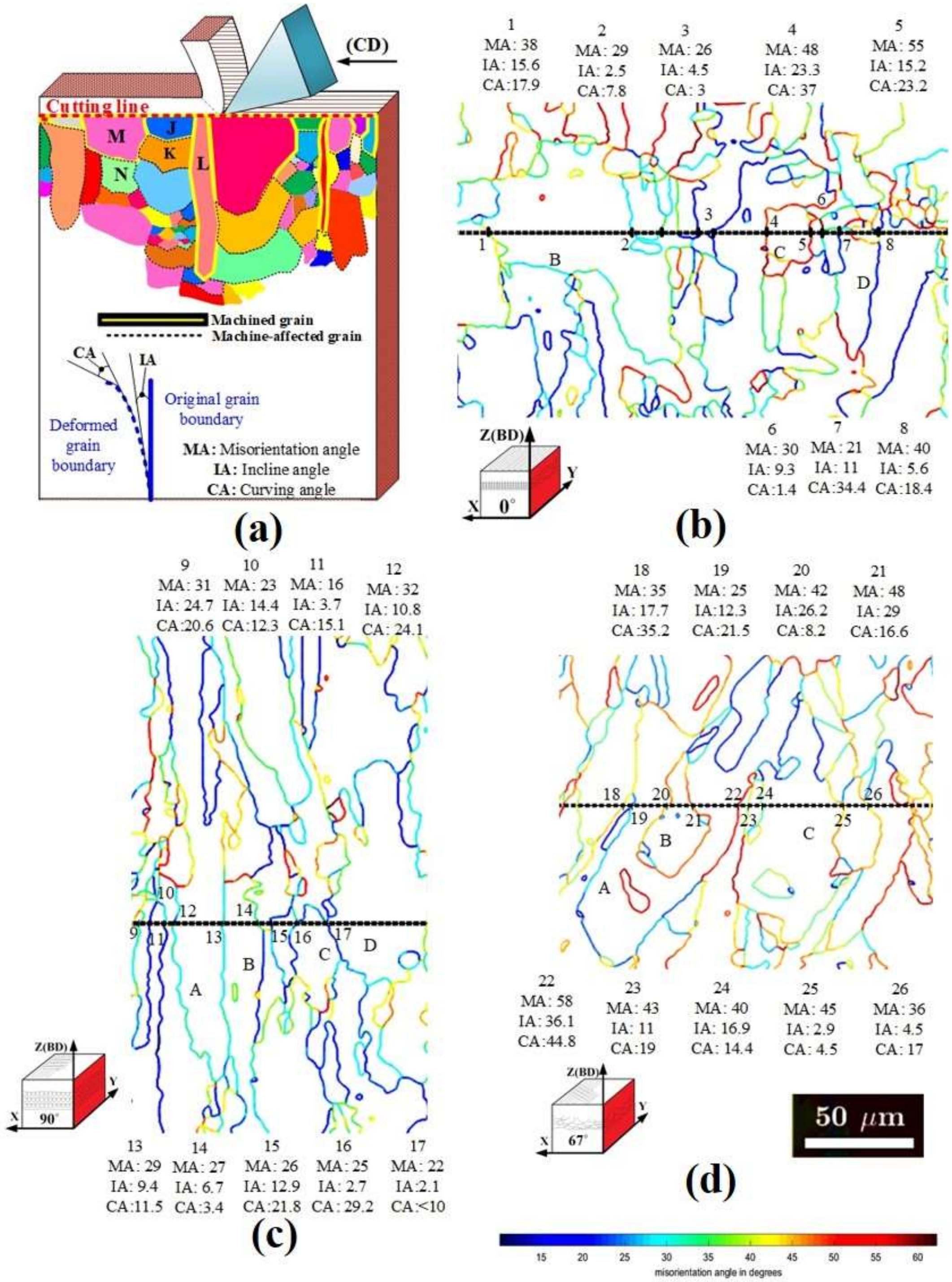

Figure 5.21: Schematics of deformed grains and misorientation angles of grain boundaries. (a) Schematics of machined grain (yellow line) and machine-affected grain (dashed line), misorientation angle (MA) between grains and incline angle (IA) as well as curving angle (CA) before and after cutting for (b) 02T, (c) 90T and (d) 67T. The colourful grain boundaries represent different MAs between grains.

The intersections of cutting line and grain boundaries were highlighted and numbered. IAs and CAs were measured before and after cutting in each sample, as shown in Figure 5.21(b)-(d) and the misorientation angles (MA) between grain boundaries were indicated by boundary colours. It can be seen from Figure 5.21(a) that large IAs and CAs are generally associated with large misorientation angles, as shown by GBs 4&5 in Figure 5.21(b) and GBs 21&22 in Figure 5.21(d). Grain boundaries with large misorientation angles usually exhibit higher incompatibility to slip transmission. This causes localised dislocation density concentration near the boundaries and consequently larger deformations near the grain boundaries. In contrast, the smallest IAs and CAs are found in 90T (Figure 5.21(c)), whose MAs were smaller than in 02T (Figure 5.21(b)) and 67T (Figure 5.21(d)), leading to higher compatibility for slip bands transmission across grains.

5.4.2 Geometrically necessary dislocations (GND)

With the increase of shear stress during orthogonal cutting, geometrically necessary dislocations (GND) increase in machined grains and concentrate at the grain boundaries as shown in Figure 5.22. High GND densities are concentrated in machined grains near the machined surface except 01T (Figure 5.22(a)) whose Kikuchi signal is missing near the machined surface as mentioned previously. The highest GND in 67T (Figure 5.22(d)) is due to the smaller grain size and significant deformation.

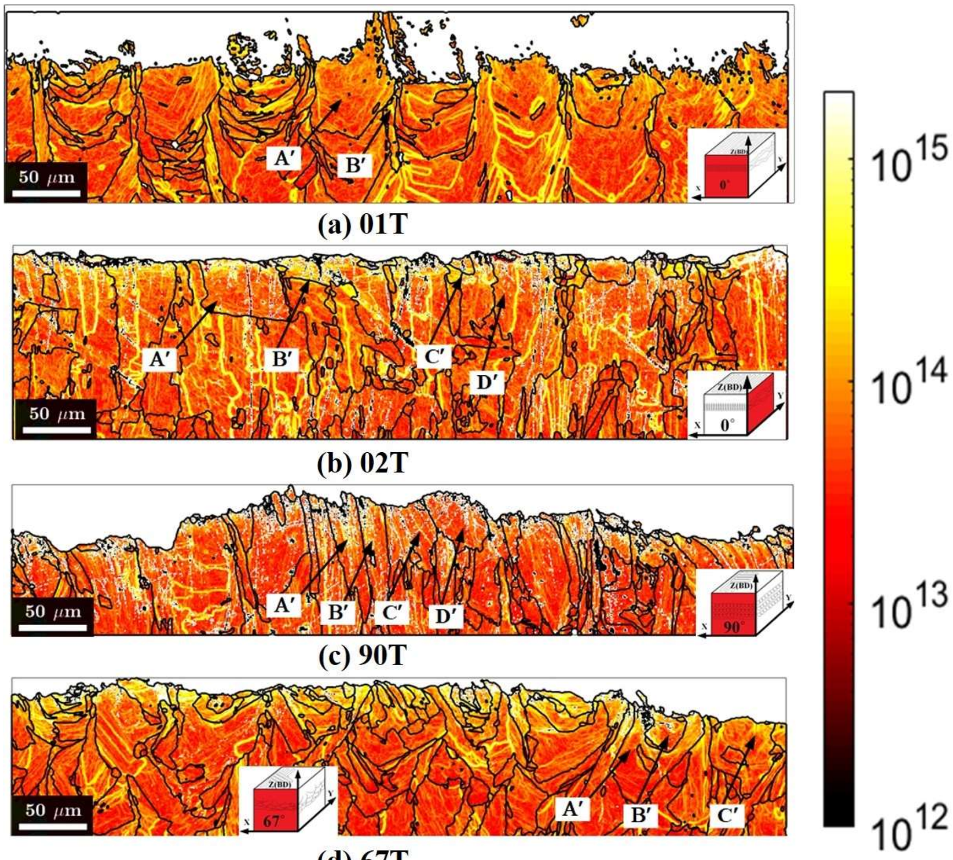

(a) 01T

(b) 02T

(c) 90T

(d) 67T

Figure 5.22: Geometrically necessary dislocation (GND) densities in four workpieces. (a) GND of machine-affected grains in 01T (the Kikuchi signal of machined grains was missing); (b) GND concentrates near the machined surface and decreases into the subsurface in 02T; (c) High GND density mainly concentrates at the grain boundaries in 90T; (d) Highest GND near the machined surface and lower GND in the subsurface for 67T. (The grains discussed in Figure 5.15, Figure 5.16, Figure 5.17 and Figure 5.18 are marked by arrows)

In fine grains, the increase of GND mainly leads to two phenomena: (1) large deformation of neighbouring grains and (2) squeezing-out effect (i.e., the grain is squeezed out of the free surface). The first phenomenon usually occurs when a large grain (e.g., Grain M) is near a fine grain (e.g., Grain J) as shown Figure 5.21(a). Compared with a large grain, the GND density was higher in a fine grain according to Ashby’s model [240], and GNDs usually concentrate on the grain boundaries when suffering the shear stress [241]. Therefore, once a small grain is adjacent to a large grain, higher GND density is stored in the fine grain, leading to non-homogeneous deformation in two adjacent grains and consequently dramatic deformation at the grain boundary. In this case, the high GND densities in fine grains provide high deformation resistance, which allows them to retain their original shape. But the GND density in fine grains can trigger the grain boundary to deform. Subsequently, significant deformation of neighbouring grain. The small grains do not undergo large plastic deformation due to high deformation resistance, but they are shifted with large inclined grain boundaries. This is indeed seen in Figure 5.21(b) that GB 5 is inclined 15.2° and curved 23.2° while GB 7 is inclined 11° and dramatically curved 34°, leading to localized large deformation.

The second phenomenon can be seen in the fine-grain zones (Figure 5.18(b)), in which the grain size in 67T is smaller than the other three workpieces, resulting in higher GND densities in fine grains as shown in Figure 5.22(d). These grains with high GND densities are then partly or totally squeezed out of the free surface, resulting in the wrinkling on the observing surface Figure 5.18(e).

The deformation in a large machined grain can gradually change along the cutting direction as shown in Figure 5.16(f) (Grain B′) that slip bands evolve from i to iv. The slip bands evolution indicates that non-homogeneous deformation occurs in a grain along the cutting direction. Sansal et al. [242] found that the dislocation is not constant within a grain but increases as the distance to the grain boundary decreases. This is also observed in Grain B′ from Figure 5.22(b) where the GND increases near the grain boundary and decreased at the centre of the grain. The dislocation density from a point to the grain boundary can be calculated by [243]:

$$\dot{\rho}^s = \frac{1}{b}(\max\left(\frac{1}{l^s},\frac{K_S}{d_g}\right) - 2y_c\rho^s)\left|\dot{\gamma}^S\right| \tag{5-1}$$

Where the K_S is a dimensionless constant that controls the storage of dislocations on the grain boundary and l^s is the dislocation mean free path along the system s. The d_g is the distance to the closest GB along the slip system and y_c is the effective annihilation distance between dislocations.

In this case, the slip band evolution within the grain was caused by increment dislocation density distribution from the centre to the grain boundary (e.g., Grain A′ in Figure 5.22(a) and Grain B′ in Figure 5.22(b)), resulting in slight deformation at the centre of the grain and dramatic deformation near the grain boundary. However, dramatic deformation also occurs within large grains as Grain A′ and Grain C′ (Figure 5.22(b)). The deformation in Grain A′ was caused by an embedded grain near the machined surface, leading to higher GND density in Grain A′ (Figure 5.22(b)). For Grain C′ in Figure 5.22(b), significant non-homogenous deformation occurred within a large grain, resulting in wrinkling in the grain. This may be caused by some perturbation during orthogonal cutting, such as material pile-up in front of the cutting tool [153]. When the machining tool cuts through the elongated grains as Grain L in Figure 5.21(a), its small grain width provides higher deformation resistance like fine grains, but their deformation depth is deeper due to the lack of grain boundaries to restrict the deformation passing downwards.

Different from the machined grain, the machine-affected grain is not cut through directly but their deformation is triggered by machined grains. As mentioned previously, the deformation gradient is decreased from the machined surface to the subsurface. And grain boundaries between machined grains and machine-affected grains hinder the deformation transmitting below. Therefore, various grain shapes result in different deformation depths (e.g., shallow deformation depth of Grain K and deep deformation depth of Grain L Figure 5.21(a)) and subsequently the deformation of machine-affected grain is triggered in different ways. For example, the deformation of a machine-affected grain (Grain K) can be triggered by machined grains from both top (Grain J) and right (Grain L) as in Figure 5.21(a), or, like Grain N, only affected by a grain above (Grain M). The deformation caused by neighboring grains is similar to "plastic buckling" reported by Udupa et al. [244]. This is the main reason those different deformation responses are observed in machine-affected grains, such as bulge (Figure 5.16(f)), depression (Figure 5.16(g)).

The plastic deformation of grain is dependent on the shear stress applied to the slip system. A slip system is activated when the stress is larger than critical resolved shear stress (CRSS) on the slip system. According to Taylor-model [245], the CRSS can be calculated by [246]:

$$\tau_c^a = \mu b \sqrt{\sum_{\beta} a^{\alpha\beta} \rho^{\beta}} \qquad \text{5-2}$$

Here, μ and b represent the shear modulus and the Burger vector respectively, and ρ^{β} stands for the dislocation density in the slip system. The dimensionless coefficients $a^{\alpha\beta}$ of the dislocation interaction matrix represent the average strength of interactions between dislocations in pairs of slip systems. The machined grains were closest to the machined surface, suffering in a higher shear stress than CRSS and generating intensive slip bands. The slip bands are also dependent on crystallographic orientations whereby the slip band is easier to be generated when the shear force direction is parallel to the slip trace based on the minimum work principle of the Taylor model. For example, since the most active slip trace in <011>//BD grains of 01T (Figure 5.15(d)) is nearly parallel to the shear force, this generates more intensive slip bands than <011>⊥BD grains in 02T (Figure 5.16(d)) and <001>//BD grains in 90T (Figure 5.17(e)). This phenomenon was reported in equal-channel angular pressing when the macro shear plane was parallel to $\{111\}\langle 11\bar{2}\rangle$, the dense shear band is observed [247]. But it is rarely reported in orthogonal cutting. Moreover, multi slip bands of different directions are found within a grain, shown as Grain C′ in Figure 5.17(e) and Grain C′ in Figure 5.18(e), indicating that grains are affected by both forces from cutting tool and neighboring grains. The complex force triggers different slip systems in a grain. As mentioned before, the slip band can transmit through GB 17 (MA: 22°) in Figure 5.21(c) (refer to Figure 5.21(e)) without direction change. This suggests that slip bands possibly have high compatibility to transmit at low misorientation angle grain boundaries. The same phenomenon was also reported in tensile tests [157]. However, at the grain boundaries with large misorientation angles, for example, GB 21 and 22 in Figure 5.21(d) (refer to Figure 5.18(d)), the slip bands do not transmit across the grain boundary. The initial slip bands are hindered by the grain boundaries and other slip bands would be activated in the subsequent grain.

The different grain responses in Figure 5.21(b)-(d) reveal the relationship between textured deformation and individual grain deformation. Most grains of the textured sample have similar grain morphologies, grain orientations and misorientation angles (MAs) between grains, resulting in similar slip systems being activated during orthogonal cutting and generating texture-based deformation. At the same time, some grains exhibit different deformation resistance due to various grain morphologies and orientations (e.g., fine grain zone in 01T (Figure 5.15(a)) and various directional grains in 02T (Figure 5.16(a))), resulting in localised non-homogeneous deformation. But the non-uniformity of localised deformation only occurs in a small region compared with the textured deformation, therefore, the deformation in the textured Alloy 718 fabricated by LPBF has textured consistency and localised grain response.

5.4.3 Full-field crystal plasticity simulations

In order to understand the complex deformation mechanism of the grains with different morphologies and orientations under machining conditions, full-field crystal plasticity simulation have been carried out with a well-established open source software [214].

The key aspect of this simulation is that it incorporates the grain orientation obtained from EBSD data prior to cutting and applies the corresponding loading resulting from the cutting operation. In order to avoid the complexity associated with modelling the cutting process to extract the shear-based loading, we calculated the loading condition with an analytical model (Eq. 3-13) by considering cutting tool geometry and cutting depth and applying it to the region above the machined surface. Although the material removal process (e.g., chip formation) is not captured in this simulation, this limitation should not impact the analysis of machined surface deformation. Retaining the EBSD data before cutting allows for accurate loading application to the original grains and validation with SEM images.

Figure 5.23 and Figure 5.24 shows different intensities of stress and strain as well as corresponding deformation patterns in four cutting cases characterised by different grain morphologies and the two colour bars below represent Von Mises stress and equivalent strain values for four simulation cases. The stress values obtained in our study are in line with those reported works regarding the simulation of orthogonal cutting for Alloy 718 [248]. The simulated results are compared with the corresponding deformation pattern from SEM to investigate the mechanism of deformation based on stress and strain at the grain level. To optimise computation efficiency, a 400 × 90 μm^2 area was selected as the simulation region, because the deepest deformation zone in the experiment did not exceed 82 μm.

The simulation results indicate that local cutting-based plastic deformation depends on grain morphology and orientation as well as adjacent grains. In 01T samples (Figure 5.23(a)), stress concentration is more likely to occur in <011>//BD columnar grains during cutting process, resulting in intensive slip bands observed at corresponding grains in Figure 5.23(c). However, the fine grain zone may interrupt such deformation pattern since grain boundary significantly hinders stress transfer from the machined surface to bulk and varies stress status to the next grain along the cutting direction. The stress concentration near the grain boundary leads to bulging instead of intensive slip bands crossing the grain boundary. The non-homogeneous deformation is found at each border of building directional blocks, causing similar deformation structure in Figure 5.23(c). Considering the predominant presence of columnar grains oriented along the <011>//BD direction in 01T, it is expected that these grains exhibit a notably similar slipping pattern as the calculated results in Figure 5.20(a) (high intensity of slip trace direction distribution). These phenomena match well with the stress status in Figure 5.23(a). The highest equivalent strain is observed in 01T (Figure 5.23(e)) compared with the other three cases, reaching about 0.8. The strain distribution is similar in each columnar grain but varies within the neighbouring narrow elongated grains. Such strain incompatibility caused by these two typical grains (i.e., columnar grain and narrow elongated grain) leads to localised inhomogeneous deformation as seen in Figure 5.23(c).

In 02T, the stress concentration is not significant as in 01T during the same cutting process. This is because grains in this case are dominated by <011>⊥BD orientations and the most active slip trace is nearly perpendicular to the shear direction (Figure 5.19(e) and (f)), leading to discrete slip bands and slight deformation as shown in Figure 5.23(d). It is also proved by the strain distribution shown in Figure 5.23(f), in which the strain value is lowest among these four cases.

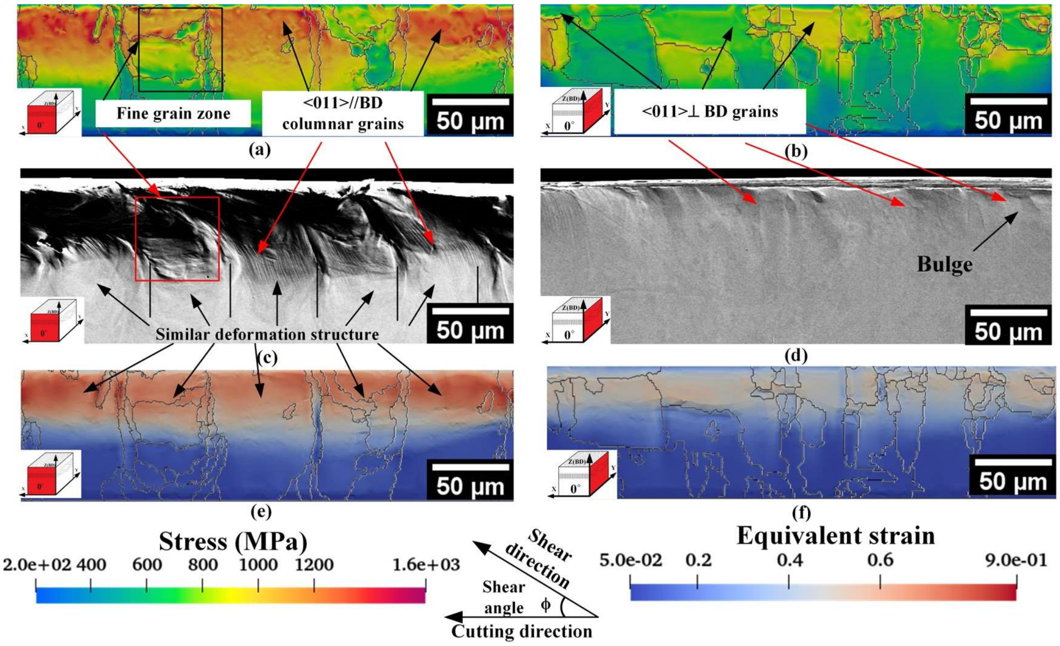

Figure 5.23: Different grain-level stress and strain caused by the same shear condition. Von Mises stress of four cases for (a) 01T and (b) 02T; equivalent strains for (e) 01T and (f) 02T. Deformation patterns: (c) Similar deformation structure in 01T; (d) slightly plastic deformation in 02T. (The two colour bars below represent the value of stress and strain respectively)

Figure 5.24(a) shows that the stress concentration is in elongated grains with <001>//BD orientation and the stress transfers to the bulk below. This leads to deeper deformation zones (red arrow in Figure 5.24(a)) when compared with the neighbouring grains. The strain distribution of this grain (Figure 5.24(e)) generally reduces from machined surface towards the bulk. Moreover, the strain transfer distance within this grain is deeper than in neighbouring grains, aligning with the deformation pattern in Figure 5.24(c). In Figure 5.24(a), stress concentration is not significant in the region where slip crosses the grain boundary. This implies that slip transfer across the boundary may occur in grains with similar orientation during orthogonal cutting, thereby reducing the stress concentration near the boundary. Therefore, a slight deformation is observed in the corresponding region in Figure 5.24(a), with no significant strain concentration occurring at the grain boundary between these two grains. The texture of 67T is characterized by weak texture and smaller grain size compared to the other three cases. As a result, the local stress distribution exhibits minimal variation grain by grain (Figure 5.23(f)) and the deformation is hard to be evaluated by a preferred slip plane. It is found that small grains impede the stress transfer to the bulk material and restrict the deformation to a narrow region in proximity to the machined surface, as shown in fine grain region that is highlighted by yellow dashed line in Figure 5.24(b). Similarly, the strain transfer is impeded by such grain boundaries as shown in Figure 5.24(f), exhibiting high strain gradient between grain boundaries. This is because the wide slip trace distribution (Figure 5.20(a) for 67T) and high grain boundary intensity varies stress transfer along the cutting axis.

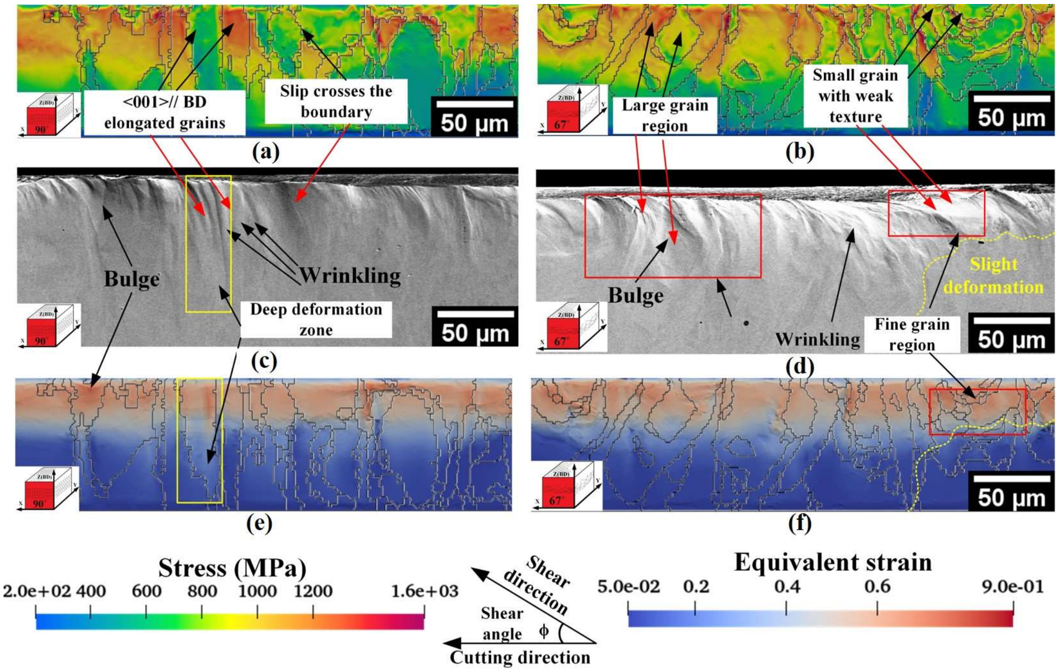

Figure 5.24: Different grain-level stress and strain caused by the same shear condition. Von Mises stress for (a) 90T and (b) 67T; equivalent strain for (e) 90T and (f) 67T. Different deformation patterns: (c) Narrow and deep deformation zone in 90T due to elongated grains and (d) significant wrinkling and bulge in 67T. (The two colour bars below represent the value of stress and strain respectively)

5.5 Discussion

5.5.1 Effect of grain morphology and texture

In the 0°-rotation scanning strategy, the laser scanning direction is not changed in adjacent layers. This provides a stable thermal pattern along BD and consequently results in two dominant cell growth patterns (elongated growth marked with yellow and 45° inclined growth marked with green) as shown in Figure 5.8(a). At the side of the melt pool, cells incline 45° to BD to grow and almost occupy all sides of the melt pools. Since FCC metals have three symmetrically equivalent <001> directions ([001], [010] and [100]), cells whose growth direction changes 90° still belong to the same grain. In this case, cells of which the growth direction changed about 90˚ (Figure 5.8(a) green arrows) should be the same grain although they were divided by the side of the melt pool boundary. The two dominant cell growth patterns finally form build-directional blocks as shown in Figure 5.15(a) and (b). In addition, the columnar-to-equiaxed transition (CET) is also observed in the blocks as shown in Zone 1 of Figure 5.15(a), due to the thermal profile perturbations caused by complex molten flow. It is noted that since few strengthening phases and Laves phase are found in as-printed Alloy 718 [92], their effects on the deformation are limited during the macro cutting process. Moreover, since the micro-segregation mainly exists in the cell structure (about 0.5 μm – 3 μm), it can be ignored at the grain scale. Therefore, the analysis of shear-based deformation in this work is mainly based on texture and grain morphology (size and shape).

Grains created by <011>//BD orientated cells occupy a large area in a block (e.g., Grain A in Figure 5.15(a)) and have lower deformation resistance than slender elongated grains (e.g., Grain B in Figure 5.15(a)) due to their large grain width along the cutting direction. The most active slip trace in these orientated grains is almost parallel to the shear direction as shown in Figure 5.19(a), resulting in significant deformation and intensive slip bands (Figure 5.15(d)). Furthermore, stress concentration is often observed within these columnar grains due to their typical orientation, and the absence of grain boundaries below allows for stress transfer deeply from the machined surface to the bulk material. In contrast, slender elongated grains at the border of blocks exhibit higher strength due to their short grain width along the cutting axis. The slip bands in columnar grain are hard to transfer to the narrow elongated grains. The combination of the above two grain shapes and their poor slip compatibility lead to a non-homogeneous deformation at the border of the block.

According to the Taylor-based shear model, the most active slip traces of <011>//BD texture are nearly parallel to the shear direction. In the case of 01T (Figure 5.20(a)), the slip traces are concentrated in a narrow range due to the strong texture intensity. This concentration therefore leads to dramatic deformation (Figure 5.23(c)) during orthogonal cutting. In contrast, for the 02T sample, the most active slip plane traces of <011>⊥BD texture (02T in Figure 5.20(a)) are perpendicular to the shear force direction. This results in less deformation and fewer slip bands after cutting, as seen in Figure 5.16(f) and (g). The grains, of which the most active slip traces are parallel to the shear direction, are easier to deform, exhibiting high strain value as shown in Figure 5.23(e). Whilst the grains with the most slip plane traces perpendicular to the shear direction show low strain distribution within grains (Figure 5.23(f)). This indicates that for the machining of components perpendicular to the building direction, the <011>⊥BD texture can reduce the bulk deformation as shown in Figure 5.23(d).

Considering texture formed by 0° rotation scanning strategy in the 3-dimensional space, <011>//BD and <011>⊥BD textures result from the same grains but the perpendicular observation direction (e.g., XZ plane or YZ plane in Figure 5.10(a)). The different stress status and plastic deformations in Figure 5.23(a)-(d) suggest that cutting direction oriented in different directions to the crystallographic texture may lead to different stress concentrations on the same surface. In this case, the cutting direction selection is important when the functional surface finish is required. However, the cubic <001>//BD texture formed by 90° rotation scanning strategy (Figure 5.10(b)) is not sensitive to the machining direction change due to its symmetrical characteristic along X or Y axis.

Although it is reported, in polycrystalline alloys, the plastic anisotropy at the grain scale differs the stress of grain from macro scale [249], in our work, the grains in 01T exhibits similar deformation structure (Figure 5.23(c)) and slip bands after cutting, which matches well with calculated most active slip trace based on the macro strain Taylor model. This indicates that the grain deformation of high-intensity textured alloys still follows the macro shear strain model. It is also verified by the simulated stress status in 01T, where the stress mainly concentrates in <011>//BD columnar grains. This is because grains in a high-intensity textured workpiece have a dominant grain orientation. Such oriented grains are more likely to generate many similar slip system combinations in terms of the Taylor model (01T in Figure 5.20(e)), resulting in a predictable deformation pattern as seen in Figure 5.23(c). When the texture intensity decreases, the slip system arrangement always changes grain by grain, resulting in a wide slip trace distribution (67T in Figure 5.20(a)) and high anisotropy between grains [250]. Therefore, the stress is more likely to concentrate near the grain boundaries as shown in Figure 5.24(b) and heterogeneous deformation between neighbouring grains is significant as seen in Figure 5.24(d).

Since most grains are formed by one or two dominant grain growth patterns in each scanning strategy (Figure 5.8) and the analysis region has a similar texture as the counterpart bulk in each case (verified by Figure 5.12(a)), the selected grains and textures are statistically meaningful to compare different texture-based deformations in this work.

5.5.2 Grain deformation map

Figure 5.25 summarises the grain deformation map for the textured Alloy 718 in the orthogonal cutting. The cutting tool motion direction and corresponding flank angle, rake angle and shear angle are included. Different from the conventional nickel-based alloy [251], in which the grain is generally recognised as equiaxed (the average aspect is close to 1.0), grain morphology formed by LPBF may change dramatically in tens of microns due to the epitaxial growth perpendicular to the melt pool boundary (Figure 5.8). The aspect ratios of grains range from 1.0 to larger than 3.0 [252]. In this case, the retained original grain morphology is the key to understanding the plastic deformation in textured Alloy 718 fabricated by LPBF at the grain scale. The grain shape in the map is represented by the equivalently normalised ellipse.

Grain distribution in the polar coordinate deformation map is decided by grain width (in cutting axis A_i (Figure 5.25)) and the angle of the most active slip trace. The scattered ellipses represent individual grains along the machining surface, and the quantified slip trace directions for four textured samples from Figure 5.20(a) are summarised in Figure 5.25 (e.g., red area for 01T, black area for 02T, green area for 90T and blue area for 67T). It is found that scattered ellipses of different textured samples are mostly overlapped with the corresponding slip trace direction window calculated from Figure 5.20(a) (i.e., the scattered red ellipses were nearly overlapped with the red shaded area). This indicates that the large-scale (hundreds of microns along the cutting direction) deformation tracing is representative of revealing the textured crystallographic deformation in LPBF-fabricated alloys.

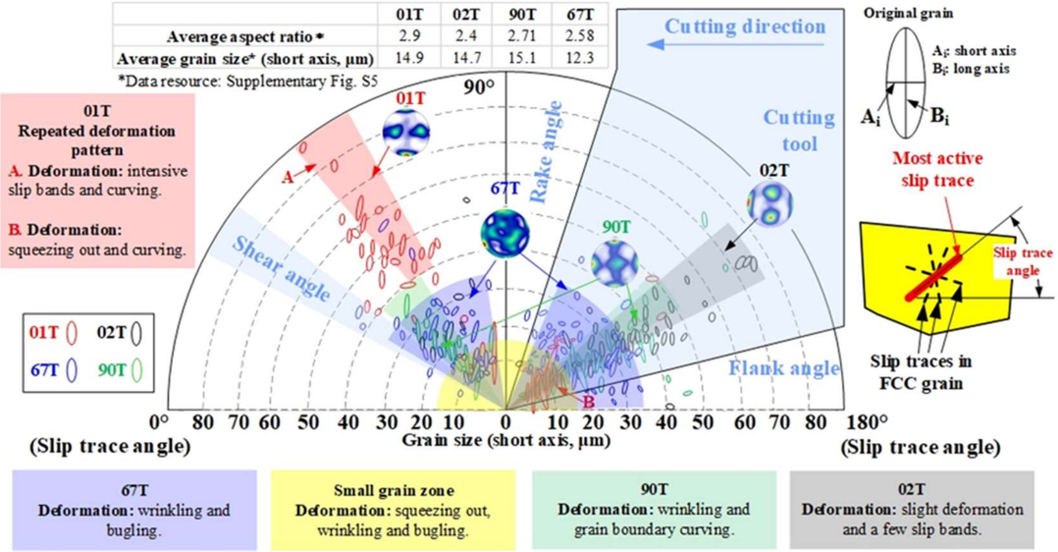

	01T	02T	90T	67T
Average aspect ratio*	2.9	2.4	2.71	2.58
Average grain size* (short axis, μm)	14.9	14.7	15.1	12.3

*Data resource: Supplementary Fig. S5

Figure 5.25: Grain deformation map for textured Alloy 718 in the orthogonal cutting. Grains from 01T, 02T, 67T and 90T are represented by red, black, blue and green ellipses respectively.

The stress status simulation results in four samples (Figure 5.23(a), (b) and Figure 5.24 (a), (b)) indicate that grains with high aspect ratio are more likely to transfer stress from machined surface to the bulk. It will lead to deeper deformation zones induced by machining, which is also proved by in strain distribution in Figure 5.23(e), (f) and Figure 5.24 (e), (f). This indicates that the deformation of grain formed via LPBF may exhibit greater sensitivity to the cutting depth compared to traditional equiaxed grains, due to their high aspect ratio. When such elongated grains are cut at different depths, the deformed depth may vary, subsequently impacting the deformation of neighbouring grains. The von Mises stress distribution is depended on grain morphologies and orientations as well as grains surrounded. However, samples with high texture intensity (e.g., those fabricated using 0° and 90° rotation strategies) are dominated by grains with typical orientations, leading to a corresponding dominance in stress distribution. High texture intensity allows grains to maintain a similar deformation pattern during orthogonal cutting, as illustrated in Figure 5.23(c), (d). And the slip bands are more likely to cross the grain boundary when the neighbouring grain has similar orientation as shown in Figure 5.17(e). In the weak texture fabricated by the 67° rotation scanning strategy, the number of grains with similar orientations decreases, resulting in a variation of stress distribution from grain to grain. Consequently, slip transfer becomes more difficult to occur and the deformation pattern tends to vary locally due to variations in grain morphology and orientation. This can be observed in the large and fine grain regions in Figure 5.24(c).

It should be noticed that the grain deformation is decided by the orthogonal cutting process, the shear angle and strain rate are dependent on the cutting parameters (e.g., tool rake angle and cutting speed). Corresponding to Figure 5.25, the distribution of the most active slip system will change with shear-angle but the grain morphology is independent of the cutting parameters in the same cutting direction. This map enables the prediction of grain deformation for textured alloys fabricated by LPBF via grain morphologies (size and shape) and orientations in the orthogonal cutting process.

When the grain size is relatively small (e.g., <15μm), as shown in the yellow highlighted region in Figure 5.25, the grain deformation is not strongly affected by the most active trace direction because grains at this scale exhibit high deformation resistance according to the Hall-Petch effect [253]. This is because the strain gradient from the machined surface to the bulk is significant, and the grain deformation is dominated by the width near the machined surface. On the other hand, the GND density was high in this small grain region according to Ashby's model [240]. Therefore, grains in this region are likely to be squeezed out of the free surface during plastic deformation due to plastic anisotropy. And these phenomena are indeed seen in small grain zones of all samples, such as Zone 1 in Figure 5.15(d) and fine grains in Figure 5.16(f), (g) and Figure 5.18(c). The grain deformation map indicates that the activated slip trace directions of the 67°-rotation scanning strategy (67T) are distributed in the range of 31° to 180° and the grain size (in cutting axis A_i) is smaller than in the other three cases (average grain size is 12.1 μm). It is highly overlapped with the yellow highlighted zone (small grain zone), where wrinkling and budge are significant as seen in Figure 5.24(c).

In the 01T sample (XZ plane of 0° rotation scanning strategy), severe plastic deformation occurs in Zone A. However, grains in Zone B have high deformation resistance, resulting in a significant squeezing-out effect and grain boundary curving. The combination of columnar grains and slender elongated grains fabricated by LPBF leads to similar deformation patterns. Such textured deformation only can be found by tracing the grain deformation along the cutting direction at a large scale (e.g., hundreds of microns).

The grain size and aspect ratio for the 02T sample (YZ plane of 0° rotation scanning strategy) are smaller than 01T and the slip trace direction is nearly perpendicular to the shear angle. Therefore, the grains exhibit higher deformation resistance than 01T and slight grain boundary curving and few slipping are observed in this sample, as shown previously in Figure 5.23(d). Grains in 90T (formed by 90° rotation scanning strategy) have a similar average grain size and aspect ratio as 01T, but the grain size mainly distributes within 40 μm. Therefore, the grains in 90T do not exhibit intensive slip bands as 01T but the deformation depth is larger when the high aspect ratio grains are deformed. This is indeed seen in Figure 5.24(c).

This deformation map statistically summarised texture-based plastic deformation in the orthogonal cutting process by considering the original grain morphology and orientation. From this quasi-in-situ EBSD investigation, the cutting tool geometry and grain orientation are linked together in Figure 5.25. However, extracting the deformation pattern from this statistically based map for an individual grain with specific size and orientation is unreliable, due to the intricate nature of grain geometry and complexity of deformation in neighbouring grains. The future machining-induced deformation theoretical model at grain scale may have to consider a deformation field that includes tens of grains with specific structures (e.g., morphologies and orientations) in front of the cutting edge to predict the possible plastic deformation.

The full-field crystal plasticity simulation results are meaningful for understanding the variations in stress status resulting from different grain structures (morphology and orientation) when an orthogonal-cutting-based loading is applied to the textured Alloy 718. However, it has to be acknowledged that the actual machining process is more intricate and multifaceted than this loading condition. Therefore, the stress status evolution in the dynamic cutting process and the influence of chip formation are needed further investigation. The method used in this work, including obtaining EBSD data before cutting, full-field crystal plasticity simulation and capturing deformation patterns after cutting without polishing, can be applied to investigate machining-induced deformation in other metal materials. However, considering the limitation of the EBSD detection area and sample preparation process, this method may not be suitable for large-area deformation tracing. Since this work is based on three commonly used scanning strategies, the deformation pattern and map are helpful for additive manufacturers to adopt favourable building directions that will enable easier post-processing (e.g. cutting operations). This work emphasises the importance of characterising the original microstructure (such as grain morphology and orientations) before cutting in the investigation of machining-induced deformation. This enables precise modelling of simulation based on EBSD data and direct validation via preserved plastic deformation patterns on the pre-polished surface. The grain obtained by AM cannot be easily estimated by average grain size. The grain shape should be considered, especially the grain width along the cutting direction. This is different from traditionally equiaxed grains.

5.6 Summary

This study presents a quasi-in-situ investigation of the grain deformation of LPBF-fabricated alloy before and after shear-based deformation via EBSD and SEM. Three scanning strategies, namely 0°, 90° and 67° rotation, were employed to fabricate the unique crystallographic textured LPBF structures (e.g. Alloy 718). It is the first time that shear-based textured deformation can be traced grain by grain along the cutting direction for hundreds of microns before and after cutting. The grain response to the shear deformation in different crystallographic textured LPBF-fabricated samples was quantified in the deformation map. A crystal plasticity model was used to simulate the grain deformation caused by the orthogonal cutting.

The results showed that significant plastic deformation was observed in <011>//BD texture whilst slight deformation was in <011>//BD texture. Moreover, the repeated deformation pattern was observed in the columnar grains formed by the 0° rotation scanning strategy. This was because stress concentration was likely to occur in the columnar grains with high texture intensity, leading to significant slipping within columnar grains. Moreover, the plastic deformation in weak texture region varies locally due to the lack of repeated microstructure (i.e., columnar grains) along the cutting direction that could lead to a dominant stress distribution. The statistical deformation tendency map exhibited the effect of textures and grain shapes as well as shear angle on the machining-induced deformation. In addition, since the unique grain growth pattern in the LPBF process fabricated grains with a high aspect ratio, the deformation of the LPBF-fabricated grain is strongly dependent on its grain width along the cutting direction.

From a generic point of view, this work provides a route to evaluate how grain shapes with high aspect ratios existent in crystallographically textured structures affect their deformation levels in machining. This is of relevance to many shear removal processes that routinely are employed after the LPBF process. In addition, this work raises awareness of the importance of capturing the microstructure details (e.g. crystallographic orientation) at the grain level before and after cutting so that the influence of cutting on the deformation of single/multiple grains can be understood; this will also provide key information for detailed modelling of cutting when considering microstructure at grain level.

Chapter 6 Chip formation mechanism of LPBF-fabricated Alloy 718 during post-machining process

It is proved that the unique grain structure and texture formed by LPBF strongly influence the deformation behaviour of the machined surface during the orthogonal cutting. Therefore, it is crucial to understand the details of grain deformation during chip formation, which significantly affects the surface quality during machining. Therefore, this chapter includes the investigation of chip formation mechanisms of three typical textured Alloy 718 formed by LPBF (Section 5.1), along with a reference case of wrought Alloy 718. A customised sample (Section 3.4.2) and the quick-stop module (Section 3.4.1) were used for the cutting test, aiming to retain the chip on the workpiece after cutting. This allows an investigation of machining-induced deformation near the primary shear zone.

6.1 Microstructure of wrought and LPBF-fabricated Alloy 718

Figure 6.1 illustrates the inverse pole figure (IPF) mappings and pole figures (PF) for wrought and LPBF-fabricated Alloy 718, corresponding to WR, 01T, 90T and 67T in Figure 6.1. The sample coordinate systems in IPFs (Figure 6.1 (a)-(d)) are the same as the PFs (Figure 6.1 (e)-(h)) and the XZ plane is used for texture characterisation. From Figure 6.1(a) and (e) it can be observed that the wrought Alloy 718 exhibits weak texture ([011] <111>) with equiaxed grains. The strong rotated Cube texture ([100] <110>) is formed by the 0° rotation strategy in LPBF (Figure 6.1 (b) and (f)). The Cube texture ([001] <001>) is created by 90° rotation strategy (Figure 6.1 (c) and (g)) while weak texture with many elongated grains are formed with 67° rotation strategy as shown in Figure 6.1(d) and (h), in line with the previous work [254].

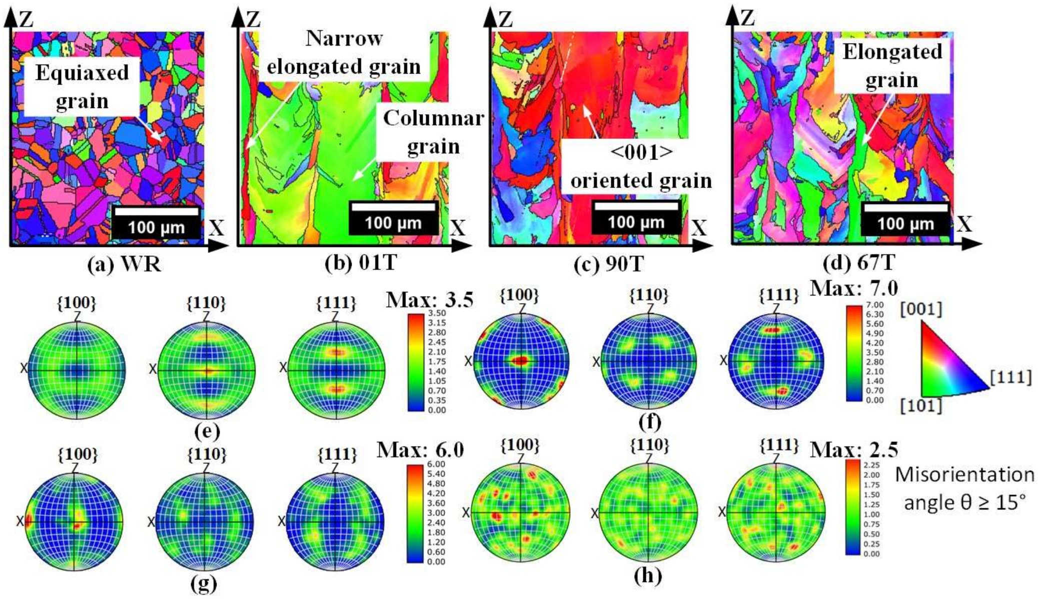

Figure 6.1: Grain structure and texture of wrought and LPBF-fabricated Alloy 718. (a) and

(e) are inverse pole figure (IPF) mapping and pole figure for wrought Alloy 718 (WR), (b) and (f) are inverse pole figure (IPF) mapping and pole figure for 01T, (c) and (g) are inverse pole figure (IPF) mapping and pole figure for 90T, (d) and (h) are inverse pole figure (IPF) mapping and pole figure for 67T.

The grain size distributions are also calculated from areas of 700 µm × 500 µm in all four cases (Figure 6.2). The area-weighted method was used to approximate the grain size distribution. The average grain size of wrought Alloy 718 is 10.5±3.4 µm, with the majority of grains distributing close to 7 µm as shown in Figure 6.2(a).

The grain size obtained from 01T is widely distributed from 10 to 200 µm because there are two dominated grain growth patterns in this scanning strategy: namely large columnar and narrow elongated grains (Figure 6.1(b)), which is similar to the previous reported microstructure [132,195].

The 90° rotation scanning strategy leads to smaller grains in Figure 6.2(c) when compared with 01T, which was due to that the 90° rotation strategy restricted the grain growth. However, since grains are more likely to grow along the BD with preferred <001> direction, grains with Cube texture (<001>) can be observed in the XZ plane (Figure 6.1(c)).

In 67T (Figure 6.2(d)), the average grain size is smaller than that in 01T and 90T due to the randomised grain growth directions induced by 67° rotation scanning strategy. This randomised grain growth pattern leads to a low texture intensity, as evidenced in Figure 6.1(h). Although the 67T and WR exhibit weak texture intensities, the unique grain growth manner in 67T causes elongated grains which are different from the grain shape in WR.

It is seen that the average grain size in Figure 6.2(b) and (c) is larger than that in

Figure 6.2(a) and (d). Since 01T and 90T exhibit much stronger texture intensity (Figure 6.1(f) and (h)), the stable grain growth condition result in larger average grain size. This is evidenced by Figure 6.2(b) of 01T sample that exhibits an average grain size of 121.3±24.3 µm, with a texture intensity of 7 from Figure 6.1(f), showing a good consistency with the previously reported studies on LPBF-produced alloys [128,255]. The grain size distributions (i.e., from equiaxed Figure 6.2(a) to columnar grain Figure 6.2(b)) can significantly change the grain boundary distribution (Figure 6.1 (a) and (b)), which may potentially cause different chip formation mechanisms in the wrought and LPBF-fabricated Alloy 718.

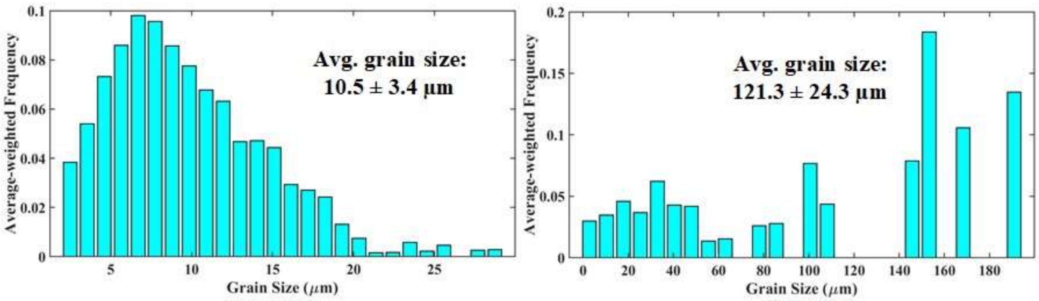

(a) WR (b) 01T

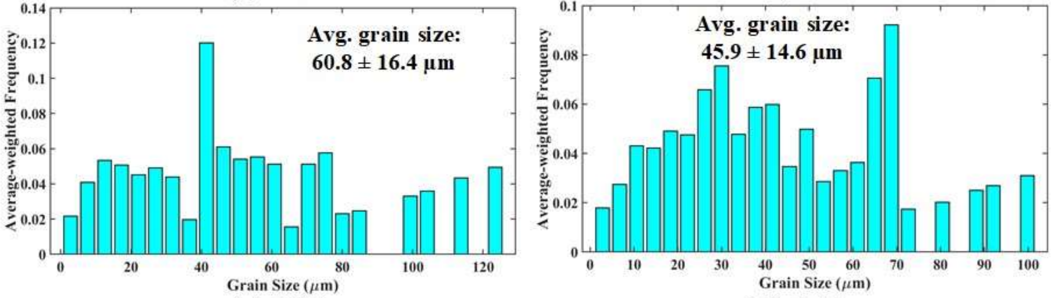

(c) 90T (d) 67T

Figure 6.2: Grain size distribution, average grain size and standard deviation for wrought and LPBF-fabricated Alloy 718. (a) WR, (b) 01T, (c) 90T and (d) 67T.

6.2 Chip formation characteristics

6.2.1 Stability and reliability validation for quick-stop cutting test

To evaluate the stability and reliability of the quick stop cutting, the cutting speed evolution from chip formation to the fracture of the weak joint was compared in Figure 6.3. The software Motion Studio was employed for the cutting speed tracking and the tracking position was on the U-shape adapter (highlighted by red arrows) to reduce the error of tracking. It was observed that the speed evolution during quick-stop cutting primarily included four stages (from A to D): chip formation (A), collision of stop pin (B), fracture of weak joint (C) and end of cutting (D).

It was measured that the cutting speeds among these four cases decreased from 106±2 m/min to 100±4 m/min during the chip formation (stage A). The decrease in cutting speed is nearly consistent with limited fluctuation in these four cases, which suggests that the chip formation process is relatively stable. Therefore, similar energy consumption during the chip formation can be assumed in these four cases. It is noted that the tracking speed is slightly smaller than the cutting speed because the tracking position is slightly away from the machined surface, leading to a small difference in linear velocity during pendulum motion. However, a significant speed decrease was observed when the stop pin collided with the stopper (stage B), reaching about 90 m/min within 1/1500 s. A speed fluctuation was observed (stage C) at the moment of the weak joint fracture. This perturbation is likely attributed to the tracking error due to the vibration of workpieces. This vibration of the workpiece is caused by collision (stage B) and fracture (stage C) along the cutting direction. The cutting speed was suddenly decreased during the collision and then tended to be stable after the fracture (stage D). This peak speed makes it easier to find the key frame of the fracture in the video. At the end of the cutting process (stage D), the lower part of the workpiece fell off, and the remaining part moved forward at a relatively stable speed. During the fracture of the weak joint, the cutting speed decreased by about 3 m/min in these four cases when compared with the cutting speed before the collision. Thus, the energy consumption for the fracture of the weak points in these four cases could also be considered similar.

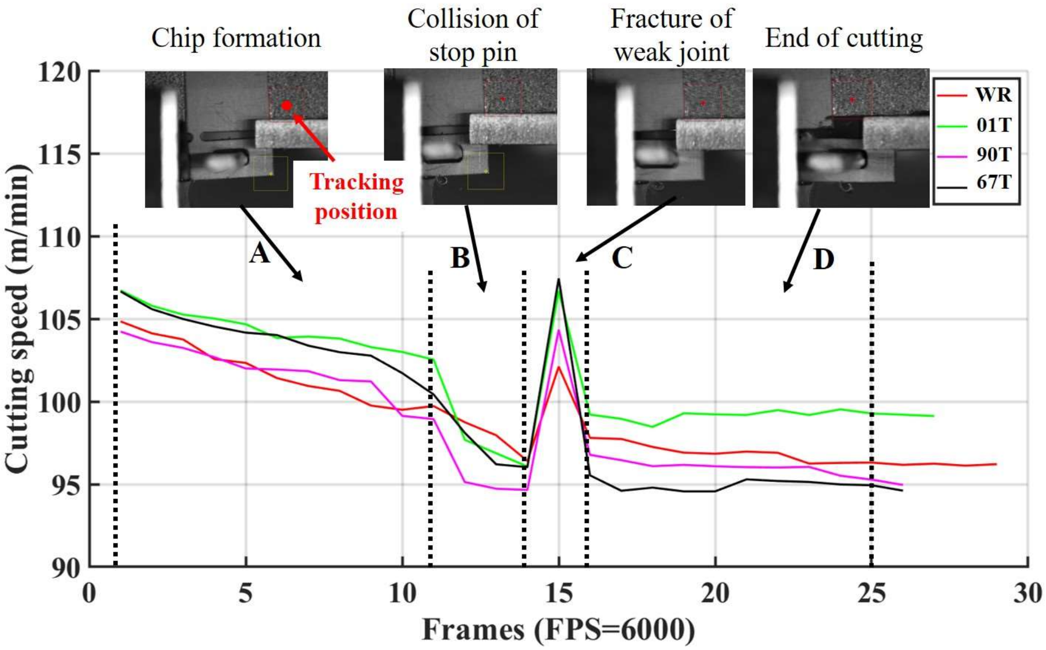

Figure 6.3: Cutting speed evolution from chip formation to fracture of weak joint. Speed evolutions of WR, 01T 90T and 67T are represented by red, green, purple and black lines, respectively. Stage A: chip formation; Stage B: the collision of the stop pin with the stopper; Stage C: Speed fluctuation due to the fracture of weak joint; Stage D: stable speed after the end of the cutting.

6.2.2 Wrought Alloy 718

The deformation in chip formation for wrought Alloy 718 is shown in Figure 6.4 and the grey areas are obtained by mixed signal of secondary electron (SE) and forescatter diodes (FSD), exhibiting the shear bands and the area that is not well indexed due to the significant plastic deformation. The IPF mapping (Figure 6.4(a)) is divided into three zones, namely Zone 1, Zone 2 and Zone 3, representing microstructure in original workpiece, shear region and chip respectively. The PFs for these three zones were statistically counted with a similar area in each zone (about 14700 μm^2). The shear plane (SP) and shear plane normal (SPN) are highlighted by red lines in the PF of Zone 3 in Figure 6.4(b). Since the deformation in the cutting process is mainly caused by shearing and the slip predominantly occurs on {111} planes for Alloy 718 (FCC alloy), the {111} pole figure (Figure 6.4(b)) is used to analyse the texture evolution [256].

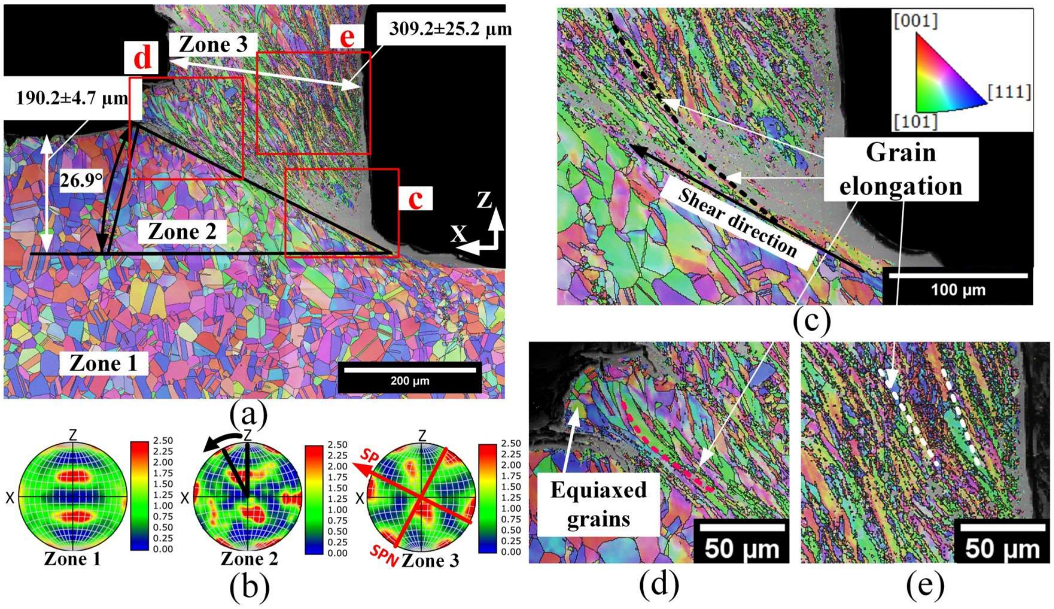

Figure 6.4: Texture evolution in chip formation for wrought Alloy 718. (a) IPF mappings for both chip and workpiece with measured uncut thickness, chip thickness and shear angle. {111} PFs in (b) are obtained from Zones 1, 2 and 3 respectively. (c), (d) and (e) are zoom-

in regions from shear zone and chip. SP and SPN are the shear plane and shear plane normal, respectively. (The grey areas are not well indexed by EBSD detector due to significant plastic deformation)

The PF in Zone 1 (Figure 6.4(b)) represents the texture of the workpiece, similar to the {111}-PF in Figure 6.1(e). In Zone 2, it is observed that the material in front of the cutting edge undergoes deformation nearly along the shear plane in the orthogonal cutting process. Grains near the primary shear zone are elongated along the shear plane as marked by dashed lines in Figure 6.4(c). Grains below the primary shear zone keep their original orientations but are slightly rotated to the shear direction. This is evidenced by the distorted grains in Zone 2 and the rotated {111} planes and <110> directions are highlighted by the arrow in the PF of Zone 2 (Figure 6.4(b)). As the cutting edge moves along the cutting direction, grains within the shear zone (Zone 2) are transferred to the chip with a similar texture in Zone 3 (Figure 6.4(b)) but the grain shape is narrower and elongated (Figure 6.4(c)). This indicates that the chip formation process for wrought 718 inherits the preferred shear texture formed in the primary shear zone.

When grains are far from the cutting edge and close to the free surface, the grains become less deformed and their elongation direction has a slight inclination as highlighted by dashed lines (Figure 6.4(d)). This is because the stress condition has changed, especially when the shear stress decreases from the cutting edge to the free surface [257]. As a result, some equiaxed grains near the free surface are less deformed and tend to keep their original shape rather than elongating (Figure 6.4 (d)). Moreover, some adjacent grains are inclined compared to the original shear direction (Figure 6.4 (d)). The serrated chip morphology is observed near the free surface, where a few grains are elongated and equiaxed grains are retained in this region (Figure 6.4(d)). For the region near the rake surface (Figure 6.4(e)), since the deformation is mainly caused by friction between the chip and the rake face of the cutting tool, the grain boundary inclined a large angle (Figure 6.4(e)) when compared with primary shear zone (Figure 6.4(c)). A chip with a thickness of 309.2±25.2 µm is formed during the material pile up and the chip ratio is about 1.6 with the uncut thickness of 190.2±4.7 µm. The chip formation process in the WR (equiaxed grains) exhibits deformation nearly along the shear plane and significant grain distortion is observed near the shear plane. This subsequently leads to a large chip thickness and chip ratio.

6.2.3 LPBF-Fabricated Alloy 718 with 0° rotation

Figure 6.5 shows the chip formation for strong [011] <001> texture with large columnar grains in 01T. The original texture is marked by the black dashed line in the PF of Zone 1 (Figure 6.5(b)). Since this crystallographic texture is dominated by the columnar grains along the z-axis (Figure 6.1(b)), the original grain structure could be used as reference to evaluate grain boundary bending during chip formation. Unlike Zone 2 in WR (Figure 6.5(a)), the shear plane cannot be clearly identified (Figure 6.5(a)) from the cutting edge to the free surface. This is because the grain boundaries along the z-axis act as strong barriers for shear deformation, impeding the slip from the cutting edge to the free surface. Therefore, the significant shear bands are only observed near the cutting edge (Figure 6.5(c)) whilst the slip hindering leads to the rotation and inclination of columnar grain near the free surface. The PF of Zone 2 in Figure 6.5(b) further supports this view that a slight lattice rotation is observed (highlighted by white dashed lines), as compared to that in Zone 1. The slip hindering effect enlarges the shear angle to about 42°, larger than the shear angle in cutting the wrought workpiece (26.9°). Such a large angle obstructs the material pile-up along the shear plane, resulting in a chip thickness ratio of nearly 1.0 in 01T.

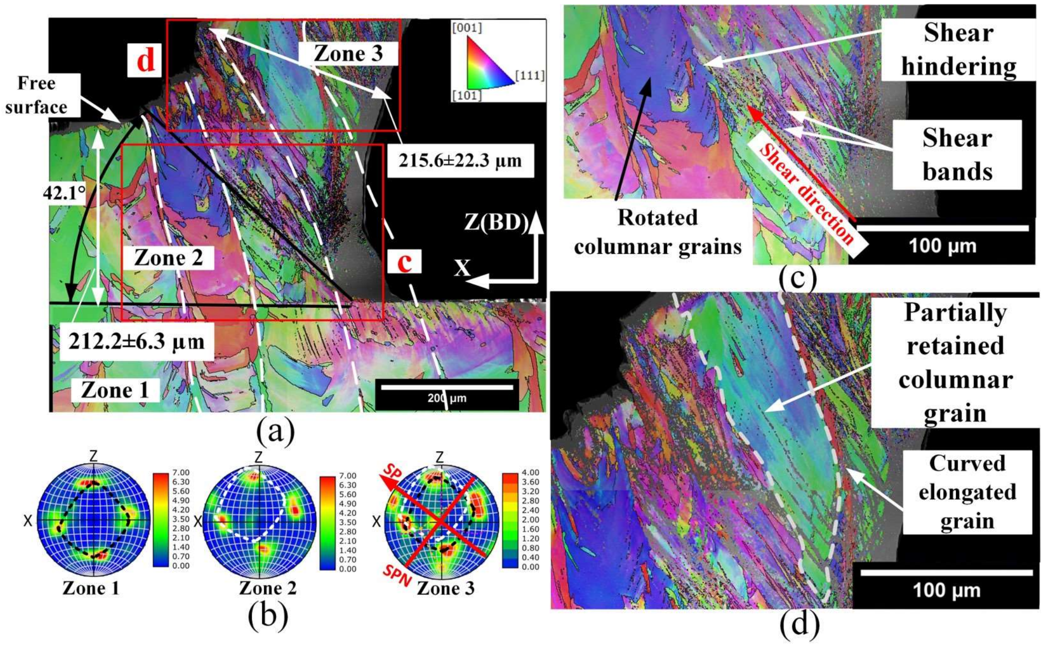

Figure 6.5: Texture evolution in chip formation for 01T. (a) IPF mappings for both chip and workpiece with measured uncut thickness, chip thickness and shear angle. {111} PFs in (b) are obtained from Zones 1, 2 and 3 respectively. (c) and (d) are zoom-in regions from the shear zone and chip. The typical texture is highlighted by dashed lines in {111} pole figure. SP and SPN in (b) are the shear plane and shear plane normal. (The grey areas are not well indexed by EBSD detector due to significant plastic deformation)

The columnar grains are highlighted by the white dashed lines to identify their deformation behaviour during the chip formation (Figure 6.5(a)). In Zone 3, a columnar grain (highlighted by white dashed line) is partially retained in the chip as shown in Figure 6.5(d). This suggests that part of this columnar grain, close to the free surface, has not undergone severe shear deformation. The slip closed to the cutting edge is hindered by the columnar grain (Figure 6.5(d)), which has a continuous grain boundary along the z-axis. Therefore, this grain is mainly deformed in the secondary shear zone, where significant grain boundary curving is observed (Figure 6.5(d)). Since limited shear deformation occurs in this grain, the material fails to pile up along the shear direction. This explains why the chip thickness ratio in this case is close to 1.0. It should be noted that not all columnar grains follow this chip formation pattern. This may be because some columnar grains also consist of small grains, which cannot completely hinder the shear slip across the grain boundaries. It is seen from the PF of Zone 3 (Figure 6.5(b)) that the texture in chip is weaker than in workpiece but the original texture pattern can also be identified. This indicates that the texture evolution is mainly caused by the lattice rotation in Zone 3 (white dashed lines in Figure 6.5(b)) whilst shear deformation occurs with a large shear angle due to the shear hindering of grain boundaries. The shear deformation in 01T (columnar and elongated grains) are easy to be hindered by long grain boundaries along the z-axis. This reduces chip ratio and is easier to retain large grains in the chip.

6.2.4 LPBF-Fabricated Alloy 718 with 90° rotation

The 90T workpiece is dominated by Cube texture ([001] <001>) with elongated grains along the z-axis as observed in Zone 1 (Figure 6.6(a)) and grain size is smaller than that in 01T. In the shear zone (Zone 2), significant shear bands are observed in front of the cutting edge (Figure 6.6(c)), indicating a significant shear deformation starting from this region. Due to most grain boundaries are parallel to the z-axis (Figure 6.6(a)), a shear hindering effect was also observed in 90T, where the shear bands were interrupted by the long grain boundaries (Figure 6.6(c)).

Moreover, there are some narrow elongated grains that the shear slipping is hard to cross along the shear direction as shown in Figure 6.6(c). Such discontinuous shear slipping near the primary shear zone prevents the chip formation from along the original shear plane. This leads to a large shear angle of about 35.9° and a low chip ratio (about 1.5).

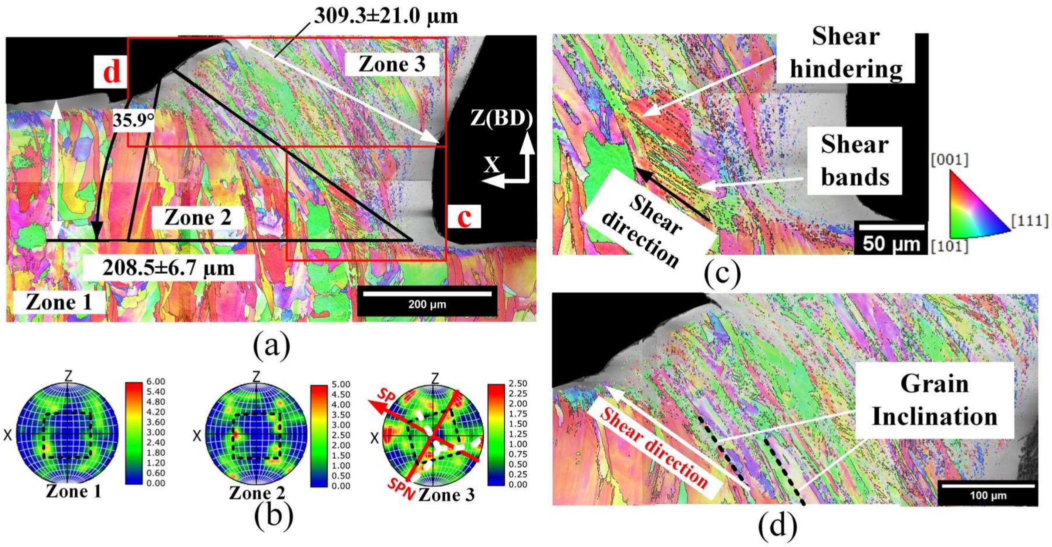

Figure 6.6: Texture evolution in chip formation for 90T. (a) IPF mappings for both chip and workpiece with measured uncut thickness, chip thickness and shear angle. {111} PFs in (b) are obtained from Zones 1, 2 and 3 respectively. (c) and (d) are zoom-in regions from shear zone and chip. The typical cube texture and shear texture is highlighted by dashed lines in {111} pole figure. SP and SPN in (b) are the shear plane and shear plane normal. (The grey areas are not well indexed by EBSD detector due to significant plastic deformation)

In Zone 3, the elongated grains are inclined to the shear direction during chip formation but they are not exactly parallel to the shear direction (Figure 6.6(d)). It is understood that largest compression occurs near the cutting edge and gradually decreases when moving towards the free surface [181]. Thus, the slip bands generated near the cutting edge are almost parallel to the shear direction (Figure 6.6(c)), but due to less compression near the free surface, the elongated grains tend to bend along the shear direction (Figure 6.6(d)). Moreover, both rotated cube texture and shear texture are found in the chip. This is evidenced by the <111> PF in Zone 3 (Figure 6.6(b)), consisting of a rotated cube texture (black dashed line) and a typical shear texture (white dashed line). The chip formation process in 90T is also affected by the shear hindering and the <001>-oriented grains tends to inclined along the shear direction. Hence, the texture in the chip is a combination of rotated cube texture and shear-induced texture.

6.2.5 LPBF-Fabricated Alloy 718 with 67° rotation

The grain orientation in 67T workpiece is randomly distributed and the grain growth direction is along the z-axis as shown in Zone 1 (Figure 6.7(a)). In the shear zone (Zone 2), a significant “S-shape” grain boundary curving is observed in front of the cutting edge (Figure 6.7(c)). This is because there are many narrow elongated grains in the 67T workpiece (Figure 6.1(d)). The length of these grain boundaries along the z-axis can reach about 160 μm, close to the uncut thickness. The elongated grains will experience two directional shear deformations from primary and secondary shear zones, forming the “S-shape” grain boundary. This is different from the chip formation pattern observed in 01T and 90T due to the grain structure difference.

The dominated shear texture is highlighted by the dashed line in the <111> PF of Zone 3 (Figure 6.7(b)). The texture is similar to the shear texture in wrought Alloy 718 (Figure 6.4(b)), indicating that most grains in these two cases follow the simple shear slip in FCC grains during chip formation. However, due to the elongated grain structure in 67T, grains are more likely to be curved instead of pure shear. The grain boundary curving disturbs the pure shear within grains during chip formation, causing a large shear angle (35.3°) and a low chip ratio (about 1.5).

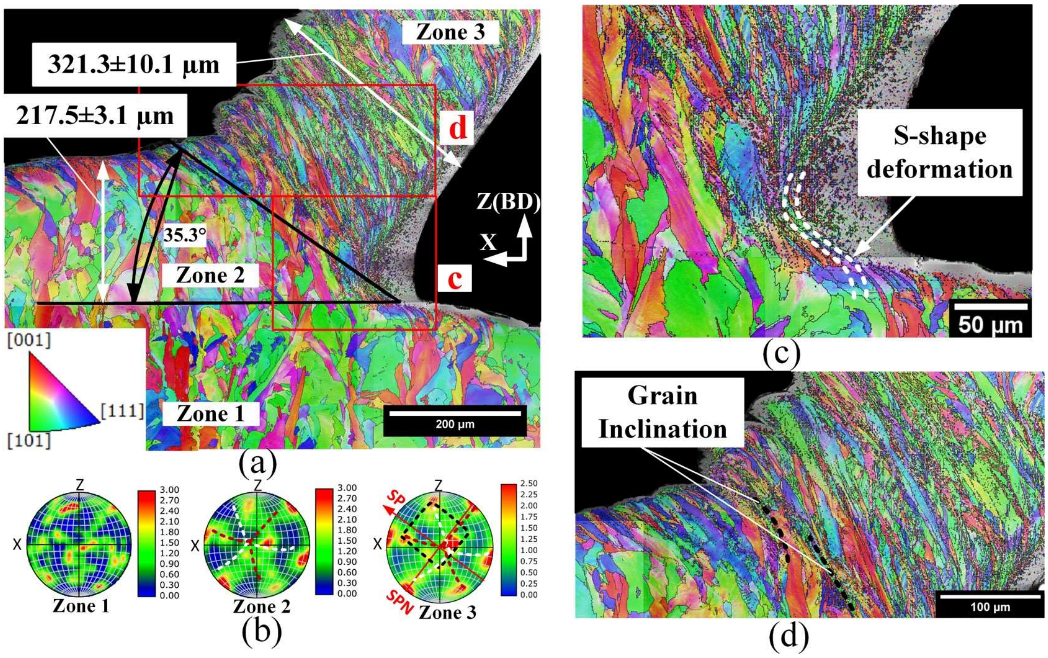

Figure 6.7: Texture evolution in chip formation for 67T. (a) IPF mappings for both chip and workpiece with measured uncut thickness, chip thickness and shear angle. {111} PFs in (b) are obtained from Zones 1, 2 and 3 respectively. (c) and (d) are zoom-in regions near the primary shear zone. The typical texture is highlighted by black dashed lines in {111} pole figure. SP and SPN in (b) are the shear plane and shear plane normal. (The grey areas are not well indexed by EBSD detector due to significant plastic deformation)

6.2.6 Chip formation comparison for steady-state and quick-stop cutting tests

Since the precondition for this work is that the quick-stop cutting test can reliably "freeze" the steady-state orthogonal cutting process, it is necessary to validate the stability of the quick-stop cutting test. To compare the chip formation process in quick-stop and steady-state cutting tests, the same cutting parameters and cutting tools were used for WR, 01T, 90T and 67T during the steady-state orthogonal cutting tests. Then, the chip formation in steady-state cutting process without quick-stop module was captured at similar locations, and the shear angles were also measured for comparison (Figure 6.8). It was observed that the shear angles of WR, 01T, 90T and 67T were 32.7°, 47.5°, 35.3° and 36.1°, respectively (Figure 6.8(a)-(d)). Moreover, the shear angles measured from steady-state cutting tests were similar to those obtained from the quick-stop cutting tests (Figure 6.8(e)). This indicated that the quick-stop test could accurately reflect the steady-state cutting process.

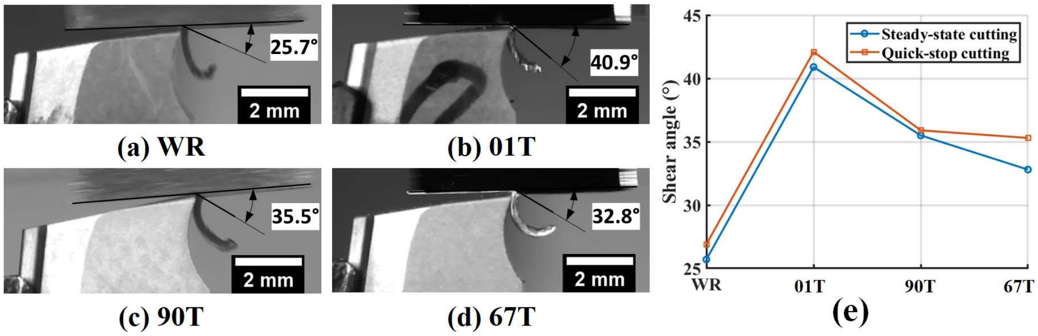

Figure 6.8: The chip formation process of steady-state orthogonal cutting and the shear angle comparison with the quick-stop cutting test. (a), (b), (c) and (d) are the chip formation processes of steady-state orthogonal cutting tests. The regions captured in (a)-(d) were close to the middle of the samples, which were similar to the frozen regions in the quick-stop cutting tests. (e) The shear angle comparison for steady-state cutting and quick-stop cutting.

According to the chip formation process in steady-state orthogonal cutting tests (Figure 6.9), slightly serrated chips were observed in all cases, which is similar to the chips obtained in the quick-stop cutting tests. This indicated that the designed H-shape spacer could reliably reduce the instability of the quick-stop cutting test to ensure a stable chip formation process. Moreover, it was also observed that the thickness of 01T was thinner than that of WR (Figure 6.9(a) and (b)), in line with the chip morphologies that were observed in quick-stop cutting tests for WR (Figure 6.4) and 01T (Figure 6.5). This indicated that quick-stop tests might not significantly influence the chip morphologies when compared with steady-state orthogonal cutting tests.

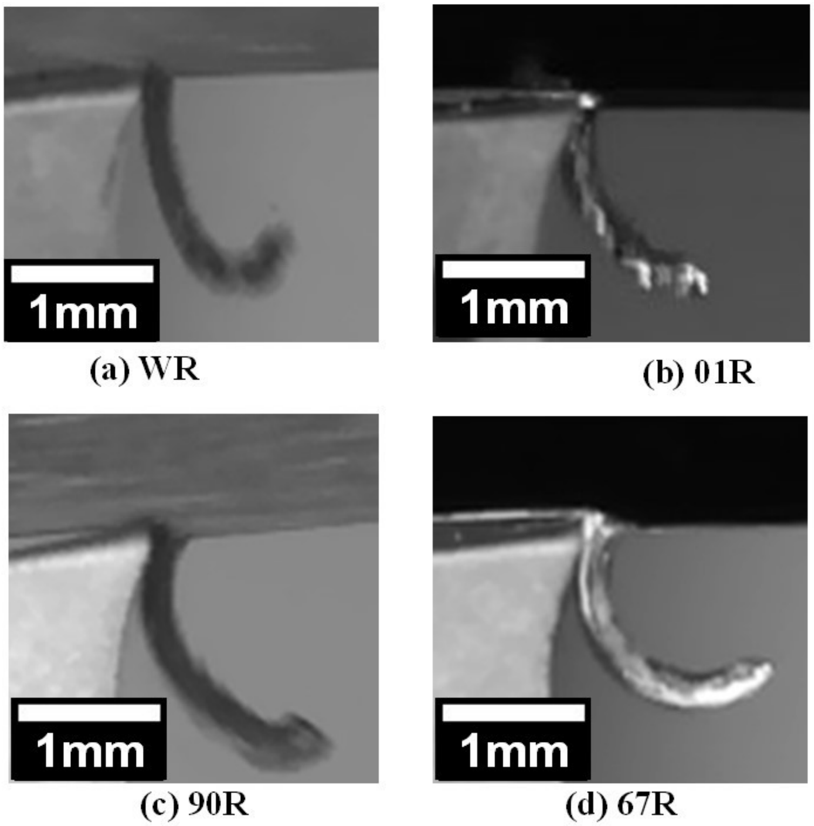

(a) WR (b) 01R

(c) 90R (d) 67R

Figure 6.9: Chip formation processes in the steady-state orthogonal cutting test (zoom-in from Fig. S1 (a)-(d)). (a) WR, (b) 01T, (c) 90T and (d) 67T.

Four cutting tools after the quick-stop cutting tests were observed under the SEM and the cutting edges were highlighted by the white arrows (Figure 6.10). It was observed that the tool wear in this work was limited due to the short cutting distance. Moreover, the rake face is only slightly affected by the built-up edge (BUE) since only a few adhesions were observed on the cutting tool. This indicated that the influence of BUE on the chip morphologies was limited.

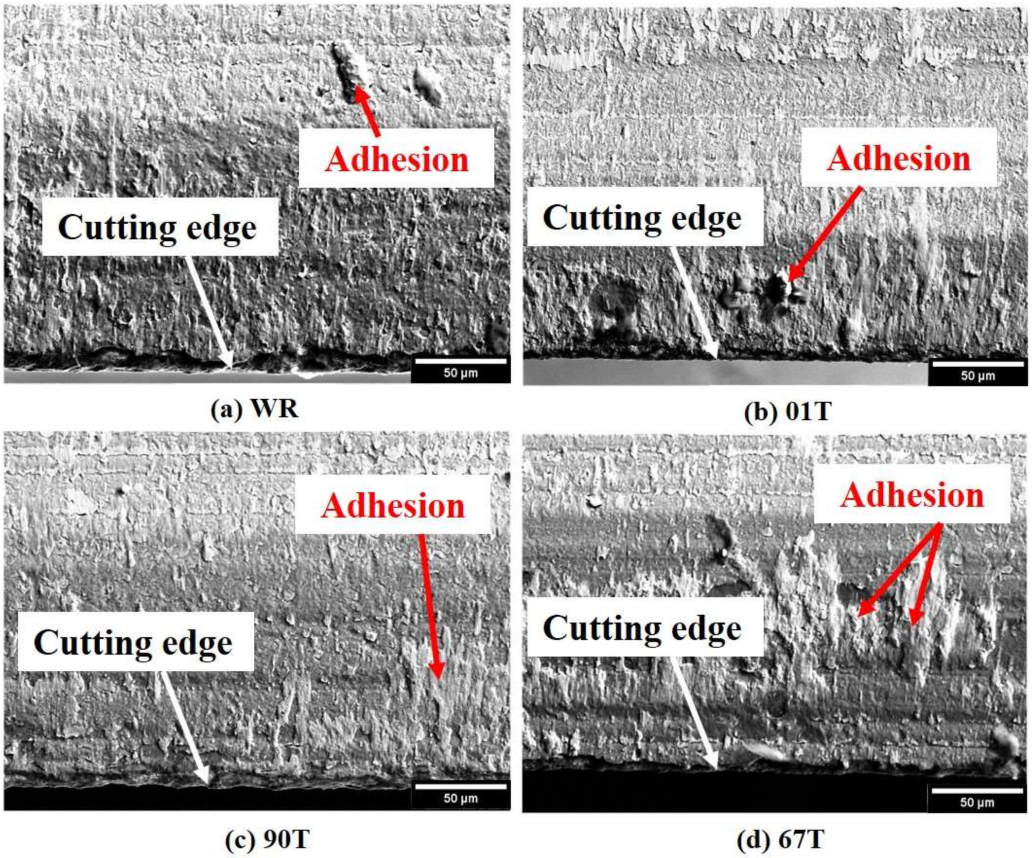

Figure 6.10: Comparison of the rake face of the cutting tool after the quick-stop cutting. (a) WR, (b) 01T, (c) 90T and (d) 67T. The cutting edge is highlighted by the white arrow and the adhesions are highlighted by red arrows.

It is observed that the rake angles in WR and 01T are smaller than those in 90T and 67T. This is mainly attributed to the different grain morphologies in these four cases. The influence of built-up edge (BUE) in front of the cutting tool is limited in these four cases, which is evidenced by the few adhesions on the cutting edge observed under the SEM (Figure 6.10) and few BUE near the chip roots. Since the chip of WR is easier to pile up in front of the cutting tool within a small shear angle, the chip may significantly incline to the cutting direction, leading to a relatively larger rake angle than LPBF-fabricated workpieces. In 01T, 90T and 67T, since the curved grain boundaries hinder the original shearing, the material tends to pile up with larger shear angle and the chips are relatively closer to the rake face of the cutting tool. Similar phenomena were also observed in the steady-state orthogonal cutting tests (Figure 6.8(b)).

6.3 Kernel average misorientation (KAM) for four different textures

The Kernel average misorientation (KAM) [258] was employed to analyse the localized deformation during chip formation (Figure 6.11 and Figure 6.12). From the KAM of the original wrought Alloy 718 (Figure 6.11(a)), it can be observed that there are no clear intragranular misorientations due to the heat treatment which eliminates the forming-induced residual stress. However, the LPBF fabricated Alloy 718 samples (Figure 6.12(b) to (d)) show clear misorientations due to the localised heating and rapid cooling cycles during fabrication [259]. This suggests higher dislocation densities are more likely to distribute within the elongated grains since such grains are formed under extremely high cooling rate during solidification when compared with neighbouring large grains. This phenomenon is in line with previous reported KAM distribution in LPBF-fabricated Alloy 718 [260].

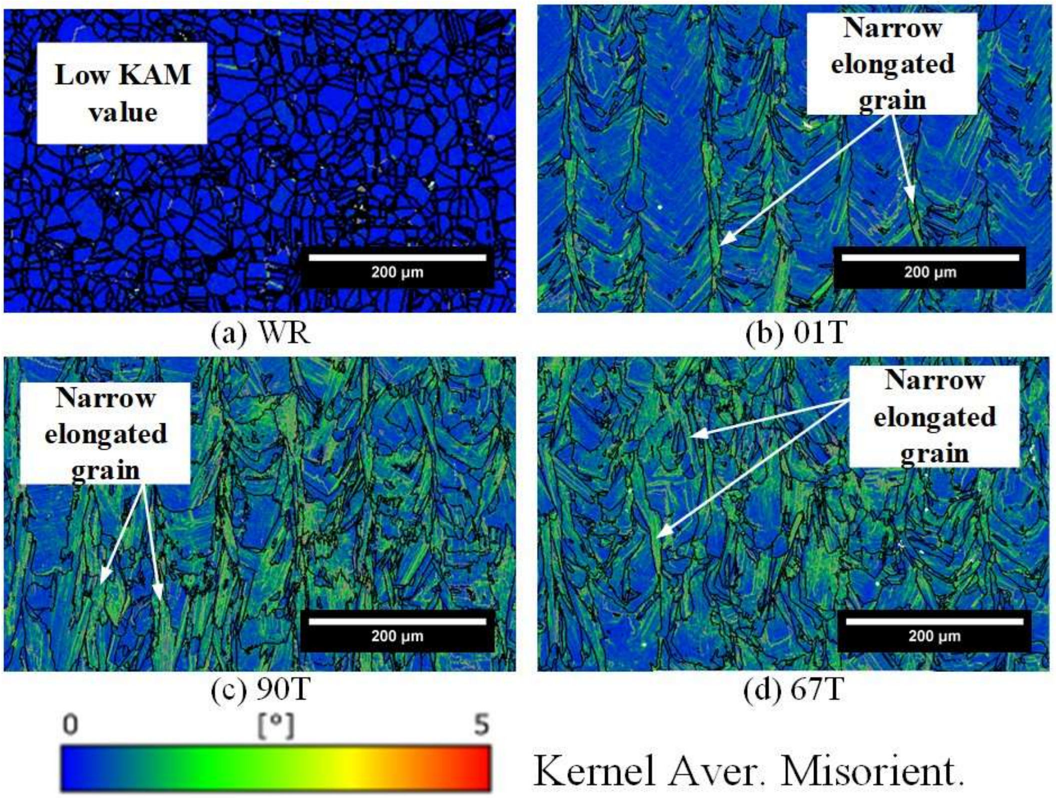

(a) WR (b) 01T (c) 90T (d) 67T

Figure 6.11: Kernel average misorientation comparison for workpieces of wrought and LPBF. (a) WR, (b) 01T, (c) 90T and (d) 67T.

During machining process, high KAM was mainly observed near the primary shear zone (dashed line in Figure 6.12(a)) and the value decreases dramatically when it is far from shear zone in wrought Alloy 718 workpiece. This is because the small equiaxed grains have a large grain boundary density [148], confining the deformation to a narrow region near the shear plane. In 01T (Figure 6.12(b)), a high KAM value is observed in the chip and columnar grain in front of the cutting edge. Since the initial shear deformation was hindered by the columnar grain, resulting in a lattice rotation (evidenced by the rotated columnar grain in Figure 6.5(c)), the high strain energy was stored in this columnar grain (Figure 6.12(b)). Moreover, different from the uniform distribution of strain energy in equiaxed grains (i.e., wrought 718), the strain energy distribution in 01T is governed by grain morphology in front of the chip. This suggests that the chip formation process (e.g., shear angle and chip thickness) in 01T is sensitive to grain morphology and the shear deformation may change dramatically in adjacent grains, which is evidenced in Figure 6.5(d). Since high dislocation density is distributed in the originally elongated grains formed by LPBF, the long grain boundaries are strengthened and exhibit higher deformation resistance. Hence, the elongated grains could hinder the shear bands by grain boundary curving and store large strain energy, exhibiting the highest KAM value (Figure 6.12(c)). Such elongated grains that originally have high KAM are more likely to store the strain energy by curving instead of shearing, resulting in the change of the original shear direction. Since the shear slipping is hard to cross such grain boundaries, large intragranular areas with less deformation are retained in the chip of LPBF-fabricated cases instead of the wrought case.

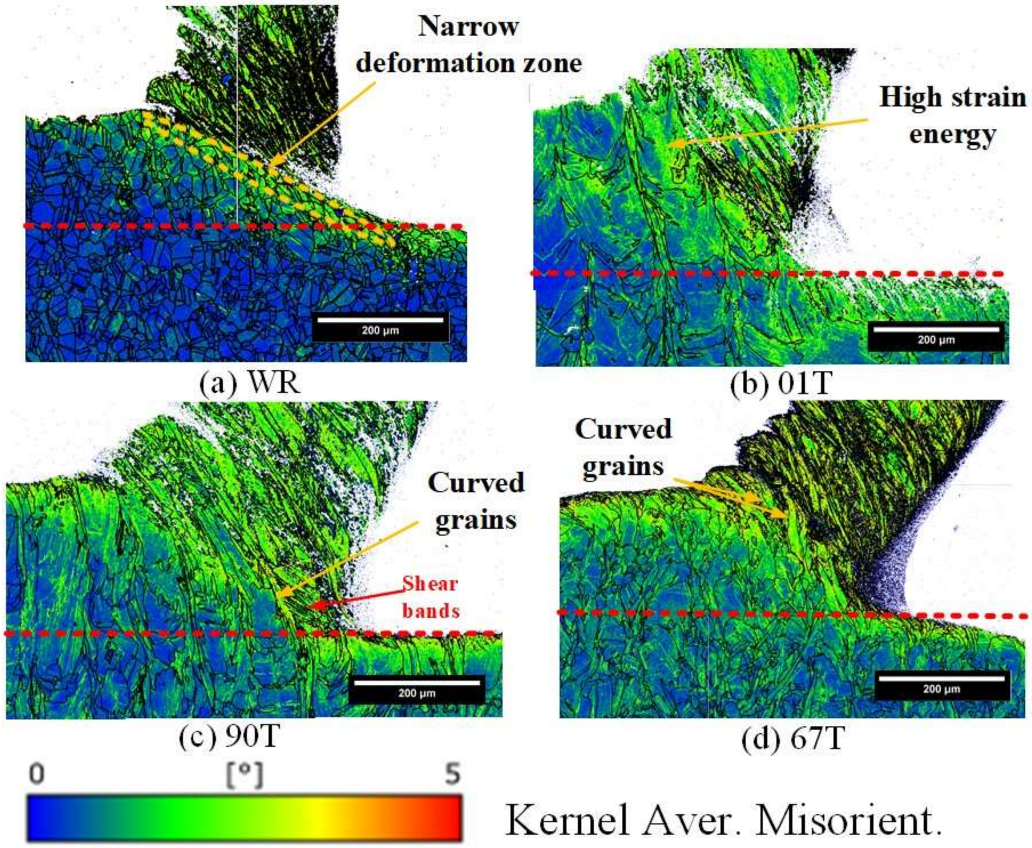

(a) WR (b) 01T (c) 90T (d) 67T

Figure 6.12: Kernel average misorientation comparison for the chip of wrought and LPBF (a), (b), (c) and (d) are chips for WR, 01T, 90T and 67T. The average misorientation angle ranges from 0° to 5°. The machined surface is marked by the red dashed line.

6.4 Texture components evolution during chip formation

In order to quantify the texture evolutions during chip formation, the texture components in the workpiece were calculated (Figure 6.13(a)) and compared with the counterparts in chips (Figure 6.13(b)). Since the deformation in the chip formation process is complex and it is hard to identify a typical pattern to represent the shear deformation in each case. The texture component analysis was therefore employed as a statistical method to understand the change of grain orientation during chip formation. The volume fractions of each texture component were calculated with a misorientation angle of 20°. The shear direction is determined by the shear angle measured in IPF mappings. The first seven textures are employed to identify the preferred grain orientations of workpiece. The specific name and Euler angle are listed in Table 6.1 while ideal miller indices and Euler angle are detailed in Table 6.2. A1 to B is used to identify the shear-introduced textures during chip formation [261]. The positions of texture are depicted in {111} pole figure in the inset of Figure 6.13(a). In the wrought Alloy 718, one of the preferred textures is the brass-type texture, which is a typical roll-based texture. Another texture (C-texture in Table 6.1) is attributed to the shear deformation during rolling process (Figure 6.13(a)). In the uncut workpiece, the dominant textures in 01T and 90T are Rotated Cube and Cube textures, in line with the PF in Figure 6.4. Moreover, few shear-induced textures are observed in such two cases. For 67T workpiece, varies textures are observed in this case due to its randomised grain orientation formed by the 67° rotation strategy.

In the chip formation process, texture components change dramatically in 01T and 90T. In 01T, the volume fraction of rotated cube texture decreases by about 65%, indicating that more than half of columnar grains are deformed during chip formation, in which the preferred shear texture is C-type texture with the {100} shear plane along <110> direction. The major component for 90T is also C-type texture whilst the original cube texture is reduced to about 5%. It should be noted that some original cube texture transfer to the rotated cube texture (RC-S) due to the grain inclination, which is evidenced by the texture in Zone 3 (Figure 6.6(b)).

This explains that the volume fraction of rotated cube texture in 90T reaches 18% in the chip. For 67T, the major components changes to Ab (($\bar{1}\bar{1}1$) [$\bar{1}10$]) and Bb (($11\bar{2}$) [$\bar{1}10$]) with the shear along <$\bar{1}10$> direction. The texture components in wrought alloy 718 doesn't show significant change when compared with the workpiece. This is because the equiaxed grains in WR is isotropic during shear deformation, there is no preferred orientation dramatically changing as in 01T and 90T (Figure 6.13(b)).

Table 6.1 Typical textures for workpiece. Brass, cube and rotated cube are typical textures for WR, 90T and 01T respectively.

Component	{hkl}<uvw>	Euler angles		
		φ1	φ	φ2
Cube (Cb)	{001}<001>	0°	0°	0°
Goss(Gs)	{011}<100>	0°	45°	0°
Brass(Bs)	{111}<112>	35°	35°	45°
Copper(Cu)	{112}<111>	90°	35°	45°
S1	{231}<346>	59°	29°	63°
Taylor (Ty)	{4 4 11}<11 11 8>	90°	27°	45°
Rotated Cube	{001}<110>	45°	0°	0°

The texture evolution demonstrates chip formation variations in wrought and LPBF-fabricated Alloy 718. For the wrought Alloy 718, it is seen previously in Figure 6.4(a) that the equiaxed grains tend to exhibit a nearly pure shear deformation pattern along the shear direction. This is further confirmed according to the quantified texture components in Figure 6.13(b) that about 80% of texture components in the chip are shear-based (counted by the fraction from A1 to B for WR). This indicates that the machining-induced deformation in wrought 718 is dominated by the plane-stress cutting condition during orthogonal cutting. However, for the LPBF-fabricated Alloy 718, the unique forming process generates elongated grains with preferred orientations, and pure shear is difficult to occur within such grains due to the shear hindering effect (Figure 6.5(c)). The deformation of such elongated (or columnar) grains tends to transfer to grain boundary curving (or lattice rotation). Such deformation patterns retain some grains with their original orientation in the chip during cutting, while some deformed texture are caused by lattice rotation instead of pure shear. Consequently, it is observed that the fraction of shear-induced texture in LPBF-fabricated Alloy 718 is only about 40% (Figure 6.13(b)). Such texture component difference indicates that the machining-induced deformation for the LPBF alloys cannot be treated as a simple shear-induced deformation as wrought alloy, because the strong textures originated from the LPBF process are partially retained, together with the newly formed shear textures.

Table 6.2 Main ideal shear orientations for FCC alloys with its miller indices and Euler angles [261]. φ1 is rotated based on shear angle (S).

Component	{hkl}<uvw>	Euler angles		
		φ1	φ	φ2
A1	$(11\bar{1})[112]$	35.26°-S	45°	0°
A2	$(1\bar{1}1)[\bar{2}\bar{1}1]$	144.74°-S	45°	0°
Ab	$(\bar{1}\bar{1}1)[\bar{1}10]$	180°-S	35.26°	45°
A	$(11\bar{1})[1\bar{1}0]$	0°-S	35.26°	45°
C	$(100)[0\bar{1}1]$	90°-S	45°	0°
Bb	$(11\bar{2})[\bar{1}10]$	180°-S	54.75°	45°
B	$(11\bar{2})[0\bar{1}1]$	0°-S	54.74°	45°

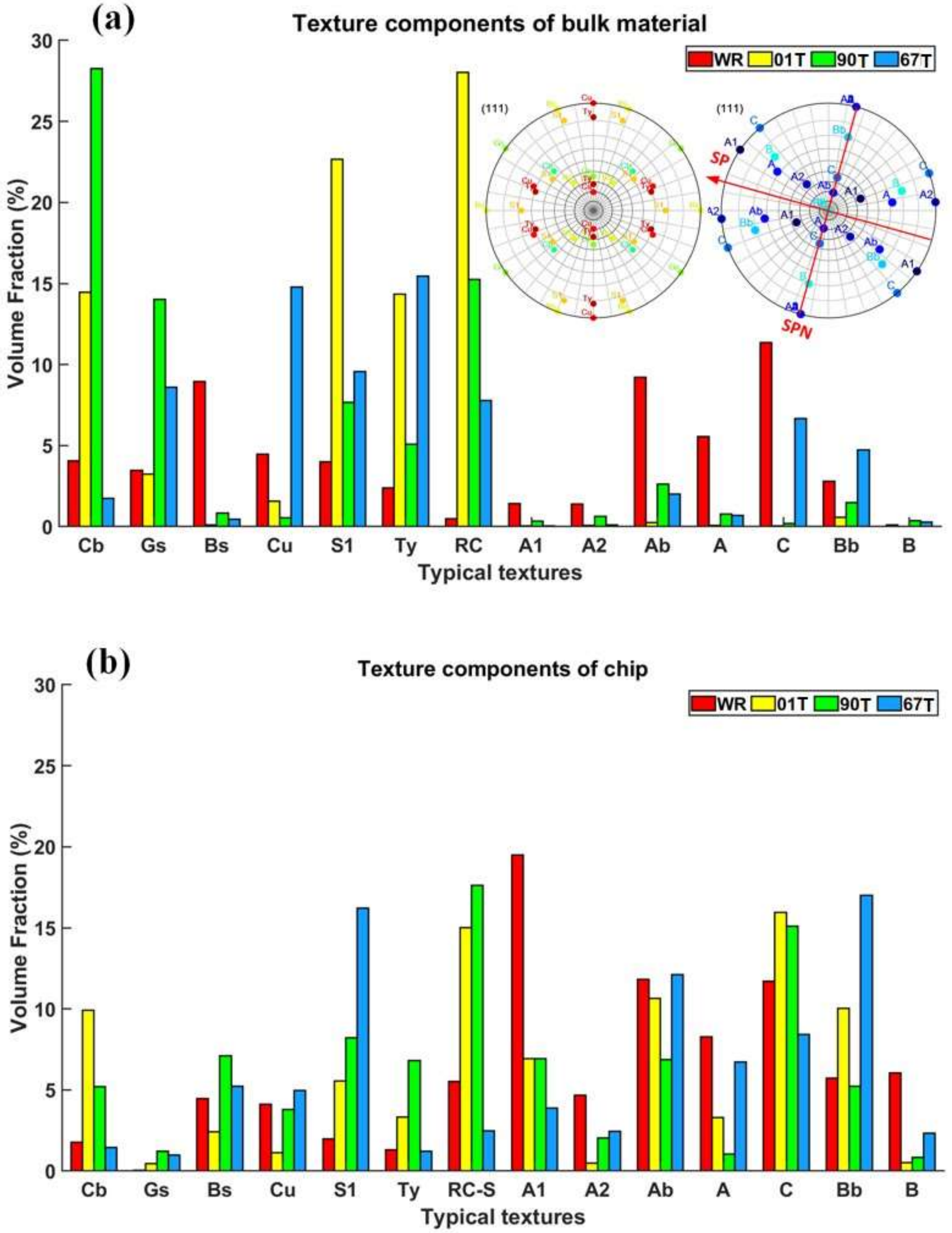

Figure 6.13: Texture components for workpiece and chip are calculated in (a) and (b). Main ideal orientations in {111} pole figure for the typical textures in the workpiece and simple shear along shear plane. Cb: cube texture {001} <100>, Gs: Goss texture {110} <001>, Bs: Brass texture {110} <112>, Cu: copper texture {112} <111>, S1: S texture {231} <346>, Ty: Taylor texture {4 4 11} <11 11 8>, RC: rotated cube texture {001} <110>, RC-S: cube texture that rotated angle equals to shear angle ({001}<110>). A1 to B correspond to ideal shear texture in FCC along the shear direction.

6.5 Discussion

6.5.1 Cutting force and micro-hardness

The micro-hardness (HV0.2) evolution from Zone 1 to Zone 3 for four cases is compared in Figure 6.14(a). The lowest micro-hardness is observed in wrought Alloy 718 of 235.9±4.6 whilst the micro-hardness of three LPBF-fabricated Alloy 718 workpieces is about 320. This is mainly attributed to the higher dislocation density (Figure 6.13) in the as-built Alloy 718 than the wrought. Since Zone 2 is a transitional zone from the original workpiece to the chip, the micro-hardness increased with significant fluctuation. A significant micro-hardness transition is observed in the wrought 718 from Zone 1 to Zone 3, increasing from 235.9±4.6 to 445.3±5.2. This matches the shear deformation zone observed in Figure 6.14(a), where the high KAM value is near the primary shear zone and fades away fast to the undeformed workpiece. Because the initial dislocation density in wrought 718 is lower than the other 3 LPBF-fabricated 718 (Figure 6.11). This indicates that the work hardening is more significant in the wrought 718 when compared to the LPBF-fabricated 718 after the orthogonal cutting. Moreover, it is interesting to observe that the difference in the micro-hardness between wrought and as-built 718 chips is insignificant when compared to their initial values. This suggests that there may be a similar work hardening level in the chip formation of Alloy 718 under the same cutting parameters. In addition, the micro-hardness in 01T is slightly lower than in the other three cases due to the large grain retaining in the chip Figure 6.5(d).

The cutting force in the steady state orthogonal cutting (Figure 6.14(b)) shows that the lowest value is in wrought 718. This may be attributed to lower KAM of wrought workpiece and a smaller deformation zone during orthogonal cutting. This result contrasts with the force reported in the previous work [149], which states that the cutting force of wrought is higher than that of LPBF Alloy 718. However, the cutting force results in this work are approximate the same as those reported by Amir et. al [147]. This suggests that the cutting force comparison for wrought and LPBF Alloy 718 may be sensitive to laser and machining parameters. In this work, it is observed that the thicker chip in the wrought Alloy 718 since the actual shear angle of wrought Alloy718 is smaller than those as-built cases. However, it seems that cutting force may not be significantly affected by the material pile-up thickness along the shear direction. This is evidenced by the thinner chip thickness of 01T (Figure 6.5(a)) but the higher cutting force (Figure 6.14(b)) than the wrought one.

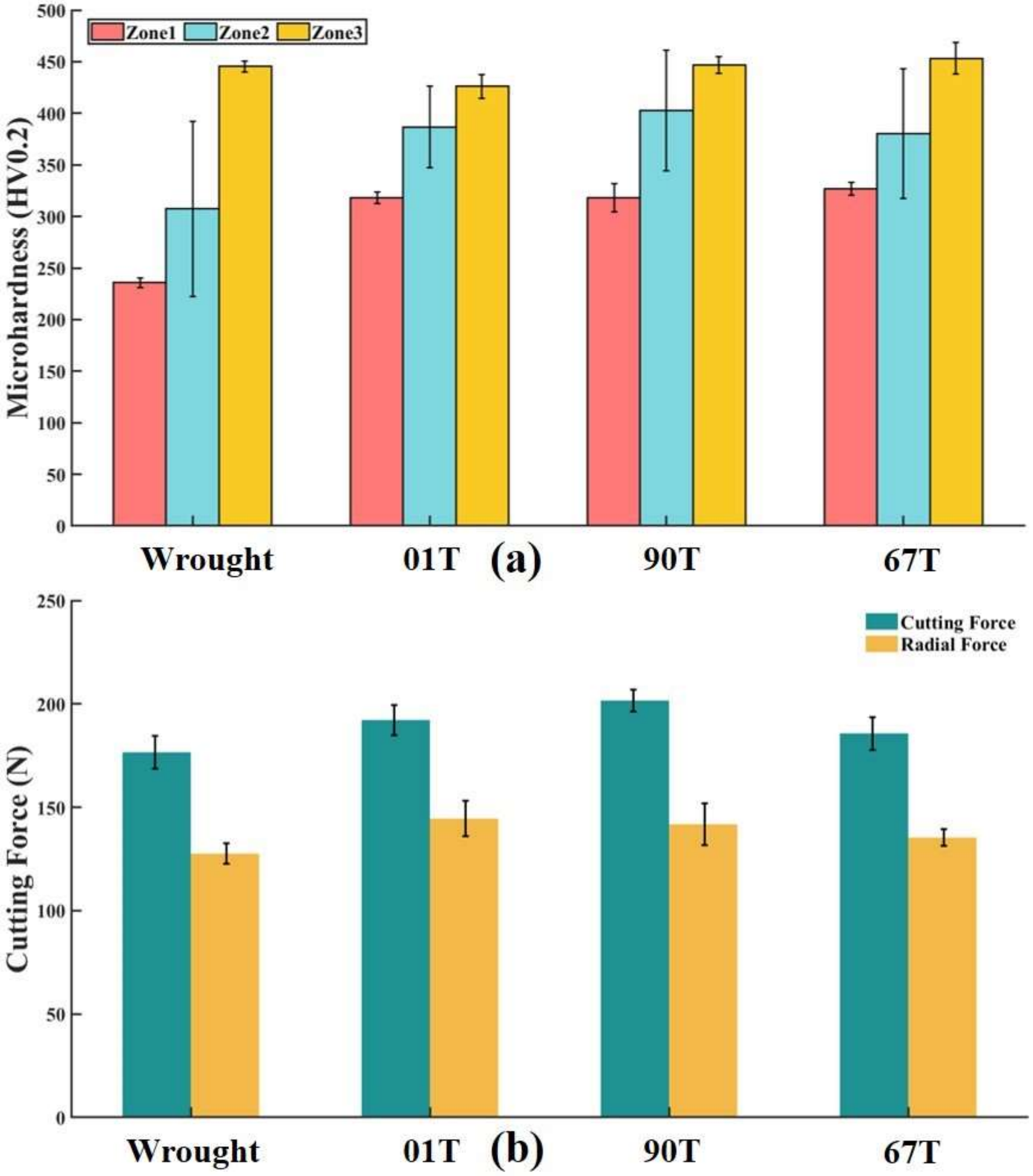

Figure 6.14: (a) Comparison of micro-hardness evolution in chip formation (Zones 1, 2 and 3 correspond to the original workpiece, shear region and chip, respectively); (b) Force (cutting force along the x-axis and radial force along the z-axis) comparison for wrought, 01T, 90T and 67T. The error bar represents the standard deviation.

6.5.2 The influence of grain morphology on chip formation mechanisms

Different chip formation mechanisms for equiaxed grains with weak texture (wrought) and elongated grains with strong texture (LPBF) are illustrated in Figure

6.15. For the equiaxed grains (Figure 6.15(a)), many grain boundaries act as barriers to confine the deformation near the primary shear zone to a narrow region above the shear plane and limited grain deformation occurs below the shear plane. The grains near the cutting edge experience significant deformation, being elongated along the shear direction and then gradually becoming curved Figure 6.4(c). Meanwhile, the grain deformation direction is not totally along the shear direction especially when it is close to the free surface (Figure 6.4(d)). This is because the compressive stress near the free surface may not be as high as the region in front of the cutting edge [262]. Thus, the grains in this area undergo less deformation along the shear plane compared to those near the cutting edge. It is indeed seen that these deformed grains are not aligned with the shear direction (Figure 6.4(c)). Moreover, some equiaxed grains are retained at the free surface in Figure 6.4(d)). Since grains near the primary shear zone exhibit different deformation patterns (e.g., elongation and curving), material pile up along the shear direction is unstable. Such shear deformation instability leads to serrate chip morphologies as shown in Figure 6.15(a) and Figure 6.4(a).

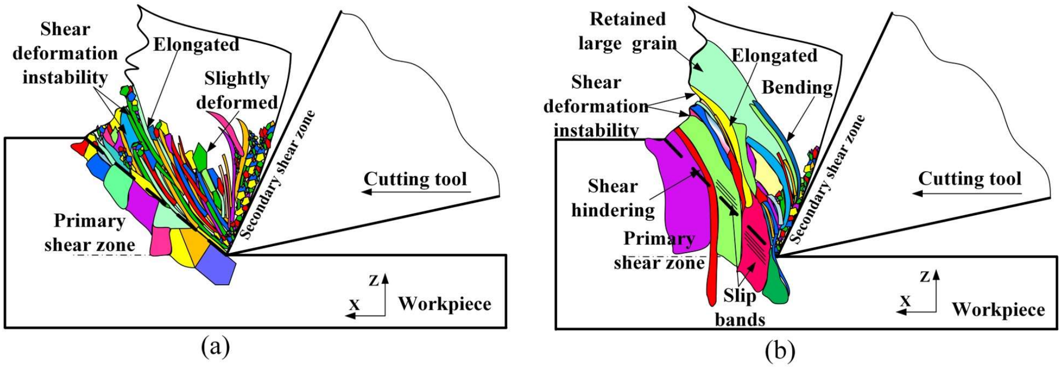

(a) (b)

Figure 6.15: Chip formation schematics for (a) equiaxed grains with weak texture and (b) elongated and retained large grains with strong texture.

In the LPBF-fabricated alloys with elongated grains and strong textures, the shear deformation usually causes significant shear bands in front of the cutting edge as illustrated in Figure 6.15(b). However, since shear deformation is hard to occur near the grain boundary [263], the shear bands are difficult to cross such a long and continuous grain boundary when it is far from the cutting edge. The shear-induced deformation is transferred to grain boundary curving during chip formation. Since large columnar grains and narrow/elongated grains are often found to exist in the LPBF process, the curved grains are eventually cut through when the cutting proceeds. Since the deformation near the free surface is not as significant as that near the cutting edge, some of the columnar grains with <011>//BD texture tend to retain their original morphology in the chip with limited lattice rotation. Moreover, since the shearing is hard to occur near the grain boundary and the distance of grain boundaries between elongated grains is narrow (about 10 μm), such grains with <001>//BD texture are likely to curve instead of shearing. These unique orientated grains finally change the chip formation process during orthogonal cutting.

The crystallographic texture evolution from the workpiece to the chip reflects the deformation history in front of the cutting edge during the chip formation. For the wrought 718 with equiaxed grain and a weak texture, the texture in front of the cutting edge transfers to the A-type texture (Figure 6.13(b)), suggesting a nearly pure shear deformation along the shear direction. This also matches the plane stress shear condition that is commonly assumed in orthogonal cutting. The weak texture is also observed in 67T fabricated by the 67° rotational scanning strategy. However, the preferred texture in the chip of 67T is B-type and grain rotation rather than shearing is also more significant than that in WR (Figure 6.13(b)). This indicates that the elongated grains formed by LPBF can change the deformation pattern in front of the cutting edge, subsequently forming a preferred texture different from wrought 718 under the same cutting conditions. For the workpieces with high-intensity textures, such as 01T and 90T, the original oriented grains partly retain within the chip during chip formation. Therefore, fewer shear textures are formed during chip formation when compared to WR. In addition, relatively larger cutting forces in 01T and 90T (Figure 6.14(b)) suggest that strong textures may require higher cutting forces. Such strong textures in 01T and 90T may be more difficult to transform into shear-based textures during chip formation.

For all cases, the micro-hardness of the chip is slightly affected by crystallographic textures. This indicates the material pile-up behaviour during chip formation may increase the dislocation density to a similar level in all Alloy 718 cases. However, due to the different original grain morphologies and textures in wrought and LPBF Alloy 718, grains among these four cases may have different deformation behaviour (e.g., shearing or curving) to pile up along their own shear directions (Figure 6.15), finally reaching the similar dislocation densities.

According to the classic Hall-Petch relationship ($\sigma_y = \sigma_0 + k_y d^{-0.5}$) [253], wrought Alloy 718 with small grain size is likely to lead to a high cutting force. Because small grain size usually corresponds to a high grain boundary density (or high grain boundary resistance). However, since the substructure formed within grains formed by LPBF [31] contributes to higher dislocation densities (high KAM value in Figure 6.11), machining of larger grains formed by LPBF exhibits a higher cutting force than the wrought Alloy 718. Furthermore, since machining only leads to a localised and significant plastic deformation near the machined surface, it may be necessary to evaluate the actual grain size along the cutting path rather than the entire workpieces [254], especially for the elongated grains with high aspect ratios that are perpendicular to the cutting direction.

The serrated chip morphology was observed in all cutting cases. In the wrought Alloy 718, the space of serrated chips changes slightly because the cutting process of equiaxed grain is relatively stable [142,178]. However, the space of serrated chips in LPBF-fabricated Alloy 718 is hard to predict because it is sensitive to the grain morphology, which is rarely reported in previous research. It is seen that the LPBF-fabricated Alloy 718 consists of a wide range of grain size (Figure 6.2) and unique columnar and narrow/elongated grains (Figure 6.1). The shear zone for the workpiece with such microstructure cannot be treated as a stable shear plane as confirmed previously (Figure 6.5 to Figure 6.7). This is reflected by the variations in the measured shear angle, which is significantly affected by unique grain morphologies in the LPBF process. For example, the columnar grains in 01T enlarge the shear angle due to the shear hindering and grain boundary curving. Consequently, the large shear angle and limited deformation in such columnar grain restrict material pile-up along the shear direction. The different grain growth patterns in the LPBF process at different scanning strategies leads to a wide grain size distribution with unique textures. Such large variations in grain morphology and crystallographic texture change the material pile-up behaviour between adjacent grains. This makes the space of serrated chips in LPBF alloys hard to predict.

6.6 Summary

Laser powder bed fusion (LPBF)-fabricated alloys usually exhibit unique grain morphologies and crystallographic textures, owing to their layer-by-layer fabrication process. It is crucial to understand the influence of such unique microstructure on chip formation during cutting. In this work, the chip formation mechanisms in different textured Alloy 718 were investigated via a pendulum-based cutting machine equipped with a quick-stop module. Since the chip was retained on the workpiece after quick-stop orthogonal cutting, the grain deformation pattern (e.g., shear or curving) and orientation change from the workpiece to the chip could be evaluated. Moreover, the texture component was quantified to identify the dominant texture after cutting.

In the LPBF-fabricated Alloy 718, it was observed that shear hindrance effect impeded the material pile-up along the original shear direction, leading to significant grain boundary curving in front of the cutting edge. This is because the long grain boundaries were formed due to the build directional grain growth direction in LPBF process. These grain boundaries were likely curved and shear bands failed to cross these long grain boundaries. Moreover, the texture components in the chip are strongly dependent on the original texture of the workpiece, leading to a nearly pure shear texture in the chip of wrought workpiece but a mixture of shear and rotated textures in the chip of LPBF workpiece, according to the texture evolution chart.

It is found that elongated grains significantly change the machining-induced shear deformation in front of the cutting edge, where the long grain boundaries that are perpendicular to the cutting direction interrupt the shear deformation. Moreover, the texture component evolution (from the workpiece to the chip) also suggests that oriented grains have their own preferred shear pattern and finally result in the unique shear texture in the chip. It is also expected that a threshold of dislocation density (KAM value) may exist in the chip for all Alloy 718 cases under this cutting condition, reaching a similar micro-hardness. The method in this work could be directly used to investigate the role of grain morphology and orientation as well as cutting parameters (e.g., cutting speed and cutting depth) in the chip formation for different materials.

Chapter 7 Conclusions

This thesis investigated the scanning strategy and machining-induced deformation of laser powder bed fusion (LPBF) Alloy 718. In particular, the effect of multi-vector length and rotational scanning strategies on the microstructure was studied. Moreover, a pendulum-based cutting machine and a quick-stop module were employed to study the machining-induced deformation and chip formation mechanisms that were influenced by LPBF-fabricated microstructures. The important conclusions are drawn as follows:

- It was observed that the actual energy density was not the same at different vector lengths when using the same laser parameters in LPBF. This was evidenced by a larger melt pool depth (about 138 μm) in the Short-vector printing compared to that in Long-vector printing (about 89 μm). This was because the actual scanning speed could not reach the target speed in short vectors and the actual energy density in the Short-vector printing (509 J/mm^3) was much higher than that in the Long-vector printing (135 J/mm^3).
- The high energy density combined with narrow melt pool at short vectors constrained the grain growth across several layers along the BD, resulting in a fine grain structure and high microhardness. It was shown that the average grain size in the Short-vector printing (less than 20 μm) was smaller than that in the Long-vector printing (larger than 50 μm). The increased grain size resulted in the reduction of microhardness from 347.6±7.5 to

298.2±4.4 HV.

- With the increment of the vector length, the melt pool morphology transitioned from keyhole mode to conduction mode since the laser scanning pattern shifted from being dominated by acceleration to a constant speed. This resulted in the grain orientation transition from <111> to <101> in BD and from <111> to <001> in the scanning direction.
- Unidirectional (i.e. 0° rotation scanning strategy) LPBF-built structures characterised by very heterogeneous crystallographic textures leaded to dramatically different strain/stress levels in two cutting directions. This was because the three-dimensional grain growth pattern (side-branching) in LPBF enables the same grain to exhibit non-equivalent textures (<011>//BD and <011>⊥BD) on XZ and YZ planes. Consequently, different activated slip systems in the cutting process led to dramatic deformation in <011>//BD texture but slight deformation in <011>⊥BD texture. For the XY surface machining, the cubic <001>//BD texture and weak texture fabricated by 90°, 67° rotation strategies were symmetrical equivalent in both XZ and YZ planes. It would not cause deformation deviation when the cutting direction changes 90°.
- Statistical deformation tendency map not only exhibited the relationship between texture/slip system and shear angle but also revealed the threshold of grain size that affected the texture-based deformation. Individual grain deformation in a textured alloy 718 strongly depended on its grain width along the cutting direction. In the large grain (large grain width along the

cutting direction) region, the grain with a small activated slip trace angle (parallel to the shear direction) was easy to deform. However, slight deformation occurred to the grain when the activated slip trace angle is large. Small grains width exhibited high deformation resistance due to the high geometrically necessary dislocation (GND), hindering the plastic deformation along the slip direction.

- Long grain boundaries formed in strong textured LPBF-fabricated Alloy 718 led to significant shear hindrance effect. This was because shear slipping was hard to cross the grain boundary, resulting in grain boundary curving. This shear hindrance effect impeded the material pile-up along the shear direction and finally reduced the chip ratio in 01T to about 1.0.
- The texture components in the chip were strongly dependent on the original texture of the workpiece, leading to a nearly pure shear texture in the chip of wrought workpiece but a mixture of shear and rotated textures in the chip of LPBF workpiece. The texture in the wrought workpiece (WR) was likely to transfer to A1-type shear texture in the chip and about 80% of texture components in the chip are shear-based. However, the cube texture and rotated cube texture possibly changed to C-type texture and only 40% of shear-based texture was found in LPBF-fabricated workpieces.
- In all cutting cases, most grain elongation/inclination directions tended to be different from the original shear direction in front of the cutting edge. This was because the shear transfer from the cutting edge to the free surface was interrupted by grain boundaries in different slip systems. Such shear

instability, caused by grains and textures, ultimately resulted in various rates of material pile-up along the shear direction. This difference in material pile-up leaded to the formation of a serrated chip morphology on the free surface for all the samples.

Chapter 8 Future Work

In this work, laser powder bed fusion (LPBF) is employed as a case study to demonstrate the capability of additive manufacturing (AM) technology in designing and manufacturing metallic components with different microstructures. It has demonstrated the effect of typical rotational scanning strategies and vector lengths on the microstructure control. Especially for the gradient microstructure fabricated by increment vectors, it appears of great potential in the fabrication of microstructural heterogeneities in metallic components. On the other hand, this further indicates that commonly used scanning strategies may not fulfil the potential of AM technology in the localised microstructure control, since a scanning strategy design usually starts from a layer instead of a vector.

This work has proven that laser parameters for each vector can be designed, and grain morphologies can be controlled by vector lengths. The next step is to change laser parameters for each vector with different lengths, investigating the possible microstructures that can be fabricated via AM technology. When the relationship of microstructure-property in AM-fabricated materials is built, the vector-based scanning strategy may enable a heterogeneous microstructure fabrication by tailoring each individual vector according to the specific end-use in industries. Vector-based scanning strategy is not limited to the fabrication of Alloy 718 in this work. However, all materials that can be manufactured by AM technology are able to be fabricated via this method.

Moreover, the real laser acceleration/deceleration phase for different materials strongly depends on the laser on/off delay. The delay time is usually a balance between quality and efficiency in a long vector. It is worth trying to extend the delay time for short vectors when the regular laser parameters (e.g., laser power, scanning speed, and hatch spacing) cannot produce high-quality parts. When employing hundreds of short vectors for thin walls and lattice structures, the acceleration phase in short vectors leads to a keyhole melting mode. To avoid exceeding the energy input, low laser power may be better in short vectors than that used in long vectors. In addition, since the melt pool formed by a short vector is narrower than that formed by a long vector due to less heat accumulation, a small hatch spacing may be beneficial for the bonding between two adjacent short vectors.

In addition, the most reported numerical simulation of melt pool evolution for LPBF is based on the assumption of constant scanning speed. However, this work has dominated that the actual scanning speed at the beginning and end of a vector is not a constant due to the acceleration/deceleration phases. A new simulation model may be needed to understand the influence of the actual laser scanning speed on melt pool morphology and thermal conditions.

Since the crystallographic texture and grain morphology are strongly dependent on laser parameters and scanning strategies during the LPBF process, it is challenging to evaluate the machinability of LPBF-fabricated alloys with different microstructures (i.e., grain morphology and orientation). We have proved that microstructures formed by three rotated scanning strategies lead to different deformation behaviours on the machined surface. An urgent issue that needs to be addressed is to find appropriate machining parameters according to these unique grain morphologies and orientations. Particularly, the anisotropy caused by LPBF manufacturing may require machining parameters modification when the machining direction changes (e.g., parallel or perpendicular to the build direction).

The “quasi-in-situ” cutting method used in this work identified the grain deformation behaviour during orthogonal cutting. This method reveals different deformation patterns such as the curving of columnar grains and slight deformations of <011>⊥BD oriented grains. However, since the cutting test is performed with a macro cutting system whilst deformation is discussed at the micro level. The force data from dynamometer failed to reflect the specific grain deformation such as grain boundary curving and dislocation density increase. It may be worth to try to build a model to quantify such deformation behaviours and link these behaviours with the cutting force (or any other indicators).

Substructure formed during LPBF process leads to a high dislocation density within grains when compared to the wrought component. Subsequently, these substructure may result in a relatively higher cutting force during orthogonal cutting. This may suggest that the grain boundary resistance and lattice friction resistance are influenced by these substructures (or cellular structures). Few works tried to build a model to analyse the effect of such structures on machining. Moreover, more cutting parameters can be designed to investigate the chip formation mechanisms for LPBF-fabricated alloys. Some ideas are listed below for the future research according to our current work:

- Investigate the scanning strategies by a combination of vector length, laser parameters and rotational angles for each layer. It is worth developing the microstructure (grain morphology and orientation) that can be formed by LPBF with different vector lengths and laser parameters. Subsequently, the laser power, scanning speed and vector length can be tailored according to the required microstructure.

- Model of the actual laser motion and its influence on melt pool morphology and grain growth pattern. By defining the actual scanning speed with the acceleration/deceleration phase in the simulation model, the influence of scanning speed on the melt pool dynamics can be further investigated.
- Investigate the effect of cutting parameters on chip formation and machinability of LPBF-fabricated components. By designing different cutting speeds, uncut chip thickness and cutting tools, the effect of unique microstructure on the machining process can be investigated.
- Model of chip formation of LPBF-fabricated alloys based on their unique grain morphologies and substructures. Considering the grain structure in the as-built LPBF alloys and the substructure within the grain, a new crystal-based model should be developed to investigate the machining and chip formation process.

References

[1] D. Gu, X. Shi, R. Poprawe, D.L. Bourell, R. Setchi, J. Zhu, Material-structure-performance integrated laser-metal additive manufacturing, Science (80-.). 372 (2021). https://doi.org/10.1126/science.abg1487.

[2] T. Mukherjee, J.W. Elmer, H.L. Wei, T.J. Lienert, W. Zhang, S. Kou, T. DebRoy, Control of grain structure, phases, and defects in additive manufacturing of high-performance metallic components, Prog. Mater. Sci. 138 (2023) 101153. https://doi.org/10.1016/j.pmatsci.2023.101153.

[3] S. Sanchez, P. Smith, Z. Xu, G. Gaspard, C.J. Hyde, W.W. Wits, I.A. Ashcroft, H. Chen, A.T. Clare, Powder Bed Fusion of nickel-based superalloys: A review, Int. J. Mach. Tools Manuf. 165 (2021) 103729. https://doi.org/10.1016/j.ijmachtools.2021.103729.

[4] F. Caiazzo, V. Alfieri, G. Corrado, P. Argenio, Laser powder-bed fusion of Inconel 718 to manufacture turbine blades, Int. J. Adv. Manuf. Technol. 93 (2017) 4023–4031. https://doi.org/10.1007/s00170-017-0839-3.

[5] D. Du, L. Wang, A. Dong, W. Yan, G. Zhu, B. Sun, Promoting the densification and grain refinement with assistance of static magnetic field in laser powder bed fusion, Int. J. Mach. Tools Manuf. 183 (2022) 103965. https://doi.org/10.1016/j.ijmachtools.2022.103965.

[6] M. Liu, K. Wei, X. Zeng, High power laser powder bed fusion of AlSi10Mg alloy: Effect of layer thickness on defect, microstructure and mechanical property, Mater. Sci. Eng. A. 842 (2022) 143107. https://doi.org/10.1016/j.msea.2022.143107.

[7] L. Yang, K. V. Patel, K. Jarosz, T. Özel, Surface integrity induced in machining additively fabricated nickel alloy Inconel 625, in: Procedia CIRP, Elsevier, 2020: pp. 351–354. https://doi.org/10.1016/j.procir.2020.02.104.

[8] N. Ahmed, I. Barsoum, G. Haidemenopoulos, R.K.A. Al-Rub, Process parameter selection and optimization of laser powder bed fusion for 316L stainless steel: A review, J. Manuf. Process. 75 (2022) 415–434. https://doi.org/10.1016/J.JMAPRO.2021.12.064.

[9] H. Jia, H. Sun, H. Wang, Y. Wu, H. Wang, Scanning strategy in selective laser melting (SLM): a review, Int. J. Adv. Manuf. Technol. 113 (2021) 2413–2435. https://doi.org/10.1007/s00170-021-06810-3.

[10] S. Suresh, Graded Materials for Resistance to Contact Deformation and Damage, Science (80-.). 292 (2001) 2447–2451. https://doi.org/10.1126/science.1059716.

[11] X. Wu, M. Yang, F. Yuan, G. Wu, Y. Wei, X. Huang, Y. Zhu, Heterogeneous lamella structure unites ultrafine-grain strength with coarse-grain ductility, Proc. Natl. Acad. Sci. 112 (2015) 14501–14505. https://doi.org/10.1073/pnas.1517193112.

[12] M. Cloots, P.J. Uggowitzer, K. Wegener, Investigations on the microstructure and crack formation of IN738LC samples processed by selective laser melting using Gaussian and doughnut profiles, Mater. Des. 89 (2016) 770–784. https://doi.org/10.1016/j.matdes.2015.10.027.

[13] J. Noronha, M. Leary, M. Qian, E. Kyriakou, M. Brandt, Geometrical parameters and mechanical properties of Ti6Al4V hollow-walled lattices, Mater. Sci. Eng. A. 840 (2022) 142667. https://doi.org/10.1016/j.msea.2022.142667.

[14] S.I. Shahabad, U. Ali, Z. Zhang, A. Keshavarzkermani, R. Esmaeilizadeh, A. Bonakdar, E. Toyserkani, On the effect of thin-wall thickness on melt pool dimensions in laser powder-bed fusion of Hastelloy X: Numerical modeling and experimental validation, J. Manuf. Process. 75 (2022) 435–449. https://doi.org/10.1016/j.jmapro.2022.01.029.

[15] C. Guo, Y. Zhou, X. Li, X. Hu, Z. Xu, E. Dong, Q. Zhu, R. Mark Ward, A comparing study of defect generation in IN738LC superalloy fabricated by laser powder bed fusion: Continuous-wave mode versus pulsed-wave mode, J. Mater. Sci. Technol. 90 (2021) 45–57. https://doi.org/10.1016/J.JMST.2021.03.006.

[16] S. Periane, A. Duchosal, S. Vaudreuil, H. Chibane, A. Morandeau, J. Cormier, R. Leroy, Machining influence on the fatigue resistance of Inconel 718 fabricated by Selective Laser Melting (SLM), Procedia Struct. Integr. 19 (2019) 415–422. https://doi.org/10.1016/j.prostr.2019.12.045.

[17] D. Liu, C. Ni, Y. Wang, L. Zhu, Review of serrated chip characteristics and formation mechanism from conventional to additively manufactured titanium alloys, J. Alloys Compd. 970 (2024) 172573. https://doi.org/10.1016/J.JALLCOM.2023.172573.

[18] K. Kadirgama, W.S.W. Harun, F. Tarlochan, M. Samykano, D. Ramasamy, M.Z. Azir, H. Mehboob, Statistical and optimize of lattice structures with selective laser melting (SLM) of Ti6AL4V material, Int. J. Adv. Manuf. Technol. 97 (2018) 495–510. https://doi.org/10.1007/s00170-018-1913-1.

[19] R. Paul, S. Anand, A new Steiner patch based file format for Additive Manufacturing processes, CAD Comput. Aided Des. 63 (2015) 86–100. https://doi.org/10.1016/j.cad.2015.01.002.

[20] I. Gibson, D. Rosen, B. Stucker, M. Khorasani, Additive manufacturing technologies, Springer, New York, NY, 2014. https://doi.org/10.1007/978-1-4939-2113-3.

[21] C. Zhang, H. Li, P. Eisenlohr, W. Liu, C.J. Boehlert, M.A. Crimp, T.R.

Bieler, Effect of realistic 3D microstructure in crystal plasticity finite element analysis of polycrystalline Ti-5Al-2.5Sn, Int. J. Plast. 69 (2015) 21–35. https://doi.org/10.1016/j.ijplas.2015.01.003.

[22] M.J. Matthews, G. Guss, S.A. Khairallah, A.M. Rubenchik, P.J. Depond, W.E. King, Denudation of metal powder layers in laser powder bed fusion processes, Acta Mater. 114 (2016) 33–42. https://doi.org/10.1016/j.actamat.2016.05.017.

[23] M. Yang, L. Wang, W. Yan, Phase-field modeling of grain evolutions in additive manufacturing from nucleation, growth, to coarsening, Npj Comput. Mater. 7 (2021) 56. https://doi.org/10.1038/s41524-021-00524-6.

[24] L. Li, H. Chen, X. Wang, Z. Liao, Effects of vector length on the melt pool morphology and grain structure characteristics of Alloy 718 in laser powder bed fusion, J. Mater. Process. Technol. 326 (2024) 118317. https://doi.org/10.1016/j.jmatprotec.2024.118317.

[25] I. Gibson, D. Rosen, B. Stucker, Directed Energy Deposition Processes, in: Addit. Manuf. Technol., Springer New York, New York, NY, 2015: pp. 245–268. https://doi.org/10.1007/978-1-4939-2113-3_10.

[26] D.G. Ahn, Directed Energy Deposition (DED) Process: State of the Art, Int. J. Precis. Eng. Manuf. - Green Technol. 8 (2021) 703–742. https://doi.org/10.1007/s40684-020-00302-7.

[27] Y.L. Yap, C. Wang, S.L. Sing, V. Dikshit, W.Y. Yeong, J. Wei, Material jetting additive manufacturing: An experimental study using designed metrological benchmarks, Precis. Eng. 50 (2017) 275–285. https://doi.org/10.1016/J.PRECISIONENG.2017.05.015.

[28] J. Dilag, T. Chen, S. Li, S.A. Bateman, Design and direct additive manufacturing of three-dimensional surface micro-structures using material jetting technologies, Addit. Manuf. 27 (2019) 167–174. https://doi.org/10.1016/j.addma.2019.01.009.

[29] S.M. Gaytan, M.A. Cadena, H. Karim, D. Delfin, Y. Lin, D. Espalin, E. MacDonald, R.B. Wicker, Fabrication of barium titanate by binder jetting additive manufacturing technology, Ceram. Int. 41 (2015) 6610–6619. https://doi.org/10.1016/j.ceramint.2015.01.108.

[30] T. Obikawa, M. Yoshino, J. Shinozuka, Sheet steel lamination for rapid manufacturing, J. Mater. Process. Technol. 89–90 (1999) 171–176. https://doi.org/10.1016/S0924-0136(99)00027-8.

[31] E.M. Fayed, M. Saadati, D. Shahriari, V. Brailovski, M. Jahazi, M. Medraj, Effect of homogenization and solution treatments time on the elevated-temperature mechanical behavior of Inconel 718 fabricated by laser powder bed fusion, Sci. Rep. 11 (2021) 1–17. https://doi.org/10.1038/s41598-021-81618-5.

[32] M.J. Paul, Q. Liu, J.P. Best, X. Li, J.J. Kruzic, U. Ramamurty, B. Gludovatz, Fracture resistance of AlSi10Mg fabricated by laser powder bed fusion, Acta Mater. 211 (2021) 116869. https://doi.org/10.1016/j.actamat.2021.116869.

[33] A. Chakraborty, R. Tangestani, R. Batmaz, W. Muhammad, P. Plamondon, A. Wessman, L. Yuan, É. Martin, In-process failure analysis of thin-wall structures made by laser powder bed fusion additive manufacturing, J. Mater. Sci. Technol. 98 (2022) 233–243. https://doi.org/10.1016/j.jmst.2021.05.017.

[34] F. Trevisan, F. Calignano, M. Lorusso, J. Pakkanen, A. Aversa, E.P. Ambrosio, M. Lombardi, P. Fino, D. Manfredi, On the selective laser melting (SLM) of the AlSi10Mg alloy: Process, microstructure, and mechanical properties, Materials (Basel). 10 (2017) 76. https://doi.org/10.3390/ma10010076.

[35] C. Ni, L. Zhu, Z. Zheng, J. Zhang, Y. Yang, R. Hong, Y. Bai, W.F. Lu, H. Wang, Effects of machining surface and laser beam scanning strategy on machinability of selective laser melted Ti6Al4V alloy in milling, Mater. Des. 194 (2020) 108880. https://doi.org/10.1016/j.matdes.2020.108880.

[36] A. Mostafa, I.P. Rubio, V. Brailovski, M. Jahazi, M. Medraj, Structure, texture and phases in 3D printed IN718 alloy subjected to homogenization and HIP treatments, Metals (Basel). 7 (2017) 1–23. https://doi.org/10.3390/met7060196.

[37] T. Scharowsky, F. Osmanlic, R.F. Singer, C. Körner, Melt pool dynamics during selective electron beam melting, Appl. Phys. A. 114 (2014) 1303–1307. https://doi.org/10.1007/s00339-013-7944-4.

[38] R. Jiang, A. Mostafaei, Z. Wu, A. Choi, P.-W.W. Guan, M. Chmielus, A.D. Rollett, Effect of heat treatment on microstructural evolution and hardness homogeneity in laser powder bed fusion of alloy 718, Addit. Manuf. 35 (2020) 101282. https://doi.org/10.1016/j.addma.2020.101282.

[39] J. Li, Z. Zhao, P. Bai, H. Qu, B. Liu, L. Li, L. Wu, R. Guan, H. Liu, Z. Guo, Microstructural evolution and mechanical properties of IN718 alloy fabricated by selective laser melting following different heat treatments, J. Alloys Compd. 772 (2019) 861–870. https://doi.org/10.1016/j.jallcom.2018.09.200.

[40] R. Wang, D. Gu, K. Lin, C. Chen, Q. Ge, D. Li, Multi-material additive manufacturing of a bio-inspired layered ceramic/metal structure: Formation mechanisms and mechanical properties, Int. J. Mach. Tools Manuf. 175 (2022) 103872. https://doi.org/10.1016/j.ijmachtools.2022.103872.

[41] C. Wei, L. Liu, Y. Gu, Y. Huang, Q. Chen, Z. Li, L. Li, Multi-material additive-manufacturing of tungsten - copper alloy bimetallic structure with a stainless-steel interlayer and associated bonding mechanisms, Addit. Manuf. 50 (2022) 102574. https://doi.org/10.1016/j.addma.2021.102574.

[42] J. Yin, D. Wang, H. Wei, L. Yang, L. Ke, M. Hu, W. Xiong, G. Wang, H. Zhu, X. Zeng, Dual-beam laser-matter interaction at overlap region during multi-laser powder bed fusion manufacturing, Addit. Manuf. 46 (2021) 102178. https://doi.org/10.1016/j.addma.2021.102178.

[43] A.R. Bakhtari, H.K. Sezer, O.E. Canyurt, O. Eren, M. Shah, S. Marimuthu, A Review on Laser Beam Shaping Application in Laser-Powder Bed Fusion, Adv. Eng. Mater. 26 (2024) 2302013. https://doi.org/10.1002/adem.202302013.

[44] SCANLAB, “Installation and Operation - RTC5”., 2014.

[45] F.H. Kim, H. Yeung, E.J. Garboczi, Characterizing the effects of laser control in laser powder bed fusion on near-surface pore formation via combined analysis of in-situ melt pool monitoring and X-ray computed tomography, Addit. Manuf. 48 (2021) 102372. https://doi.org/10.1016/j.addma.2021.102372.

[46] D.M. Goodarzi, J. Pekkarinen, A. Salminen, Effect of process parameters in laser cladding on substrate melted areas and the substrate melted shape, J. Laser Appl. 27 (2015) S29201. https://doi.org/10.2351/1.4906376.

[47] B. Cheng, S. Shrestha, K. Chou, Stress and deformation evaluations of scanning strategy effect in selective laser melting, Addit. Manuf. 12 (2016) 240–251. https://doi.org/10.1016/j.addma.2016.05.007.

[48] W. Shi, Y. Liu, X. Shi, Y. Hou, P. Wang, G. Song, Beam Diameter Dependence of Performance in Thick-Layer and High-Power Selective Laser Melting of Ti-6Al-4V, Materials (Basel). 11 (2018). https://doi.org/10.3390/ma11071237.

[49] E. Vaglio, T. De Monte, A. Lanzutti, G. Totis, M. Sortino, L. Fedrizzi, Single tracks data obtained by selective laser melting of Ti6Al4V with a small laser spot diameter, Data Br. 33 (2020) 106443. https://doi.org/10.1016/j.dib.2020.106443.

[50] X. Wang, T. Keya, K. Chou, Build Height Effect on the Inconel 718 Parts Fabricated by Selective Laser Melting, Procedia Manuf. 5 (2016) 1006–1017. https://doi.org/10.1016/j.promfg.2016.08.089.

[51] D. Zhang, Z. Feng, C. Wang, W. Wang, Z. Liu, W. Niu, Comparison of microstructures and mechanical properties of Inconel 718 alloy processed by selective laser melting and casting, Mater. Sci. Eng. A. 724 (2018) 357–367. https://doi.org/10.1016/j.msea.2018.03.073.

[52] E. Chlebus, K. Gruber, B. Kuźnicka, J. Kurzac, T. Kurzynowski, Effect of heat treatment on the microstructure and mechanical properties of Inconel 718 processed by selective laser melting, Mater. Sci. Eng. A. 639 (2015) 647–655. https://doi.org/10.1016/j.msea.2015.05.035.

[53] K.N. Amato, S.M. Gaytan, L.E. Murr, E. Martinez, P.W. Shindo, J.

Hernandez, S. Collins, F. Medina, Microstructures and mechanical behavior of Inconel 718 fabricated by selective laser melting, Acta Mater. 60 (2012) 2229–2239. https://doi.org/10.1016/j.actamat.2011.12.032.

[54] U. Scipioni Bertoli, A.J. Wolfer, M.J. Matthews, J.-P.R. Delplanque, J.M. Schoenung, On the limitations of Volumetric Energy Density as a design parameter for Selective Laser Melting, Mater. Des. 113 (2017) 331–340. https://doi.org/10.1016/j.matdes.2016.10.037.

[55] M. Ghayoor, K. Lee, Y. He, C. Chang, B.K. Paul, S. Pasebani, Selective laser melting of 304L stainless steel: Role of volumetric energy density on the microstructure, texture and mechanical properties, Addit. Manuf. 32 (2020) 101011. https://doi.org/10.1016/j.addma.2019.101011.

[56] J. Metelkova, Y. Kinds, K. Kempen, C. de Formanoir, A. Witvrouw, B. Van Hooreweder, On the influence of laser defocusing in Selective Laser Melting of 316L, Addit. Manuf. 23 (2018) 161–169. https://doi.org/10.1016/j.addma.2018.08.006.

[57] L. Wang, Q.S. Wei, Y.S. Shi, J.H. Liu, W.T. He, Experimental Investigation into the Single-Track of Selective Laser Melting of IN625, Adv. Mater. Res. 233–235 (2011) 2844–2848. https://doi.org/10.4028/www.scientific.net/AMR.233-235.2844.

[58] T. Yang, T. Liu, W. Liao, E. MacDonald, H. Wei, X. Chen, L. Jiang, The influence of process parameters on vertical surface roughness of the AlSi10Mg parts fabricated by selective laser melting, J. Mater. Process. Technol. 266 (2019) 26–36. https://doi.org/10.1016/j.jmatprotec.2018.10.015.

[59] Y. Huang, L.J. Yang, X.Z. Du, Y.P. Yang, Finite element analysis of thermal behavior of metal powder during selective laser melting, Int. J. Therm. Sci. 104 (2016) 146–157. https://doi.org/10.1016/j.ijthermalsci.2016.01.007.

[60] H.C.. Ho, I. Gibson, W.. Cheung, Effects of energy density on morphology and properties of selective laser sintered polycarbonate, J. Mater. Process. Technol. 89–90 (1999) 204–210. https://doi.org/10.1016/S0924-0136(99)00007-2.

[61] V.E. Beal, R.A. Paggi, G. V. Salmoria, A. Lago, Statistical evaluation of laser energy density effect on mechanical properties of polyamide parts manufactured by selective laser sintering, J. Appl. Polym. Sci. 113 (2009) 2910–2919. https://doi.org/10.1002/app.30329.

[62] K. V. Yang, P. Rometsch, T. Jarvis, J. Rao, S. Cao, C. Davies, X. Wu, Porosity formation mechanisms and fatigue response in Al-Si-Mg alloys made by selective laser melting, Mater. Sci. Eng. A. 712 (2018) 166–174. https://doi.org/10.1016/j.msea.2017.11.078.

[63] H.Y. Wan, Z.J. Zhou, C.P. Li, G.F. Chen, G.P. Zhang, Effect of scanning strategy on grain structure and crystallographic texture of Inconel 718

processed by selective laser melting, J. Mater. Sci. Technol. 34 (2018) 1799–1804. https://doi.org/10.1016/j.jmst.2018.02.002.

[64] Y. Lu, S. Wu, Y. Gan, T. Huang, C. Yang, L. Junjie, J. Lin, Study on the microstructure, mechanical property and residual stress of SLM Inconel-718 alloy manufactured by differing island scanning strategy, Opt. Laser Technol. 75 (2015) 197–206. https://doi.org/10.1016/j.optlastec.2015.07.009.

[65] K.S. Al-Rubaie, S. Melotti, A. Rabelo, J.M. Paiva, M.A. Elbestawi, S.C. Veldhuis, Machinability of SLM-produced Ti6Al4V titanium alloy parts, J. Manuf. Process. 57 (2020) 768–786. https://doi.org/10.1016/j.jmapro.2020.07.035.

[66] B. Liu, B.-Q. Li, Z. Li, Selective laser remelting of an additive layer manufacturing process on AlSi10Mg, Results Phys. 12 (2019) 982–988. https://doi.org/10.1016/j.rinp.2018.12.018.

[67] L.N. Carter, C. Martin, P.J. Withers, M.M. Attallah, The influence of the laser scan strategy on grain structure and cracking behaviour in SLM powder-bed fabricated nickel superalloy, J. Alloys Compd. 615 (2014) 338–347. https://doi.org/10.1016/j.jallcom.2014.06.172.

[68] S.-H. Sun, K. Hagihara, T. Nakano, Effect of scanning strategy on texture formation in Ni-25 at.%Mo alloys fabricated by selective laser melting, Mater. Des. 140 (2018) 307–316. https://doi.org/10.1016/j.matdes.2017.11.060.

[69] L. Zhou, A. Mehta, B. McWilliams, K. Cho, Y. Sohn, Microstructure, precipitates and mechanical properties of powder bed fused inconel 718 before and after heat treatment, J. Mater. Sci. Technol. 35 (2019) 1153–1164. https://doi.org/10.1016/j.jmst.2018.12.006.

[70] D. Ramos, F. Belblidia, J. Sienz, New scanning strategy to reduce warpage in additive manufacturing, Addit. Manuf. 28 (2019) 554–564. https://doi.org/10.1016/j.addma.2019.05.016.

[71] M. Calandri, S. Yin, B. Aldwell, F. Calignano, R. Lupoi, D. Ugues, Texture and microstructural features at different length scales in Inconel 718 produced by selective laser melting, Materials (Basel). 12 (2019). https://doi.org/10.3390/ma12081293.

[72] L. Thijs, K. Kempen, J.-P. Kruth, J. Van Humbeeck, Fine-structured aluminium products with controllable texture by selective laser melting of pre-alloyed AlSi10Mg powder, Acta Mater. 61 (2013) 1809–1819. https://doi.org/10.1016/j.actamat.2012.11.052.

[73] T. Larimian, M. Kannan, D. Grzesiak, B. AlMangour, T. Borkar, Effect of energy density and scanning strategy on densification, microstructure and mechanical properties of 316L stainless steel processed via selective laser melting, Mater. Sci. Eng. A. 770 (2020) 138455. https://doi.org/10.1016/j.msea.2019.138455.

[74] H.Y.Y. Wan, Z.J.J. Zhou, C.P.P. Li, G.F.F. Chen, G.P.P. Zhang, Effect of scanning strategy on mechanical properties of selective laser melted Inconel 718, Mater. Sci. Eng. A. 753 (2019) 42–48. https://doi.org/10.1016/j.msea.2019.03.007.

[75] A. De Bartolomeis, S.T. Newman, I.S. Jawahir, D. Biermann, A. Shokrani, Future research directions in the machining of Inconel 718, J. Mater. Process. Technol. 297 (2021) 117260. https://doi.org/10.1016/j.jmatprotec.2021.117260.

[76] T. Sonar, V. Balasubramanian, S. Malarvizhi, T. Venkateswaran, D. Sivakumar, An overview on welding of Inconel 718 alloy - Effect of welding processes on microstructural evolution and mechanical properties of joints, Mater. Charact. 174 (2021) 110997. https://doi.org/10.1016/j.matchar.2021.110997.

[77] E. Hosseini, V.A. Popovich, A review of mechanical properties of additively manufactured Inconel 718, Addit. Manuf. 30 (2019) 100877. https://doi.org/10.1016/j.addma.2019.100877.

[78] R. Lawitzki, S. Hassan, L. Karge, J. Wagner, D. Wang, J. von Kobylinski, C. Krempaszky, M. Hofmann, R. Gilles, G. Schmitz, Differentiation of γ′- and γ″- precipitates in Inconel 718 by a complementary study with small-angle neutron scattering and analytical microscopy, Acta Mater. 163 (2019) 28–39. https://doi.org/10.1016/j.actamat.2018.10.014.

[79] D. Connétable, M. Mathon, J. Lacaze, First principle energies of binary and ternary phases of the Fe-Nb-Ni-Cr system, Calphad Comput. Coupling Phase Diagrams Thermochem. 35 (2011) 588–593. https://doi.org/10.1016/j.calphad.2011.09.004.

[80] A. Strondl, R. Fischer, G. Frommeyer, A. Schneider, Investigations of MX and γ′/γ″ precipitates in the nickel-based superalloy 718 produced by electron beam melting, Mater. Sci. Eng. A. 480 (2008) 138–147. https://doi.org/10.1016/j.msea.2007.07.012.

[81] L.Y. Wang, Z.J. Zhou, C.P. Li, G.F. Chen, G.P. Zhang, Comparative investigation of small punch creep resistance of Inconel 718 fabricated by selective laser melting, Mater. Sci. Eng. A. 745 (2019) 31–38. https://doi.org/10.1016/j.msea.2018.12.083.

[82] Z.H. Xiong, S.L. Liu, S.F. Li, Y. Shi, Y.F. Yang, R.D.K. Misra, Role of melt pool boundary condition in determining the mechanical properties of selective laser melting AlSi10Mg alloy, Mater. Sci. Eng. A. 740–741 (2019) 148–156. https://doi.org/10.1016/j.msea.2018.10.083.

[83] Y.-N. Zhang, X. Cao, P. Wanjara, M. Medraj, Tensile properties of laser additive manufactured Inconel 718 using filler wire, J. Mater. Res. 29 (2014) 2006–2020. https://doi.org/10.1557/jmr.2014.199.

[84] L.-S.-B. Ling, Z. Yin, Z. Hu, J.-H. Liang, Z.-Y. Wang, J. Wang, B.-D. Sun,

Effects of the γ″-Ni3Nb Phase on Mechanical Properties of Inconel 718 Superalloys with Different Heat Treatments, Materials (Basel). 13 (2019) 151. https://doi.org/10.3390/ma13010151.

[85] J.F. Radavich, The Physical Metallurgy of Cast and Wrought Alloy 718, in: Superalloys 718 Metall. Appl., TMS, 2004: pp. 229–240. https://doi.org/10.7449/1989/Superalloys_1989_229_240.

[86] J.F. Radavich, Metallography of Alloy 718, JOM. 40 (1988) 42–43. https://doi.org/10.1007/BF03258150.

[87] X. Li, J.J. Shi, C.H. Wang, G.H. Cao, A.M. Russell, Z.J. Zhou, C.P. Li, G.F. Chen, Effect of heat treatment on microstructure evolution of Inconel 718 alloy fabricated by selective laser melting, J. Alloys Compd. 764 (2018) 639–649. https://doi.org/10.1016/j.jallcom.2018.06.112.

[88] M.J. Donachie, S.J. Donachie, Superalloys, ASM International, 2002. https://doi.org/10.31399/asm.tb.stg2.9781627082679.

[89] M.C. Chaturvedi, Y. Han, Strengthening mechanisms in Inconel 718 superalloy, Met. Sci. 17 (1983) 145–149. https://doi.org/10.1179/030634583790421032.

[90] Y. Han, P. Deb, M.C. Chaturvedi, Coarsening behaviour of γ″- and γ′-particles in Inconel alloy 718, Met. Sci. 16 (1982) 555–562. https://doi.org/10.1179/030634582790427118.

[91] M. Zheng, L. Wei, J. Chen, Q. Zhang, G. Zhang, X. Lin, W. Huang, On the role of energy input in the surface morphology and microstructure during selective laser melting of Inconel 718 alloy, J. Mater. Res. Technol. 11 (2021) 392–403. https://doi.org/10.1016/j.jmrt.2021.01.024.

[92] P. Tao, H. Li, B. Huang, Q. Hu, S. Gong, Q. Xu, The crystal growth, intercellular spacing and microsegregation of selective laser melted Inconel 718 superalloy, Vacuum. 159 (2019) 382–390. https://doi.org/10.1016/j.vacuum.2018.10.074.

[93] S. Luo, W. Huang, H. Yang, J. Yang, Z. Wang, X. Zeng, Microstructural evolution and corrosion behaviors of Inconel 718 alloy produced by selective laser melting following different heat treatments, Addit. Manuf. 30 (2019) 100875. https://doi.org/10.1016/j.addma.2019.100875.

[94] T. Pinomaa, A. Laukkanen, N. Provatas, Solute trapping in rapid solidification, MRS Bull. 45 (2020) 910–915. https://doi.org/10.1557/mrs.2020.274.

[95] M.J. Sohrabi, H. Mirzadeh, M. Rafiei, Solidification behavior and Laves phase dissolution during homogenization heat treatment of Inconel 718 superalloy, Vacuum. 154 (2018) 235–243. https://doi.org/10.1016/j.vacuum.2018.05.019.

[96] V.A. Popovich, E.V. Borisov, A.A. Popovich, V.S. Sufiiarov, D.V. Masaylo,

L. Alzina, Impact of heat treatment on mechanical behaviour of Inconel 718 processed with tailored microstructure by selective laser melting, Mater. Des. 131 (2017) 12–22. https://doi.org/10.1016/j.matdes.2017.05.065.

[97] M. Ni, C. Chen, X. Wang, P. Wang, R. Li, X. Zhang, K. Zhou, Anisotropic tensile behavior of in situ precipitation strengthened Inconel 718 fabricated by additive manufacturing, Mater. Sci. Eng. A. 701 (2017) 344–351. https://doi.org/10.1016/j.msea.2017.06.098.

[98] M.M. Kirka, D.A. Greeley, C. Hawkins, R.R. Dehoff, Effect of anisotropy and texture on the low cycle fatigue behavior of Inconel 718 processed via electron beam melting, Int. J. Fatigue. 105 (2017) 235–243. https://doi.org/10.1016/j.ijfatigue.2017.08.021.

[99] D.H. Smith, J. Bicknell, L. Jorgensen, B.M. Patterson, N.L. Cordes, I. Tsukrov, M. Knezevic, Microstructure and mechanical behavior of direct metal laser sintered Inconel alloy 718, Mater. Charact. 113 (2016) 1–9. https://doi.org/10.1016/j.matchar.2016.01.003.

[100] S.A. Khairallah, A. Anderson, Mesoscopic simulation model of selective laser melting of stainless steel powder, J. Mater. Process. Technol. 214 (2014) 2627–2636. https://doi.org/10.1016/j.jmatprotec.2014.06.001.

[101] K.Q. Le, C.H. Wong, K.H.G. Chua, C. Tang, H. Du, Discontinuity of overhanging melt track in selective laser melting process, Int. J. Heat Mass Transf. 162 (2020) 120284. https://doi.org/10.1016/j.ijheatmasstransfer.2020.120284.

[102] H. Gu, C. Wei, L. Li, Q. Han, R. Setchi, M. Ryan, Q. Li, Multi-physics modelling of molten pool development and track formation in multi-track, multi-layer and multi-material selective laser melting, Int. J. Heat Mass Transf. 151 (2020) 119458. https://doi.org/10.1016/j.ijheatmasstransfer.2020.119458.

[103] Z. Wang, M. Liu, Dimensionless analysis on selective laser melting to predict porosity and track morphology, J. Mater. Process. Technol. 273 (2019) 116238. https://doi.org/10.1016/j.jmatprotec.2019.05.019.

[104] J.J.S.S. Dilip, S. Zhang, C. Teng, K. Zeng, C. Robinson, D. Pal, B. Stucker, Influence of processing parameters on the evolution of melt pool, porosity, and microstructures in Ti-6Al-4V alloy parts fabricated by selective laser melting, Prog. Addit. Manuf. 2 (2017) 157–167. https://doi.org/10.1007/s40964-017-0030-2.

[105] J.I. Arrizubieta, A. Lamikiz, F. Klocke, S. Martínez, K. Arntz, E. Ukar, Evaluation of the relevance of melt pool dynamics in Laser Material Deposition process modeling, Int. J. Heat Mass Transf. 115 (2017) 80–91. https://doi.org/10.1016/j.ijheatmasstransfer.2017.07.011.

[106] K. Solberg, D. Wan, F. Berto, Fatigue assessment of as-built and heat-treated Inconel 718 specimens produced by additive manufacturing including notch

effects, Fatigue Fract. Eng. Mater. Struct. 43 (2020) 2326–2336. https://doi.org/10.1111/ffe.13300.

[107] S. Tabaie, F. Rézaï-Aria, M. Jahazi, F. Réza\"\i-Aria, M. Jahazi, F. Rézaï-Aria, M. Jahazi, Microstructure evolution of selective laser melted inconel 718: Influence of high heating rates, Metals (Basel). 10 (2020) 587. https://doi.org/10.3390/met10050587.

[108] R. Zhao, Z. Zhao, P. Bai, W. Du, L. Zhang, H. Qu, Effect of Heat Treatment on the Microstructure and Properties of Inconel 718 Alloy Fabricated by Selective Laser Melting, J. Mater. Eng. Perform. 31 (2022) 353–364. https://doi.org/10.1007/s11665-021-06212-2.

[109] X. Li, J.J. Shi, G.H. Cao, A.M. Russell, Z.J. Zhou, C.P. Li, G.F. Chen, Improved plasticity of Inconel 718 superalloy fabricated by selective laser melting through a novel heat treatment process, Mater. Des. 180 (2019) 107915. https://doi.org/10.1016/j.matdes.2019.107915.

[110] J. Lee, M. Lee, I.D. Jung, J. Choe, J.-H. Yu, S. Kim, H. Sung, Correlation Between Microstructure and Tensile Properties of STS 316L and Inconel 718 Fabricated by Selective Laser Melting (SLM), J. Nanosci. Nanotechnol. 20 (2020) 6807–6814. https://doi.org/10.1166/jnn.2020.18792.

[111] M. Amirjan, H. Sakiani, A. Mostafa, S. Hassan, Effect of scanning strategy and speed on the microstructure and mechanical properties of selective laser melted IN718 nickel-based superalloy, Int. J. Adv. Manuf. Technol. 103 (2019) 1769–1780. https://doi.org/10.1007/s00170-019-03545-0.

[112] D. Wang, S. Wu, F. Fu, S. Mai, Y. Yang, Y. Liu, C. Song, Mechanisms and characteristics of spatter generation in SLM processing and its effect on the properties, Mater. Des. 117 (2017) 121–130. https://doi.org/10.1016/j.matdes.2016.12.060.

[113] M. Simonelli, C. Tuck, N.T. Aboulkhair, I. Maskery, I. Ashcroft, R.D. Wildman, R. Hague, A Study on the Laser Spatter and the Oxidation Reactions During Selective Laser Melting of 316L Stainless Steel, Al-Si10-Mg, and Ti-6Al-4V, Metall. Mater. Trans. A. 46 (2015) 3842–3851. https://doi.org/10.1007/s11661-015-2882-8.

[114] V. Gunenthiram, P. Peyre, M. Schneider, M. Dal, F. Coste, I. Koutiri, R. Fabbro, Experimental analysis of spatter generation and melt-pool behavior during the powder bed laser beam melting process, J. Mater. Process. Technol. 251 (2018) 376–386. https://doi.org/10.1016/j.jmatprotec.2017.08.012.

[115] S. Shrestha, K. Chou, Computational Analysis of Thermo-Fluid Dynamics with Metallic Powder in SLM, in: TMS Annu. Meet. Exhib., Springer, Cham, 2018: pp. 85–95. https://doi.org/10.1007/978-3-319-72059-3_9.

[116] W. Gao, J. Lu, J. Zhou, L. Liu, J. Wang, Y. Zhang, Z. Zhang, Effect of grain size on deformation and fracture of Inconel718: An in-situ SEM-EBSD-DIC

investigation, Mater. Sci. Eng. A. 861 (2022) 144361. https://doi.org/10.1016/j.msea.2022.144361.

[117] C. Wang, Y. Hu, C. Zhong, C. Lan, W. Li, X. Wang, Microstructural evolution and mechanical properties of pure Zn fabricated by selective laser melting, Mater. Sci. Eng. A. 846 (2022) 143276. https://doi.org/10.1016/j.msea.2022.143276.

[118] N. Kouraytem, J. Varga, B. Amin-Ahmadi, H. Mirmohammad, R.A. Chanut, A.D. Spear, O.T. Kingstedt, A recrystallization heat-treatment to reduce deformation anisotropy of additively manufactured Inconel 718, Mater. Des. 198 (2021) 109228. https://doi.org/10.1016/j.matdes.2020.109228.

[119] S. Holland, X. Wang, X.Y. Fang, Y.B. Guo, F. Yan, L. Li, Grain boundary network evolution in Inconel 718 from selective laser melting to heat treatment, Mater. Sci. Eng. A. 725 (2018) 406–418. https://doi.org/10.1016/j.msea.2018.04.045.

[120] C.-H. Yu, R.L. Peng, T.L. Lee, V. Luzin, J.-E. Lundgren, J. Moverare, Anisotropic behaviours of LPBF Hastelloy X under slow strain rate tensile testing at elevated temperature, Mater. Sci. Eng. A. 844 (2022) 143174. https://doi.org/10.1016/j.msea.2022.143174.

[121] V.P. Sabelkin, G.R. Cobb, B.M. Doane, R.A. Kemnitz, R.P. O’Hara, Torsional behavior of additively manufactured nickel alloy 718 under monotonic loading and low cycle fatigue, Mater. Today Commun. 24 (2020) 101256. https://doi.org/10.1016/j.mtcomm.2020.101256.

[122] J.H. Yi, J.W. Kang, T.J. Wang, X. Wang, Y.Y. Hu, T. Feng, Y.L. Feng, P.Y. Wu, Effect of laser energy density on the microstructure, mechanical properties, and deformation of Inconel 718 samples fabricated by selective laser melting, J. Alloys Compd. 786 (2019) 481–488. https://doi.org/10.1016/j.jallcom.2019.01.377.

[123] K. Moussaoui, W. Rubio, M. Mousseigne, T. Sultan, F. Rezai, Effects of Selective Laser Melting additive manufacturing parameters of Inconel 718 on porosity, microstructure and mechanical properties, Mater. Sci. Eng. A. 735 (2018) 182–190. https://doi.org/10.1016/j.msea.2018.08.037.

[124] S. Holland, X. Wang, J. Chen, W. Cai, F. Yan, L. Li, Multiscale characterization of microstructures and mechanical properties of Inconel 718 fabricated by selective laser melting, J. Alloys Compd. 784 (2019) 182–194. https://doi.org/10.1016/j.jallcom.2018.12.380.

[125] B. Farhang, B.B. Ravichander, J. Ma, A. Amerinatanzi, N. Shayesteh Moghaddam, The evolution of microstructure and composition homogeneity induced by borders in laser powder bed fused Inconel 718 parts, J. Alloys Compd. 898 (2022) 162787. https://doi.org/10.1016/j.jallcom.2021.162787.

[126] B. Stegman, A. Shang, L. Hoppenrath, A. Raj, H. Abdel-Khalik, J. Sutherland, D. Schick, V. Morgan, K. Jackson, X. Zhang, Volumetric energy

density impact on mechanical properties of additively manufactured 718 Ni alloy, Mater. Sci. Eng. A. 854 (2022) 143699. https://doi.org/10.1016/j.msea.2022.143699.

[127] V.A. Popovich, E. V. Borisov, A.A. Popovich, V.S. Sufiiarov, D. V. Masaylo, L. Alzina, Functionally graded Inconel 718 processed by additive manufacturing: Crystallographic texture, anisotropy of microstructure and mechanical properties, Mater. Des. 114 (2017) 441–449. https://doi.org/10.1016/j.matdes.2016.10.075.

[128] O. Gokcekaya, T. Ishimoto, S. Hibino, J. Yasutomi, T. Narushima, T. Nakano, Unique crystallographic texture formation in Inconel 718 by laser powder bed fusion and its effect on mechanical anisotropy, Acta Mater. 212 (2021) 116876. https://doi.org/10.1016/j.actamat.2021.116876.

[129] X. Liu, K. Wang, P. Hu, X. He, B. Yan, X. Zhao, Formability, microstructure and properties of inconel 718 superalloy fabricated by selective laser melting additive manufacture technology, Materials (Basel). 14 (2021) 1–18. https://doi.org/10.3390/ma14040991.

[130] B. Dovgyy, A. Piglione, P.A. Hooper, M.-S. Pham, Comprehensive assessment of the printability of CoNiCrFeMn in Laser Powder Bed Fusion, Mater. Des. 194 (2020) 108845. https://doi.org/10.1016/j.matdes.2020.108845.

[131] A. Piglione, B. Dovgyy, C. Liu, C.M. Gourlay, P.A. Hooper, M.S. Pham, Printability and microstructure of the CoCrFeMnNi high-entropy alloy fabricated by laser powder bed fusion, Mater. Lett. 224 (2018) 22–25. https://doi.org/10.1016/j.matlet.2018.04.052.

[132] M.-S. Pham, B. Dovgyy, P.A. Hooper, C.M. Gourlay, A. Piglione, The role of side-branching in microstructure development in laser powder-bed fusion, Nat. Commun. 11 (2020) 749. https://doi.org/10.1038/s41467-020-14453-3.

[133] Z. Hao, F. Ji, Y. Fan, N. Zhang, Failure feature and characterization of material of shear band in cutting Inconel718, J. Manuf. Process. 45 (2019) 154–165. https://doi.org/10.1016/j.jmapro.2019.06.016.

[134] A. Barari, H.A. Kishawy, F. Kaji, M.A. Elbestawi, On the surface quality of additive manufactured parts, Int. J. Adv. Manuf. Technol. 89 (2017) 1969–1974. https://doi.org/10.1007/s00170-016-9215-y.

[135] K. Karami, A. Blok, L. Weber, S.M. Ahmadi, R. Petrov, K. Nikolic, E. V. Borisov, S. Leeflang, C. Ayas, A.A. Zadpoor, M. Mehdipour, E. Reinton, V.A. Popovich, Continuous and pulsed selective laser melting of Ti6Al4V lattice structures: Effect of post-processing on microstructural anisotropy and fatigue behaviour, Addit. Manuf. 36 (2020) 101433. https://doi.org/10.1016/j.addma.2020.101433.

[136] A. la Monaca, J.W. Murray, Z. Liao, A. Speidel, J.A. Robles-Linares, D.A. Axinte, M.C. Hardy, A.T. Clare, Surface integrity in metal machining - Part

II: Functional performance, Int. J. Mach. Tools Manuf. 164 (2021) 103718. https://doi.org/10.1016/j.ijmachtools.2021.103718.

[137] E. Abbá, A. Speidel, Z. Liao, D. Axinte, D. Novovic, A bar of cutting fluid: Deep Eutectic Fluids with a novel flavour, Mater. Today Adv. 16 (2022) 100291. https://doi.org/10.1016/j.mtadv.2022.100291.

[138] A. Malakizadi, D. Mallipeddi, S. Dadbakhsh, R. M'Saoubi, P. Krajnik, Post-processing of additively manufactured metallic alloys – A review, Int. J. Mach. Tools Manuf. 179 (2022) 103908. https://doi.org/10.1016/j.ijmachtools.2022.103908.

[139] Z. Zhao, L. Li, W. Yang, Y. Zeng, Y. Lian, Z. Yue, A comprehensive study of the anisotropic tensile properties of laser additive manufactured Ni-based superalloy after heat treatment, Int. J. Plast. 148 (2022) 103147. https://doi.org/10.1016/j.ijplas.2021.103147.

[140] S. Ghorbanpour, M.E. Alam, N.C. Ferreri, A. Kumar, B.A. McWilliams, S.C. Vogel, J. Bicknell, I.J. Beyerlein, M. Knezevic, Experimental characterization and crystal plasticity modeling of anisotropy, tension-compression asymmetry, and texture evolution of additively manufactured Inconel 718 at room and elevated temperatures, Int. J. Plast. 125 (2020) 63–79. https://doi.org/10.1016/j.ijplas.2019.09.002.

[141] J. Yi, J. Kang, T. Wang, X. Wang, T. Feng, Y. Feng, P. Wu, Microstructure and mechanical behavior of bright crescent areas in Inconel 718 sample fabricated by selective laser melting, Mater. Des. 197 (2021) 109259. https://doi.org/10.1016/j.matdes.2020.109259.

[142] A. Shu, J. Ren, J. Zhou, Z. Wang, Grain refinement mechanism in chip and the machined subsurface during high-speed machining of Inconel 718 alloy, Mater. Charact. 207 (2024) 113559. https://doi.org/10.1016/j.matchar.2023.113559.

[143] Q. Yin, Z. Liu, B. Wang, Q. Song, Y. Cai, Recent progress of machinability and surface integrity for mechanical machining Inconel 718: a review, Int. J. Adv. Manuf. Technol. 109 (2020) 215–245. https://doi.org/10.1007/s00170-020-05665-4.

[144] S.R. Singh, R.G. Mote, S.K. Mishra, The effect of microstructures and precipitates (γ', γ″, δ) on machinability of Inconel-718 nickel-based superalloy in turning process, J. Manuf. Process. 82 (2022) 374–389. https://doi.org/10.1016/j.jmapro.2022.08.004.

[145] P. Malm, A. Hagberg, Material deformation mechanisms during machining of superalloys, (2010).

[146] P. Hoier, A. Malakizadi, P. Stuppa, S. Cedergren, U. Klement, Microstructural characteristics of Alloy 718 and Waspaloy and their influence on flank wear during turning, Wear. 400–401 (2018) 184–193. https://doi.org/10.1016/j.wear.2018.01.011.

[147] A. Malakizadi, T. Hajali, F. Schulz, S. Cedergren, J. Ålgårdh, R. M'Saoubi, E. Hryha, P. Krajnik, The role of microstructural characteristics of additively manufactured alloy 718 on tool wear in machining, Int. J. Mach. Tools Manuf. 171 (2021) 103814. https://doi.org/10.1016/j.ijmachtools.2021.103814.

[148] J.D. Pérez-Ruiz, L.N.L. de Lacalle, G. Urbikain, O. Pereira, S. Martínez, J. Bris, On the relationship between cutting forces and anisotropy features in the milling of LPBF Inconel 718 for near net shape parts, Int. J. Mach. Tools Manuf. 170 (2021) 103801. https://doi.org/10.1016/j.ijmachtools.2021.103801.

[149] J. Weng, J. Saelzer, G. Brock, N. Ostermann, T. Grimm, J.T. Sehrt, D. Xu, K. Zhuang, D. Biermann, On machining-induced surface integrity of Inconel 718 fabricated by powder bed fusion, J. Mater. Process. Technol. 328 (2024) 118406. https://doi.org/10.1016/j.jmatprotec.2024.118406.

[150] S. Imbrogno, S. Rinaldi, D. Umbrello, L. Filice, R. Franchi, A. Del Prete, A physically based constitutive model for predicting the surface integrity in machining of Waspaloy, Mater. Des. 152 (2018) 140–155. https://doi.org/10.1016/j.matdes.2018.04.069.

[151] Z. Liao, M. Polyakov, O.G. Diaz, D. Axinte, G. Mohanty, X. Maeder, J. Michler, M. Hardy, Grain refinement mechanism of nickel-based superalloy by severe plastic deformation - Mechanical machining case, Acta Mater. 180 (2019) 2–14. https://doi.org/10.1016/j.actamat.2019.08.059.

[152] H. Liu, H. Han, Q. Jiang, M. He, B. Zhang, Characterization and Analysis of Inconel 718 Alloy Ground at Different Speeds, Chinese J. Mech. Eng. 37 (2024) 34. https://doi.org/10.1186/s10033-024-01017-5.

[153] D. Xu, T.E.J. Edwards, Z. Liao, X. Maeder, R. Ramachandramoorthy, M. Jain, J. Michler, D. Axinte, Revealing Nanoscale deformation mechanisms caused by shear-based material removal on individual grains of a Ni-based superalloy, Acta Mater. 212 (2021) 116929. https://doi.org/10.1016/j.actamat.2021.116929.

[154] B. Yang, C. Shi, R. Lai, D. Shi, D. Guan, G. Zhu, Y. Cui, G. Xie, Y. Li, A. Chiba, J. LLorca, Identification of active slip systems in polycrystals by Slip Trace - Modified Lattice Rotation Analysis (ST-MLRA), Scr. Mater. 214 (2022) 114648. https://doi.org/10.1016/j.scriptamat.2022.114648.

[155] D. Agius, A. Kareer, A. Al Mamun, C. Truman, D.M. Collins, M. Mostafavi, D. Knowles, A crystal plasticity model that accounts for grain size effects and slip system interactions on the deformation of austenitic stainless steels, Int. J. Plast. 152 (2022) 103249. https://doi.org/10.1016/j.ijplas.2022.103249.

[156] Y. Guan, B. Chen, J. Zou, T. Ben Britton, J. Jiang, F.P.E. Dunne, Crystal plasticity modelling and HR-DIC measurement of slip activation and strain

localization in single and oligo-crystal Ni alloys under fatigue, Int. J. Plast. 88 (2017) 70–88. https://doi.org/10.1016/j.ijplas.2016.10.001.

[157] T.R. Bieler, R. Alizadeh, M. Peña-Ortega, J. Llorca, An analysis of (the lack of) slip transfer between near-cube oriented grains in pure Al, Int. J. Plast. 118 (2019) 269–290. https://doi.org/10.1016/j.ijplas.2019.02.014.

[158] S. Haouala, R. Alizadeh, T.R. Bieler, J. Segurado, J. LLorca, Effect of slip transmission at grain boundaries in Al bicrystals, Int. J. Plast. 126 (2020) 102600. https://doi.org/10.1016/j.ijplas.2019.09.006.

[159] W. Zhang, H. Wu, S. Wang, Y. Hu, K. Fang, X. Wang, Investigation of Stress Corrosion Cracking Initiation in Machined 304 Austenitic Stainless Steel in Magnesium Chloride Environment, J. Mater. Eng. Perform. 29 (2020) 191–204. https://doi.org/10.1007/s11665-020-04558-7.

[160] W. Grzesik, Advanced Machining Processes of Metallic Materials: Theory, Modelling, and Applications, Elsevier, Oxford, 2016.

[161] T.G. Molnar, S. Berezvai, A.K. Kiss, D. Bachrathy, G. Stepan, Experimental investigation of dynamic chip formation in orthogonal cutting, Int. J. Mach. Tools Manuf. 145 (2019) 103429. https://doi.org/10.1016/j.ijmachtools.2019.103429.

[162] Q. Liu, Z. Liao, J. Cheng, D. Xu, M. Chen, Mechanism of chip formation and surface-defects in orthogonal cutting of soft-brittle potassium dihydrogen phosphate crystals, Mater. Des. 198 (2021) 109327. https://doi.org/10.1016/j.matdes.2020.109327.

[163] Y. Chen, J. Wang, Q. An, Mechanisms and predictive force models for machining with rake face textured cutting tools under orthogonal cutting conditions, Int. J. Mech. Sci. 195 (2021) 106246. https://doi.org/10.1016/j.ijmecsci.2020.106246.

[164] D. Xu, Z. Liao, D. Axinte, M. Hardy, R. M'Saoubi, A quick method for evaluating the thresholds of workpiece surface damage in machining, CIRP Ann. 68 (2019) 61–64. https://doi.org/10.1016/j.cirp.2019.03.015.

[165] M. Meurer, T. Augspurger, B. Tekkaya, D. Schraknepper, A.P. Lima, T. Bergs, Development of a Methodology for Strain Field Analysis during Orthogonal Cutting, in: Procedia CIRP, Elsevier, 2020: pp. 444–449. https://doi.org/10.1016/j.procir.2020.03.004.

[166] E. Ceretti, M. Lucchi, T. Altan, FEM simulation of orthogonal cutting: serrated chip formation, J. Mater. Process. Technol. 95 (1999) 17–26. https://doi.org/10.1016/S0924-0136(99)00261-7.

[167] G.W. Rowe, Principles of machining by cutting, abrasion and erosion, 1978.

[168] B. Liu, X. Zhou, X. Zhang, Orthogonal machining introduced microstructure modification in AA7150-T651 aluminium alloy, Mater. Charact. 123 (2017) 91–98. https://doi.org/10.1016/j.matchar.2016.11.015.

[169] B. Haddag, S. Atlati, M. Nouari, A. Moufki, Dry Machining Aeronautical Aluminum Alloy AA2024-T351: Analysis of Cutting Forces, Chip Segmentation and Built-Up Edge Formation, Metals (Basel). 6 (2016) 197. https://doi.org/10.3390/met6090197.

[170] M.Q. Jiang, L.H. Dai, Formation mechanism of lamellar chips during machining of bulk metallic glass, Acta Mater. 57 (2009) 2730–2738. https://doi.org/10.1016/j.actamat.2009.02.031.

[171] W. Ma, X. Chen, F. Shuang, The chip-flow behaviors and formation mechanisms in the orthogonal cutting process of Ti6Al4V alloy, J. Mech. Phys. Solids. 98 (2017) 245–270. https://doi.org/10.1016/j.jmps.2016.07.023.

[172] M. M'hamdi, S. BenSalem, M. Boujelbene, D. Katundi, E. Bayraktar, F. Chinesta, Y. Chastel, M. El Mansori, Effect of cutting parameters on the chip formation in orthogonal cutting, in: J. Achiev. Mater. Manuf. Eng., 2011: pp. 1101–1106. https://doi.org/10.1063/1.3552327.

[173] S. Sun, M. Brandt, M.S. Dargusch, Characteristics of cutting forces and chip formation in machining of titanium alloys, Int. J. Mach. Tools Manuf. 49 (2009) 561–568. https://doi.org/10.1016/j.ijmachtools.2009.02.008.

[174] M.S. Dargusch, S. Sun, J.W. Kim, T. Li, P. Trimby, J. Cairney, Effect of tool wear evolution on chip formation during dry machining of Ti-6Al-4V alloy, Int. J. Mach. Tools Manuf. 126 (2018) 13–17. https://doi.org/10.1016/j.ijmachtools.2017.12.003.

[175] C. Siemers, B. Zahra, D. Ksiezyk, P. Rokicki, Z. Spotz, L. Fusova, J. Rösler, K. Saksl, Chip Formation and Machinability of Nickel-Base Superalloys, Adv. Mater. Res. 278 (2011) 460–465. https://doi.org/10.4028/www.scientific.net/AMR.278.460.

[176] R. Suresh, S. Basavarajappa, V.N. Gaitonde, G.L. Samuel, J.P. Davim, State-of-the-art research in machinability of hardened steels, Proc. Inst. Mech. Eng. Part B J. Eng. Manuf. 227 (2013) 191–209. https://doi.org/10.1177/0954405412464589.

[177] G. Su, Z. Liu, L. Li, B. Wang, Influences of chip serration on micro-topography of machined surface in high-speed cutting, Int. J. Mach. Tools Manuf. 89 (2015) 202–207. https://doi.org/10.1016/j.ijmachtools.2014.10.012.

[178] A. la Monaca, D.A. Axinte, Z. Liao, R. M'Saoubi, M.C. Hardy, Temperature-dependent shear localisation and microstructural evolution in machining of nickel-base superalloys, Mater. Des. 219 (2022) 110792. https://doi.org/10.1016/j.matdes.2022.110792.

[179] J. Hwang, S. Chandrasekar, Contact conditions at the chip-tool interface in machining, Int. J. Precis. Eng. Manuf. 12 (2011) 183–193. https://doi.org/10.1007/s12541-011-0026-7.

[180] A. Mahato, Y. Guo, N.K. Sundaram, S. Chandrasekar, Surface folding in metals: a mechanism for delamination wear in sliding, Proc. R. Soc. A Math. Phys. Eng. Sci. 470 (2014) 20140297. https://doi.org/10.1098/rspa.2014.0297.

[181] Y. Huang, K.-M. Lee, J. Ji, W. Li, Digital Image Correlation Based on Primary Shear Band Model for Reconstructing Displacement, Strain, and Stress Fields in Orthogonal Cutting, IEEE/ASME Trans. Mechatronics. 25 (2020) 2088–2099. https://doi.org/10.1109/TMECH.2020.2991421.

[182] H. Zouabi, M. Calamaz, V. Wagner, O. Cahuc, G. Dessein, Kinematic Fields Measurement during Orthogonal Cutting Using Digital Images Correlation: A Review, J. Manuf. Mater. Process. 5 (2021) 7. https://doi.org/10.3390/jmmp5010007.

[183] S.P.F.C. Jaspers, J.H. Dautzenberg, Material behaviour in metal cutting: strains, strain rates and temperatures in chip formation, J. Mater. Process. Technol. 121 (2002) 123–135. https://doi.org/10.1016/S0924-0136(01)01227-4.

[184] M.G. Stevenson, P.L.B. Oxley, An Experimental Investigation of the Influence of Strain-Rate and Temperature on the Flow Stress Properties of a Low Carbon Steel Using a Machining Test, Proc. Inst. Mech. Eng. 185 (1970) 741–754. https://doi.org/10.1243/PIME_PROC_1970_185_088_02.

[185] M. Shunmugavel, M. Goldberg, A. Polishetty, J. Nomani, S. Sun, G. Littlefair, Chip formation characteristics of selective laser melted Ti–6Al–4V, Aust. J. Mech. Eng. 17 (2019) 109–126. https://doi.org/10.1080/14484846.2017.1364833.

[186] M.B. Mhamdi, W. Rajhi, M. Boujelbene, S. Ben Salem, S. Ezeddini, M. Ben Amara, A new quick-stop device to study the chip formation mechanism in metal cutting: Computational and experimental investigation, Proc. Inst. Mech. Eng. Part C J. Mech. Eng. Sci. 236 (2022) 2884–2900. https://doi.org/10.1177/09544062211034210.

[187] H. Ghadbeigi, S.R. Bradbury, C. Pinna, J.R. Yates, Determination of micro-scale plastic strain caused by orthogonal cutting, Int. J. Mach. Tools Manuf. 48 (2008) 228–235. https://doi.org/10.1016/j.ijmachtools.2007.08.017.

[188] L. Guo, H. Wang, H. Liu, Y. Huang, Q. Wei, C.L.A. Leung, Y. Wu, H. Wang, Understanding keyhole induced-porosities in laser powder bed fusion of aluminum and elimination strategy, Int. J. Mach. Tools Manuf. 184 (2023) 103977. https://doi.org/10.1016/j.ijmachtools.2022.103977.

[189] L. Englert, S. Czink, S. Dietrich, V. Schulze, How defects depend on geometry and scanning strategy in additively manufactured AlSi10Mg, J. Mater. Process. Technol. 299 (2022) 117331. https://doi.org/10.1016/j.jmatprotec.2021.117331.

[190] J. Liu, G. Li, Q. Sun, H. Li, J. Sun, X. Wang, Understanding the effect of

scanning strategies on the microstructure and crystallographic texture of Ti-6Al-4V alloy manufactured by laser powder bed fusion, J. Mater. Process. Technol. 299 (2022) 117366. https://doi.org/10.1016/j.jmatprotec.2021.117366.

[191] Z. Yang, L. Zhu, J. Ning, S. Wang, P. Xue, P. Xu, Y. Dun, B. Xin, G. Zhang, Revealing the influence of ultrasound/heat treatment on microstructure evolution and tensile failure behavior in 3D-printing of Inconel 718, J. Mater. Process. Technol. 305 (2022) 117574. https://doi.org/10.1016/j.jmatprotec.2022.117574.

[192] P. Van Cauwenbergh, V. Samaee, L. Thijs, J. Nejezchlebová, P. Sedlák, A. Iveković, D. Schryvers, B. Van Hooreweder, K. Vanmeensel, Unravelling the multi-scale structure–property relationship of laser powder bed fusion processed and heat-treated AlSi10Mg, Sci. Rep. 11 (2021) 6423. https://doi.org/10.1038/s41598-021-85047-2.

[193] D. Zhang, H. Li, X. Guo, Y. Yang, X. Yang, Z. Feng, An insight into size effect on fracture behavior of Inconel 718 cross-scaled foils, Int. J. Plast. 153 (2022) 103274. https://doi.org/10.1016/j.ijplas.2022.103274.

[194] A. Keshavarzkermani, R. Esmaeilizadeh, U. Ali, P.D. Enrique, Y. Mahmoodkhani, N.Y. Zhou, A. Bonakdar, E. Toyserkani, Controlling mechanical properties of additively manufactured hastelloy X by altering solidification pattern during laser powder-bed fusion, Mater. Sci. Eng. A. 762 (2019) 138081. https://doi.org/10.1016/j.msea.2019.138081.

[195] A. Rezaei, A. Rezaeian, A. Kermanpur, M. Badrossamay, E. Foroozmehr, M. Marashi, A. Foroozmehr, J. Han, Microstructural and mechanical anisotropy of selective laser melted IN718 superalloy at room and high temperatures using small punch test, Mater. Charact. 162 (2020) 110200. https://doi.org/10.1016/j.matchar.2020.110200.

[196] X. Wang, J. Kang, T. Wang, P. Wu, T. Feng, L. Zheng, Effect of layer-wise varying parameters on the microstructure and soundness of selective laser melted INCONEL 718 alloy, Materials (Basel). 12 (2019) 2165. https://doi.org/10.3390/ma12132165.

[197] X. Zhang, H. Xu, Z. Li, A. Dong, D. Du, L. Lei, G. Zhang, D. Wang, G. Zhu, B. Sun, Effect of the scanning strategy on microstructure and mechanical anisotropy of Hastelloy X superalloy produced by Laser Powder Bed Fusion, Mater. Charact. 173 (2021) 110951. https://doi.org/10.1016/j.matchar.2021.110951.

[198] G.E. Bean, T.D. McLouth, D.B. Witkin, S.D. Sitzman, P.M. Adams, R.J. Zaldivar, Build Orientation Effects on Texture and Mechanical Properties of Selective Laser Melting Inconel 718, J. Mater. Eng. Perform. 28 (2019) 1942–1949. https://doi.org/10.1007/s11665-019-03980-w.

[199] P.R. Gradl, D.C. Tinker, J. Ivester, S.W. Skinner, T. Teasley, J.L. Bili,

Geometric feature reproducibility for laser powder bed fusion (L-PBF) additive manufacturing with Inconel 718, Addit. Manuf. 47 (2021) 102305. https://doi.org/10.1016/J.ADDMA.2021.102305.

[200] C. Tan, S. Li, K. Essa, P. Jamshidi, K. Zhou, W. Ma, M.M. Attallah, Laser Powder Bed Fusion of Ti-rich TiNi lattice structures: Process optimisation, geometrical integrity, and phase transformations, Int. J. Mach. Tools Manuf. 141 (2019) 19–29. https://doi.org/10.1016/j.ijmachtools.2019.04.002.

[201] H. Yeung, F.H. Kim, M.A. Donmez, J. Neira, Keyhole pores reduction in laser powder bed fusion additive manufacturing of nickel alloy 625, Int. J. Mach. Tools Manuf. 183 (2022) 103957. https://doi.org/10.1016/j.ijmachtools.2022.103957.

[202] S.A. Khairallah, A.T. Anderson, A. Rubenchik, W.E. King, Laser powder-bed fusion additive manufacturing: Physics of complex melt flow and formation mechanisms of pores, spatter, and denudation zones, Acta Mater. 108 (2016) 36–45. https://doi.org/10.1016/J.ACTAMAT.2016.02.014.

[203] L. Guo, H. Liu, H. Wang, Q. Wei, Y. Xiao, Z. Tang, Y. Wu, H. Wang, Identifying the keyhole stability and pore formation mechanisms in laser powder bed fusion additive manufacturing, J. Mater. Process. Technol. 321 (2023) 118153. https://doi.org/10.1016/j.jmatprotec.2023.118153.

[204] M. Pothen, K. Winands, F. Klocke, Compensation of scanner based inertia for laser structuring processes, J. Laser Appl. 29 (2017) 12017. https://doi.org/10.2351/1.4974906.

[205] Z. Liao, A. la Monaca, J. Murray, A. Speidel, D. Ushmaev, A. Clare, D. Axinte, R. M'Saoubi, Surface integrity in metal machining - Part I: Fundamentals of surface characteristics and formation mechanisms, Int. J. Mach. Tools Manuf. 162 (2021) 103687. https://doi.org/10.1016/j.ijmachtools.2020.103687.

[206] Z. Wang, J. Zhang, Z. Xu, J. Zhang, G. Li, H. Zhang, Z. Li, H. ul Hassan, F. Fang, A. Hartmaier, Y. Yan, T. Sun, Crystal anisotropy-dependent shear angle variation in orthogonal cutting of single crystalline copper, Precis. Eng. 63 (2020) 41–48. https://doi.org/10.1016/j.precisioneng.2020.01.006.

[207] D. Axinte, H. Huang, J. Yan, Z. Liao, What micro-mechanical testing can reveal about machining processes, Int. J. Mach. Tools Manuf. 183 (2022) 103964. https://doi.org/10.1016/j.ijmachtools.2022.103964.

[208] Y.J. Lee, H. Wang, Current understanding of surface effects in microcutting, Mater. Des. 192 (2020) 108688. https://doi.org/10.1016/j.matdes.2020.108688.

[209] E. Demir, A Taylor-based plasticity model for orthogonal machining of single-crystal FCC materials including frictional effects, Int. J. Adv. Manuf. Technol. 40 (2009) 847–856. https://doi.org/10.1007/s00170-008-1409-5.

[210] W. Grzesik, Orthogonal and Oblique Cutting Mechanics, in: Adv. Mach. Process. Met. Mater., Elsevier, 2017: pp. 93–111. https://doi.org/10.1016/B978-0-444-63711-6.00006-5.

[211] P.L.B. Oxley, M.C. Shaw, Mechanics of Machining: An Analytical Approach to Assessing Machinability, J. Appl. Mech. 57 (1990) 253–253. https://doi.org/10.1115/1.2888318.

[212] E. Demir, C. Mercan, A physics-based single crystal plasticity model for crystal orientation and length scale dependence of machining response, Int. J. Mach. Tools Manuf. 134 (2018) 25–41. https://doi.org/10.1016/j.ijmachtools.2018.06.004.

[213] H.J. Bunge, Some applications of the Taylor theory of polycrystal plasticity, Krist. Und Tech. 5 (1970) 145–175. https://doi.org/10.1002/crat.19700050112.

[214] M. Yaghoobi, S. Ganesan, S. Sundar, A. Lakshmanan, S. Rudraraju, J.E. Allison, V. Sundararaghavan, PRISMS-Plasticity: An open-source crystal plasticity finite element software, Comput. Mater. Sci. 169 (2019) 109078. https://doi.org/10.1016/j.commatsci.2019.109078.

[215] K.S. Stopka, M. Yaghoobi, J.E. Allison, D.L. McDowell, Simulated effects of sample size and grain neighborhood on the modeling of extreme value fatigue response, Acta Mater. 224 (2022) 117524. https://doi.org/10.1016/j.actamat.2021.117524.

[216] P. Fernandez-Zelaia, Y. Lee, S. Dryepondt, M.M. Kirka, Creep anisotropy modeling and uncertainty quantification of an additively manufactured Ni-based superalloy, Int. J. Plast. 151 (2022) 103177. https://doi.org/10.1016/j.ijplas.2021.103177.

[217] D. Depriester, R. Kubler, MTEX2Gmsh: a tool for generating 2D meshes from EBSD data, J. Open Source Softw. 5 (2020) 2094. https://doi.org/10.21105/joss.02094.

[218] G. Ruan, C. Liu, H. Qu, C. Guo, G. Li, X. Li, Q. Zhu, A Comparative Study on Laser Powder Bed Fusion of In718 Powder Produced by Gas Atomization and Plasma Rotating Electrode Process, SSRN Electron. J. (2022). https://doi.org/10.2139/ssrn.4021763.

[219] I. Yadroitsev, A. Gusarov, I. Yadroitsava, I. Smurov, Single track formation in selective laser melting of metal powders, J. Mater. Process. Technol. 210 (2010) 1624–1631. https://doi.org/10.1016/j.jmatprotec.2010.05.010.

[220] A. Liang, K.S. Pey, T. Polcar, A.R. Hamilton, Effects of rescanning parameters on densification and microstructural refinement of 316L stainless steel fabricated by laser powder bed fusion, J. Mater. Process. Technol. 302 (2022) 117493. https://doi.org/10.1016/j.jmatprotec.2022.117493.

[221] O. Andreau, I. Koutiri, P. Peyre, J.-D. Penot, N. Saintier, E. Pessard, T. De

Terris, C. Dupuy, T. Baudin, Texture control of 316L parts by modulation of the melt pool morphology in selective laser melting, J. Mater. Process. Technol. 264 (2019) 21–31. https://doi.org/10.1016/j.jmatprotec.2018.08.049.

[222] J. Pauza, A. Rollett, Simulation Study of Hatch Spacing and Layer Thickness Effects on Microstructure in Laser Powder Bed Fusion Additive Manufacturing using a Texture-Aware Solidification Potts Model, J. Mater. Eng. Perform. 30 (2021) 7007–7018. https://doi.org/10.1007/s11665-021-06110-7.

[223] W.M. Tucho, P. Cuvillier, A. Sjolyst-Kverneland, V. Hansen, Microstructure and hardness studies of Inconel 718 manufactured by selective laser melting before and after solution heat treatment, Mater. Sci. Eng. A. 689 (2017) 220–232. https://doi.org/10.1016/j.msea.2017.02.062.

[224] E.M. Fayed, D. Shahriari, M. Saadati, V. Brailovski, M. Jahazi, M. Medraj, Influence of homogenization and solution treatments time on the microstructure and hardness of Inconel 718 fabricated by laser powder bed fusion process, Materials (Basel). 13 (2020). https://doi.org/10.3390/ma13112574.

[225] Q. Guo, C. Zhao, M. Qu, L. Xiong, S.M.H. Hojjatzadeh, L.I. Escano, N.D. Parab, K. Fezzaa, T. Sun, L. Chen, In-situ full-field mapping of melt flow dynamics in laser metal additive manufacturing, Addit. Manuf. 31 (2020) 100939. https://doi.org/10.1016/j.addma.2019.100939.

[226] L. Wang, Y. Zhang, H.Y. Chia, W. Yan, Mechanism of keyhole pore formation in metal additive manufacturing, Npj Comput. Mater. 8 (2022) 22. https://doi.org/10.1038/s41524-022-00699-6.

[227] C. Tian, X. Li, Z. Liu, G. Zhi, G. Guo, L. Wang, Y. Rong, Study on grindability of inconel 718 superalloy fabricated by selective laser melting (SLM), J. Mech. Eng. 64 (2018) 319–328. https://doi.org/10.5545/sv-jme.2017.4864.

[228] G.V. de Leon Nope, L.I. Perez-Andrade, J. Corona-Castuera, D.G. Espinosa-Arbelaez, J. Muñoz-Saldaña, J.M. Alvarado-Orozco, Study of volumetric energy density limitations on the IN718 mesostructure and microstructure in laser powder bed fusion process, J. Manuf. Process. 64 (2021) 1261–1272. https://doi.org/10.1016/j.jmapro.2021.02.043.

[229] H.C. Taylor, R.B. Wicker, Impacts of microsecond control in laser powder bed fusion processing, Addit. Manuf. 60 (2022) 103239. https://doi.org/10.1016/j.addma.2022.103239.

[230] Z. Wu, S.P. Narra, A. Rollett, Exploring the fabrication limits of thin-wall structures in a laser powder bed fusion process, Int. J. Adv. Manuf. Technol. 110 (2020) 191–207. https://doi.org/10.1007/s00170-020-05827-4.

[231] G. Wang, X. Chen, C. Qiu, On the macro- and micro-deformation

mechanisms of selectively laser melted damage tolerant metallic lattice structures, J. Alloys Compd. 852 (2021) 156985. https://doi.org/10.1016/j.jallcom.2020.156985.

[232] E.L. Papazoglou, N.E. Karkalos, A.P. Markopoulos, A comprehensive study on thermal modeling of SLM process under conduction mode using FEM, Int. J. Adv. Manuf. Technol. 111 (2020) 2939–2955. https://doi.org/10.1007/s00170-020-06294-7.

[233] B. Liu, G. Fang, L. Lei, An analytical model for rapid predicting molten pool geometry of selective laser melting (SLM), Appl. Math. Model. 92 (2021) 505–524. https://doi.org/10.1016/j.apm.2020.11.027.

[234] A.A. Martin, N.P. Calta, S.A. Khairallah, J. Wang, P.J. Depond, A.Y. Fong, V. Thampy, G.M. Guss, A.M. Kiss, K.H. Stone, C.J. Tassone, J. Nelson Weker, M.F. Toney, T. van Buuren, M.J. Matthews, Dynamics of pore formation during laser powder bed fusion additive manufacturing, Nat. Commun. 10 (2019). https://doi.org/10.1038/s41467-019-10009-2.

[235] T. Iida, Physical properties of liquid metals [IV] surface tension and electronic transport properties of liquid metals, Weld. Int. 8 (1994) 766–770. https://doi.org/10.1080/09507119409548692.

[236] H. Zhang, M. Xu, P. Kumar, C. Li, W. Dai, Z. Liu, Z. Li, Y. Zhang, Enhancement of fatigue resistance of additively manufactured 304L SS by unique heterogeneous microstructure, Virtual Phys. Prototyp. 16 (2021) 125–145. https://doi.org/10.1080/17452759.2021.1881869.

[237] A.R. Balachandramurthi, N.R. Jaladurgam, C. Kumara, T. Hansson, J. Moverare, J. Gårdstam, R. Pederson, On the Microstructure of Laser Beam Powder Bed Fusion Alloy 718 and Its Influence on the Low Cycle Fatigue Behaviour, Materials (Basel). 13 (2020) 5198. https://doi.org/10.3390/ma13225198.

[238] J.J. Marattukalam, D. Karlsson, V. Pacheco, P. Beran, U. Wiklund, U. Jansson, B. Hjörvarsson, M. Sahlberg, The effect of laser scanning strategies on texture, mechanical properties, and site-specific grain orientation in selective laser melted 316L SS, Mater. Des. 193 (2020) 108852. https://doi.org/10.1016/j.matdes.2020.108852.

[239] L.L. Li, Z.J. Zhang, P. Zhang, J.B. Yang, Z.F. Zhang, Distinct fatigue cracking modes of grain boundaries with coplanar slip systems, Acta Mater. 120 (2016) 120–129. https://doi.org/10.1016/j.actamat.2016.06.032.

[240] M.F. Ashby, The deformation of plastically non-homogeneous materials, Philos. Mag. 21 (1970) 399–424. https://doi.org/10.1080/14786437008238426.

[241] W. Amin, M.A. Ali, N. Vajragupta, A. Hartmaier, Studying Grain Boundary Strengthening by Dislocation-Based Strain Gradient Crystal Plasticity Coupled with a Multi-Phase-Field Model, Materials (Basel). 12 (2019) 2977.

https://doi.org/10.3390/ma12182977.

[242] C. de Sansal, B. Devincre, L.P. Kubin, Grain Size Strengthening in Microcrystalline Copper: A Three-Dimensional Dislocation Dynamics Simulation, Key Eng. Mater. 423 (2009) 25–32. https://doi.org/10.4028/www.scientific.net/KEM.423.25.

[243] S. Haouala, J. Segurado, J. LLorca, An analysis of the influence of grain size on the strength of FCC polycrystals by means of computational homogenization, Acta Mater. 148 (2018) 72–85. https://doi.org/10.1016/j.actamat.2018.01.024.

[244] A. Udupa, K. Viswanathan, Y. Ho, S. Chandrasekar, The cutting of metals via plastic buckling, Proc. R. Soc. A Math. Phys. Eng. Sci. 473 (2017) 20160863. https://doi.org/10.1098/rspa.2016.0863.

[245] B.G. I Taylor, R. Society Yarrow Professor, The mechanism of plastic deformation of crystals. Part I.—Theoretical, Proc. R. Soc. London. Ser. A, Contain. Pap. a Math. Phys. Character. 145 (1934) 362–387. https://doi.org/10.1098/rspa.1934.0106.

[246] P. Franciosi, M. Berveiller, A. Zaoui, Latent hardening in copper and aluminium single crystals, Acta Metall. 28 (1980) 273–283. https://doi.org/10.1016/0001-6160(80)90162-5.

[247] S. Katayama, H. Miyamoto, A. Vinogradov, S. Hashimoto, Influence of a Slip Plane Orientation with Respect to the Shear Plane of ECAP on Microstructure of Copper Single Crystal Subject to One Pressing at Room Temperature, Mater. Sci. Forum. 584–586 (2008) 387–392. https://doi.org/10.4028/www.scientific.net/MSF.584-586.387.

[248] E. Soufian, R. Darabi, M. Abouridouane, A. Reis, T. Bergs, Numerical predictions of orthogonal cutting–induced residual stress of super alloy Inconel 718 considering dynamic recrystallization, Int. J. Adv. Manuf. Technol. 122 (2022) 601–617. https://doi.org/10.1007/s00170-022-09846-1.

[249] M.P. Petkov, E. Elmukashfi, E. Tarleton, A.C.F. Cocks, Evaluation of local stress state due to grain-boundary sliding during creep within a crystal plasticity finite element multi-scale framework, Int. J. Mech. Sci. 211 (2021) 106715. https://doi.org/10.1016/j.ijmecsci.2021.106715.

[250] H.M. Zbib, T. Diaz de la Rubia, A multiscale model of plasticity, Int. J. Plast. 18 (2002) 1133–1163. https://doi.org/10.1016/S0749-6419(01)00044-4.

[251] A. la Monaca, D.A. Axinte, Z. Liao, R. M'Saoubi, M.C. Hardy, Towards understanding the thermal history of microstructural surface deformation when cutting a next generation powder metallurgy nickel-base superalloy, Int. J. Mach. Tools Manuf. 168 (2021) 103765. https://doi.org/10.1016/j.ijmachtools.2021.103765.

[252] E. Paccou, M. Mokhtari, C. Keller, J. Nguejio, W. Lefebvre, X. Sauvage, S.

Boileau, P. Babillot, P. Bernard, E. Bauster, Investigations of powder reusing on microstructure and mechanical properties of Inconel 718 obtained by additive manufacturing, Mater. Sci. Eng. A. 828 (2021) 142113. https://doi.org/10.1016/j.msea.2021.142113.

[253] L. Jiang, H. Fu, H. Zhang, J. Xie, Physical mechanism interpretation of polycrystalline metals' yield strength via a data-driven method: A novel Hall–Petch relationship, Acta Mater. 231 (2022) 117868. https://doi.org/10.1016/j.actamat.2022.117868.

[254] L. Li, H. Chen, Z. Liao, Y. Yang, D. Axinte, Investigation of the grain deformation to orthogonal cutting process of the textured Alloy 718 fabricated by laser powder bed fusion, Int. J. Mach. Tools Manuf. 190 (2023) 104050. https://doi.org/10.1016/j.ijmachtools.2023.104050.

[255] C. Ni, L. Zhu, Z. Zheng, J. Zhang, Y. Yang, J. Yang, Y. Bai, C. Weng, W.F. Lu, H. Wang, Effect of material anisotropy on ultra-precision machining of Ti-6Al-4V alloy fabricated by selective laser melting, J. Alloys Compd. 848 (2020) 156457. https://doi.org/10.1016/j.jallcom.2020.156457.

[256] J. Duan, D. Farrugia, C. Davis, Z. Li, Texture Development During Annealing in a Low-Carbon Formable Steel Containing Impurities from Increased Scrap Use, Metall. Mater. Trans. A. 54 (2023) 983–997. https://doi.org/10.1007/s11661-022-06952-3.

[257] E. Uhlmann, S. Henze, K. Brömmelhoff, Influence of the Built-up Edge on the Stress State in the Chip Formation Zone During Orthogonal Cutting of AISI1045, Procedia CIRP. 31 (2015) 310–315. https://doi.org/10.1016/j.procir.2015.03.101.

[258] L. Saraf, Kernel Average Misorientation Confidence Index Correlation from FIB Sliced Ni-Fe-Cr alloy Surface, Microsc. Microanal. 17 (2011) 424–425. https://doi.org/10.1017/S1431927611002996.

[259] P. Karimi, E. Sadeghi, P. Åkerfeldt, J. Ålgårdh, J. Andersson, Influence of successive thermal cycling on microstructure evolution of EBM-manufactured alloy 718 in track-by-track and layer-by-layer design, Mater. Des. 160 (2018) 427–441. https://doi.org/10.1016/j.matdes.2018.09.038.

[260] J.H. Park, G.B. Bang, K.-A. Lee, Y. Son, W.R. Kim, H.G. Kim, Effect on microstructural and mechanical properties of Inconel 718 superalloy fabricated by selective laser melting with rescanning by low energy density, J. Mater. Res. Technol. 10 (2021) 785–796. https://doi.org/10.1016/j.jmrt.2020.12.053.

[261] S.N. Kumaran, S.K. Sahoo, C. Haase, L.A. Barrales-Mora, L.S. Toth, Nano-structuring of a high entropy alloy by severe plastic deformation: Experiments and crystal plasticity simulations, Acta Mater. 250 (2023) 118814. https://doi.org/10.1016/j.actamat.2023.118814.

[262] G.G. Ye, M.Q. Jiang, S.F. Xue, W. Ma, L.H. Dai, On the instability of chip

flow in high-speed machining, Mech. Mater. 116 (2018) 104–119. https://doi.org/10.1016/j.mechmat.2017.02.006.

[263] B. Zhou, Y. Li, L. Wang, H. Jia, X. Zeng, The role of grain boundary plane in slip transfer during deformation of magnesium alloys, Acta Mater. 227 (2022) 117662. https://doi.org/10.1016/j.actamat.2022.117662.

[264] Q. Teng, S. Li, Q. Wei, Y. Shi, Investigation on the influence of heat treatment on Inconel 718 fabricated by selective laser melting: Microstructure and high temperature tensile property, J. Manuf. Process. 61 (2021) 35–45. https://doi.org/10.1016/j.jmapro.2020.11.002.

Appendix A

The matlab code used to mesh EBSD data via Gmsh and MTEX:

```
clear all
clc
%% Import Script for EBSD Data
%% Specify Crystal and Specimen Symmetries
% crystal symmetry
CS = {'notIndexed',...
crystalSymmetry('m-3m',  [3.157  3.157  3.157],  'mineral',  'Ni'  ,
'color', 'red'),...
%crystalSymmetry('6/mmm',  'mineral',  'Ni  Niobium'  ,  'color',
'green')
};
SS = specimenSymmetry('cubic');


% % path to files
pname = '~\data';
% which files to be imported
fname = [pname '\data.ctf'];


%% Import the Data
% create an EBSD variable containing the data
ebsd = EBSD.load(fname,'CS',CS,'ColumnNames', ...
{'Phase' 'x' 'y' 'Bands' 'Error' 'Euler1' 'Euler2' 'Euler3' 'MAD'
'BC' 'BS'}, 'Bunge')

setMTEXpref('xAxisDirection','west');
setMTEXpref('yAxisDirection','south');
setMTEXpref('zAxisDirection','OutofPlane');


%% restricting to a region of interest
region = [0 0 58 38] * 10;%original region
figure(1);plot (ebsd)
rectangle('position',region,'edgecolor','b','linewidth',2)
condition = inpolygon(ebsd, region);
ebsd = ebsd(condition);
ebsd = rotate(ebsd,rotation('axis',yvector,'angle', 0*degree));


%% Filling missing data
ebsd = ebsd('indexed');
cS = crystalShape.cube(ebsd('Ni').CS);
%reconstruct the grain structure
%,ebsd.mis2mea

[grains,ebsd.grainId] = calcGrains(ebsd,'angle', 15*degree);
```

```
% remove some very small grains
ebsd(grains(grains.grainSize<10)) = [];


%% redo grain segementation
grains = calcGrains(ebsd('indexed'),'boundary','tight');


%%smooth grain boundaries
grains = cond_smooth(grains);
ebsd = smooth(ebsd, splineFilter,'fill',grains);
ebsd = ebsd('indexed');


%% define an ipf color for phase
ipfKey = ipfColorKey(ebsd);
ipfKey.inversePoleFigureDirection = vector3d.Y;
colors = ipfKey.orientation2color(ebsd.orientations);

%% mesh
ebsd=ebsd('indexed');
grains=calcGrains(ebsd);
V=grains.V;
ori=min(V);
grains.V=V - repmat(ori,size(grains.V,1),1);
G=gmshGeo(grains);
max(grains.V);
G=simplify(G);

mesh(G,'hex_01T_top_final.inp','ElementSize',5,'elementType','Hex
Only','thickness', 2);
exportGrainProps(G,'hex_01T_top_final_normal.csv')
```

Code for PRISMS-Plasticity simulation:

```
# Listing of Parameters
# ---------------------

#####################################
# FE parameters
#####################################
# Basis function interpolation order (1-linear)
set Order of finite elements                        = 1

# Quadrature point order n^3 (2->8 quadrature points)
set Order of quadrature                             = 2

#####################################
# Domain parameters
#####################################
# Number of physical dimensions for the simulation
set Number of dimensions                            = 3

# The size of the domain in the x direction.
set Domain size X                                   = 1.0

# The size of the domain in the y direction.
set Domain size Y                                   = 1.0

# The size of the domain in the z direction.
set Domain size Z                                   = 1.0

#####################################
# Mesh parameters
#####################################
# The number of mesh subdivisions in the x direction.
set Subdivisions X                                  = 1

# The number of mesh subdivisions in the y direction.
set Subdivisions Y                                  = 1

# The number of mesh subdivisions in the z direction.
set Subdivisions Z                                  = 1

# The number of initial refinements of the coarse mesh.
set Refine factor                                   = 3

# Only written for serial runs and if number of elements < 10000
set Write Mesh To EPS                               = false

#####################################
# Solver output parameters
#####################################
# Flag to write output vtu and pvtu files
set Write Output                                    = true

# Output Directory
# Need to create directory before using this. Will be corrected
in future versions of the software
```

```
set Output Directory                              = results

# Skip Output Steps
set Skip Output Steps                             = 0

# Output Equivalent strain
set Output Equivalent strain                      = true

# Output Equivalent stress
set Output Equivalent stress                      = true

# Output Grain ID
set Output Grain ID                               = true

# Output Twin fractions
set Output Twin fractions                         = false

####################################
# Boundary condition information
####################################
#File name containing BC information
set Boundary condition filename                   = BCinfo.txt

#BC file number of header lines
set BC file number of header lines                = 2

#Number of boundary conditions
set Number of boundary conditions                 = 4

####################################
# Solver parameters
####################################
#delta T for every increment
set Time increments                               = 0.005

#Total simulation time
set Total time                                    = 1

# Maximum iterations for linear solver
set Maximum linear solver iterations              = 50000

# Relative linear solver tolerance
set Relative linear solver tolerance              = 1.0e-10

# Maximum no. of non-linear iterations
set Maximum non linear iterations                 = 4


####################################
# Elasticity parameters
####################################

#   Elastic Stiffness Matrix -Voigt Notation (MPa)
set Elastic Stiffness row 1                       = 170.0e3,
124.0e3, 124.0e3, 0, 0, 0

#   Elastic Stiffness Matrix -Voigt Notation (MPa)
```

```
set Elastic Stiffness row 2                      = 124.0e3,
170.0e3, 124.0e3, 0, 0, 0

#   Elastic Stiffness Matrix -Voigt Notation (MPa)
set Elastic Stiffness row 3                      = 124.0e3,
124.0e3, 170.0e3, 0, 0, 0

#   Elastic Stiffness Matrix -Voigt Notation (MPa)
set Elastic Stiffness row 4                      = 0, 0, 0,
75.0e3, 0, 0

#   Elastic Stiffness Matrix -Voigt Notation (MPa)
set Elastic Stiffness row 5                      = 0, 0, 0, 0,
75.0e3, 0

#   Elastic Stiffness Matrix -Voigt Notation (MPa)
set Elastic Stiffness row 6                      = 0, 0, 0, 0, 0,
75.0e3

####################################
# Slip parameters
####################################
# Number of Slip Systems
set Number of Slip Systems                       = 12

# Latent Hardening Ratio
set Latent Hardening Ratio filename                       =
LatentHardeningRatio.txt

# RSS of the slip sytems
set Initial Slip Resistance                      = 16.0, 16.0,
16.0, 16.0, 16.0, 16.0, 16.0, 16.0, 16.0, 16.0, 16.0, 16.0

# Heardening moduli of slip systems
set Initial Hardening Modulus                    = 180.0, 180.0,
180.0, 180.0, 180.0, 180.0, 180.0, 180.0, 180.0, 180.0, 180.0,
180.0

# Power law coefficient
set Power Law Exponent                           = 2.25, 2.25,
2.25, 2.25, 2.25, 2.25, 2.25, 2.25, 2.25, 2.25, 2.25, 2.25

# Saturation stress
set Saturation Stress                            = 148.0, 148.0,
148.0, 148.0, 148.0, 148.0, 148.0, 148.0, 148.0, 148.0, 148.0,
148.0

# Slip Directions File
set Slip Directions File                         =
slipDirections.txt

# Slip Normals File
set Slip Normals File                            =
slipNormals.txt

####################################
# Constitutive model parameters
```

```
####################################
# Stress tolerance for the yield surface (MPa)
set Stress Tolerance                             = 1.0e-6


# Maximum no. of active slip search iterations
set Max Slip Search Iterations                   = 1

# Maximum no. of iterations to achieve non-linear convergence
set Max Solver Iterations                        = 1


####################################
# Input microstructure
####################################
# Number of voxels in x direction
set Voxels in X direction                        = 32

# Number of voxels in y direction
set Voxels in Y direction                        = 32

# Number of voxels in z direction
set Voxels in Z direction                        = 32

# Grain ID file name
set Grain ID file name                           = grainID.txt

# Number of header Lines in grain ID file
set Header Lines GrainID File                    = 5

# Grain orientations file name
set Orientations file name                       =
orientations.txt
```

Slip Directions

```
  0 0.707   -0.707
 -0.707 0.0 0.707
  0.707 -0.707  0.0
  0 -0.707  -0.707
  0.707 0.0 0.707
 -0.707 0.707   0.0
  0 0.707   -0.707
  0.707 0.0 0.707
 -0.707 -0.707  0.0
  0 -0.707  -0.707
 -0.707 0.0 0.707
  0.707 0.707   0.0
```

Slip Normals

```
0.577  0.577       0.577
 0.577       0.577       0.577
 0.577       0.577       0.577
```

```
-0.577      -0.577       0.577
-0.577      -0.577       0.577
-0.577      -0.577       0.577
-0.577       0.577       0.577
-0.577       0.577       0.577
-0.577       0.577       0.577
 0.577      -0.577       0.577
 0.577      -0.577       0.577
 0.577      -0.577       0.577
```

Latent Hardening Ratio

```
1 1 1 1.4 1.4 1.4 1.4 1.4 1.4 1.4 1.4 1.4
1 1 1 1.4 1.4 1.4 1.4 1.4 1.4 1.4 1.4 1.4
1 1 1 1.4 1.4 1.4 1.4 1.4 1.4 1.4 1.4 1.4
1.4 1.4 1.4 1 1 1 1.4 1.4 1.4 1.4 1.4 1.4
1.4 1.4 1.4 1 1 1 1.4 1.4 1.4 1.4 1.4 1.4
1.4 1.4 1.4 1 1 1 1.4 1.4 1.4 1.4 1.4 1.4
1.4 1.4 1.4 1.4 1.4 1.4 1 1 1 1.4 1.4 1.4
1.4 1.4 1.4 1.4 1.4 1.4 1 1 1 1.4 1.4 1.4
1.4 1.4 1.4 1.4 1.4 1.4 1 1 1 1.4 1.4 1.4
1.4 1.4 1.4 1.4 1.4 1.4 1.4 1.4 1.4 1 1 1
1.4 1.4 1.4 1.4 1.4 1.4 1.4 1.4 1.4 1 1 1
1.4 1.4 1.4 1.4 1.4 1.4 1.4 1.4 1.4 1 1 1
```

Grain ID

```
**Total header lines = 5
**Grain ID File
**3D Volume has dimensions [32 x32 x 32] voxels
**Data arranged in a 2D array of 1024 x 32 integer values
**
14 14 14 27 27 84 84 84 84 20 20 20 20 20 20 20 20 20 30 30 30 66
29 29 29 24 24 24 14 14 14 14
14 14 14 14 27 84 84 84 20 20 20 20 20 20 20 20 20 30 30 30 30 66
66 29 24 24 24 77 77 77 77 14
77 77 77 77 77 84 84 84 20 20 20 20 20 20 20 20 30 30 30 30 30 66
66 24 24 24 77 77 77 77 77 77
77 77 77 77 77 5 5 5 20 20 20 20 20 50 50 30 30 30 30 30 30 30 66
66 77 77 77 77 77 77 77 77
77 77 77 77 77 5 5 5 50 50 50 50 50 50 50 50 50 50 30 30 86 86 73
73 73 63 63 63 63 77 77 77
…
```

Corresponding Orientations

```
**Grain ID, Rodrigues vector r_x, r_y, r_z
1 0.217235622228494 0.119677575300848 -0.315639678263808
2 0.337158795969753 -0.136385831569383 -0.0451232414784514
3 -0.112751674092984 0.306554302202483 0.0417816337773640
4 -0.318341596949184 0.394231954524069 -0.124733568696447
5 0.337262392546855 -0.137704882272509 -0.0466765073250908
6 0.405755162068059 0.209949108571507 0.318682476064558
```

```
7 0.0384581188524811 -0.0156554309584217 -0.110033527772506
8 0.114266801597890 -0.122128540704537 0.340913752088645
9 0.114266801597890 -0.122128540704537 0.340913752088645
10 -0.0152373705120258 0.0867637330697546 0.309727833412636
11 0.404431320072339 -0.135953749658450 0.0878321668096234
12 0.00874483513602116 -0.301944119310717 -0.215174195972202
13 0.183633720338559 0.0840944417145517 -0.0783020965347754
14 0.184600435776865 0.0845148154118419 -0.0755861098475753
15 0.376714217606242 -0.0769718445481327 -0.306309587082006
16 -0.0268810258453196 0.247476517304731 0.334952778670146
17 -0.192363046325014 -0.190945502218549 -0.117732130057011
18 -0.0121089802612619 0.0910642520713899 -0.0359080748300855
19 0.408973870050836 -0.345658997758128 0.162105311779461
20 -0.0286187617251639 0.246256341385179 0.334730354894685
21 -0.282004934534613 -0.172317214824116 0.0793734069367810
22 -0.190487384360723 -0.190697736283995 -0.117985602736374
23 0.258120898010547 -0.232625552814395 -0.279335766714658
24 0.309800975374891 0.215831386191239 -0.103964817254165
25 0.320292786872595 0.139609259824124 0.147513567643945
26 0.289292995457164 0.340683117783460 -0.247997056884472
27 0.403936762049908 -0.346242989088756 0.158669133209096
28 0.103609428187153 0.0520698429389427 -0.121992477331553
29 0.390408813853531 0.0908116835710692 -0.0316532186361649
30 0.0936598848269736 -0.0206395149168438 -0.393840610562767
…
```

Appendix B

This XML. format code is used for editing laser parameters and vector position:

```
<?xml version="1.0" encoding="utf-8"?>
<Build>
   <Layer>
      <Z>0</Z>
      <Datablock>
         <P>135</P>
         <S>800</S>
         <Vector>
            <Xs>27.415</Xs>
            <Ys>22</Ys>
            <Xe>27.435</Xe>
            <Ye>22</Ye>
         </Vector>
      </Datablock>
      <Datablock>
         <P>135</P>
         <S>800</S>
         <Vector>
            <Xs>27.635</Xs>
            <Ys>22</Ys>
            <Xe>27.675</Xe>
            <Ye>22</Ye>
         </Vector>
      </Datablock>
      <Datablock>
         <P>135</P>
         <S>800</S>
         <Vector>
            <Xs>27.875</Xs>
            <Ys>22</Ys>
            <Xe>27.935</Xe>
            <Ye>22</Ye>
         </Vector>
      </Datablock>

…(the same structure until the end)

      <Datablock>
         <P>135</P>
         <S>800</S>
         <Vector>
            <Xs>66.92</Xs>
            <Ys>24.72</Ys>
            <Xe>66.84</Xe>
            <Ye>24.72</Ye>
         </Vector>
      </Datablock>
```

```
      <Datablock>
         <P>135</P>
         <S>800</S>
         <Vector>
            <Xs>66.84</Xs>
            <Ys>24.72</Ys>
            <Xe>66.76</Xe>
            <Ye>24.72</Ye>
         </Vector>
      </Datablock>
      <Datablock>
         <P>135</P>
         <S>800</S>
         <Vector>
            <Xs>66.76</Xs>
            <Ys>24.72</Ys>
            <Xe>66.68</Xe>
            <Ye>24.72</Ye>
         </Vector>
      </Datablock>
      <Datablock>
         <P>135</P>
         <S>800</S>
         <Vector>
            <Xs>66.68</Xs>
            <Ys>24.72</Ys>
            <Xe>66.6</Xe>
            <Ye>24.72</Ye>
         </Vector>
      </Datablock>
   </Layer>
</Build>
```

Appendix C

Publications as a co-author

Hao Chen, Liangyi Sun, **Lingshan Li**, Weiqiang Zhu, Gong, Q., Castro, R.D., Adam Rushworth. Microstructure evolution and grain growth characteristics of IN625 in laser surface melting: Effects of laser power and scanning speed. J. Mater. Process. Technol. 331, 118525. 2024, https://doi.org/10.1016/j.jmatprotec.2024.118525

Hao Chen, **Lingshan Li**, Rui Yang, Weiqiang Zhu, Adam Rushworth, Yichuan Yin, Xiaoming Wang, "Microstructure and thermophysical properties of as-cast CoNiCrAl bond coat alloys at different Al contents". J. Alloys Compd. 918, 2022, https://doi.org/10.1016/j.jallcom.2022.165575

Hao Chen, Zhuoer Li, **Lingshan Li**, Hanmo Guo, Adam Rushworth, Xiaoming Wang, "Microstructure evolution of as-cast CoNiCrAl bond coat alloys after isothermal heat treatments". Mater. Charact, 204, 2023, https://doi.org/10.1016/j.matchar.2023.113183

Hao Chen, Jingchen Li, **Lingshan Li**, Weiqiang Zhu, Liang Wei, Yichuan Yin, Xiaoming Wang, "Experimental and modelling study on the β-phase depletion behaviour under the growth of spinel oxides and alumina in a CoNiCrAlY coating", Surf. Coatings Technol, 429, 2022, https://doi.org/10.1016/j.surfcoat.2021.127859

Hao Chen, M. Fan, **Lingshan Li**, Weiqiang Zhu, Haonan Li, Jingchen Li, Yichuan Yin, "Effects of internal oxide contents on the oxidation and β-phase depletion behaviour in HOVF CoNiCrAlY coatings", Surf. Coatings Technol, 424, 2021, https://doi.org/10.1016/j.surfcoat.2021.127666

Conference

Li Lingshan, Chen Hao, Liao Zhirong, "The 14th National Conference on Surface Engineering", May 2024, Ningbo, China